

UNIVERSITY OF BELGRADE

FACULTY OF PHYSICS

Bojana N. Blagojević

**Theoretical Predictions of Highly Energetic
Particles Energy Loss in Quark-Gluon
Plasma**

Doctoral Dissertation

Belgrade, 2018

УНИВЕРЗИТЕТ У БЕОГРАДУ
ФИЗИЧКИ ФАКУЛТЕТ

Бојана Н. Благојевић

Теоријска предвиђања губитака енергије високо
енергијских честица у кварк- глюонској плазми

докторска дисертација

Београд, 2018

Ментор:

научни саветник, др, Магдалена Ђорђевић,

Универзитет у Београду,

Институт за физику Београд

Чланови комисије:

1. редовни професор, проф. др, Воја Радовановић,

Универзитет у Београду,

Физички факултет

2. редовни професор, проф. др, Петар Аџић,

Универзитет у Београду,

Физички факултет

Датум одбране: 27. децембар 2018. године

Acknowledgments

I would like to express my gratitude to my advisor, Magdalena Djordjevic, for her teaching, support and valuable advice throughout my PhD studies: her brilliant intuition, great knowledge, dedication to this field and her students, positive attitude and inexhaustible ideas.

I would also like to thank Marko Djordjevic and Lidia Zivkovic for their collaboration on high energy project.

I am grateful to Maja Buric, Voja Radovanovic, Dragan Popovic, Djordje Sijacki, Petar Adzic, Ljiljana Simic for their teaching and support throughout my undergraduate and PhD studies. I am also grateful to my Diploma thesis advisor Marija Vranjes Milosavljevic for her guidance through my first scientific year.

Thank you to Jussi Auvinen for discussions and encouragement.

I would like to thank Marko Djordjevic for his dedicated mentoring on biophysics and computational systems biology and to Andjela Rodic and Jelena Guzina for collaboration and creating friendly atmosphere.

I would especially like to thank my husband to be Marko Ilic, my parents Boja and Nedo Blagojevic, my sister Marjana Blagojevic and Jean Michael for their patience, love and support.

This work is supported by the European Research Council, grant ERC-2016-COG: 725741, by Marie Curie International Reintegration Grant within the 7th European Community Framework Programme PIRG08-GA-2010-276913 and by the Ministry of Science and Technological Development of the Republic of Serbia, under project numbers ON171004 and ON173052.

Theoretical Predictions of Highly Energetic Particles Energy Loss in Quark-Gluon Plasma

Today, it is considered that the reached collision energies in the ultra-relativistic heavy ion collisions (HIC) at the RHIC and the LHC are sufficiently high for the new state of matter – quark-gluon plasma (QGP), consisting of liberated quarks, anti-quarks and gluons, to be created under controlled experimental conditions. Upon establishing that QGP is created, one of the main goals of heavy ion program at the RHIC and the LHC is understanding the properties of newly created state of matter. Thus created QGP is constituted of low-energetic particles, which represent $\sim 99.9\%$ of quarks and gluons created in ultra-relativistic HIC. The remaining $\sim 0.1\%$ are high-energy particles (tomographic probes), which are the subject of this thesis.

The suppression of high transverse momentum (p_{\perp}) particles is considered to be an excellent tomographic tool for mapping the properties of QGP, which requires comparison of the available suppression data with the theoretical predictions. This comparison tests various theoretical models and provides an insight into the underlying QGP physics. Since jet-quenching is a consequence of the leading parton energy loss in created medium, an accurate energy loss calculation is generally considered to be the crucial ingredient for obtaining the reliable suppression predictions. To this end, the subjects of this thesis are: *i)* testing the up-to-date dynamical energy loss model and the numerical procedure, developed by Djordjevic *et al.*, against the experimental suppression data; *ii)* studying the importance of different ingredients of this model; and *iii)* implementing improvements, i.e. relaxing one of the approximations, in such model predecessor.

The advantage of the dynamical energy loss formalism, which is based on a finite temperature pQCD calculations, is that it takes into account more details of high p_{\perp} parton-medium interactions than any other energy loss model, and uses no fitting parameters when comparing to experimental data. Thus, it includes: both radiative and collisional energy loss in finite size optically thin medium, dynamical scattering centers, finite magnetic mass and running coupling. This state-of-the-art model is further incorporated in up-to-date numerical procedure, that can generate suppression predictions. This procedure also includes: initial parton momentum

distribution, multi-gluon and path-length fluctuations, as well as, fragmentation and decay functions.

Regarding the first task of this thesis, note that the model is more reliable the more it is capable of providing matching suppression predictions with experimental data for broader range of probes (both light and heavy flavor), collision energies (both RHIC and LHC) and experimental conditions (all available centrality ranges). Therefore, apart for extending the dynamical energy loss formalism towards generating suppression predictions for non-central collisions, we also provided suppression predictions for both RHIC and LHC energies (200 GeV and 2.76 TeV, respectively) and diverse set of particles (light: charged hadrons, neutral pions; heavy: D mesons and non-prompt J/ψ). These predictions were generated by the same theoretical formalism and within the same numerical procedure. We obtained a very good agreement for all probes, collision energies and all (at that time) available non-central experimental suppression measurements, for all momentum ranges larger than 10 GeV. Our results imply that dynamical energy loss model, incorporated in above mentioned numerical procedure, can realistically model the jet-medium interactions within QGP created in ultra-relativistic HIC, and the adequacy of applying pQCD in modeling these interactions.

Another convenience of the dynamical energy loss model and the numerical procedure presents its reliable predictive power. Therefore, we predicted that suppressions in central 2.76 TeV and 5.02 TeV $Pb + Pb$ collisions at LHC are practically the same for light probes (charged hadrons), which afterwards obtained its experimental validation. Another prediction for 5.02 TeV collision energy is that, at the high momentum range $p_{\perp} > 100$ GeV, B and D meson suppressions will nearly overlap. Additionally, at the same momentum range, we also predict unexpected suppression decrease of charged hadron compared to heavier probes, such as D and B mesons at central 5.02 TeV collisions, due to fragmentation functions effect. This, at the time, presented a pure prediction to be tested in the future.

We also address the issue of which particles and at which p_{\perp} range are the most adequate for mass tomography of the QGP. Namely, particles with different masses should interact differently (lose different amounts of energy) in the QGP medium, which highlights the mass tomography as another excellent tool for mapping the

QGP properties. We obtained that notable mass hierarchy (tomography effects) for single particles can be observed below 50 GeV, due to different suppressions (energy losses) of underlying bottom, on one side, and the charm/light quarks, on the other. We suggest that this study provides guidelines on where the future experimental efforts, regarding the mass tomography, should be focused: on $p_{\perp} < 50$ GeV region and on measuring B meson suppression, as a clear b suppression probe, instead of non-prompt J/ψ .

In the second part of the thesis, upon obtaining experimental verification for the dynamical energy loss model and the numerical procedure, we address the relative importance of the above mentioned energy loss ingredients in obtaining accurate suppression predictions. The significance of this undertaking reflects in a fact that all these effects have to be included (based on theoretical grounds), but however, at that time, the role of each effect in adequately explaining the experimental data was unclear, while other approaches to suppression predictions neglected some or most of these effects. To this end, we studiously examine how different ingredients affect D meson suppression predictions (clear energy loss probe) at top RHIC and LHC energies. We obtained that the most important effect in modeling the jet-medium interactions is taking into account that medium constituents are dynamical (moving) particles, which leads also to inclusion of collisional, apart from the usual radiative energy loss. However, we found that all other effects are also important, and need to be included, as they contribute to a finer agreement with the data. Therefore, we conclude that the robust agreement between the theoretical predictions and the experimental data is a cumulative effect of all considered energy loss effects.

In the final (theoretical) part of this thesis, we relax one of the most common, and most widely used, assumptions used in calculating radiative energy loss of high p_{\perp} particles in QGP – the soft-gluon approximation. This approximation assumes that radiated gluon carries away only a small fraction of initial parton’s energy and longitudinal momentum. While the soft-gluon approximation is convenient, its validity was questioned by the obtained considerable radiative energy loss within different theoretical models. On the other hand, the dynamical energy loss model, enclosing the same approximation, reported a robust agreement with experimental suppression data (as previously mentioned), implicitly suggesting the applicability of this

approximation. However, the approximation clearly breaks-down for intermediate momentum range $5 < p_{\perp} < 10$ GeV (note that our predictions were reliable for p_{\perp} only above 10 GeV), and primarily for gluons, due to the relative color factor of $9/4$ compared to quarks. Therefore, we relax the soft-gluon approximation for high p_{\perp} gluons, and since the calculations are technically very demanding, we divided them into several steps: *1)* first for massless gluons in the system of static scattering centers (within GLV formalism), *2)* then we include effective gluon mass (within DGLV formalism, a predecessor of dynamical energy loss model) and *3)* finally we discuss generalizing this relaxation to the dynamical QGP medium.

The obtained analytical expressions to the 1st order in opacity beyond soft-gluon (*bsg*) approximation are quite different and significantly more complex compared to their soft-gluon (*sg*) analogons. However, we surprisingly obtained that numerical predictions for fractional radiative energy loss and number of radiated gluons are only slightly altered compared to the soft-gluon case, although in opposite directions, so that their superposition results in almost indistinguishable suppression predictions in *bsg* and *sg* cases. Additionally, we obtained that, due to exponentially decreasing initial gluon momentum distribution, the main contribution to suppression predictions comes from the region $x \lesssim 0.4$, making this region the most relevant one for differentiating between *bsg* and *sg* suppression predictions. Consequently, high p_{\perp} quarks are even less likely to be affected by this relaxation. This implies that, contrary to commonly held doubts, the soft-gluon approximation remains well-founded within DGLV formalism. Finally, based on our derivations, we also expect that the soft-gluon approximation can be reliably applied when dynamical medium is considered, which is out-of-scope of this thesis, and remains to be rigorously tested in the future.

Keywords: heavy-ion collisions, parton's energy loss, suppression, high p_{\perp} particle, beyond soft-gluon approximation, nuclear modification factor

Physics

High-energy and nuclear physics

UDK number: 539.12 (043.3)

CONTENTS

List of Figures	viii
1. Introduction	1
1.1. A brief introduction to QCD	1
1.2. Phases of hadronic matter, introduction of QGP and its importance	5
1.2.1. Lattice QCD at finite temperature	6
1.2.2. Detailed description of hadronic matter phase diagram	12
1.2.3. The importance of QGP studying	13
1.3. The ultra-relativistic heavy ion collisions	14
1.3.1. Overview of heavy ion colliders	15
1.3.2. Space-time picture of ultra-relativistic heavy ion collisions	17
1.4. Probes of QGP matter	23
1.4.1. The pQCD factorization formula	23
1.4.2. Observables classification	26
1.4.3. The nuclear modification factor	29
1.5. Empirical evidence of QGP discovery	31
1.5.1. Historically	31
1.5.2. The updated experimental evidence	35
1.6. Outline of the thesis	46
2. Historical overview of energy loss models used in this thesis	48
2.1. Overview of collisional energy loss models	48
2.2. Overview of radiative energy loss models for static scatterers: GLV and DGLV	50
2.2.1. GLV	51
2.2.2. DGLV	54
3. Dynamical energy loss model and numerical procedure	56
3.1. The historical development of the model: From static to dynamical	57
3.2. Suppression computational formalism	64
4. Experimental validation of dynamical energy loss model and numerical	

procedure	69
4.1. A very good agreement with suppression data	69
4.2. The predictions for upcoming measurements	75
4.3. Conclusions	80
5. The importance of different energy loss effects in Dynamical energy loss model	81
5.1. Introduction	82
5.2. Theoretical framework	83
5.3. Numerical results	88
5.3.1. Adequacy of static approximation	88
5.3.2. Radiative energy loss R_{AA} : static vs. dynamical cases	90
5.3.3. Dynamical formalism: radiative vs. collisional energy loss	
R_{AA}	92
5.3.4. The importance of LPM effect	94
5.3.5. The importance of finite magnetic mass and running coupling	95
5.4. Conclusions	99
6. Radiative energy loss beyond soft-gluon approximation	100
6.1. Introduction	101
6.2. Theoretical framework	103
6.3. Zeroth order radiative energy loss	105
6.4. First order radiative energy loss in massless case	107
6.5. Radiative energy loss in finite temperature QGP	110
6.6. Numerical results	113
6.7. Conclusions	122
7. Conclusions and outlook	124
7.1. Summary of conclusions	125
7.2. Outlook	127
References	128
A. Expressions for collisional energy loss	139

B. Beyond soft-gluon approximation calculus	141
B.1. Notations and useful formulas	141
B.2. Assumptions	143
B.3. Amplitude numeration	145
B.4. Gluon jet M_0	146
B.5. Diagrams $M_{1,1,0}$, $M_{1,0,0}$, $M_{1,0,1}$	148
B.5.1. Computation of $M_{1,1,0}$ diagram	149
B.5.2. Computation of $M_{1,0,0}$ diagram	152
B.5.3. Computation of $M_{1,0,1}$ diagram	153
B.6. Diagram M_{220}	154
B.7. Diagrams $M_{2,0,3}$ and $M_{2,0,0}$	158
B.8. Diagrams $M_{2,0,1}$ and $M_{2,0,2}$	161
B.9. Diagrams $M_{2,1,0}$ and $M_{2,1,1}$	166
B.10. Calculation of radiative energy loss	169
B.11. Diagrams and radiative energy loss with gluon mass included	173

LIST OF FIGURES

1.1	Deep Inelastic scattering. Illustration of deep inelastic scattering of electron on proton. At leading order of perturbation theory virtual electroweak gauge boson (γ, Z, W^\pm) "knocks" a quark (q) "out" of proton. The arrows indicate quark fragmentation into detectable hadron. Figure adapted from Deutsches Elektronen-Synchotron (DESY).	3
1.2	Running coupling $\alpha_s(Q)$ as a function of energy scale Q . The figure contains the summary of $\alpha_s(Q)$ measurements (as indicated in legend). Figure adapted from [14].	4

1.3	The energy density obtained by Lattice QCD. The figure shows energy density of QCD matter, scaled by T^4 as a function of temperature from lQCD [21, 25]. Three different cases are considered, i.e. medium consisting of: two massless quarks u, d (red curve), three massless quarks u, d, s (blue curve) and the most realistic $2 + 1$ case - two massless quark u, d and s quark with its real mass (green curve). The arrows indicate the corresponding ideal gas limits, described by Stefan-Boltzmann law. Figure adapted from [25].	7
1.4	Heavy quark-antiquark potential with three flavor QCD for different temperatures. The band of lines corresponds to the confining Cornell potential normalized by the square root of the string tension $V(r)/\sqrt{\sigma} = -\alpha/(\sqrt{\sigma}r) + \sqrt{\sigma}r$, where $\alpha = 0.25 \pm 0.05$. Figure adapted from [27].	8
1.5	Lattice QCD calculations of the criticalness of the hadronic matter phase transition. The left panel shows phase diagram at zero baryon density, for $m_u = m_d \neq m_s$. Figure adapted from [31]. Possible phases of hadronic matter as a function of temperature and baryon number density, in $2 + 1$ case, are presented in the right panel. Endpoint denotes the critical point. Figure adapted from [32].	10
1.6	Illustration of a possible QCD phase diagram. Hadronic matter phase diagram as a function of both: temperature and baryon chemical potential. The green oriented curve presents commonly accepted evolution path of the universe. Figure adapted from [49].	13
1.7	Space-time evolution of the heavy ion collision. The scheme of different stages of a HIC as a function of longitudinal coordinate z (beam axis) and time t is given on the left. The inserted figure on the right embodies the particles, from nuclei to detectable hadrons, and is synchronized to the figure on left. τ denotes the Lorentz-invariant proper time ($\tau \equiv \sqrt{t^2 - z^2}$), which is constant along the hyperbolic curves separating different stages. Figure adapted from [52].	18

1.8	Proton's partons distribution functions. The gluon distribution function as a function of x_B for different values of Q^2 from DGLAP fits to HERA [64] is presented in the left panel. The right panel shows MSTW2008 next-to-leading order (NLO) PDFs at scale $Q^2 = 10\text{GeV}^2$ for the LHC. Figure adapted from [64, 65].	20
1.9	Phase diagram for parton evolution in QCD. Each colored circle in figure depicts a parton with transverse area $\sim 1/Q^2$ and longitudinal momentum equal to xP , where x is a fractional momentum of a parton at a given resolution scale Q (or in DIS case Bjorken $x = \frac{Q^2}{2Pq}$ is a fraction of proton momentum carried away by parton), and P being proton momentum. The straight line is a saturation line, separating the dense from dilute regimes. In this thesis we consider a dilute limit, where DGLAP evolution is applicable. Figure adapted from [86].	24
1.10	Illustration of pQCD factorization. The figure shows an inclusive $A + B \rightarrow h + X$ process, where A and B denote colliding nuclei. The production of initial parton c is depicted at the leading order, upon which parton c traverses the medium and loses energy via gluon bremsstrahlung. Finally c fragments (denoted by arrows) into hadron h (the leading particle).	25
1.11	Illustration of the hard probes. Layout of hard probes (on the left-hand side) together with the QCD matter features that the corresponding probe provides (on the right-hand side). Figure adapted from [92].	28
1.12	Transfer of spatial into momentum azimuthal anisotropy. The figure illustrates the peripheral collision of two nuclei, where the overlapping region (QGP) lose its spherical shape and becomes almond-like (elliptic). Broken spatial isotropy produces uneven pressure gradients in-plane and out-of-plane (indicated in figure), leading to momentum anisotropy and elliptic collective behavior. The left panel is adapted from [98], while the right panel is adapted from [99].	29

1.13	A + A vs. p(d) + A collisions. The illustration of nucleus + nucleus (left) and proton + nucleus (right) collision is shown. The gray area in the left panel presents formed QGP medium after the collision. The gray area in the right panel raises a question of QGP formation in p(d)+A systems. Figure adapted from [104].	30
1.14	RHIC vs. SPS R_{AA} as a function of p_{\perp} . Comparison of neutral pion suppression data from SPS (triangles and stars) and RHIC (squares and circles) indicates the occurrence of jet quenching at RHIC [116], in distinction to previously observed enhancement at SPS (see [115] and references therein). Figure adapted from [115].	32
1.15	Suppression due to hot and not cold QCD matter confirmed by all four RHIC experiments. In the left panel the cover of Phys. Rev. Letters from 13 August 2003 is shown, confirming in all four RHIC experiments no suppression in $d+Au$ collisions. PHENIX light hadron R_{AA} data from that volume [116] for $d + Au$ and $Au + Au$ collisions at $\sqrt{s_{NN}} = 200$ GeV are presented in the right panel. Figure adapted from [104].	33
1.16	Empirical evidence of QGP formation. Elliptic flow v_2 data as a function of p_{\perp} , extracted from STAR [117] (full symbols) and PHENIX [118] (open symbols), are shown in the left panel. Hydrodynamical predictions are also plotted [119]. Right panel compares two-particle azimuthal distributions in cases of $p + p$, central $d + Au$ and $Au + Au$ collisions, and is adapted from [120].	34
1.17	Suppression of high p_{\perp} light particles. Measurements of R_{AA} as a function of p_{\perp} in central collisions at four different center-of-mass energies (as indicated in legend), for π^{\pm} (at SPS), π^0 (at SPS, RHIC), h^{\pm} (at RHIC) and charged particles (at LHC) are gathered. The newest CMS data at $\sqrt{s_{NN}} = 5.02$ TeV are presented by yellow rectangles. For experimental and theoretical references see [123]. Figure adapted from [123].	36

- 1.18 Suppression of heavy flavor particles. In the left panel comparison of suppression predictions between prompt D meson (black circles); and charged particles (magenta squares) and π^\pm (green circles) as a function of p_\perp in central $Pb + Pb$ collisions at $\sqrt{s_{NN}} = 2.76$ TeV is shown [124]. The middle panel presents CMS D^0 (green squares) and charged hadron (orange circles) R_{AA} predictions as a function of p_\perp in $\sqrt{s_{NN}} = 5.02$ TeV $Pb + Pb$ collisions. CMS R_{AA} vs. p_\perp data for charged hadrons (black circles), D^0 (green squares) and B^+ (bluesquares) at $\sqrt{s_{NN}} = 5.02$ TeV $Pb + Pb$ collisions are shown in the right panel. The middle and right panel are adapted from [125]. . 37
- 1.19 Azimuthal di-hadron correlations. The left panel shows per-trigger jet pair yield, where trigger is π^0 , while associated hadron is h^\pm in $p + p$ (open circles) and $Au + Au$ (solid circles) $\sqrt{s_{NN}} = 200$ GeV collisions at PHENIX [126]. p_\perp regions for trigger and associated hadrons, as well as centrality range are indicated in legend. The central panel presents trigger charged particles for $6.0 < p_\perp^{trig} < 10.0$, and associated ones for $2.5 < p_\perp^{assoc} < 4$ GeV/c in central $d + Au$ (open circles) and $Au + Au$ (full circles and open squares) collisions at STAR [127]. Per-trigger pair yield for associated charged particles $4 < p_T^{assoc} < 6$ GeV/c, and trigger ones $8.0 < p_T^{trig} < 15.0$ GeV/c for central $Pb + Pb$ events (histogram), peripheral $Pb + Pb$ events (red circles) and $p + p$ events (blue squares) at $\sqrt{s_{NN}} = 2.76$ TeV ALICE [128]. Figure adapted from [126–128]. 38
- 1.20 Suppression of electroweak particles. R_{AA} dependence on transverse momentum for electroweak particles: γ (green stars), W^\pm (open crosses) and Z^0 (downward-pointing blue triangle) in central $\sqrt{s_{NN}} = 2.76$ TeV at CMS is shown. Comparison with charged particles suppression in central $\sqrt{s_{NN}} = 2.76$ TeV $Pb + Pb$ (red squares for ALICE, pink triangles for CMS), and in $\sqrt{s_{NN}} = 5.02$ $p + Pb$ (blue circles) collisions at ALICE is also displayed (for experimental references see [130]). Figure adapted from [130]. 39

- 1.21 Thermal photons. In the left panel the direct photon spectra in $Pb + Pb$ collisions at $\sqrt{s_{NN}} = 2.76$ TeV for the following centrality bins: 0 – 20% (scaled by a factor of 100), 20 – 40% (scaled by a factor of 10) and 40 – 80% are compared to next-to-leading-order pQCD predictions for the direct photon production in $p + p$ collisions at the same collision energy, scaled by N_{bin} for each centrality bin. The orange dashed curves correspond to prompt photon component. In the right panel only thermal photon spectra data in $Pb + Pb$ collisions at $\sqrt{s_{NN}} = 2.76$ TeV (ALICE) and in $Au + Au$ $\sqrt{s_{NN}} = 200$ GeV (PHENIX) are presented. The full curves correspond to exponential fits. Figure adapted from [132]. 41
- 1.22 J/ψ suppression measurements as a function of transverse momentum. Comparison of J/ψ R_{AA} data between $\sqrt{s_{NN}} = 200$ GeV $Au + Au$ PHENIX (black squares) and $\sqrt{s_{NN}} = 2.76$ TeV $Pb + Pb$ ALICE (blue squares) collisions is presented in the left panel. For experimental references see [139]. In the right panel, the J/ψ suppression data from $\sqrt{s_{NN}} = 5.02$ TeV $Pb + Pb$ collisions at ALICE are shown for two different decay channels (for references see [140]). Figure adapted from [139, 140]. 44
- 1.23 The sequential suppression of bottomonium family. Invariant mass distribution of muon pairs, originating from Υ family decay, in $p + p$ (fits to data represented by dashed blue curve) and $Pb + Pb$ (black squares, fits to data represented by red curve) $\sqrt{s_{NN}} = 5.02$ TeV collisions is given in the left panel. The three peaks in $p + p$ case correspond to separate yields for each individual Υ state (from left to right: ground state $\Upsilon(1S)$ and higher resonances $\Upsilon(2S)$ and $\Upsilon(3S)$ respectively). R_{AA} dependence on N_{part} for $\Upsilon(1S)$ (red circles), $\Upsilon(2S)$ (blue squares) and $\Upsilon(3S)$ (green symbols) under the same CMS conditions as in the left panel is shown in the right panel. Figure adapted from [141]. 45

1.24	Elliptic flow coefficients measured in $\sqrt{s_{NN}} = 5.02$ TeV $Pb + Pb$ and $p + Pb$ at ALICE. In the left panel the flow coefficients $v_n(p_\perp)$ for charged particles in 30 – 40% central $Pb + Pb$ collisions are shown by symbols (as indicated in legend). Comparison with the corresponding data in $\sqrt{s_{NN}} = 2.76$ TeV (shaded areas) is also presented. The right panel corresponds to elliptic flow of inclusive and identified hadrons (as denoted in legend) in $p + Pb$ collisions. Figure adapted from [144, 145].	46
3.1	Representative 2-HTL Feynman diagram and three on-shell cuts. The left, central and right panels correspond to the central, left and right cut of the same diagram, respectively. In infinite dynamical QGP medium, only left diagram is included, while in finite dynamical medium all tree cuts contribute to the 1 st order in opacity quark radiative energy loss. Gray ellipse represents quark-jet source and the large dashed circles ("blob") represent effective HTL gluon propagators (see B appendix from [188]). The radiated gluon is denoted by momentum k and color c , whereas the exchanged gluon is denoted by momentum q and color a . p corresponds to the final quark. Figure adapted from [196].	60
3.2	Suppression computational scheme. The chronological order of each independent step, separated by vertical dashed lines, in our numerical formalism: high p_\perp parton production (yellow ellipse), medium induced energy loss, fragmentation into hadron in vacuum and decay of heavy measons (D, B) into $e, J/\psi$. Figure adapted from [211].	65

3.3	<p>Representative diagrams in calculating energy loss in finite size dynamical QGP medium. The left panel corresponds to the collisional process (originating from 1-HTL), while the right panel corresponds to radiative process (upper (lower) originating from 1-HTL (2-HTL) gluon propagator). The black ellipse denotes parton source, the "blob" (gray ellipse) represents the effective HTL gluon propagator for collisional interactions, while denotes the transverse gluon propagator with the effective gluon mass for radiative processes. Figure adapted from [213].</p>	67
4.1	<p>Comparison of charged hadron suppression predictions with LHC experimental data at different centralities. The panels show the comparison of charged hadron suppression predictions (gray band) with ALICE [219] (the red circles) and CMS [223] (the blue squares) R_{AA} data in 2.76 TeV $Pb + Pb$ collisions at LHC, for different (fixed) centrality regions, as a function of transverse momentum. The upper (lower) boundary of gray band on each panel corresponds to $\frac{\mu_M}{\mu_E} = 0.6$ ($\frac{\mu_M}{\mu_E} = 0.4$). The centrality ranges, for which the predictions are presented, are indicated in the lower right corner of each panel. Note that, on the third and the fourth panel, the same CMS data for centrality range 10 – 30% are shown; then, on the fifth and the sixth panel, the same CMS data for centrality range 30 – 50% are presented; similarly on the seventh and the eight panel, the CMS data for centrality range 50 – 70% are shown, while on the ninth panel CMS data for centrality region of 70 – 90% are presented. Figure adapted from [225].</p>	71

- 4.2 Comparison of D meson suppression predictions with LHC experimental data at different centralities, as a function of transverse momentum. The theoretical predictions are presented by gray bands, where upper (lower) boundary of each band corresponds to $\frac{\mu_M}{\mu_E} = 0.6$ ($\frac{\mu_M}{\mu_E} = 0.4$). The centrality regions, for which the predictions are presented, are denoted in the upper right corner of each panel. At that time D meson R_{AA} experimental data for only two centrality bins were available: 0 – 7.5% central 2.76 $Pb + Pb$ collisions at LHC [230] (the red triangles in the left panel), and 30 – 50% ALICE data [231] (the red triangles in the third panel). Figure adapted from [225]. 72
- 4.3 Comparison of neutral pion suppression predictions with RHIC experimental data at different centralities. The panels show the comparison of π^0 suppression predictions (gray band) with PHENIX [232] R_{AA} data at 200 GeV $Au + Au$ collisions at RHIC (the purple triangles), for different (fixed) centrality regions, as a function of transverse momentum. The upper (lower) boundary of gray band on each panel corresponds to $\frac{\mu_M}{\mu_E} = 0.6$ ($\frac{\mu_M}{\mu_E} = 0.4$). The centrality bins, for which the predictions and the data are presented, are denoted in the lower right corner of each panel. Figure adapted from [225]. 73
- 4.4 Suppression dependence on the number of participants for light and heavy flavor at RHIC and LHC. The first panel compares R_{AA} predictions with PHENIX experimental data [232] for neutral pion in 200 GeV $Au + Au$ collisions at RHIC, where π^0 momentum is larger than 7 GeV. The remaining panels compare R_{AA} predictions with experimental data from 2.76 TeV $Pb + Pb$ collisions at LHC, for: charged hadrons [219], with momentum in 6 – 12 GeV range (the second panel), D mesons [233], with momentum in 8 – 16 GeV range (the third panel) and non-prompt J/ψ [234], with momentum in 6.5 – 30 GeV range (the last panel). Theoretical predictions are presented by gray bands, where upper (lower) boundary of each band corresponds to $\frac{\mu_M}{\mu_E} = 0.6$ ($\frac{\mu_M}{\mu_E} = 0.4$). Figure adapted from [225]. 74

- 4.5 Comparison of charged hadron R_{AA} predictions at 2.76 and 5.02 TeV. Suppression predictions for h^\pm , as a function of transverse momentum in 0 – 10% central $Pb + Pb$ collisions at the LHC, are shown as white bands with full (dashed) boundaries for 5.02 TeV (2.76 TeV) center-of-mass energies. The upper (lower) boundary of each band corresponds to $\frac{\mu_M}{\mu_E} = 0.6$ ($\frac{\mu_M}{\mu_E} = 0.4$). Figure adapted from [237]. 76
- 4.6 R_{AA} as a function of participants number for single particles in $\sqrt{s_{NN}} = 2.76$ TeV $Pb + Pb$ collisions at the LHC. The left panel shows comparison of our suppression predictions and CMS experimental data for D mesons [239] in $8 < p_\perp < 16$ GeV region (red triangles) and non-prompt J/ψ [234] in $6.5 < p_\perp < 30$ GeV region (orange circles). Gray bands with dashed, and dot-dashed boundaries, correspond to our theoretical predictions for D mesons and non-prompt J/ψ in the appropriate momentum regions, respectively. The right panel compares our R_{AA} predictions for h^\pm (white band with full boundaries), D (white band with dashed boundaries) and B meson (white band with dot-dashed boundaries) with ATLAS h^\pm data [240] (green squares) in $60 < p_\perp < 95$ GeV momentum region. On each panel, the upper (lower) boundary of each band corresponds to $\frac{\mu_M}{\mu_E} = 0.6$ ($\frac{\mu_M}{\mu_E} = 0.4$). Figure adapted from [237]. 77

- 4.7 Contributions of initial distribution and energy loss to suppression. (a) R_{AA} predictions as a function of N_{part} are compared for D mesons in $8 < p_{\perp} < 16$ GeV region (dashed curve) and non-prompt J/ψ in $6.5 < p_{\perp} < 30$ GeV region (dot-dashed curve). Gray curve shows the analogous non-prompt J/ψ predictions, if the originating bottom quark would have the same energy loss as charm quark in QGP. (b) R_{AA} predictions as a function of N_{part} are compared for D and B mesons in $8 < p_{\perp} < 16$ GeV region. (c) R_{AA} predictions as a function of p_{\perp} are compared for D and B mesons. The full arrow denotes the contribution of the different initial distributions to the difference in the suppression between D meson and non-prompt J/ψ (or B meson), while the dashed arrow indicates the contribution of the different energy losses to the difference between D meson and the non-prompt J/ψ (or B meson) suppression. On each panel the legend is the same as in the first panel. Magnetic to electric mass ratio is set to $\mu_M/\mu_E = 0.4$. Figure adapted from [237]. 78
- 4.8 Single particles suppression predictions as a function of p_{\perp} in 0–10% central 5.02 TeV $Pb + Pb$ collisions at the LHC. (a) R_{AA} predictions for h^{\pm} , D and B meson are presented by white bands with full, dashed and dot-dashed boundaries, respectively. The upper (lower) boundary of each band corresponds to $\mu_M/\mu_E = 0.6$ ($\mu_M/\mu_E = 0.4$). (b) Bare quark R_{AA} predictions for u (dotted curve), c (dashed curve) and b quarks (dot-dashed curve). (c) Comparison of R_{AA} predictions for bare u quark (dotted curve) with h^{\pm} (full curve). In (b) and (c) panels μ_M/μ_E is set to 0.4. Figure adapted from [237]. 79

- 5.1 Static radiative vs. collisional energy loss R_{AA} . D meson suppression predictions dependence on transverse momentum, is shown assuming only radiative energy loss in static QGP medium (dotted curve), and considering only collisional energy loss in dynamical QGP medium (dot-dashed curve). Left (right) panel corresponds to RHIC (LHC) conditions. Right panel also contains the D meson R_{AA} experimental data for 0 – 7.5% central 2.76 TeV $Pb + Pb$ collisions at the LHC [221, 233] (red triangles). The standard values for the parameters are assumed: Debye mass $\mu_E = gT$, coupling constant $\alpha_s = 0.3$ ($\alpha_s = 0.25$) for RHIC (LHC). A finite size QGP medium is considered, while the finite magnetic mass effect is not included (i.e. $\mu_M = 0$). Figure adapted from [159]. 89
- 5.2 Static vs. dynamical radiative energy loss R_{AA} . D meson suppression predictions dependence on transverse momentum is plotted, assuming only radiative energy loss in static (dotted curve) and in dynamical (dashed curve) QGP medium. Left (right) panel corresponds to the RHIC (LHC) conditions. Right panel also shows the D meson R_{AA} experimental data for 0 – 7.5% central 2.76 TeV $Pb + Pb$ collisions at LHC [221, 233] (red triangles). The standard values for the parameters are assumed: Debye mass $\mu_E = gT$, coupling constant $\alpha_s = 0.3$ ($\alpha_s = 0.25$) for RHIC (LHC). A finite size QGP medium is considered, while no finite magnetic mass effect is included (i.e. $\mu_M = 0$). Figure adapted from [159]. 91

- 5.3 Radiative vs. collisional energy loss R_{AA} in dynamical formalism. D meson suppression predictions dependence on transverse momentum is shown for radiative (dashed curve), collisional (dot-dashed curve) and total, i.e. radiative + collisional (solid curve) energy loss. Left (right) panel corresponds to the RHIC (LHC) conditions. Right panel also contains the D meson R_{AA} data for 0 – 7.5% central 2.76 TeV $Pb + Pb$ collisions at LHC [221, 233] (red triangles). Debye mass is $\mu_E = gT$, coupling constant is $\alpha_s = 0.3$ ($\alpha_s = 0.25$) for RHIC (LHC). QGP medium of a finite size is assumed and no finite magnetic mass effect is taken into account (i.e. $\mu_M = 0$). Figure adapted from [159]. 93
- 5.4 Finite size effect on R_{AA} in dynamical formalism. D meson suppression predictions dependence on transverse momentum is plotted with (solid curve) and without (dashed curve) finite size effect included. The first (the second) row corresponds to RHIC (LHC) conditions. Left, central and right column shows, respectively, the finite size effect on radiative, collisional and total (radiative + collisional) energy loss in a dynamical QGP medium. The standard values for the parameters are assumed: Debye mass $\mu_E = gT$, coupling constant $\alpha_s = 0.3$ ($\alpha_s = 0.25$) for RHIC (LHC), whereas no finite magnetic mass effect is included. Figure adapted from [159]. 94
- 5.5 Magnetic mass effect on R_{AA} in dynamical formalism. D meson suppression predictions dependence on transverse momentum is shown for (total) radiative + collisional energy loss in dynamical QGP medium of a finite size, with (gray band) and without (solid curve) magnetic mass included. Left (right) panel corresponds to the RHIC (LHC) conditions. Right panel also contains the D meson R_{AA} data for 0 – 7.5% central 2.76 TeV $Pb + Pb$ collisions at LHC [221, 233] (red triangles). Debye mass is $\mu_E = gT$ and coupling constant is $\alpha_s = 0.3$ ($\alpha_s = 0.25$) for RHIC (LHC). Upper (lower) boundary of each band corresponds to $\frac{\mu_M}{\mu_E} = 0.6$ ($\frac{\mu_M}{\mu_E} = 0.4$). Figure adapted from [159]. . . . 96

- 5.6 Running coupling effect on R_{AA} in dynamical formalism. D meson suppression predictions dependence on transverse momentum is plotted in case of constant coupling $\alpha_s = 0.3$ ($\alpha_s = 0.25$) for RHIC (LHC) (solid curve) and when running coupling (dashed curve) is included. No finite magnetic mass effect is assumed (i.e. $\mu_M = 0$). In both cases radiative + collisional contributions in dynamical QCD medium of a finite size are considered. Left (right) panel corresponds to RHIC (LHC) conditions. Right panel also shows the D meson R_{AA} data for 0 – 7.5% central 2.76 TeV $Pb + Pb$ collisions at LHC [221, 233] (red triangles). Figure adapted from [159]. 97
- 5.7 Joint effect of magnetic mass and running coupling on R_{AA} . D meson suppression predictions dependence on transverse momentum, with the constant coupling $\alpha_s = 0.3$ ($\alpha_s = 0.25$) for RHIC (LHC) (light gray band) and with the running coupling (dark gray band) accounted. In both cases (total) radiative + collisional contributions in dynamical QGP medium of a finite size are considered. Upper (lower) boundary of each band corresponds to $\frac{\mu_M}{\mu_E} = 0.6$ ($\frac{\mu_M}{\mu_E} = 0.4$). Left (right) panel corresponds to the RHIC (LHC) conditions. Right panel also contains the D meson R_{AA} data for 0 – 7.5% central 2.76 TeV $Pb + Pb$ collisions at LHC [221, 233] (red triangles). Figure adapted from [159]. 98
- 6.1 Zeroth order diagram that includes no interaction with the QCD medium, and contributes to gluon radiation amplitude to the 1st order in opacity. The dashed circle represents the source J , which at longitudinal coordinate z_0 produces an off-shell gluon jet, propagating along z -axis. z denotes longitudinal coordinate at which the gluon is radiated. k denotes 4-momentum of the radiated gluon carrying the color c , and p denotes 4-momentum of the final gluon jet carrying the color d 105

- 6.2 Representative diagrams that include interaction with the QCD medium, and potentially contribute to gluon radiation amplitude to the 1st order in opacity. The left panel corresponds to one interaction with QGP medium, while the right panel corresponds to two interactions with the medium, which only in contact-limit ($z_1 = z_2$) case contributes to the 1st order emission spectrum (for more details see Appendices B.6 to B.9). z_i , where $i = 1, (2)$, denotes longitudinal coordinate of the interactions with the consecutive scattering centers. Crossed circles represent scatterers that exchange transverse momentum \vec{q}_i with the jet. Remaining labeling is the same as in Fig. 6.1. 109
- 6.3 Integrated variables: Effect of relaxing soft-gluon approximation to the 1st order in opacity of DGLV formalism, as a function of p_\perp . The top left panel compares gluon fractional radiative energy loss without (the solid curve) and with (the dashed curve) the soft-gluon approximation. The top right panel quantifies the effect of relaxing the soft-gluon approximation on $\frac{\Delta E^{(1)}}{E}$ and expresses it in percentage. The bottom left panel compares number of radiated gluons without (the solid curve) and with (the dashed curve) soft-gluon approximation, whereas the bottom right panel shows the relative change in this number with respect to soft-gluon limit. Figure adapted from [248]. . 114
- 6.4 Differential variables: Effect of relaxing soft-gluon approximation to the 1st order in opacity of DGLV formalism, as a function of x . The comparison of bsg (the solid curve) and sg (the dashed curve) fractional differential gluon radiative energy loss ($\frac{1}{E} \frac{dE^{(1)}}{dx}$) for different values of initial jet p_\perp (5 GeV, 10 GeV, 50 GeV, as indicated in the lower right corner of panels) is presented in the first column. The second column shows comparison of bsg (the solid curve) and sg (the dashed curve) single gluon radiation (spectrum) distribution in momentum fraction ($\frac{dN_g^{(1)}}{dx}$) for the same values of p_\perp , as in the first column. The relative change of the single gluon radiation spectrum when the soft-gluon approximation is relaxed with respect to the soft-gluon limit is presented in the third column. Figure adapted from [248]. 116

6.5	Relative change of single gluon radiation distribution in momentum fraction in <i>bsg</i> compared to <i>sg</i> case for different p_{\perp} values. The percentage of $\frac{dN_g^{(1)}}{dx}$ change when soft-gluon approximation is relaxed with respect to <i>sg</i> case, calculated to the 1 st order in opacity of DGLV formalism, for different values of initial transverse momentum (as indicated in the legend) is plotted as a function of x . The curves fade as transverse momentum increases. Figure adapted from [248].	117
6.6	The effect of relaxing the soft-gluon approximation on gluon R_{AA} . The comparison of gluon nuclear modification factor R_{AA} between <i>bsg</i> (the solid curve) and <i>sg</i> (the dashed curve) cases is assessed in the left panel, as a function of the final p_{\perp} . The right panel provides a percentage of gluon suppression change when soft-gluon approximation is relaxed. Figure adapted from [248].	119
6.7	The effect of relaxing the soft-gluon approximation on gluon R_{AA} when uniform longitudinal distance distribution is considered. The comparison of gluon nuclear modification factor R_{AA} between <i>bsg</i> (the solid curve) and <i>sg</i> (the dashed curve) cases is assessed in the left panel, as a function of the final p_{\perp} . The relative change of gluon suppression when soft-gluon approximation is relaxed with respect to <i>sg</i> limit is presented in the right panel.	119
6.8	Illustrative figure of initial gluon distribution constraining the relevant x region. The initial gluon distribution as a function of p_{\perp} (the solid black curve) at the LHC is extracted from [212]. The final gluon transverse momentum, set at $p_{\perp} = 30$ GeV, is represented by vertical dot-dashed gray boundary. For each x , the dotted arrow links the descendant gluon with its parent gluon (of the corresponding initial transverse momenta), that lost momentum fraction equal to x . The arrows fade as x increases (as indicated in the legend). Figure adapted from [248].	120

- 6.9 The relevant x region for studying importance of relaxing sg approximation. The comparison of gluon R_{AA} predictions between bsg (the solid curve) and combined: bsg for $x \leq 0.4$ + sg for $x > 0.4$ (the dashed curve) cases is assessed in the left panel, as a function of the final p_{\perp} . The right panel provides a percentage of gluon suppression change when soft-gluon-approximation relaxation is omitted at $x > 0.4$. 122
- B.1 Zeroth order diagram that includes no interaction with the QCD medium, and contributes to gluon radiation amplitude to the first order in opacity L/λ . The dashed circle represents the source J , which at longitudinal coordinate z_0 produces an off-shell gluon jet, propagating along z -axis. z denotes longitudinal coordinate at which the gluon is radiated. Latin indices denote color charges, while Greek indices denote components of 4-vectors. k denotes 4-momentum of the radiated gluon carrying the color c , and p denotes 4-momentum of the final gluon jet carrying the color d . . 146
- B.2 Three diagrams, corresponding to interaction with one static scattering center, that contribute to gluon-jet radiation amplitude to the first order in opacity L/λ . z_1 denotes longitudinal coordinate of the interactions with one scattering center. Crossed circle represents scatterer that exchange transverse momentum \vec{q}_1 with the jet. Note that, all three diagrams assume equivalently ordered Latin and Greek indices as indicated by the first diagram. Remaining labeling is the same as in Fig. B.1. 149
- B.3 Feynman diagram $M_{2,2,0}$ and its contribution to the first order in opacity gluon-jet radiative energy loss: contact-limit $M_{2,2,0}^c$. z_i , where $i = 1, 2$, denotes longitudinal coordinate of the interactions with the consecutive scattering centers (or in the contact limit $z_1 = z_2$). Crossed circles represent scatterers that exchange transverse momentum \vec{q}_i with the jet, which in contact-limit case merge into one gridded ellipse. Note that, all the following figures assume equivalently ordered Latin and Greek indices as in this figure. Remaining labeling is the same as in Figs.(B.1, B.2). 155

B.4	Feynman diagrams $M_{2,0,3}$ and $M_{2,0,0}$ in well separated (left column) and in contact-limit case ($z_1 = z_2$), which contributes to the first order in opacity of gluon-jet radiative energy loss: $M_{2,0,3}^c$ and $M_{2,0,0}^c$ (right column). Remaining labeling is the same as in Fig. B.3.	158
B.5	Topologically indistinct Feynman diagrams $M_{2,0,1}^c$ and $M_{2,0,2}^c$ in contact limit ($z_1 = z_2$), which contribute to the first order in opacity of gluon-jet radiative energy loss. Remaining labeling is the same as in Fig. B.3.	161
B.6	Illustration of calculating Cauchy principal value (I_{PV}) in the case when singularity on the real axis arises.	163
B.7	Feynman diagrams $M_{2,1,0}^c$ and $M_{2,1,1}^c$ in contact limit ($z_1 = z_2$), which have negligible contribution to the first order in opacity gluon-jet radiative energy loss. Remaining labeling is the same as in Fig. B.3.	165

1. INTRODUCTION

1.1. A brief introduction to QCD

This subsection comprises a brief overview of how human knowledge of elementary matter constituents developed historically and consequently, of the quantum chromodynamics (QCD) development. The late 1940' marked the expansion of quantum field theory (QFT) with Quantum Electrodynamics and another 30 years needed to pass for QFT to overcome the obstacles and to regain the primacy in understanding, explaining and trying to unite the nature's forces, with the development of electroweak [1] and the physics of the strong force: QCD [2] theories (as stated in [3]). The QCD came under the spotlight, again in 2000', simultaneously with building new facilities for heavy ion (HI) collisions, such as the Relativistic Heavy Ion Collider (RHIC) at Brookhaven National Laboratory (BNL) and the Large Hadron Collider (LHC) at CERN, with its promising ability to interpret the measurements and as a tool for tomography of a new phase on the horizon.

There were two lines of the QCD development: *i*) First was the recognition of the elementary particles [4, 5] that interact through strong forces and *ii*) As a second, accurately defining the interaction dynamics between the theory constituents.

The humans knowledge of the elementary matter constituents and the forces among them has alternated along the time, such that not until the late 19th century Faraday, Maxwell and Heaviside unified electric and magnetic fields (fields with macroscopic manifestations) through the famous Maxwell's equations. The experimental discovery of an electron, as an indivisible particle, by J. J. Thomson [6] in 1897 was a milestone in properly modeling the atomic structure. This represented a guideline for Ernest Rutherford to run the well-known experiment [7] by shooting a beam of α particles (He^{2+}) into a gold foil. This resulted in the atom model [8] in 1911, where electrons, as negative charges, orbited around the positively charged nucleus. Rutherford named the hydrogen atom nucleus as proton in 1920. After J. Chadwick's [9] discovery of neutron in 1932, the picture of atom was rounded. Finally, along with the advancement of quantum mechanics and consequently, the

quantum electrodynamics, both the particles and forces were well described.

However, this opened new questions of nucleons substructures and the "nuclear force", and once again neither the set of fundamental particles nor their dynamic was known and adequately addressed. To that end, in 1964 Gell-Mann [4] and Zweig [5] independently formulated a model of proton consisting of three elementary particles of spin 1/2 and fractional charge, which Gell-Mann named quarks. Thus, the first question of particles classification was theoretically resolved, as all known particles could be described by the representation of the group $SU(3)_f$. This also analytically suggested the more elementary particles than hadrons. Namely, the particles fitting into fundamental (3 dimensional) representation of $SU(3)$ flavor group are quarks (u, d, s), while mesons and baryons are referred to as quark-antiquark states $q\bar{q}$ (basis vectors of 8 dimensional representation or singlet state) and as three bound quark states qqq (basis vectors of 8 or 10 dimensional representations or singlet state), respectively. Later, along with discovery of J/ψ meson by Richter and Ting at SLAC in 1974, the fourth quark - charm quark was added to the list, expanding the symmetry group. Subsequently, in 1977 (by Lederman) and 1995 (at Fermilab) two additional, and final quarks were discovered: top and bottom quarks, expanding the flavor symmetry to $SU(6)_f$.

Additionally, e.g. Δ^{++} resonance is composed of 3 up quarks, has spin 3/2 and in spin state $s_z = +3/2$ the quarks in ground state would have to be in (orbital and spin) totally symmetric state, which violates Pauli principle of Fermi-Dirac statistics. Due to this inconsistency, an additional degree of freedom emerged (Greenberg [10] and Nambu [11]): the color, allowing each quark to be in one of the three color states (denoted by index a) red (R), green (G), blue (B). In order to prevent the unrealistic increase of particles number of states, all hadrons (detectable particles) should be color singlets. The group of color symmetry is also $SU(3)_c$, where, as usual, quarks are transforming according to the fundamental representation and the antiquarks according to the complex conjugate representation. This makes total Δ^{++} wave function antisymmetric:

$$\varepsilon^{abc}u_a u_b u_c = u_R u_G u_B - u_G u_R u_B - u_R u_B u_G + u_B u_R u_G - u_B u_G u_R + u_G u_B u_R, \quad (1.1.1)$$

which resolves the issue of Pauli principle. Also, it is straightforward to verify that

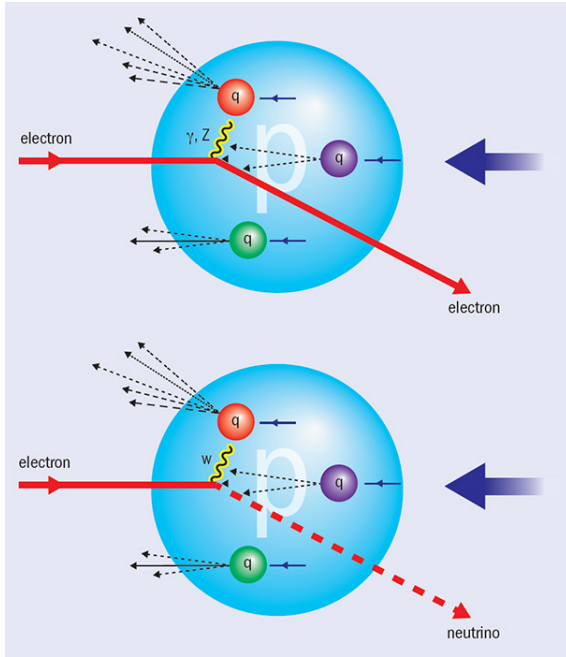


Figure 1.1: Deep Inelastic scattering. Illustration of deep inelastic scattering of electron on proton. At leading order of perturbation theory virtual electroweak gauge boson (γ, Z, W^\pm) "knocks" a quark (q) "out" of proton. The arrows indicate quark fragmentation into detectable hadron. Figure adapted from Deutsches Elektronen-Synchotron (DESY).

mesons are $SU(3)_c$ color singlets ($q_R \bar{q}_R + q_G \bar{q}_G + q_B \bar{q}_B$).

The experimental validation of their model came in 1968 from electron-proton deep-inelastic scattering (Fig. 1.1) at SLAC [12] (Stanford Linear Accelerator Center), in which electron was used to probe hadron structure. It confirmed that proton consists of three spin 1/2 particles, which provided convincing evidence of quarks existence. However, from the current point of view, this is a simplified picture of hadron's structure, since apart from enclosing two (mesons) or three (baryons) valence quarks (antiquarks), it is known that hadron also consists of numerous virtual quarks and antiquarks (also known as sea quarks) and gluons. From then on, QCD, as the theory of strongly interacting particles (quarks) mediated via gluons became the prevailing theory describing elementary particles.

It was still, however, unresolved why free quarks are not observed in nature, but exist only as confined form of matter within the hadrons and the only way to produce them as free particles was in deep-inelastic scattering. The idea of deconfined state of the matter, which allowed quarks and gluons to move freely over the distances larger than the size of hadron, was born within the QCD. In 1973 Politzer, Wilczek and Gross [13] succeeded in proving that non-Abelian gauge theories, such as QCD, are asymptotically free. Namely, the asymptotic freedom implies that at large distances (i.e. for small exchanged momenta, consistently with Heisenberg's uncertainty prin-

ple) between the quarks and/or gluons the coupling is stronger, leading to the confinement into hadrons. This could be intuitively understood through comparison with rubber band: the wider one stretches it, the larger is the tension. On the other hand, the coupling becomes weak at small distances (i.e. for large exchanged momenta), allowing quarks to behave as a free particles. The exact expression for running strong coupling is given by:

$$\alpha_s(Q^2) = \frac{4\pi}{(11 - 2/3n_f) \ln(\frac{Q^2}{\Lambda_{QCD}^2})}, \quad (1.1.2)$$

where n_f denotes the number of the effective light-quark flavors and Λ_{QCD} is perturbative QCD scale (200 MeV). From the expression for running strong coupling constant (1.1.2), we infer that the deconfinement occurs at extremely high energies (i.e. temperatures), and/or, as will be demonstrated in subsequent sections, at very large baryon number densities. The experimental confirmation of the asymptotic freedom is shown in Fig. 1.2. For the discovery of the asymptotic freedom, Politzer, Wilczek and Gross were awarded by Nobel prize in 2004.

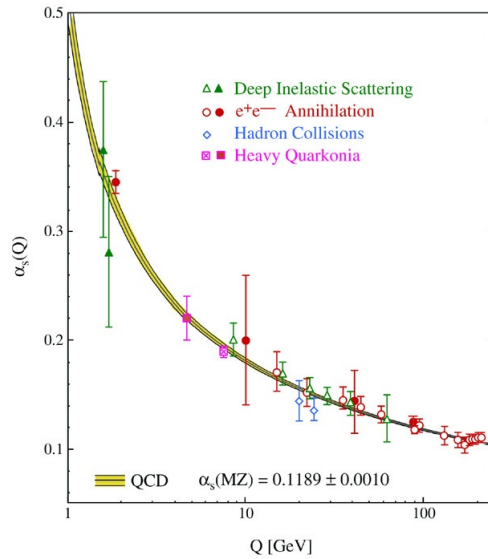


Figure 1.2: Running coupling $\alpha_s(Q)$ as a function of energy scale Q . The figure contains the summary of $\alpha_s(Q)$ measurements (as indicated in legend). Figure adapted from [14].

1.2. Phases of hadronic matter, introduction of QGP and its importance

The fact that, the matter surrounding us, can be found in thermodynamically distinct phases, is well-known. Since long ago, the phase transitions among these phases, which assumed that small changes in temperature or pressure led to drastic and abrupt changes in macroscopic properties of such matter, were also well understood and described. However, in that case, both the existence of the various phases and the phase transitions are governed by electromagnetic forces between atoms and molecules.

By submerging deeper into subatomic world, where the strong force is dominant one, the question of different phases of hadronic matter arose. Note that, contrary to macroscopic matter, now, the number of particles is not conserved but instead the baryonic number, i.e. the difference between number of baryons and anti-baryons, is conserved [15]. So, the following three parameters describe thermodynamic properties of the strongly interacting relativistic matter: temperature (T), pressure and baryon number density μ_b [15].

The discovery of asymptotic freedom within pQCD influenced the birth of an idea of the existence of new form of matter [16, 17], in which quarks, anti-quarks and gluons are liberated at extremely high energy densities $\epsilon \sim 1\text{GeV}/\text{fm}^3$. Historically, the name for this form of matter was changing, so the terms: superdense matter, quark soup [16] (1975), hot quark soup and plasma-like phase [18] (1978) all stand for what is today known as "quark-gluon plasma" (QGP), the phrase that Edward Shuryak coined 40 years ago [19]. Besides at high energy densities (i.e. when the energy density of matter is of the order as the one in a proton, that is about an order of magnitude larger than the energy density inside atomic nuclei), the transition into QGP can also occur at very large baryon number densities [20].

There are two ways to achieve this state: 1) by compressing the nuclear matter, so that nucleons overlap, or 2) by introducing a large amount of energy into nuclear matter. The first way leads to the production of cold QGP, such as the one believed to exist in neutron stars, supernovae, which is characterized by low temperature and high baryon number density. The other way, which is relevant for the experiments and consequently this study, leads to the formation of hot QGP, characterized by

very large temperature and sufficient energy density.

1.2.1. Lattice QCD at finite temperature

The transition from ordinary hadronic matter to the QGP, which corresponds to the non-perturbative domain, can be studied numerically by applying lattice QCD (lQCD) methods [21], that was the first to propose phase transition [18, 22]. Thus, the estimates of thermodynamical properties of the phase transition are provided by lQCD, such as critical temperature T_c and critical energy density ϵ_c , which were roughly estimated to be 160 MeV and $\sim 1\text{GeV}/\text{fm}^3$, respectively. Note, however, that this temperature is very close to the limiting 'ultimate' temperature of hadronic matter T_H , as phenomenologically estimated in 1968 (before the QCD formulation, and partons discovery) by Hagedorn [23].

One of the most relevant results of lQCD method [18, 22] is presented in Fig. 1.3, which represents temperature dependence of energy density. We observe that in a narrow temperature window of 10 – 20 MeV around the critical (point) temperature T_c , the energy density changes for an order of magnitude. This rapid change in energy density is subjected to the large change in the degrees of freedom. Namely, at $T \ll T_c$, there are usually considered to be 3 active hadronic degrees of freedom corresponding to a dilute gas of 3 charge states of pions [24]. Above T_c , the QGP is formed and free gluons contribute by (8 colors times two helicity states) 16 degrees of freedom, while quarks contribute by ($n_f \approx 2 - 3$ active light quark flavors, for T not far above T_c , times 2 accounting for the anti-quarks, times two spin states and three colors) 24 – 36 degrees of freedom. Thus, in the quark gluon plasma phase, there are about 40 – 50 internal degrees of freedom in the temperature range $(1 - 3)T_c$. Since energy density, entropy and pressure are all proportional to the number of degrees of freedom, the large change in degrees of freedom could explain the rapid rise of ϵ in deconfined, compared to confined states.

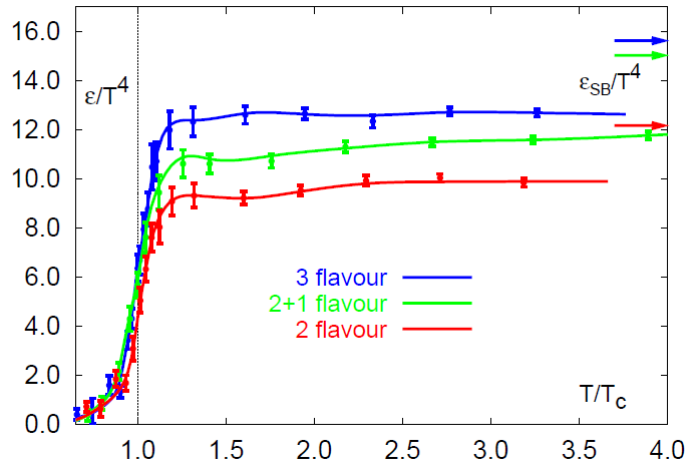


Figure 1.3: The energy density obtained by Lattice QCD. The figure shows energy density of QCD matter, scaled by T^4 as a function of temperature from IQCD [21, 25]. Three different cases are considered, i.e. medium consisting of: two massless quarks u, d (red curve), three massless quarks u, d, s (blue curve) and the most realistic $2 + 1$ case - two massless quark u, d and s quark with its real mass (green curve). The arrows indicate the corresponding ideal gas limits, described by Stefan-Boltzmann law. Figure adapted from [25].

Another important evidence of deconfinement is related to the Fig. 1.4, which represents temperature dependence of the heavy quark potential (color screening potential [26] for quarkonium formation, where term quarkonium denotes the bound state of a heavy quark and its anti-quark, i.e. either charm or bottom) for three flavor QCD [27]. The comparison with the confining Cornell potential: $V(r) = -\alpha/r + \sigma r$, which corresponds to the quarkonium potential in QCD vacuum, i.e. in hadronic matter and not in the QGP, is also addressed. We observe that at lower temperatures, i.e. $T \lesssim 0.5T_c$ the quarkonium potential curve agrees to a great extent with Cornell potential, while with increasing temperature deviation from confining potential is more pronounced, implying possibility of different phase of matter. Additionally, we see that the screening starts to become important at small distances, which strongly suggests melting of heavy quark bound states, i.e. quarkonia.

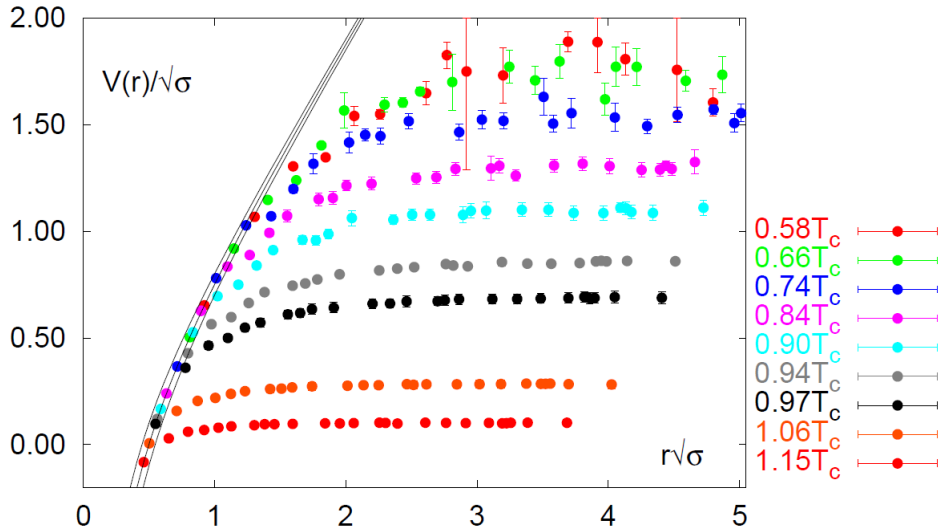


Figure 1.4: Heavy quark-antiquark potential with three flavor QCD for different temperatures. The band of lines corresponds to the confining Cornell potential normalized by the square root of the string tension $V(r)/\sqrt{\sigma} = -\alpha/(\sqrt{\sigma}r) + \sqrt{\sigma}r$, where $\alpha = 0.25 \pm 0.05$. Figure adapted from [27].

Nevertheless, despite acknowledging the existence of deconfined phase and of sharp changes of thermodynamical properties, it still remained unclear whether this transition is a textbook case of phase transition in statistical mechanical sense. According to the definition, the first-order phase transition requires a discontinuity in the first derivative of the free energy (or equivalently, a discontinuity in energy density) with respect to some thermodynamical variable at T_c , while the second-order phase transition assumes discontinuity in the second (first) derivative of the free energy (energy density). So, although we observe a rapid change in Fig. 1.3, it does not necessarily imply the phase transition, but could actually present a crossover.

Additionally, massless QCD Lagrangian possesses $SU(3)_L \otimes SU(3)_R$ symmetry, i.e. is invariant under the flavor and chiral transformations, while the existence of pions represents breaking of the chiral symmetry [26]. This is known as spontaneous symmetry breaking, since this term denotes the phenomenon when the Lagrangian respects the symmetry, while its eigenstates at low energies (vacuum) do not. Also, the symmetry at higher energy should be restored. Indeed, the chiral

symmetry is a good symmetry of QCD Lagrangian consisting of u and d quarks, since $m_u, m_d \ll \Lambda_{QCD}$, but would not be valid if strange quarks were involved. That is, the non-zero masses of the quarks explicitly break the chiral symmetry of the QCD Lagrangian, therefore nothing prevents quarkonium states to survive the "phase" transition (see section 1.5). Also, the spontaneous breaking of the chiral symmetry is predicted by QCD, which therefore also predicts the existence of the Goldstone bosons (order parameter - condensate $\langle q\bar{q} \rangle$): the pions, kaons and eta mesons. The chiral symmetry of QCD is restored at higher temperatures.

The restoration of the chiral symmetry would present a sufficient condition for the existence of a QCD phase transition. For better understanding of this correlation between symmetry breaking/restoration and phase transition, the comparison with the macroscopic (more comprehensible) phenomenon - ferromagnetic phase transition - is made [26]. In the latter case the symmetry is the isotropy, which exists at high energy, as there is no preferable space direction (invariance under rotation); but which is spontaneously broken at low temperatures, as microscopic magnetic moments of the matter constituents are aligned, producing macroscopic magnetization of the system. Additionally, isotropy symmetry can be explicitly broken by the external non-zero magnetic field (analogon of non-zero quark masses). This links spontaneous symmetry breaking with phase transition.

However, it is not clear whether this phase transition, also called *chiral transition*, implies deconfinement of quarks, anti-quarks and gluons, i.e. coincides with the aforementioned *deconfinement transition* to QGP. The one way to resolve this issue within IQCD is to assess if the two critical temperatures coincide. To this end, earlier lattice QCD calculations studied the order parameters of the chiral and deconfinement transitions, obtained the same T_c and concluded that they represent the same transition [28]. However, nowadays it is believed that the relationship between chiral and deconfinement transition is more complicated than earlier lattice studies suggested, indicating that chiral transition differs from the deconfinement one, that it is model dependent and/or that the "phase" transition consists of several stages (for an overview, see [29]). Additionally, it appears that there is no transition temperature that can be associated with the deconfining stage of the transition for physical masses of the light quarks [30].

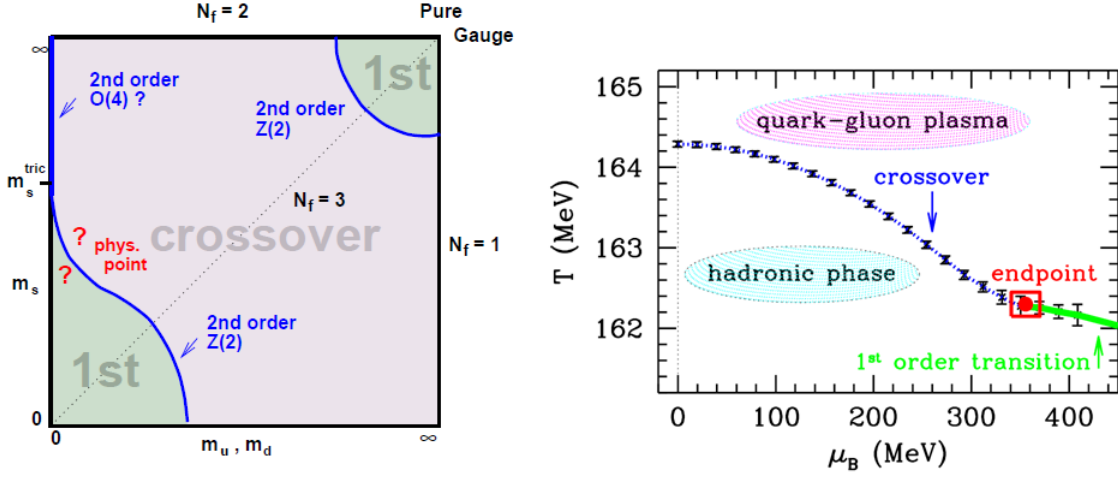


Figure 1.5: Lattice QCD calculations of the criticalness of the hadronic matter phase transition. The left panel shows phase diagram at zero baryon density, for $m_u = m_d \neq m_s$. Figure adapted from [31]. Possible phases of hadronic matter as a function of temperature and baryon number density, in $2 + 1$ case, are presented in the right panel. Endpoint denotes the critical point. Figure adapted from [32].

The issue of whether there is a phase transition or cross-over, for zero baryonic density, is addressed in the left panel of Fig. 1.5, which examines the criticalness of the transition as a function of the quark masses. The masses of up and down quarks are considered identical. Thus, the lQCD calculations suggest [31] that for massive quarks, at both low and large masses, the first-order phase transition occurs. The cross-over transition is predicted to take place for intermediate quark masses, while the second-order phase transition occurs in the border line between the first-order and cross-over regions. Nowadays, there has been consensus that for the physical quark masses and $\mu_b = 0$ there is not a phase transition but a cross-over [25, 26, 28]. The cross-over nature of the transition (for $\mu_b \simeq 0$) has been known for years [33], but the most recent lQCD calculations (assuming chiral transition) imply that the first-order phase transition is excluded down to $m_\pi = 80$ MeV [34], while the starting temperature of cross-over ($\mu_b = 0$) equals to 156.5 ± 1.5 MeV [35] for real quark masses (3 flavor case). On the other hand, also for chiral transition the most recently obtained critical temperature in $2 + 1$ flavor case, where $m_u, m_d \rightarrow 0$, is $T_c = 138 \pm 5$ MeV [34] (for zero baryonic number density).

Next, we display different phases of QCD matter as a function of both: temperature and the baryon number density [32] (the right panel in Fig. 1.5). We observe that at low baryon number density, there is probably a very fast cross-over from the low density hadronic matter to the QGP phase. At higher baryon number density, there is believed to be the first-order phase transition [32, 36], but the position of this (critical) end point is still undetermined and the search for it is work in progress using different numerical methods, with major theoretical obstacles being so-called sign problem [37] (fermionic determinant is complex so that Monte Carlo simulations are not feasible), and introduction of real physical quark masses.

Note that throughout this section, we use the same label T_c (critical temperature) with few different meanings: critical point (where critical point denotes the end point of a phase equilibrium curve, i.e. the curve on which two different phases coexist), temperature of phase transition (either deconfining, or chiral) and cross-over temperature, although in the latter case it is not well-defined quantity.

The phase above T_c , is named quark-gluon plasma due to the analogy with electromagnetic plasma, where ion and electron dissociation took a place, whereas in QGP, one observes dissociation of color degrees of freedom. Additionally, another resemblance between these two plasmas, is in charge screening, so that color screening in QGP (Yukawa potential) corresponds to the charge screening by the adjacent moving charges in QED plasma ($q \rightarrow qe^{-r/\alpha}$). The major difference is that QGP obeys non-Abelian theory.

Like the QED plasma, the QGP recognizes two limiting regimes [16, 38]: *i*) the strongly coupled, and *ii*) the weakly coupled limit. The strongly coupled limit, which is attainable at RHIC and LHC, assumes the temperatures in the vicinity of critical temperature, i.e. $(1 - 3)T_c$, and is predicted by non-perturbative lQCD or AdS/CFT correspondence [39–42] (anti-de Sitter/conformal field theory correspondence), which represents conjectured relationship between quantum gravity and QCD-like theories. The weakly coupled limit, which implies extremely high energies (T well above T_c), is predicted by pQCD.

1.2.2. Detailed description of hadronic matter phase diagram

The contemporary view on hadronic matter phase diagram distinguishes two major regions [26]: the region where electromagnetic force between atoms and molecules dominates (for $T < 10^{10}$ K ~ 1 MeV and $p < 10^{30}$ Pa $\sim 10^{-2} \text{MeV}/\text{fm}^3$); and the region where strong interaction prevails (for $T > 1$ MeV and/or $p > 1 \text{MeV}/\text{fm}^3$). In the electromagnetic region hadrons are confined within atoms and molecules, while with increasing T over 100 MeV, hadronic gas is formed. The transition into deconfined state of quarks, anti-quarks and gluons (QGP) occurs at approximately $T \sim 150$ MeV (for $\mu_b = 0$), which is 10^5 times higher temperature than at the center of the Sun. Note that, Fig. 1.6 corresponds to the chiral transition, while deconfinement transition curve departs from it, in upward direction, at higher baryon number densities (baryon chemical potential). The Universe, however, developed in the reverse order.

At low temperature and $p > 1 \text{MeV}/\text{fm}^3$ the matter can be described as degenerated gas of neutrons and is believed to exist in neutron stars (cold nuclear matter). By heating this neutron matter up to several MeV, it should turn into the gas of nucleons, and due to similarities between nucleon-nucleon potential and Van der Waals interaction of molecules, this transition is referred to as nuclear liquid-gas phase transition. On the other hand, for even higher pressures $p > 10^3 \text{MeV}/\text{fm}^3$ (or baryon chemical potential $> 10^3$) MeV, at low temperatures, the formation of quark-quark Cooper pairs [43] occurs, leading to the exotic state of color superconductivity [44]. It is a QCD analogon of condensed matter physics superconductivity [45] (with quarks replacing electrons), which despite being a quantum effect (a result of electron-phonon interactions), can qualitatively be explained in the following classical manner. In a metal lattice electrons are free and, due to their same (negative) charges, they repel each other. On the other hand, the electron attracts positively charged ions, that are located at the lattice nodes. This causes the lattice distortion, moving the ions slightly toward the electron. Thus the positive charge density increases in the electron proximity, attracting the other electrons. At long distances, effectively this attraction between electrons, can overpower their repulsion, leading to their pairing-up.

It is worth noting that recently it has been discovered that Cooper-pairing is also responsible for superfluidity of the pair of Li atoms (system of ultracold fermionic atoms) at low temperatures [46] and under additional specific experimental conditions. Additionally, hydrodynamical models estimated that QGP behaves as a nearly perfect fluid, with the shear viscosity to entropy ratio close to the lowest bound predicted by Ads/CFT correspondence [47]. Consequently, the coldest and the hottest known matter surprisingly share the same property (phenomenon), which is known to be very rare on the Earth [48], and which therefore presents an even more interesting coincidence.

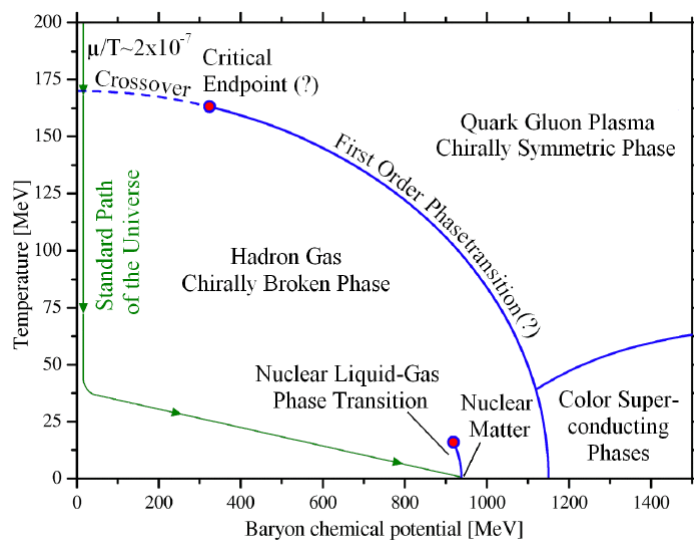


Figure 1.6: Illustration of a possible QCD phase diagram. Hadronic matter phase diagram as a function of both: temperature and baryon chemical potential. The green oriented curve presents commonly accepted evolution path of the universe. Figure adapted from [49].

1.2.3. The importance of QGP studying

There are multiple reasons for studying QGP and its properties, such as [24]:

- According to the current Cosmology [50], it is considered to be a primordial form of matter, that existed at a first $10 \mu s$ after the Big Bang;

- It represents an example of phase transition that may have occurred at high temperatures of the early universe;
- The nature of quark confining into hadrons and the origin of mass for matter could be explained by studying QGP properties;
- It is considered to be the ultimate, primordial form of QCD matter at high T or μ_b (at least up to the electro-weak scale at $T_{EW} \sim 10^3 T_c$), and finally:
- It is assumed to be a constituent of supernova and neutron stars, color superconductivity [51] as matter at high baryon number density and relatively low temperature.

Taking all these points into consideration, the only way to create and study QGP, i.e. the matter of energy density of the order $\sim 1\text{GeV}/fm^3$, under the controlled laboratory conditions are ultra-relativistic heavy ion collisions. As expected, the probability of creating such a dense hot matter increases with colliding larger nuclei and with higher collision energies. This marked the beginning of the new era in building upgraded collider facilities, although they are multipurpose detectors also used for different studies such as for instance: testing the Standard Model (e.g. Higgs boson) and its different extensions (e.g. Supersymmetry), searching for Grand Unification Theory, examining the nature of dark matter, etc.

1.3. The ultra-relativistic heavy ion collisions

Today, the experimental method of examining hadronic matter consists in accelerating the heavy nucleus beams and colliding them. The range of accelerated beam energies varies from GeV to TeV at laboratories, such as GSI (Darmstadt, Germany), BNL (New York, USA) and CERN (Geneva, Switzerland) [26]. For different center-of-mass energy per nucleon pair ($\sqrt{s_{NN}}$), different regions of the phase diagram of hadronic matter can be studied.

During the collision of ultra-relativistically accelerated ions a fraction of the initial center of mass energy is being released, due to inelastic collisions between the constituent, it converts, consistently with Einstein energy-mass equivalence, into

new degrees of freedom (new particles) of the system, creating the QGP under the laboratory conditions. Therefore ultra-relativistic HIC are termed as a Little Bang.

1.3.1. Overview of heavy ion colliders

The first heavy ion beams accelerated to relativistic energies were produced at the Alternating Gradient Synchrotron (AGS) at Brookhaven National Laboratory (BNL, USA) and at the Super Proton Synchrotron (SPS, CERN, Switzerland) in the 80's [26]. They represented a fixed target accelerators, where highly accelerated particles were shot at stationary ones. However, significantly higher collision energies are accessible in the other type of heavy ion colliders (HIC) – colliding beam accelerators, such as the RHIC and the LHC.

The Relativistic Heavy Ion Collider (RHIC) is the first ever build colliding beam heavy ion (accelerator) collider and is still operating. It is sited at BNL in Upton, New York. Its injector is AGS, that accelerates two nucleus beams within two separate rings and in opposite directions. Further, the beams proceed to RHIC collider, where they are being accelerated to their nominal energies and stored in two rings of 3.85 km circumference length. There were four interaction points along the RHIC ring, where the bunches of the two beams collided, also known as: PHENIX, STAR, PHOBOS and BRAHMS experiments. Today, only the two of them, PHENIX (Pioneering High Energy Nuclear Interaction eXperiment) and STAR (Solenoidal Tracker at RHIC) are operating and collecting the data. So far the following types of particle combinations have been explored at RHIC: $p + p$, $p + Al$, $p + Au$, $d + Au$, ${}^3He + Au$, $Cu + Cu$, $Cu + Au$, $Au + Au$ and $U + U$. RHIC provided the first $Au + Au$ collisions at $\sqrt{s_{NN}} = 130$ GeV in June 2000 and reached in 2001 its nominal energy of $\sqrt{s_{NN}} = 200$ GeV. In these collisions the high enough energy density (in the latter case $\epsilon \approx 5$ GeV/fm³) was produced, so it was safe to claim that QGP was finally formed [26]. The evidences of deconfined state formation will be discussed in section 1.5. In the near future, a fixed target program will also start at STAR, where 3 – 7.7 GeV $Au + Au$ collisions will be used to examine high baryon density regime $\mu_b \sim 420 - 720$ MeV, in attempt to study the first order phase transition as well as the QCD critical point. To date RHIC has had 17 runs.

Currently, the largest and the most powerful particle collider in the world is the Large Hadron Collider (LHC), at CERN, located near Geneva, on France-Switzerland boarder. It uses SPS as an injector, has 27 km in circumference and lies 175 m underground. However, it is worth noting that, the heavy ion fixed-target experiments at SPS *first* hinted at the existence of new state of matter consisting of freely roaming quarks, antiquarks and gluons, but as established later, the initial temperature of thus obtained system appeared to be insufficient for such a transition. In November 2010, LHC provided the first $Pb + Pb$ collisions at $\sqrt{s_{NN}} = 2.76$ TeV, which represented ~ 14 times higher center-of mass energy compared to the RHIC. The produced matter had $\epsilon \sim 10 \text{ GeV}/\text{fm}^3$, which is well above the transition point, ensuring that the deconfined state of QGP is reached within this collider (which will be, as discussed above, well-argued in section 1.5).

The LHC has four crossing points, around which seven detectors are positioned, corresponding to the seven experiments: ALICE, CMS, ATLAS, LHCb, TOTEM, LHCf, MoEDAL. Four of them participate in the heavy ion program: ALICE (A Large Ion Collider Experiment), CMS (Compact Muon Solenoid), ATLAS (A Toroidal LHC Apparatus) and LHCb (LHC-beauty). ALICE was the first/only LHC experiment dedicated to study the QGP, but presently the wealth of data is coming from the remaining three experiments as well. It collides the following particle pairs: $p + p$, $p + Pb$, $Pb + Pb$, and lately started program with smaller system than the one created in $Pb + Pb$ collisions: $Xe + Xe$. Now, the top colliding energies for $Pb + Pb$ and $Xe + Xe$ systems are 5.02 TeV and 5.44 TeV, and the run 2 data analysis is in full swing.

The remote future experimental plans in high-energy heavy-ion physics are building of 100 km in circumference Future Circular Collider at CERN and Super pp Collider (SPPC) at China.

Along with these two the most renowned colliders, there are also other facilities/experiments dedicated to studying some specific regions of hadronic matter diagram. Thus, GSI Heavy Ion Synchrotron SIS18, in Darmstadt, Germany is built for studying the onset of phase transition, i.e. pursuit for the first order transition and critical point at high μ_b , while at the same place Facility for Antiproton and Ion Research (FAIR) is being built. The similar function will have Nuclotron-based Ion

Collider facility (NICA), whose putting into operation is foreseen for 2021 in Dubna, Russia and HIAF in China.

Additionally, also the facilities such as Electron-Ion colliders, that explore the nuclear parton distribution function (nPDF), i.e. the properties of cold nuclear matter (CNM), and QCD at extremely high gluon densities (saturation), which provides the knowledge of the nuclei just before the $A + A$ collision occurs, are very important. Thus, SLAC and HERA were the leading ones, whereas the future facilities are: Jefferson Laboratory's Electron-Ion Collider (JLEIC), at Newport, Virginia, the upgrade of RHIC to eRHIC and Large Hadron electron Collider (LHeC).

1.3.2. Space-time picture of ultra-relativistic heavy ion collisions

The accepted picture of all preceding and subsequent phases of QGP formation in ultra-relativistic HIC is illustrated in Fig. 1.7. Since nuclei are accelerated nearly to the speed of light, they are Lorentz contracted along the beam direction in centre-of-mass frame, and seen as two "pancakes", i.e. gluonic sheets.

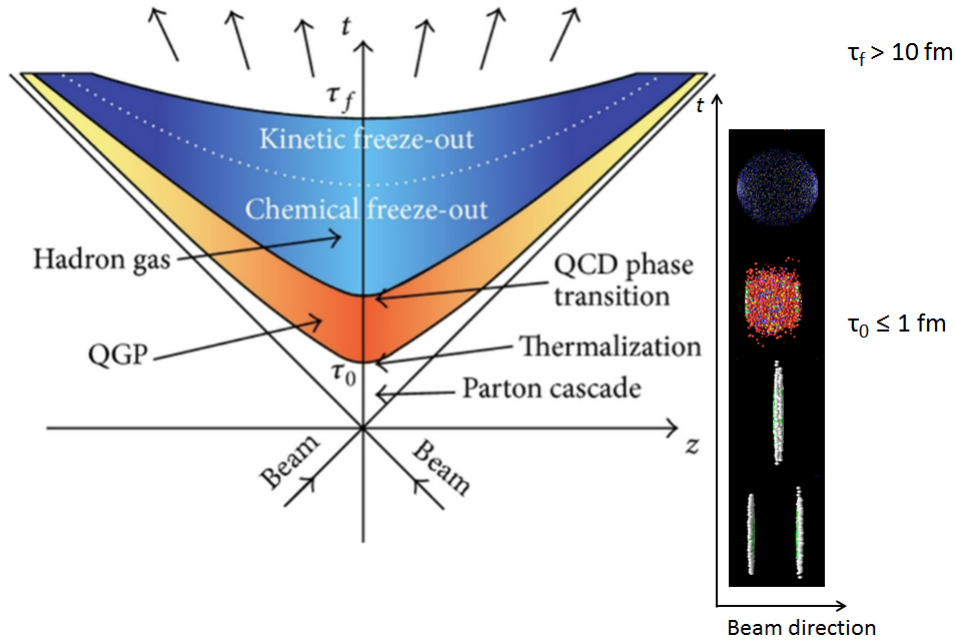


Figure 1.7: Space-time evolution of the heavy ion collision. The scheme of different stages of a HIC as a function of longitudinal coordinate z (beam axis) and time t is given on the left. The inserted figure on the right embodies the particles, from nuclei to detectable hadrons, and is synchronized to the figure on left. τ denotes the Lorentz-invariant proper time ($\tau \equiv \sqrt{t^2 - z^2}$), which is constant along the hyperbolic curves separating different stages. Figure adapted from [52].

Historically, the first and the most simplified scenario of the system evolution considers the Bjorken expansion, which is applicable for central collisions at the top RHIC energy and at LHC energies, but is not a part of present-day most advanced hydro-models. According to Bjorken scenario [53], the crossing time of the nuclei τ_{cross} can be estimated as $\tau_{cross} = 2R/\gamma$, where R denotes nucleus radius, while γ is Lorentz factor. Additionally, he proposed that the crossing time should be smaller than the time scale of the strong interactions $\tau_s \sim 1/\Lambda_{QCD} \sim 1 \text{ fm}/c$, i.e. $\tau_{cross} < \tau_s$, which is satisfied unless $\gamma < 12$. This assumption ensures that the particles generated by the strong interaction between the nucleon partons, are created once the nuclei have already passed each other. Note that, both RHIC and LHC meet this condition, as in these collisions the order of magnitude of γ is well above the threshold, i.e. 10^2 and 10^3 , respectively. The scenario also assumes the

uniform distribution of the particle multiplicity as a function of the rapidity. This assumption greatly facilitates the hydrodynamical calculations of system evolution, because it provides a rapidity symmetry of the system, resulting in a uniform energy density in different rapidity slices.

Today it is considered that, in ultra-relativistic HIC, nuclei pass through each other, practically intact, and that due to the enormous release of collision energy new degrees of freedom are formed. Also, the QGP formation is first examined in transverse plane (transverse to the beam axis, corresponding to mid-rapidity region), in order to study the new matter under the zero baryonic number conditions (all baryons are still enclosed and carried away within nuclei). Note also that we will only generate predictions for mid-rapidity region. The first, therefore the fastest, partons (hard probes) are produced within 0.2 fm/c post-collision[24]. However, still the produced partons are not forming thermalized/equilibrated state called QGP. This initial stage of parton (pre)production is described by different Initial state models (for references see [54]), such as: Glauber [55] models (optical, Monte-Carlo), QCD scattering in the Dipole Picture (which includes initial-state energy loss and shadowing [56–58]) and Color Glass Condensate and Glasma (KLN models [59] and IP glasma [60]), which assumes Lorentz contraction, then CGC [61, 62] stage before the collision, and Glasma [63] right after the nuclei pass each other. Note that under pre-production stage, one considers nucleus state just before the collision, while under production stage one assumes the created partonic stage immediately after nuclei cross each other.

A starting point of the glasma-based models (or CGC-inspired models, such as KLP), which are considered most up-to-date ones (IP-Glasma), is the assumption of nuclei before the collision being described by Color Glass Condensate (CGC). This was motivated by HERA (Hadron Elektron Ring Anlage at DESY, Hamburg) data [64] on gluon distribution function in $e + p$ collisions, and could be explained in following manner. One could argue that gluons dominate QCD dynamics. Namely, at large energies, smaller fractional momentum x_B (Bjorken $x_B = Q^2/(2Pq) = -q^2/(2M\nu)$, where P is proton momentum, while $q^2 = -Q^2$ and ν are the square of the four momentum and energy transferred from the lepton (electron) to the target nucleon (proton) at rest in laboratory frame in DIS, respectively; M is proton mass)

and larger energy scales Q regions become accessible. With decreasing Bjorken x_B the gluon density increases much faster than quark density, due to non-Abelian nature of QCD (i.e. due to 3- and 4-gluon vertices, that is, the color charge). Thus, the intrinsic non-linearity of QCD causes gluon showers to produce more lower x_B gluon showers - generating an exponential avalanche toward small x_B [24]. Additionally, the number of gluons rises more rapidly than their transverse area. Thus, the gluon density $xG(x, Q^2)$ increases sharply with decreasing x_B or increasing Q (Fig. 1.8). Note that, low x_B gluons are closely packed together in the transverse plane, resulting in a weakly coupled ($\alpha_s \ll 1$), but dense system called CGC. The opposite process, that competes with gluon shower production ($\propto \rho$), is the gluon fusion ($\propto -\alpha_s \rho^2$). Consequently, at high enough energies, the transverse phase space gluon density $\rho = \frac{1}{R^2 \pi} \frac{dN}{dy d^2 p_\perp}$ (y denotes the rapidity) eventually reaches the saturation point $\rho_{sat} \propto 1/\alpha_s(Q)$ [24]. Since α_s is very small, the quantum mechanical states are multiply occupied by colored gluons, which justifies the name Condensate.

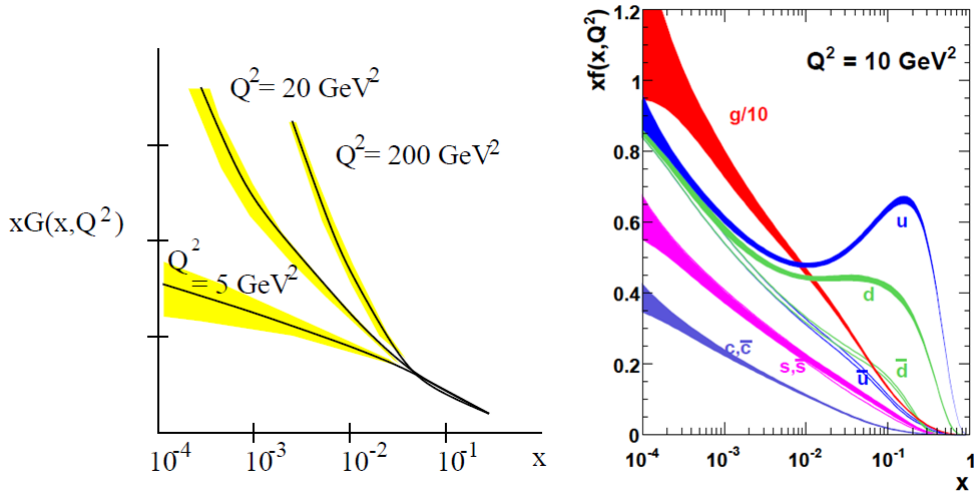


Figure 1.8: Proton's partons distribution functions. The gluon distribution function as a function of x_B for different values of Q^2 from DGLAP fits to HERA [64] is presented in the left panel. The right panel shows MSTW2008 next-to-leading order (NLO) PDFs at scale $Q^2 = 10 \text{ GeV}^2$ for the LHC. Figure adapted from [64, 65].

Additionally, from the right panel of Fig. 1.8 we observe that the HERA data for DIS confirm that gluons totally dominate the dynamics for $x_B < 0.01$.

Also note that, the bound proton parton distribution function (PDF) in heavy

nucleus, differs from the one in free proton. As x_B decreases toward small values ($x_B \lesssim 0.01$), the ratio of the bound proton PDF (nPDF) $f_i^{p/A}(x, Q^2)$ and the free proton PDF $f_i^p(x, Q^2)$ is smaller than 1. This effect is known as shadowing or screening [56–58], and it was first observed in photon-nucleus collision experiments. The name comes from the fact that the cross section per nucleon in heavy nuclei is smaller than the one in deuterium. In practice, this means that, the nuclear PDF in heavy nucleus (nPDF) can not be simply expressed by the normalized sum of free protons and free neutrons (nucleons) PDFs. And also, this affects the PDF evolution equations such as DGLAP [66–68].

Upon production, free partons interact among each other until reaching QGP equilibrium phase, which is considered to be accomplished few fm/c upon the nuclei collision. The experimental data support the idea of very fast thermalization $\tau_0 < 1$ fm [53], but theory still fails to explain this phenomenon, which remained an open question [69]. If indeed, the system reached the equilibrium very fast, then its subsequent evolution could be described by relativistic perfect-fluid hydrodynamics. The hydrodynamic expansion leads to more dilute system, and eventually the phase transition from QGP to hadronic gas occurs.

There are various models describing hydrodynamic expansion, and additionally hybrid models, which combine fluid dynamics with subsequent hadronic phase and/or preceding partonic phase. Thus, there are hydrodynamic expansion models which assume strong coupling, which is in accordance with the temperatures near T_c (for a review see [70, 71]), and include dissipative relativistic hydrodynamics. Some of the more advanced models belonging to the second (hybrid) group are: simulations combining 2D+1, 3D+1 viscous codes for QGP evolution with UrQMD [72] (Ultra relativistic Quantum Molecular Dynamics) cascade for hadronic phase, VISHNU [73] (Viscous Israel Stewart Hydrodynamics and UrQMD), MUSIC+UrQMD [74], SONIC [75], EPOS3 [76]. On the other hand, the models which assume weakly coupled gas (at higher T), belong to Parton transport theory [77, 78], such as state-of-the-art: perturbative QCD based transport model BAMPS [79] (Boltzmann approach to multiparton scatterings), PHSD [80] (Parton-Hadron Sting Dynamics) and AMPT [81] (A Multi-Phase transport model).

Thus obtained strongly-interacting hot hadron gas exists within 2 fm/c, whereas

the transition into weakly-interacting system of hadrons happens through at least two stages: chemical and kinetic (thermal) freeze-out, that ends 10 fm/c after the nuclei collision took place. The freeze-out is the general term used to describe the stage of matter development, where the final hadrons are being emitted. Usually, the chemical freeze-out takes place before the kinetic one.

Namely, at low colliding (rescattering) energies of hadrons the elastic cross sections are larger than the inelastic cross sections, which results in earlier fading away of inelastic than the elastic (the same number of initial and final particles) collisions. The moment when inelastic collisions cease is considered as the *chemical freeze-out*. As the system evolves from chemical to thermal freeze-out, the dominant processes are elastic cross sections and strong decays of heavier resonances into stable hadrons. Note that, the measured ratios of hadron abundances are frozen at chemical-freeze-out. The chemical freeze-out is studied by statical and thermal models, which aspire to explain the ratio of hadron multiplicities. For an overview of the models, see [82]. It is also considered that T_{chem} is approximately equal to 153 MeV [83].

On the other hand, the thermal (kinetic) freeze-out is defined as the stage of matter evolution when the particles stop interacting. The thermal freeze-out marks the transition from strongly interacting hadron gas to the weakly coupled one (assuming freely streaming hadrons). This freeze-out is induced by the expansion of the medium, which leads to rapidly growing mean free path λ_{mfp} . So, when timescale connected with the collision $\tau_{coll} \sim \lambda_{mfp}$ becomes larger then the expansion time scale τ_{exp} [84] of the medium, the *thermal freeze-out* occurs. Thus, the particles depart from each other very fast, which decreases the probability of collision happening. Although different particles may have different freeze-out points, the fast expansion implies fast thermal freeze-out, and is approximately assumed to be universal for all types of particles. During this process, momentum distributions of particles are frozen, and they do not change until particles (hadrons) reaching the detectors. The thermal freeze-out is studied by hydro-inspired models, which analyse the transverse momentum spectra and correlations. For an overview of the models see [85].

1.4. Probes of QGP matter

In this section we give a brief review of the observables that can be measured in ultra-relativistic HIC and their classification. These observables are expected to be able to provide an answer whether the QGP is formed in these collisions, and if so, to give deeper insight into the properties of this extreme form of matter.

1.4.1. The pQCD factorization formula

Before embarking on the relevant observables, we outline the idea of the collinear factorization, which is very important for both theoretical and experimental study of the matter created in ultra-relativistic HIC.

From Fig. 1.9, which represents DIS parton (predominantly gluon) evolution in QCD, we distinguish three regions, that are accessible in ultra-relativistic HIC: 1) non-perturbative region for $Q^2 < \Lambda_{QCD}^2$ (virtuality $Q^2 \equiv -q^2 > 0$, where q presents exchanged momentum in DIS case), where interactions among partons are too strong, keeping them confined within hadrons; 2) CGC region for large densities and relatively small Q^2 , where gluon saturation occurs (as discussed above); and 3) dilute region for low densities and high $Q^2(x)$, where the parton densities evolution is described by linear Dokshitzer, Gribov, Lipatov, Altarelli and Parisi (DGLAP) equations [66–68]. As mentioned earlier, in the last region, the perturbative QCD (pQCD) is suitable, and it represents the region of deconfinement, i.e. the phase-space where quark-gluon plasma can be formed. Further, we will concentrate on this region.

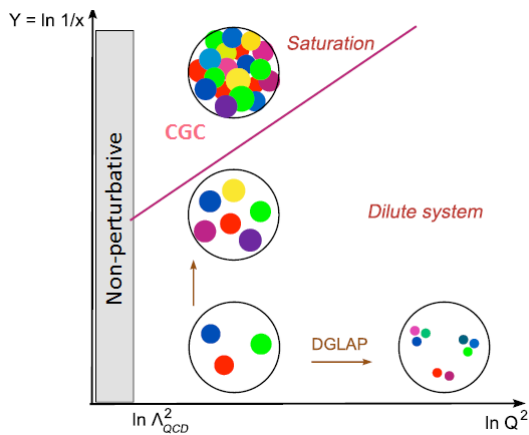


Figure 1.9: Phase diagram for parton evolution in QCD. Each colored circle in figure depicts a parton with transverse area $\sim 1/Q^2$ and longitudinal momentum equal to xP , where x is a fractional momentum of a parton at a given resolution scale Q (or in DIS case Bjorken $x = \frac{Q^2}{2Pq}$ is a fraction of proton momentum carried away by parton), and P being proton momentum. The straight line is a saturation line, separating the dense from dilute regimes. In this thesis we consider a dilute limit, where DGLAP evolution is applicable. Figure adapted from [86].

In our region of interest, an empirical pQCD factorization formula [87] is assumed to be applicable, which considers that the differential hadron cross section in ultra-relativistic HIC can be disentangled into three independent processes: 1) initial parton production; 2) parton energy loss within QGP medium; and 3) fragmentation (and decay) into detectable hadrons.

The generic pQCD factorized formula for inclusive hadron h production, i.e. $A + B \rightarrow h + X$, as depicted in Fig. 1.10 (where A and B denote accelerated heavy or light ions and X all remaining detectable particles) reads:

$$\frac{1}{T_{AB}(\mathbf{b})} \frac{dN^{AB}(b)}{dyd^2\mathbf{p}_\perp} = \sum_{a,b,c,d} \int dx_a dx_b f^{a/A}(x_a, Q_a^2) f^{b/B}(x_b, Q_b^2) \frac{d\sigma^{ab \rightarrow cd}}{d\hat{t}} \times \int_0^1 d\epsilon P(\epsilon) \frac{1}{1-\epsilon} \frac{D^{h/c}(\frac{z_c}{1-\epsilon}, Q_c^2)}{\pi z_c}, \quad (1.4.1)$$

where a and b present produced initial partons, originating from A and B , respectively. As previously explained, $f^{a/A}(x_a, Q_a^2)$ and $f^{b/B}(x_b, Q_b^2)$ denote corresponding PDFs, where x_a and x_b (Bjorken x) stand for initial momentum fractions carried

away by the corresponding hard-scattered partons. Note that, $d\sigma^{ab\rightarrow cd}/d\hat{t}$ is differential cross section for the process on partonic level. In our case $P(\epsilon)$ is pQCD distribution of parton fractional energy loss, whereas $z_c = p_h/p_c$ is a momentum fraction carried away by the leading hadron h . $D^{h/c}$ denotes fragmentation function (FF) of parton c hadronizing into h . The scaling factor of proton-proton collision is given by so-called nuclear thickness (overlap) function, for a given impact parameter \mathbf{b} (a relative distance between nucleus centers in a transverse plane): $T_{AB}(\mathbf{b}) = \int d^2\mathbf{s} T_A(\mathbf{s})T_B(\mathbf{s} - \mathbf{b})$, where $T_A(\mathbf{s}) = \int dz_A \rho(\mathbf{s}, z_A)$ denotes the probability per unit transverse area of a given nucleon being located in the target/projectile flux tub, which is all well-defined within Glauber [55] model of HIC.

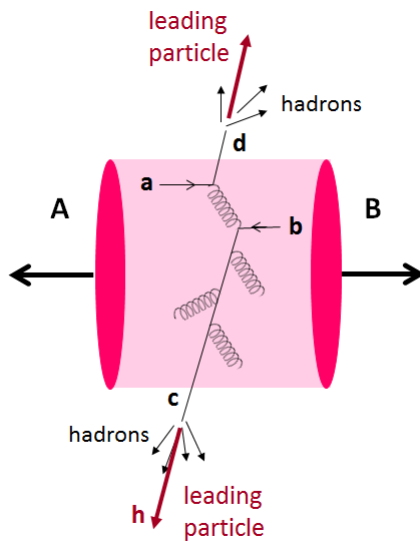


Figure 1.10: Illustration of pQCD factorization. The figure shows an inclusive $A + B \rightarrow h + X$ process, where A and B denote colliding nuclei. The production of initial parton c is depicted at the leading order, upon which parton c traverses the medium and loses energy via gluon bremsstrahlung. Finally c fragments (denoted by arrows) into hadron h (the leading particle).

The asset of using the pQCD factorization formula reflects in ability to theoretically study the complicated ultra-relativistic HIC processes, such as: production, energy loss and fragmentation, as separate entities. The obtained separate numerical results, when combined together produce a prediction, which can be further tested against the data.

Since the subject of this thesis is the energy loss of high p_{\perp} particles in QGP, we will further focus our theoretical striving only on energy loss step. Also, we assume that only high p_{\perp} parton energy loss occur in QGP, while its production, which takes place well before thermalized QGP is formed, and fragmentation (and decay) occur in QCD vacuum.

1.4.2. Observables classification

The heavy-ion observables, accessible to measurements with RHIC and LHC, serve not only as an evidence of QGP formation, but also as a tomographic tool for studying properties of this new state of matter. They are gathered in two groups:

1. Hard (perturbative) probes, i.e. particles with large transverse momentum and/or large mass ($p_{\perp}, m \gtrsim \mathcal{O}(1 \text{ GeV}) \gg \Lambda_{QCD}$), which represent perfect tomographic tool for studying QGP medium, since they are considered to: *i*) be produced very early ($\tau \sim 1/p_{\perp} \lesssim 0.2 \text{ fm}/c$ [24] after the HIC), and *ii*) originate from initial partonic scatterings with large momentum transfer Q^2 . Therefore, these partons are assumed to traverse the entire QGP medium, eventually to be affected by the medium and to encode "tomographic" information of the hottest and densest phases of the collision. Additionally, they can be theoretically studied within pQCD (pQCD factorization formula); and
2. Soft (bulk) observables, which are linked to the collective behavior of the created system and mainly refer to the expansive phases of QGP evolution, and consequently are studied within relativistic hydrodynamics. They provide constraints on the collective properties, such as entropy density, viscosity, etc., of the produced strongly-interacting medium. Among many of these observable, we will refer only to the elliptic flow v_2 , as one of the smoking guns of QGP formation and the one responsible for the coin "nearly perfect fluid" used to describe the quark-gluon plasma.

Namely $\sim 99.9\%$ of quarks and gluons created in ultra-relativistic HIC are low-energetic particles ($\sim k_B T$) and they constitute QGP (bulk). The remaining $\sim 0.1\%$

are high-energy particles, that is hard probes (tomographic probes), which are the subject of this thesis. Note that, QGP matter, due to its short-living, cannot be tested by some external particles, which makes hard probes, as self-generated particles, the only tool for exploring the medium properties. Also, throughout the thesis we use the term hard probes for both: the high p_{\perp} parent parton, or its fragmentation product: hadron. These probes yield: gluon rapidity density dN^g/dy , transport coefficient \hat{q} (average transverse momentum squared transferred to the traversing particle per unit path-length), critical energy density ϵ_{crit} , critical temperature T_{crit} or they serve to control the validity of the pQCD factorization formula (i.e. $\sigma_{AA} = A^2\sigma_{pp}$), and to constrain the nPDFs.

Hard probes [88, 89] refer to the following processes (as schematically shown in Fig. 1.11) and the corresponding observables (for clarification of each see subsection 1.5):

- Jet quenching [90], i.e. "the attenuation or disappearance of the spray of hadrons resulting from the fragmentation of a parton having lost energy in the dense plasma produced in the reaction" [91]. The corresponding observables include the suppression of:
 - high p_T hadron spectrum,
 - heavy-quarks (i.e. D and B mesons),
 - unbalanced back-to-back high- p_{\perp} di-hadron azimuthal correlations;
- Non-attenuated yield of electroweak particles (γ, W and Z bosons);
- γ jets, i.e. enhanced yield of thermal (secondary) photons, which provides an estimate for the mean and consequently the initial temperature of QGP, with the help of various hydro models.
- Quarkonium dissociation, where quarkonium denotes the bound state of heavy quark and its anti-quark $q\bar{q}$, that is charmonium ($c\bar{c}$) and bottomonium ($b\bar{b}$) families.

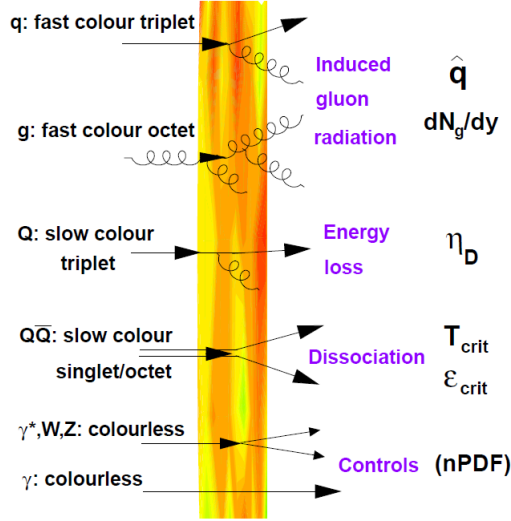


Figure 1.11: Illustration of the hard probes. Layout of hard probes (on the left-hand side) together with the QCD matter features that the corresponding probe provides (on the right-hand side). Figure adapted from [92].

On the other hand, soft (bulk) observables [93] include: charged hadron multiplicity $dN_{ch}/d\eta$, inclusive identified hadron spectra (dN/dp_{\perp}), radiative v_1 , elliptic flow v_2 [94] and higher harmonics, etc.

Historically, the most prominent soft observable was elliptic flow (of light $2 - 3$ GeV/c transverse momentum particles), the collective phenomenon which occurs in peripheral $A + A$ collisions, and only if QGP thermalizes quickly enough $\tau \sim 0.5 - 1$ fm/c [24, 95]. It is quantified via the (non-zero) second Fourier coefficient $v_2(p_{\perp}, y) \equiv \langle \cos(2\Delta\Phi) \rangle$ of the azimuthal expansion of the single inclusive hadron spectra with respect to the reaction plan (RP) [96, 97]:

$$E \frac{d^3 N}{dp^3} = \frac{1}{2\pi} \frac{d^2 N}{p_{\perp} dp_{\perp} dy} \left(1 + 2 \sum_{n=1}^{\infty} v_n \cos[n(\Phi - \Phi_{RP})] \right). \quad (1.4.2)$$

The reaction plain is determined by beam direction and impact parameter (see Fig. 1.12), while $\Delta\Phi = \Phi - \Phi_{RP}$. The explanation for the elliptic collective behavior is following: in peripheral collisions the overlapping nuclei region is azimuthally anisotropic (almond-shaped), and due to larger pressure gradient "in-plane" compared to the "out-of-plane" (see left panel of Fig. 1.12) the initial coordinate-space anisotropy translates into the final momentum-space asymmetry, i.e. elliptic flow (see right panel of Fig. 1.12).

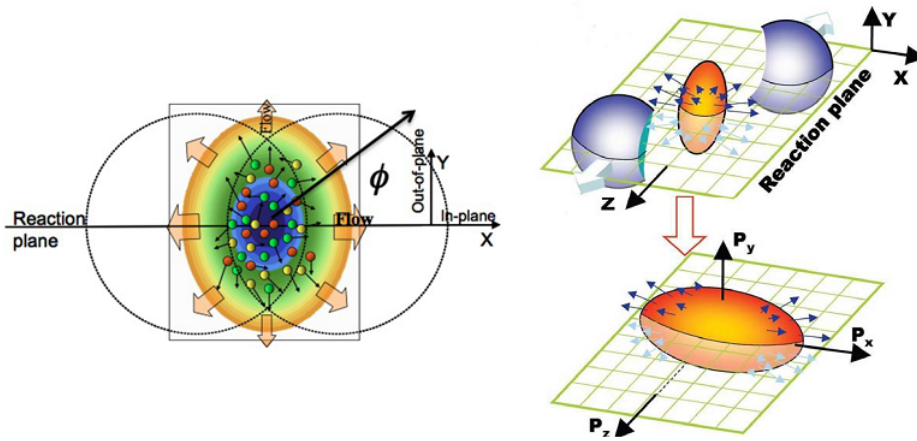


Figure 1.12: Transfer of spatial into momentum azimuthal anisotropy. The figure illustrates the peripheral collision of two nuclei, where the overlapping region (QGP) lose its spherical shape and becomes almond-like (elliptic). Broken spatial isotropy produces uneven pressure gradients in-plane and out-of-plane (indicated in figure), leading to momentum anisotropy and elliptic collective behavior. The left panel is adapted from [98], while the right panel is adapted from [99].

1.4.3. The nuclear modification factor

As discussed earlier, ultra-relativistic $A + A$ (A is a heavy ion) collisions are considered to be the only source of quark-gluon plasma in experiments, while in $p(d) + A$ collisions its precursor, i.e. the cold nuclear matter (CGC), can be studied (see descriptive Fig. 1.13). Nowadays, there is a debate about whether a small droplet of QGP could be produced in this smaller systems ($p(d, {}^3\text{He}) + A$), since they also exhibit a collective behaviour (see the next section). However, $p + p$ collisions are still considered as a source of so-called "QCD vacuum". Therefore, in order to extract thermodynamic and transport properties of QGP, the results for a given observable obtained in $A + A$ collisions need to be compared with the one measured in $p + p$ collisions [92], which thus serve as a baseline:

$$R_{AA} = \frac{\text{Yield}(AA)}{\text{Yield}(pp)} = \frac{\text{"hot/dense QCD medium"}}{\text{"QCD vacuum"}}. \quad (1.4.3)$$

Along the same lines, the properties of CGC could be inferred by substituting $\text{Yield}(AA)$ by $\text{Yield}(p(d)A)$ in the numerator of the previous equation.

Finally, we define one of the central observables in this thesis, that quantifies the medium effect on the yield of a hard probe in a $A + A$ collision — *nuclear modification factor* [92]:

$$R_{AA}(p_{\perp}, y; \mathbf{b}) = \frac{d^2 N_{AA}/dydp_{\perp}}{\langle T_{AA}(\mathbf{b}) \rangle \times d^2 \sigma_{pp}/dydp_{\perp}}, \quad (1.4.4)$$

which is a quantitative form of descriptive Eq. (1.4.3), and which, due to the pQCD factorization formula (Eq. (1.4.1)), measures the deviation of $A + A$ (for a given impact parameter) from an incoherent superposition of nucleon-nucleon collisions (which corresponds to $R_{AA} = 1$). Thus, if the probe is unaffected by the medium then $R_{AA} = 1$ (e.g. electroweak probes), if it is enhanced then $R_{AA} > 1$, and for suppression [90] $R_{AA} < 1$.

It is worth noting, that throughout this thesis, we use angular averaged form [100, 101] of the nuclear modification factor:

$$R_{AA}(p_{\perp}) = \frac{dN_{AA}/dp_{\perp}}{N_{bin}dN_{pp}/dp_{\perp}}, \quad (1.4.5)$$

which represents the ratio of the quenched $A + A$ spectrum to $p + p$ spectrum, scaled by the number of binary (nucleon-nucleon) collisions (N_{bin}), and which is shown to be weakly sensitive to the details of medium evolution [102, 103], i.e. can be characterized by medium averaged properties (e.g. T_{eff}).



Figure 1.13: $A + A$ vs. $p(d) + A$ collisions. The illustration of nucleus + nucleus (left) and proton + nucleus (right) collision is shown. The gray area in the left panel presents formed QGP medium after the collision. The gray area in the right panel raises a question of QGP formation in $p(d)+A$ systems. Figure adapted from [104].

The subsequent section gives an answer to whether initial state or final state effects are responsible for suppression.

1.5. Empirical evidence of QGP discovery

In this subsection first we will give historical review on dilemmas that scientist encountered and experimental signatures of the QGP formation in the previously mentioned colliders. Then we provide the updated measurements of the relevant observables.

1.5.1. Historically

One of the historically most relevant observables for studying QGP formation and properties is the jet quenching, as first proposed in [105, 106]. The reason behind this choice, was the belief that at sufficiently high colliding energies at RHIC and LHC, the radiative energy loss of high p_{\perp} parton would become large enough to lead to the softening of p_{\perp} spectra. At that time, it was still believed that the main energy loss channel was the gluon bremsstrahlung, while the collisional energy loss was considered practically negligible [107, 108] (which is now considered incorrect assumption). Namely, at its way through the quark-gluon plasma, high p_{\perp} is considered to interact with medium constituents, and eventually radiate gluons. For large enough initial parton's momentum, this radiative energy loss can be calculated within pQCD, and is considered responsible for attenuation of p_{\perp} spectra compared to the spectra, with no medium present. Based on the data from combined experiments at SPS, CERN [109] on February 10th 2000 announced the creation of new state of matter—the QGP, but later measurements proved that the collision energy was not large enough either for such a transition or for creation of thermalized QGP (collective flow measurements).

In the later years, the higher particle momenta become available at RHIC, that led to Fig. 1.14, which presents one of the most important experimental result at the time. In this figure the comparison of RHIC and SPS $\pi^0 R_{AA}$ data as a function of p_{\perp} is presented. The SPS results display a significant enhancement of $Pb+Pb$ spectrum compared to scaled $p+p$ spectrum. This is a consequence of Cronin effect [110–114], which, on partonic level, could be explained in terms of multiple scatterings of "projectal" partons from proton or nucleus off partons from the other nucleus, where

"projectal" partons acquire a transverse momentum kick, shifting their momentum spectra toward higher values. Quantitatively, it can be expressed in the following manner: $Ed\sigma/d^3p(H + A \rightarrow h + x) = A^{n(p_\perp)}Ed\sigma/d^3p(H + N \rightarrow h + x)$, where A stands for the nucleon number, N and H denote the nucleon and the incoming hadron, respectively, h is the produced hadron, while $n(p_\perp) > 1$. Nowadays, it is considered that Cronin effect occurs in $p + A$ and $A + A$ collisions for $2 \lesssim p_\perp \lesssim 6$ GeV/c [110–114].

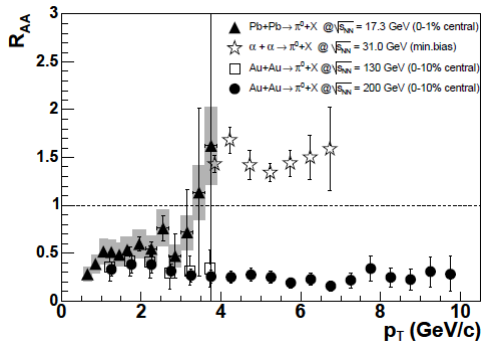


Figure 1.14: RHIC vs. SPS R_{AA} as a function of p_\perp . Comparison of neutral pion suppression data from SPS (triangles and stars) and RHIC (squares and circles) indicates the occurrence of jet quenching at RHIC [116], in distinction to previously observed enhancement at SPS (see [115] and references therein). Figure adapted from [115].

However, in central $Au + Au$ collisions at RHIC no enhancement was detected, but instead the factor of 4 – 5 suppression (R_{AA}) of π^0 , which might indicate the formation of QGP [115]. Keep in mind that, at the time of this measurement it was unclear whether the suppression is a consequence of the initial state effect (i.e. the saturation of gluon distribution, shadowing [56–58]) or the final state effect (energy loss in QGP, i.e. jet quenching). Since, the initial state (cold nuclear matter) effects are studied in $p(d) + A$, while both initial and final state (hot nuclear matter —QGP) effects are considered to be achievable in energetic $A + A$ collisions (see descriptive Fig. 1.13), the final resolution to the suppression origin came by comparing the particle suppression in these two collisions. Thus, in the summer of 2003 Physical Review Letters published their famous issue (see the cover in the

left panel of Fig. 1.15), where all four RHIC experiments (PHENIX, PHOBOS, BRAHMS and STAR) preliminarily obtained that the suppression is due to the hot nuclear matter effect.

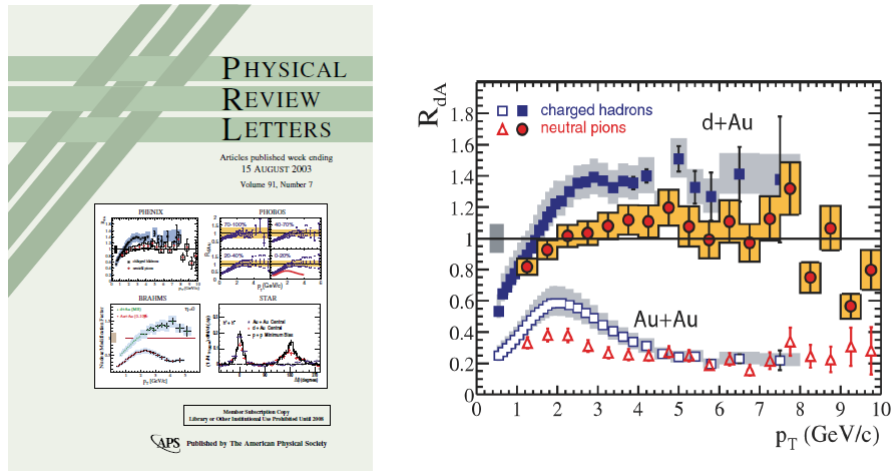


Figure 1.15: Suppression due to hot and not cold QCD matter confirmed by all four RHIC experiments. In the left panel the cover of Phys. Rev. Letters from 13 August 2003 is shown, confirming in all four RHIC experiments no suppression in $d + Au$ collisions. PHENIX light hadron R_{AA} data from that volume [116] for $d + Au$ and $Au + Au$ collisions at $\sqrt{s_{NN}} = 200$ GeV are presented in the right panel. Figure adapted from [104].

The most striking experimental evidence is given by the right panel of Fig. 1.15, which shows the nuclear modification factor for non-identified charged hadrons (h^\pm) and π^0 -mesons measured by PHENIX [116] in $\sqrt{s_{NN}} = 200$ GeV $d + Au$ and central $Au + Au$ as a function of p_\perp . The large suppression observed in $Au + Au$ collision is absent from $d + Au$ collision. Besides this result, there were also another "smoking guns" of QGP formation [24], such as: bulk collective flow (e.g. elliptic flow signature), breakdown of bulk collectivity and other jet quenching results [90, 105, 106].

Among these, the most representative ones are presented in Fig. 1.16. Thus, the left panel of Fig. 1.16 shows the STAR [117] and PHENIX [118] data for the elliptic flow, whose notable digression from zero value implies strong collective behavior of the produced matter in peripheral 200 GeV $Au + Au$ collisions. The exceptional agreement of the v_2 data with hydrodynamical predictions [119] was an unexpected

finding, suggesting that the QCD matter produced at RHIC behaves as nearly perfect fluid.

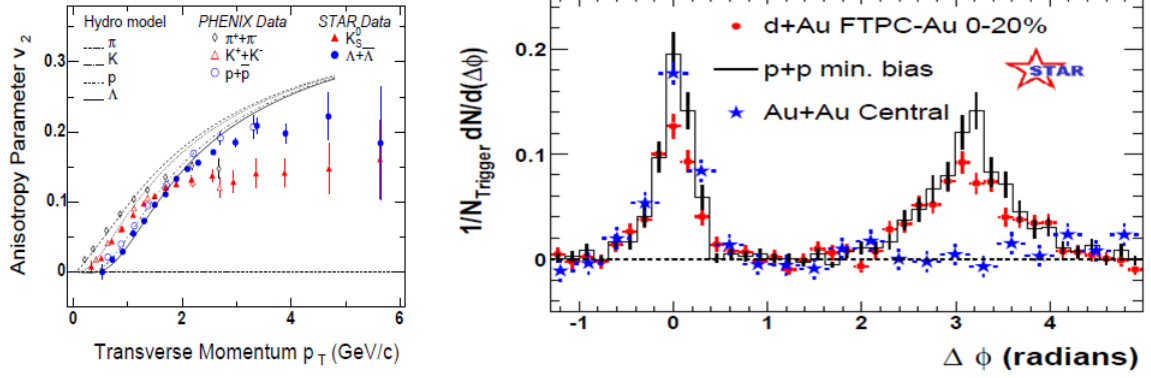


Figure 1.16: Empirical evidence of QGP formation. Elliptic flow v_2 data as a function of p_\perp , extracted from STAR [117] (full symbols) and PHENIX [118] (open symbols), are shown in the left panel. Hydrodynamical predictions are also plotted [119]. Right panel compares two-particle azimuthal distributions in cases of $p + p$, central $d + Au$ and $Au + Au$ collisions, and is adapted from [120].

Additionally, RHIC experiments detected another jet-quenching observable — unbalanced back-to-back high- p_\perp di-hadron azimuthal correlation. Namely, the detection of high p_\perp hadron evokes an expectation of detecting its partner jet in an opposite direction, and due to momentum conservation low. The detected particle is called *trigger* particle, whereas the particle, that is expected to be detected at the azimuthal angle $\Delta\phi = \phi - \phi_{\text{trig}} = \pi$ is referred to as *associated* hadron. It is measured that in $p + p$ collision at midrapidity ($\eta = 0$), a di-jet signal appears as two distinct back-to-back Gaussian-like peaks at $\Delta\phi \approx 0$ (near-side) and at $\Delta\phi \approx \pi$ (away-side), representing an enhanced correlation, due to correlation of fragments originating from a single jet (either near-side or away-side jet). From right panel of Fig. 1.16, which presents two particle azimuthal distribution relative to a triggered hadron, we observe the same pattern in $d + Au$ as in $p + p$ collision, i.e. both near-side and away-side picks. However, STAR [120] measurements showed a monojet-like signal in central $Au + Au$ collision, with a complete disappearance of the away-side peak for $4 < p_\perp(\text{trig}) < 6$ GeV/c ($p_\perp(\text{assoc}) < p_\perp(\text{trig})$). Again, the difference between $d + Au$ and central $Au + Au$ collisions suggests that the reason for

the away-side jet being depleted is related with the medium produced in $Au + Au$ (QGP), but absent from $d + Au$ collision.

All these measurements represent an empirical evidence of the formation of quark-gluon plasma in $\sqrt{s_{NN}} = 200$ GeV $Au + Au$ collisions at RHIC. Even though, the experimental data collected in 2005 also expressed strong support of QGP discovery at the RHIC [121], not until 2010 the formal confirmation has arrived [122].

1.5.2. *The updated experimental evidence*

In this subsection we display the up-to-date experimental measurements of the most relevant QGP matter probes, both the hard and the soft ones. Following the same observable sequence listed in subsection 1.4.2, first we show the most recent suppression data of high transverse momentum light particles. More specifically, Fig. 1.17 comprises the suppression data from SPS era, over RHIC and $\sqrt{s_{NN}} = 2.76$ TeV LHC to $\sqrt{s_{NN}} = 5.02$ TeV LHC, for neutral and charged pions and charged hadrons.

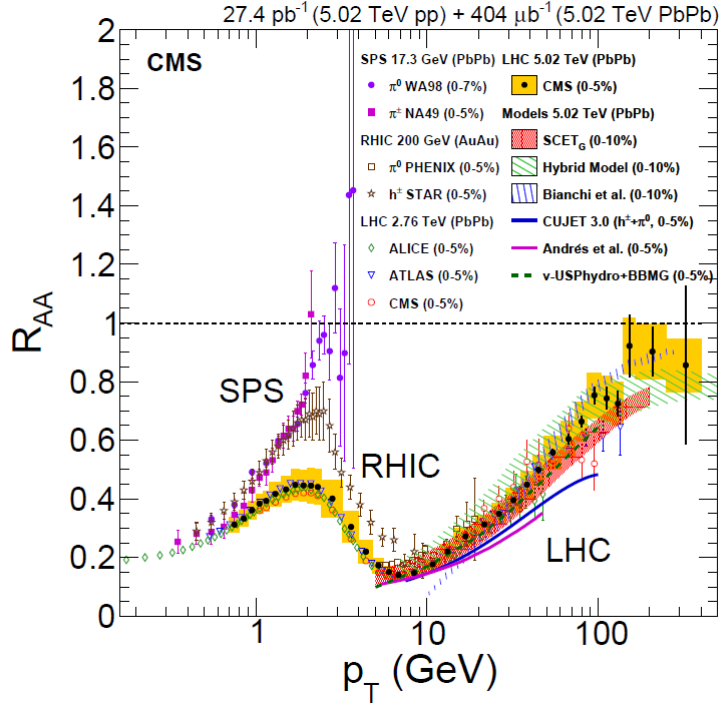


Figure 1.17: Suppression of high p_{\perp} light particles. Measurements of R_{AA} as a function of p_{\perp} in central collisions at four different center-of-mass energies (as indicated in legend), for π^{\pm} (at SPS), π^0 (at SPS, RHIC), h^{\pm} (at RHIC) and charged particles (at LHC) are gathered. The newest CMS data at $\sqrt{s_{NN}} = 5.02$ TeV are presented by yellow rectangles. For experimental and theoretical references see [123]. Figure adapted from [123].

From Fig. 1.17 we observe that at $\sqrt{s_{NN}} = 5.02$ TeV LHC energies, the reachable light particle momentum is ≈ 300 GeV, which is quite broader than at RHIC (~ 20 GeV) and even $\sqrt{s_{NN}} = 2.76$ TeV LHC (≈ 100 GeV). Interestingly, we see that at these two LHC collision energies the light particle suppressions practically overlap.

Next we refer to heavy flavor particles, that is D and B mesons suppression predictions. From Fig. 1.18 the following interesting observations emerge: *i*) D mesons have nearly the same suppression as light particles (the left panel of Fig. 1.18) in central ($0 - 10\%$) $\sqrt{s_{NN}} = 2.76$ TeV $Pb + Pb$ collisions, while in other two panels we observe: *ii*) the suppression of heavy flavor (i.e. D meson) is practically the same at $\sqrt{s_{NN}} = 2.76$ TeV and $\sqrt{s_{NN}} = 5.02$ TeV $Pb + Pb$ collisions (compare the left and the central panel, which are given for the same centrality); and *iii*) there

is no significant flavor dependence of R_{AA} at high p_{\perp} (the right panel). Also, we notice that the increase of collision energy raises the p_{\perp} upper limit of detected heavy flavors from ≈ 30 GeV/ c to ≈ 100 GeV/ c .

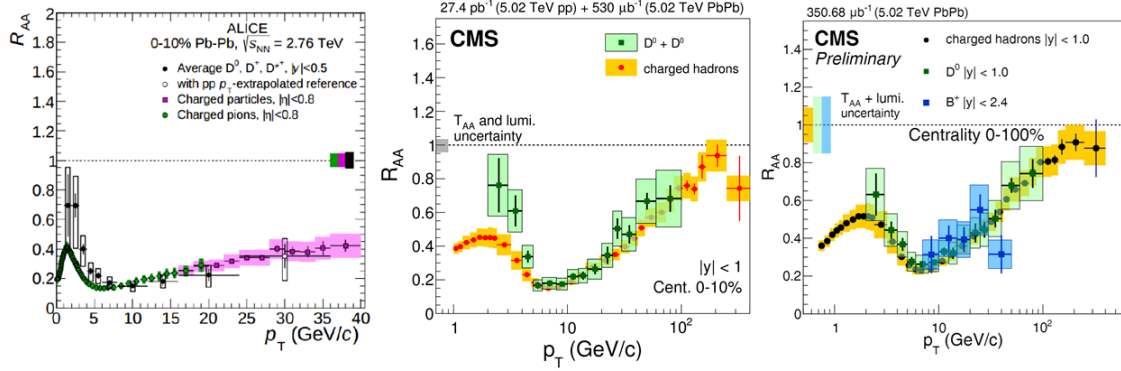


Figure 1.18: Suppression of heavy flavor particles. In the left panel comparison of suppression predictions between prompt D meson (black circles); and charged particles (magenta squares) and π^{\pm} (green circles) as a function of p_{\perp} in central $Pb + Pb$ collisions at $\sqrt{s_{NN}} = 2.76$ TeV is shown [124]. The middle panel presents CMS D^0 (green squares) and charged hadron (orange circles) R_{AA} predictions as a function of p_{\perp} in $\sqrt{s_{NN}} = 5.02$ TeV $Pb + Pb$ collisions. CMS R_{AA} vs. p_{\perp} data for charged hadrons (black circles), D^0 (green squares) and B^+ (bluesquares) at $\sqrt{s_{NN}} = 5.02$ TeV $Pb + Pb$ collisions are shown in the right panel. The middle and right panel are adapted from [125].

The updated experimental data for high p_{\perp} di-hadron azimuthal correlations are shown in Fig. 1.19, and confirm the previous observation of away-side jet quenching in central collisions. From Fig. 1.19 we see that in most central collision, when certain conditions are met, the away-side peak in $A + A$ central collisions gets quenched compared to $p + p$ and $d + A$ collisions (left and central panels). Also from the right panel of this figure we observe that in 5% most central $Pb - Pb$ collisions the yield of associated charged particles with $p_{\perp} > 3$ GeV/ c on the away-side decreases by approximately 60% compared to collisions (while on the near-side a moderate enhancement of 20 – 30% is detected).

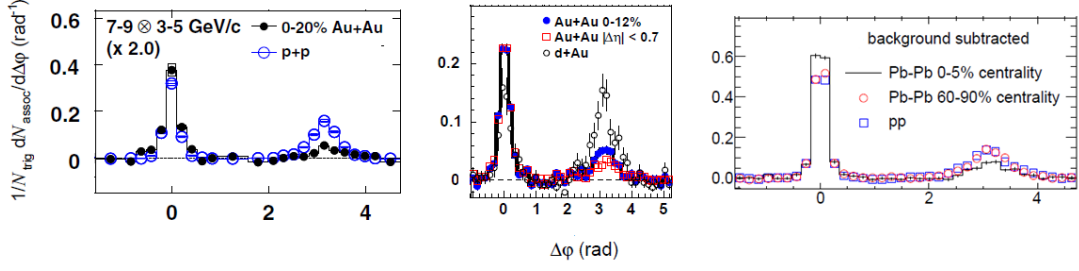


Figure 1.19: Azimuthal di-hadron correlations. The left panel shows per-trigger jet pair yield, where trigger is π^0 , while associated hadron is h^\pm in $p + p$ (open circles) and $Au + Au$ (solid circles) $\sqrt{s_{NN}} = 200$ GeV collisions at PHENIX [126]. p_\perp regions for trigger and associated hadrons, as well as centrality range are indicated in legend. The central panel presents trigger charged particles for $6.0 < p_\perp^{trig} < 10.0$, and associated ones for $2.5 < p_\perp^{assoc} < 4$ GeV/c in central $d + Au$ (open circles) and $Au + Au$ (full circles and open squares) collisions at STAR [127]. Per-trigger pair yield for associated charged particles $4 < p_T^{assoc} < 6$ GeV/c, and trigger ones $8.0 < p_T^{trig} < 15.0$ GeV/c for central $Pb + Pb$ events (histogram), peripheral $Pb + Pb$ events (red circles) and $p + p$ events (blue squares) at $\sqrt{s_{NN}} = 2.76$ TeV ALICE [128]. Figure adapted from [126–128].

Next we concentrate on weakly interacting particles, which comprise electro-weak gauge bosons such as isolated photons ($p_\perp \gtrsim 20$ GeV/c), W and Z bosons. Due to absence of color charge they do not participate in strong interactions with QGP medium constituents. Therefore, it is expected that these particles traverse QGP unaffected by final-state interactions in the produced medium, which also obtained its experimental verification. Consequently, electro-weak particles present an excellent benchmark [129] in $A + A$ collisions ($R_{AA} \approx 1$). They also allow one to experimentally confirm the validity of the perturbative (A^2) scaling of the $p + p$ cross sections and, on the other hand, they provide constraints on the nuclear PDFs which, in particular for the Pb case, are still work in progress within deep-inelastic $e + A$ data.

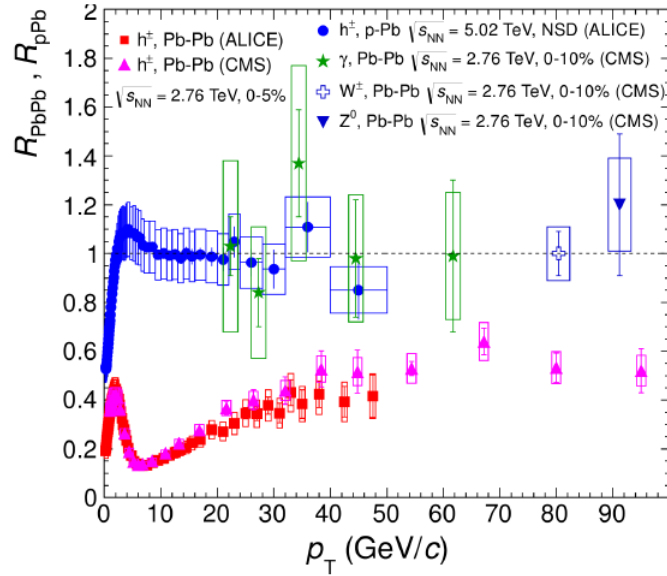


Figure 1.20: Suppression of electroweak particles. R_{AA} dependence on transverse momentum for electroweak particles: γ (green stars), W^\pm (open crosses) and Z^0 (downward-pointing blue triangle) in central $\sqrt{s_{NN}} = 2.76$ TeV at CMS is shown. Comparison with charged particles suppression in central $\sqrt{s_{NN}} = 2.76$ TeV $Pb+Pb$ (red squares for ALICE, pink triangles for CMS), and in $\sqrt{s_{NN}} = 5.02$ $p+Pb$ (blue circles) collisions at ALICE is also displayed (for experimental references see [130]). Figure adapted from [130].

Fig. 1.20 is in consistency with the above discussion, and thus we observe that electroweak particles are unaffected by QGP medium, i.e. $R_{AA} \approx 1$. Additional information from Fig. 1.20 is that for light particles no suppression is observed in $p+A$ (even at larger collision energy 5.02 TeV) as opposed to $A+A$ collisions (the same conclusion holds for heavy flavors as well).

Then we provide state-of-the-art experimental measurements of *thermal direct* photons, which are defined as photons radiated during both thermalized partonic and hadronic phases of QGP, but not originating from hadron decays nor hard scatterings of incoming partons (prompt photons). At transverse momentum of $p_\perp \lesssim 4$ GeV/c the production of these photons is enhanced compared to the prompt one and their spectrum is practically exponential (see left panel of Fig. 1.21). Additionally, the yield of thermal photons in $A+A$ collisions is also in excess (although slightly, as

$R_{AA} \approx 1$) compared to $p + p$ collisions.

Note that, in experiments only the inclusive direct photons are measured (prompt + thermal), so to obtain the thermal photons spectrum the subtraction of the prompt photon component (the orange dashed curve, for which NLO pQCD calculations were applied) from the inclusive direct photon spectrum is needed. The remaining excess yield is fit with an exponential function $\propto \exp^{-p_{\perp}/T_{eff}}$, from which the estimate of an effective (mean QGP) temperature T_{eff} can be inferred as an inverse slope [131] (see right panel of Fig 1.21). Thus, the obtained T_{eff} in 0 – 20% central 2.76 TeV $Pb + Pb$ collisions at ALICE is approximately equal to ≈ 297 MeV [132], whereas in 0 – 20% central 200 GeV $Au + Au$ collisions at PHENIX is ≈ 221 MeV [133, 134] or ≈ 239 MeV [132], depending on the applied hydro model. The references of different hydrodynamical models, that are in good agreement with the data, are listed in [132]. Note also that, by using an adequate hydrodynamical model the initial QGP temperature can be estimated. Thus, as expected, larger initial temperature at LHC than at RHIC is obtained. It is worth noting that, T_{eff} differs (is somewhat higher than) from the evolving true temperature of the fireball, because the large photon emission rates at the highest T (initial QGP stage) are compensated by an expanded space-time volume and blue-shift due to radial flow [132] (later evolution stage).

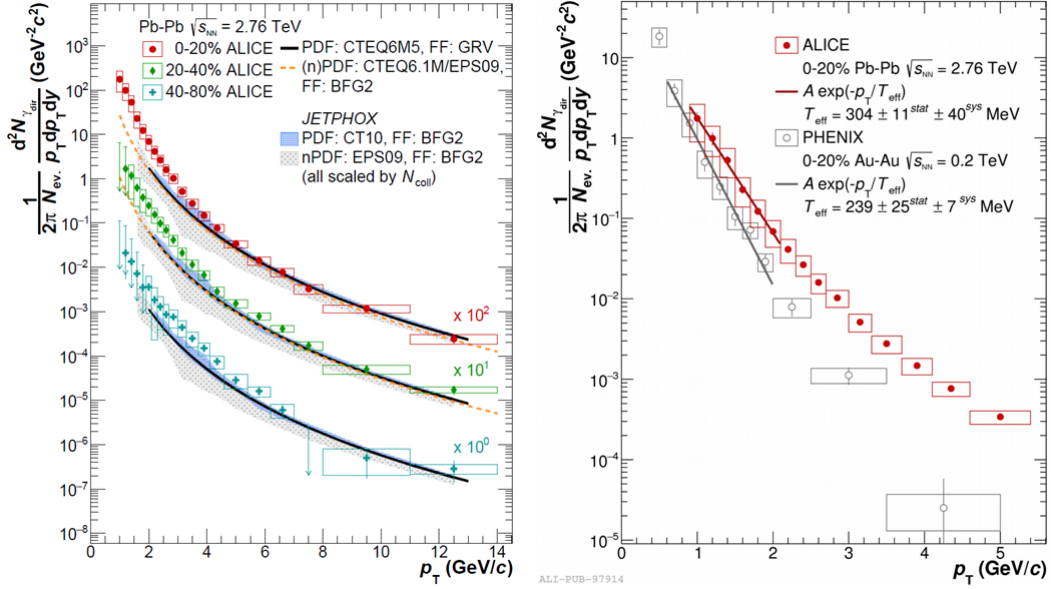


Figure 1.21: Thermal photons. In the left panel the direct photon spectra in $Pb+Pb$ collisions at $\sqrt{s_{NN}} = 2.76$ TeV for the following centrality bins: 0–20% (scaled by a factor of 100), 20–40% (scaled by a factor of 10) and 40–80% are compared to next-to-leading-order pQCD predictions for the direct photon production in $p+p$ collisions at the same collision energy, scaled by N_{bin} for each centrality bin. The orange dashed curves correspond to prompt photon component. In the right panel only thermal photon spectra data in $Pb+Pb$ collisions at $\sqrt{s_{NN}} = 2.76$ TeV (ALICE) and in $Au + Au$ $\sqrt{s_{NN}} = 200$ GeV (PHENIX) are presented. The full curves correspond to exponential fits. Figure adapted from [132].

The quarkonium, denoting the bound state of heavy quark ($Q = c, b$) and its antiquark (\bar{Q}), has also been considered as a sensitive probe of the matter produced in ultra-relativistic HIC. Note that, the transition to QGP state affects only the light quark flavors (u, d and s are considered massless), for which the chiral symmetry is a good assumption. However, charm and bottom quarks do not fit into that picture, as due to their large masses, these particles explicitly break the chiral symmetry. Therefore, nothing constrains them from existing in the bound state (quarkonium) even in the deconfined phase (QGP) [26]. Thus, quarkonia, which includes charmonium ($c\bar{c}$) and bottomonium ($b\bar{b}$) families, emerged as important probes for measuring the temperature of the QGP [26]. The charmonium family

consists of η_c , J/ψ , $\Psi(2S)$, χ_c ... whereas the bottomonium family includes Υ 's and χ_b .

In the following lines, we will summarize the qualitative reasoning, as displayed in [26], for why is quarkonium a good QGP temperature probe. Although, the results are not exact, the conclusions are valid. As previously mentioned, in vacuum the interaction between Q and its \bar{Q} is modeled by the Cornell potential [135], where, for simplicity, we leave only the Columbian-like potential $V^{vac}(r) \approx -\alpha/r$, which is a dominant term at small distances. When $Q\bar{Q}$ is surrounded by the QGP, the free color charges of the QGP modify the interaction potential between heavy quark and its antiquark. This phenomenon is known as screening of the potential, which in QGP at temperature T acquires the following form: $V^{QGP}(r) \approx -\alpha/r \times e^{-r/\lambda_D}$. Here, the role of the screening length has the Debye length λ_D .

In [26], it was also assumed, for the simplicity, that the average distance between Q and \bar{Q} in a ground (i.e. $1S$) quarkonium state (J/ψ or $\Upsilon(1S)$, for charmonium or bottomonium family, respectively) is given by the Bohr radius: $r_B = 1/(\alpha m_Q)$. For $r_B \ll \lambda_D$ the screened potential reduces to the Coulombian one and the bound state in the QGP effectively behaves as in the vacuum. On contrary, for $r_B \geq \lambda_D$ (i.e. when Debye color screening radius of the QGP falls below $Q\bar{Q}$ binding radius), the potential is screened by the QGP medium compared to the vacuum value, leading to possible unstable state and melting of the quarkonium. If we consider the same relation between Debye length and the temperature as in electromagnetic plasmas [136]: $\lambda_D = \sqrt{T/(8\pi\alpha\rho)}$, and assume the charge density as in ultra-relativistic gases: $\rho \propto T^3$, the following expression [26] is obtained: $\lambda_D \sim 1/(T\sqrt{8\pi\alpha})$. From the last formula, one could infer the temperature T_d above which the quarkonium dissociate:

$$T_d \sim \frac{1}{\sqrt{8\pi\alpha(T)r_B}}. \quad (1.5.1)$$

On an intuitive level, this simplified model provides an explanation for why charmonium excited state (resonance) $\Psi(2S)$ dissociates at lower T , than the charmonium ground state J/ψ ($r_B(\Psi(2S)) > r_B(J/\psi)$), and the latter at lower T than the bottomonium ground state $\Upsilon(1S)$ ($m_B > m_C$, since $r_B \sim \frac{1}{m}$).

Since long, the quarkonium dissociation study has served as an excellent tool

for determination of critical (cross-over), as well as the initial temperature of the QGP. Thus, the finite temperature lQCD [137] calculations confirmed the qualitative tendencies (that is, the dissociation of different $Q\bar{Q}$ states at different T , for which temperature dependent Debye length becomes lower than the $Q\bar{Q}$ binding radius) and obtained the temperatures for charmonium and bottomonium families dissociation, as well as the sequential bottomonium suppression. Also, from that calculation they inferred T_c , predicting that $\Upsilon(1S)$ survives up to $\sim 4T_c$.

Additionally, the well known effect of anomalous J/ψ suppression is worth mentioning (see [92] and references therein). Namely, the experimentally obtained similar J/ψ suppression at SPS and RHIC energies, although counter-intuitive (since larger collision energies would imply larger T , ergo larger suppression), latter found its explanation within lQCD. According to sequential-dissociation lattice predictions, J/ψ survives up to $T \approx 2T_c$, while its excited states ($\Psi(2S)$, χ_c) already melt at $T \approx T_c$, due to larger r_B than the ground state's one. Thus, the similar suppression at different center-of-mass collision energies, could be explained by the lack of feed-down decay contribution of the resonances at RHIC (at higher RHIC temperature, resonances dissociate more than at lower SPS temperature, where they can through decay contribute to J/ψ yield). Note that, the decay of higher resonances play a significant role in J/ψ yield, that is around 40% [92]. Thus, lQCD obtained the upper limit of initial RHIC temperature $T \lesssim 2T_c$, which does not allow dissociation of J/ψ bound state.

Also, the anomalous J/ψ suppression for lower p_\perp at LHC (see the left panel of Fig. 1.22) could be explained by the recombination [138] effect, where higher collision energy implies larger production of free c and \bar{c} , enhancing J/ψ production. However, for larger p_\perp at LHC energies the J/ψ suppression is larger than at RHIC (left panel of Fig. 1.22), indicating the obtained initial QGP temperatures higher than $2T_c$, leading to depletion of J/ψ .

This $J/\psi R_{AA}$ vs. p_\perp pattern, which is very similar for 5.02 TeV and 2.76 TeV LHC energies (compare the panels in Fig. 1.22), underlines that the small suppression at low p_\perp is due to (regeneration) recombination, while the large suppression at higher p_\perp is a consequence of the dissociation, and an indicator of the obtained high enough initial T for ground state to dissociate.

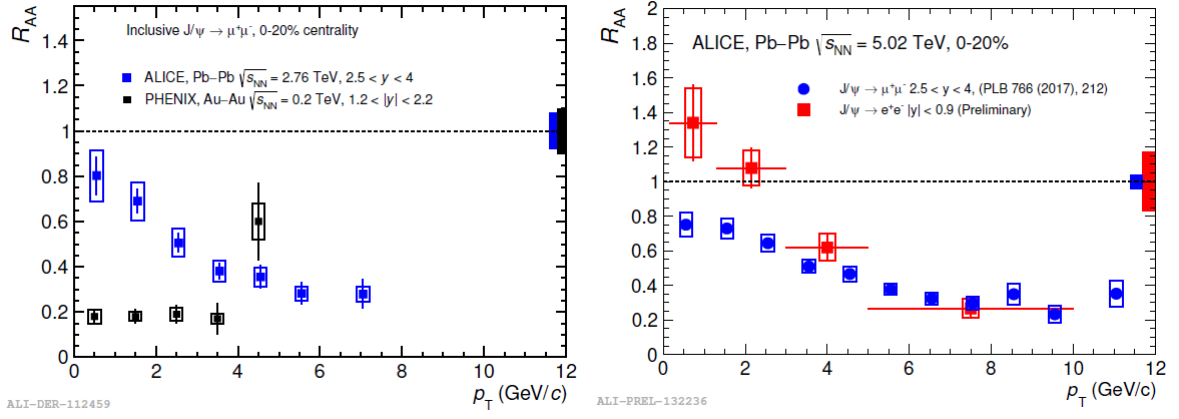


Figure 1.22: J/ψ suppression measurements as a function of transverse momentum. Comparison of J/ψ R_{AA} data between $\sqrt{s_{NN}} = 200$ GeV $Au + Au$ PHENIX (black squares) and $\sqrt{s_{NN}} = 2.76$ TeV $Pb + Pb$ ALICE (blue squares) collisions is presented in the left panel. For experimental references see [139]. In the right panel, the J/ψ suppression data from $\sqrt{s_{NN}} = 5.02$ TeV $Pb + Pb$ collisions at ALICE are shown for two different decay channels (for references see [140]). Figure adapted from [139, 140].

With increasing collision energies at the LHC, the high temperatures became approachable, so the bottomonium family could finally be experimentally studied (due to the abundant production of heavy b quarks). From left panel of Fig. 1.23 we observe the diminished yield of the the Υ family in $Pb + Pb$ compared to the $p + p$ collisions, in accordance with the sequential dissociation picture. From the right panel of Fig. 1.23, we see that even the ground state $\Upsilon(1S)$ is suppressed, although less than resonances, which suggests no feed-down contributions of the heavily-suppressed (dissociated) excited states (which is already mentioned to largely contribute to ground state yield). Note that, the R_{AA} is measured against the number of participants N_{part} , which is directly proportional to centrality of the collision (the more central collision is, the larger is N_{part} , where 0% denotes the most central collision).

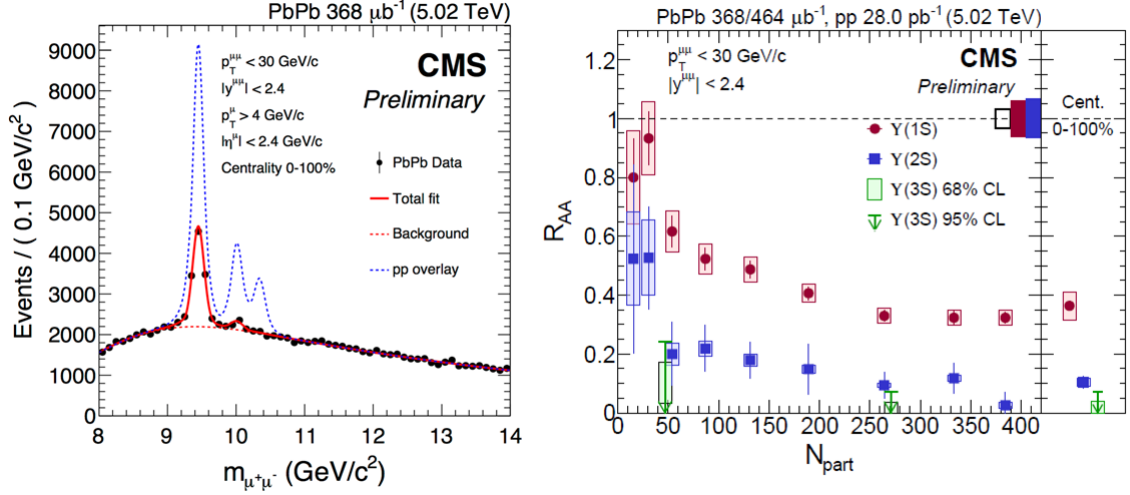


Figure 1.23: The sequential suppression of bottomonium family. Invariant mass distribution of muon pairs, originating from Υ family decay, in $p + p$ (fits to data represented by dashed blue curve) and $Pb + Pb$ (black squares, fits to data represented by red curve) $\sqrt{s_{NN}} = 5.02$ TeV collisions is given in the left panel. The three peaks in $p + p$ case correspond to separate yields for each individual Υ state (from left to right: ground state $\Upsilon(1S)$ and higher resonances $\Upsilon(2S)$ and $\Upsilon(3S)$ respectively). R_{AA} dependence on N_{part} for $\Upsilon(1S)$ (red circles), $\Upsilon(2S)$ (blue squares) and $\Upsilon(3S)$ (green symbols) under the same CMS conditions as in the left panel is shown in the right panel. Figure adapted from [141].

Additionally, the significantly suppressed ground state implies reaching the initial temperature of $\Upsilon(1S)$ dissociation, which according to lQCD models [142] amounts $\sim 500 - 700$ MeV and $\sim 600 - 800$ MeV for 2.76 TeV and 5.02 GeV collisions, respectively.

For a very long time, one of the soft probes, the elliptic flow (or higher harmonics) has been considered as an imprint of QGP formation and very fast thermalization (since it was absent in $p + p$ collisions), but a recent interest in small-systems led to discovery of this collective phenomena also in $p(d) + A$ systems (even in $p + p$, see e.g. [143]), leaving an open question, if it is a truly exclusively related to QGP, or a consequence of initial fluctuations.

Thus, a preliminary ALICE $v_n(p_\perp)$ data is given in Fig. 1.24, confirming the existence of elliptic flow in peripheral $\sqrt{s_{NN}} = 5.02$ TeV both $Pb + Pb$ and $p + Pb$

collisions at the LHC, that are even comparable. One observing from the left panel of this figure is that elliptic flow does not change appreciably between $\sqrt{s_{NN}} = 2.76$ TeV and $\sqrt{s_{NN}} = 5.02$ TeV energies. From the right panel we infer of Fig. 1.24 that there is a clear mass ordering in small systems.

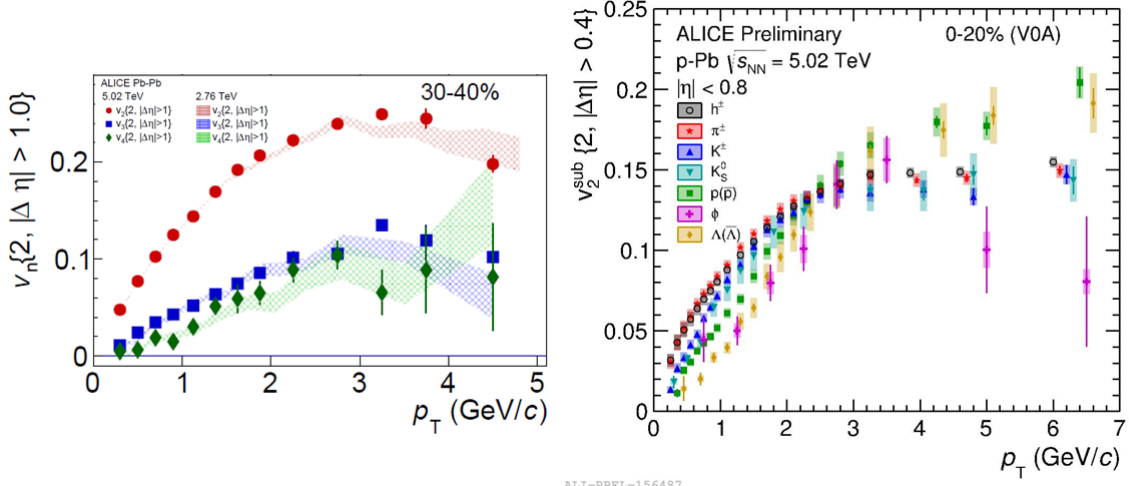


Figure 1.24: Elliptic flow coefficients measured in $\sqrt{s_{NN}} = 5.02$ TeV $Pb + Pb$ and $p + Pb$ at ALICE. In the left panel the flow coefficients $v_n(p_\perp)$ for charged particles in 30–40% central $Pb + Pb$ collisions are shown by symbols (as indicated in legend). Comparison with the corresponding data in $\sqrt{s_{NN}} = 2.76$ TeV (shaded areas) is also presented. The right panel corresponds to elliptic flow of inclusive and identified hadrons (as denoted in legend) in $p + Pb$ collisions. Figure adapted from [144, 145].

Further we concentrate on investigating QGP medium properties through high p_\perp energy loss and suppression, i.e. nuclear modification factor, theoretically and phenomenologically.

1.6. Outline of the thesis

The outline of the thesis is the following: In Section 2 we provide a concise historical review of: 1) collisional and 2) radiative in static QGP medium, that is Gyulassy-Levai-Vitev (GLV) and Djordjevic-Gyulassy-Levai-Vitev (DGLV), energy losses, whereas in Section 3 we outline the development of the state-of-the-art dy-

namical energy loss formalism, by gradually transitioning from static to dynamical medium, introducing all improvements to the model; and present the up-to-date suppression computational formalism, that we use. Sections 4 to 6 represent our original contribution. They are arranged in two parts: Sections 4 and 5 belong to our phenomenological contribution, while Section 6 presents our theoretical contribution, although the detailed calculations are presented in Appendices B.

In Section 4, we generate R_{AA} predictions by applying the dynamical energy loss model incorporated in suppression computational formalism, as explained in Section 3. First we compare suppression predictions with the comprehensive set of experimental data, which span from RHIC to the most recent LHC experimental conditions, across a large variety of particles and which takes into account all available heavy-ion collisions centrality ranges. And finally, this section ends with generating suppression predictions for the upcoming LHC measurements, that remain (or already are) to be tested in the future.

Section 5 is dedicated to addressing the importance of each individual improvement (effect) introduced in dynamical energy loss model, with DGLV model serving as a starting point. The idea is to isolate an individual effect of the dynamical energy loss model, if possible, which is responsible for enhanced reliability of the suppression predictions outlined in Section 4.

In Section 6 we relax the widely-used soft-gluon approximation, which assumes that high p_{\perp} parton propagating through dense QGP medium loses only a small fraction of its initial energy via gluon bremsstrahlung, in radiative energy loss calculations to the 1st order in opacity. This is an important task, as validity of the approximation was rightly questioned, and regardless also used in dynamical energy loss model. Since this task is theoretically very demanding, we divided it into three steps: 1) first, we relaxed the assumption within GLV formalism, 2) then within DGLV model and 3) finally, we discuss generalization onto dynamical medium.

Finally, in Section 7 we give an overall conclusion based on the results presented in this thesis. We also discuss some open problems that should be addressed in the future.

2. HISTORICAL OVERVIEW OF ENERGY LOSS MODELS USED IN THIS THESIS

2.1. Overview of collisional energy loss models

Already in 1982, Bjorken [90] was the first to start theoretical study of energetic parton collisional energy loss. He assumed that, in the region between the Lorentz-contracted hadrons, QGP in thermal equilibrium was formed and considered an elastic scattering ($2 \rightarrow 2$) of a massless high-energy parton (quark or gluon), propagating through an ideal uniform quark-gluon gas, from medium constituents. He calculated differential energy loss for the dominant, small momentum transfers, ergo only the Mandelstam t-channel. Since he was using only tree-level diagrams, the result was logarithmically infrared-divergent, so the cut off was introduced by hand. For the lower and the upper limit of exchanged gluon momentum transfer q (3D-momentum) the physically reasonable values of thermal parton mass $M \sim 0.5 - 1$ GeV and $\sqrt{s}/2$ are taken, respectively. He neglected the leading-order part and kept only the $\ln \frac{q_{max}}{q_{min}}$ dependent term. The obtained average collisional energy loss per unit length ($\frac{dE}{dL}$) was $\ll 1$ GeV/fm for a particle of 20 GeV energy, assuming medium temperature $T = 0.3$ GeV and the coupling constant $\alpha_s = 0.2$.

The study of collisional energy loss was continued by Thoma and Gyulassy [146] at the early '90s, within plasma and high temperature QCD approach. The significant improvement compared to the Bjorken's case is adequately accounting for the chromoelectric screening (represented by Debye mass $\mu_E \sim g_s T$), resulting only in naturally setting the lower boundary for momentum transfer equal to μ_E . Thus, the infrared divergences are automatically self-regulated. The ultraviolet divergences are artificially regulated by setting a reasonable upper limit of exchanged gluon momentum at hard quark momentum for light, and at a temperature dependent value for heavy quarks. For $T = 0.25$ GeV, and the other parameters same as in Bjorken's calculation, they again obtained small $\frac{dE}{dL} \approx 0.2$ GeV/fm for light quarks, and even smaller values for heavy quarks. The shortcoming of Thoma and Gyulassy model was not only in non-physically setting the upper q limit, but also in neglecting the

recoil of the scattered thermal quark or gluon, and which become important at high momentum transfer.

Thus, the next step was to construct the theory that would: *i*) naturally regulate both: the infrared and the ultraviolet divergences to the leading order in g_s , and *ii*) correctly account for high momentum transfer, which was accomplished by Braaten and Thoma [147, 148]. In order to separate soft ($\sim g_s T$) and hard ($\sim T$) ranges of momentum transfer, the arbitrary momentum scale q^* was introduced. In the soft momentum transfer range $q < q^*$, the exchanged gluon propagator is obtained by resummation of hard thermal loop corrections (so-called effective gluon propagator, that captures the screening), while in the hard momentum transfer range $q > q^*$, only the tree level exchanged gluon propagator is considered. Upon adding the contributions from soft and hard momentum transfer regions, the arbitrary momentum scale dependence of the final result is lost. Thus obtained differential energy loss for heavy quarks was of the similar order of magnitude as in the previous two models.

Since the collisional energy loss calculations failed to deliver a substantial energy loss, the radiative energy loss comes to the focus of attention. Gyulassy, Thoma, Plumer and Wang are considered the pioneers of this undertaking. They applied Gunion-Bertsch [149] radiation spectrum in calculating Bjorken-like radiative energy loss, and conveniently obtained significantly larger radiative compared to collisional energy loss [107, 108]. That conclusion marked the beginning of radiative energy loss dominance era (see subsection 2.2).

However, it's worth mentioning, that the more recent collisional energy loss calculations, driven by heavy flavor RHIC experimental results [150, 151] (such as single electron puzzle [152]), by Thoma [153] and Mustafa [154, 155] showed a similar collisional and radiative quenching factors. Namely, the RHIC experiment obtained very similar suppressions for both: light and heavy flavor particles, despite the dead cone effect [156], connected with the heavy (bottom) quarks, which would reduce their radiative energy loss compared to the light quarks (i.e. gluon radiation is suppressed at angles $\theta < M/E$). This raised a question of validity of previous collisional energy loss models.

Further, Djordjevic [157] introduced a finite size effect in calculating 0^{th} order collisional energy loss within HTL approach (see subsection 3.1 for more details).

The detailed study of collisional energy loss importance, within dynamical energy loss formalism, is presented in paper [159], and will be comprehensively discussed in Section 5.

2.2. Overview of radiative energy loss models for static scatterers: GLV and DGLV

Awaken interest in radiative energy loss put a new phenomena, earlier studied for QED, ahead of the researchers: a Landau-Pomeranchuk-Migdal (LPM) effect [160]. Namely, the LPM effect can be explained as follows: an energetic particle, i.e. jet, under eikonal approximation (i.e. experiencing a minor deflecting from the initial direction), undergoing multiple soft scatterings from adjacent static target sites, experiences interference effects between radiation amplitudes. The final amplitude to radiate a single gluon is obtained after summation over the following cases: amplitude for gluon emitted from any internal, initial and final jet lines (corresponding to the absence of final gluon interactions), and amplitude involving only one three gluon vertex (corresponding to existence of final gluon interaction). With decreasing longitudinal momentum transfer, the particles wavelength increases, due to uncertainty principle, and when the wavelength becomes larger than the mean free path in the medium (the average distance between scattering sites), the scatterings can no longer be treated as independent. This is contrary to Bethe-Heitler limit for multiple scattering induced radiation, which assumes independent scatterings and where the radiation intensity is additive in the number of scatterings. Note also that Bethe-Heitler limit considers on-shell jets produced at remote past. The LPM effect leads to destructive interference, i.e. to the suppression of radiation spectrum compared to the Bethe-Heitler case.

To that end, Gyulassy and Wang [161], together with Plumer [162] were the first to investigate non-abelian analogon of this effect for static QCD medium. The cause of the destructive interference is a finite large formation time, that, due to being inversely proportional to relative eikonal phase, leads to disappearance of phase difference between the amplitudes, resulting in coherent amplitude summation, and

consequently radiation intensity suppression. The formation time:

$$\tau_f(k) \sim 1/\Delta E(k) \sim 2\omega/\mathbf{k}^2 \sim 2/\omega\theta^2, \quad (2.2.1)$$

where $k = (\omega, k_z, \mathbf{k})$ denotes the radiated gluon momentum, and $\theta \approx \mathbf{k}/\omega$ is the angle between emitted gluon and incident parton, can also be interpreted as the minimal time needed to differentiate the transverse wavepacket of gluon, having $\Delta x \sim 1/\mathbf{k}$ from its high-energy parent wavepacket ($E \gg \omega$). Again, the destructive interference occurs when $\tau_f \gg \lambda$ (so-called *factorization limit*, λ is the mean free path), i.e. when the emitted gluon cannot resolve different scattering centers. They assumed that the mean free path λ of the projectile is much larger than the screening radius, $\lambda \gg \mu^{-1}$, which allows treating the successive scatterings as independent. Also, under the assumptions (soft gluon: $x \ll 1$ and $|\mathbf{k}| \ll \mu_E$, where μ_E denotes Debye screening), for energetic quark of 30 GeV propagating through QCD medium of $T = 300$ MeV, and $\alpha = 0.3$, they obtained that radiative energy loss is 3 times larger than the collisional, thus dominating over elastic process.

2.2.1. GLV

Contrary to some energy loss models (such as BDMPS-Z [163] to [171], AMY [172] to [179]), which assumed "thick" plasma, meaning that the high p_\perp parent parton undergoes multiple soft scatterings with the medium ($n_s \gg 1$, where n_s stands for the number of jet scatterings with medium partons), Gyulassy, Lavai and Vitev [180–184] considered the opposite limit of Gyulassy-Wang model: the "thin" plasma ($n_s \sim 1$). The GLV addresses the computation of the energy loss of an energetic light (massless) parton traversing a finite quark-gluon plasma, in which jet-medium interactions were, as in Gyulassy-Wang case [161], modeled by static (Debye) color-screened Yukawa potential. The Fourier and color structure of Yukawa potential acquires the following form:

$$V_n = V(q_n)e^{iq_n x_n} = 2\pi\delta(q_n^0)v(\vec{\mathbf{q}}_n)e^{-i\vec{\mathbf{q}}_n \vec{x}_n} \\ \times T_{a_n}(R) \otimes T_{a_n}(n), \quad (2.2.2)$$

$$v(\vec{\mathbf{q}}_n) = \frac{4\pi\alpha_s}{\vec{\mathbf{q}}_n^2 + \mu_E^2}, \quad (2.2.3)$$

where x_n denotes time-space coordinate of the n^{th} scattering center, μ_E is Debye screening mass, $\alpha_s = g_s^2/4\pi$ is strong coupling constant, while $T_{a_n}(R)$ and $T_{a_n}(n)$ denote the generators in $SU(N_c = 3)$ color representation of jet and the target (scattering center), respectively. $v(\vec{\mathbf{q}}_n)$ stands for effective cross section, sometimes denoted by v_{eff} .

Since for finite nuclei $L/\lambda < 10$ is not that large, and it is also considered that a great amount of jets are produced within nuclear "corona", that is $L/\lambda \leq 3$, only few collisional interactions with medium needed to be accounted. Here L/λ represents the opacity, which, for a medium of a constant size, is given by the product of the medium density with the scattering cross section, integrated along the path of the parton. Therefore, GLV formalism is also referred to as "opacity expansion" model. Thus, the expansion in the powers of opacity is equivalent to the expansion in number of scattering events suffered by traversing parton. Additionally, 1st order in opacity corresponds to one collisional interaction with the medium constituents (one exchanged gluon), accompanied by radiation of a single gluon. Thus, effectively they assumed $n_s = L/\lambda \leq 3$, that implied calculation of $2^{n_s+1} - 1$ amplitudes, which was still a reasonably small number of pQCD calculations.

Note that, for expressing all in terms of opacity, the GW elastic cross section where applied. The small transverse momentum transfer elastic cross section for interaction between the jet and target parton in GW approach [161, 180] is given by:

$$\frac{d\sigma_{el}}{d^2\mathbf{q}_1} = \frac{C_R C_2(T)}{d_G} \frac{|v(0, \mathbf{q}_1)|^2}{(2\pi)^2}, \quad (2.2.4)$$

where \mathbf{q}_1 corresponds to transverse momentum of exchanged gluon, d_G is dimension of adjoint representation, C_R represents Casimir operator in color $SU(N_c = 3)$ representation of jet, whereas $C_2(T)$ denotes Casimir operator in target (T) representation.

Historically, Gunion and Bertsch [149] were the first to study soft gluon radiation associated with a single rescattering with the target, but they assumed the incident on-shell quark produced at remote past $t_0 = -\infty$ relative to the collision time t_1 . With distinction to GB, in GLV model a short time between parton production and rescattering is assumed, and also off-shell partons are included. In particular, in [180, 181] they calculated "self-quenching", i.e. initial jet radiation, and extra

quenching associated with gluon radiation induced by the final state interactions of the jet with static medium constituents. The soft-gluon and soft-rescattering approximations were assumed, while explicit calculations for interactions with: 1, 2 and 3 scattering centers (where both jet and gluon final state interactions are accounted) were presented.

The GLV model was further improved by generalizing energy loss calculations to all orders in powers of the opacity, within reaction-operator approach [182, 183]. They grouped diagrams which contribute to the specific order n_s in opacity radiation distribution into classes. For instance, to the 1st order in opacity, i.e. one scattering center, two different diagram types combination contribute to the result: 1) first which includes one scattering interaction with the medium constituents in both the amplitude and in its complex conjugate; 2) second where two scattering interactions with the medium constituents are contained in the amplitude and no scattering interaction in the complex conjugate (or vice versa). With reference to this, they built an operator which, upon knowing one and two-scattering combinations at order n_s , generates the gluon radiation distribution at order $n_s + 1$ in opacity. Thus this recursive method enables calculations up to any order in opacity expansion.

However, they concluded that higher orders in opacity ($n_s \geq 2$) have a very little effect on fractional radiative energy loss and the mean number of radiated gluons at RHIC. They found that 1st order in opacity is the dominant term, whereas the second and third orders almost cancelled each other. Thus, at 0th order in opacity the self-quenching (the gluon emission from hard production vertex) reads:

$$\frac{x d^3 N_g^{(0)}}{dx d\mathbf{k}^2} = \frac{C_R \alpha_s}{\pi^2} \frac{1}{\mathbf{k}^2}, \quad (2.2.5)$$

while, induced radiation intensity spectrum in the 1st order in opacity acquires a form:

$$x \frac{dN_g^{(1)}}{dx} = \frac{C_R \alpha_s}{\pi} \frac{L}{\lambda} \int \frac{d^2 \mathbf{q}_1}{\pi} \frac{\mu_E^2}{(\mathbf{q}_1^2 + \mu_E^2)^2} \int \frac{d\mathbf{k}^2}{\mathbf{k}^2} 2 \frac{\mathbf{k} \cdot \mathbf{q}_1 (\mathbf{k} - \mathbf{q}_1)^2}{\left(\frac{4xE}{L}\right)^2 + (\mathbf{k} - \mathbf{q}_1)^4}, \quad (2.2.6)$$

where \mathbf{k} corresponds to radiated gluon transverse momentum, E represents initial jet energy, while λ denotes mean free path. Additionally, in the case of small effective formation probability $\gamma = \frac{L\mu_E^2}{4xE}$ the fractional energy loss recovers the L^2 path-length dependence.

And finally, the multi-gluon fluctuations [184] were also incorporated in the formalism. The assumption was that fluctuations of the radiated gluon number are uncorrelated, and therefore the spectrum of total radiative energy loss is expressed via Poisson expansion, accounting for possibility that a certain number of gluons can be radiated (for more details see [184] and subsection 3.2).

2.2.2. DGLV

The GLV formalism continued its expansion through the work of Djordjevic and Gyulassy, who firstly introduced non-abelian QCD analogon of Ter-Mikayelian [185, 186] plasmon effect within HTL approach [187] in paper [188]. Naimly, the Ter-Mikayelian effect could be summarized by the statement that in plasma, even the 0^{th} order in opacity radiation is modified by the dielectric properties of the medium compared to the vacuum case. It is well-known that gluons embedded in dielectric medium (QGP) have modified dispersion relations and both transverse and longitudinal polarizations (resumed HTL propagator). To this end, they calculated both transverse and longitudinal contributions to the 0^{th} order in opacity radiative heavy quark (c and b) energy loss, and obtained that longitudinal is negligible compared to the transverse contribution for both charm and bottom quarks, at lower Debye masses (lower temperatures) accessible at the colliders. Quantitatively, the Ter-Mikayelian effect reduced charm quark energy loss by $\approx 30\%$ (for $\mu_E = 0.5$ GeV), while bottom quark remained practically intact, due to dead cone effect [156]. Remarkably, they also demonstrated that gluon propagator in a hot dense medium can be approximated simply by $\frac{-i\delta_{ab}P_{\mu\nu}}{p^2 - m_g^2 + i\epsilon}$, where $P_{\mu\nu}$ denotes transverse projector, while dynamical gluon mass can be approximated by the effective one, equal to the asymptotic value $m_g \approx m_\infty = \mu_E/\sqrt{2}$ (for a moderate range of temperatures $0.5 \leq \mu_E \leq 1$ GeV). Again the same assumptions of soft-gluon and soft-rescattering radiation were applied throughout this subsection.

The next improvement to the DGLV formalism, governed by the same authors, was the introduction of heavy quark mass M (together with Ter-Mikayelian effect, in terms of including effective gluon mass m_g in transverse modes only) in radiative

energy loss in static [161] finite size QGP medium, also known as DGLV formalism [189]. It was also shown that the reaction operator method [183] can be applied when massive quarks and gluons are taken into account, which therefore presents generalization of GLV results to the case of massive heavy quarks to all orders in opacity. Their main analytical result was simple mapping rule for radiation distribution expressions between the massive and massless (GLV) cases of heavy quarks - the energy shift by $\frac{m_g^2+x^2M^2}{2xE}$ in all GLV frequencies. In massless limit DGLV recovers GLV results. In particular, the 0^{th} order DGLV radiation spectrum reads:

$$\frac{xd^3N_g^{(0)}}{dx d\mathbf{k}^2} = \frac{C_R\alpha_s}{\pi^2} \frac{\mathbf{k}^2}{(\mathbf{k}^2 + m_g^2 + x^2M^2)^2}, \quad (2.2.7)$$

which clearly displays reduction of radiation in dead cone, i.e. for the angles $\theta < \theta_c = \frac{\sqrt{m_g^2+x^2M^2}}{xE}$, in the case of heavy quarks. The 1^{st} order in opacity differential energy loss in DGLV formalism is given by:

$$\begin{aligned} \frac{dE^{(1)}}{dx} &= \frac{C_R\alpha_s}{\pi} \frac{L}{\lambda} E \int \frac{d^2\mathbf{q}_1}{\pi} \frac{\mu_E^2}{(\mathbf{q}_1^2 + \mu_E^2)^2} \int \frac{d\mathbf{k}^2}{\mathbf{k}^2 + m_g^2 + x^2M^2} \\ &\times 2 \frac{\mathbf{k} \cdot \mathbf{q}_1 (\mathbf{k} - \mathbf{q}_1)^2 + (m_g^2 + x^2M^2) \mathbf{q}_1 (\mathbf{q}_1 - \mathbf{k})}{\left(\frac{4xE}{L}\right)^2 + ((\mathbf{k} - \mathbf{q}_1)^2 + m_g^2 + x^2M^2)^2}. \end{aligned} \quad (2.2.8)$$

Thus, the main qualitative achievement (also numerically supported) of [189], is that by increasing M the inverse formation time factor $\left(\frac{4xE}{L}\right)^2$ becomes more irrelevant in the denominator of Eq. (2.2.8). Note that the incoherent limit (short formation time) of radiation is reproduced by setting this factor to zero. Consequently, the finite quark mass brings heavy quark energy loss closer to the incoherent Gunion-Bertsch limit, and also its thickness dependence closer to the linear ($\sim L$) Bethe-Heitler limit. This is contrary to the quadratic ($\sim L^2$) thickness dependence typical for light quarks (BDMS [156]) in the LPM limit.

And finally, Wicks, Horowitz, Djordjevic and Gyulassy generalized energy loss probability $P(E_i \rightarrow E_f)$ to include both radiative and collisional energy loss (which appeared to be of the same order) and their fluctuations combined with path length fluctuations (for more details on the last topic see [190, 191] or subsection 3.2). They obtained better agreement with experimentally measured R_{AA} for non-photonic single electrons compared to a case when only DGLV radiative energy loss is accounted. However, note that although by including both energy loss contribution they paved the way for future theoretical striving, these contributions were not developed

within same formalism. In particular, inelastic energy loss in finite size static QGP medium is calculated within DGLV formalism, while for elastic contribution they used TG [146] or BT [147, 148] model. It was latter shown that this inconsistency led to some erroneous assumptions and results, that gained their correction in [157], but waited for consistent inclusion in formalism.

Note that common kinematic assumptions are made for majority of radiative energy loss models, and thus also for GLV, DGLV and subsequent dynamical energy loss model (see the following section):

- Eikonal approximation (soft rescattering approximation), which assumes that partons energies and longitudinal momenta are high compare to their transverse momenta, which prevents the radiated and the final gluon from digressing much from the initial longitudinal direction;
- Soft-gluon approximation, which considers that radiated gluon takes away a small fraction of initial jet energy and longitudinal momentum;

Thus, throughout this thesis we will use this assumptions in generating predictions for high p_{\perp} particles (also referred to as jets), except in section 6, which is dedicated to relaxing the soft-gluon approximation.

3. DYNAMICAL ENERGY LOSS MODEL AND NUMERICAL PROCEDURE

In the previous section, we introduced DGLV model, which assumes QGP medium consisting of randomly distributed static scattering centers. In static medium collisional energy loss is equal to zero. However, some studies [192] implied that radiative energy loss alone is insufficient to explain the heavy flavor R_{AA} data at RHIC. Additionally, in series of studies [154, 155, 157, 193], it was shown for the first time that collisional energy loss is comparable with radiative one under standard RHIC conditions. Therefore, a need for more realistic medium modeling approach emerged, and consequently the requirement for radiative energy loss revision within this approach.

This section is dedicated to addressing this issue by Djordjevic *et al.*, i.e. to the introduction of dynamical medium constituents (along with the other improvements)

in energy loss calculations. The dynamical energy loss model is currently the most sophisticated model (that does not assume time dependent QGP medium) and the phenomenological part of this Thesis is based on it.

In this section we provide the outline of dynamical energy loss model development and all its individual improvements in chronological order, the introduction of the suppression numerical procedure fundamental for generating R_{AA} predictions, while the comparison of our predictions with exhaustive set of experimental data in order to validate our energy loss model and also the numerical procedure itself will be presented in section 4.

3.1. The historical development of the model: From static to dynamical

The first step toward the state-of-the-art dynamical energy loss model was made by Djordjevic in 2006 [157], by calculating quark's collisional energy loss in a *finite* size QGP up to the 0^{th} order in opacity. The computation was done within finite temperature pQCD, with contribution to collisional energy loss coming from 1-HTL diagram, explaining the origin of the term " 0^{th} order in opacity" through the analogy with radiative energy loss (see the subsection 3.2 below). The reason for constraining collisional energy loss onto final dimensions (and comparing the result with the one recalculated for infinite medium), besides more reliably reproducing created medium at RHIC and LHC, was to revise the importance of finite size effect in collisional energy loss, since in a first study of that kind, made by Peigne *et al.* [158], some omissions were found. Another motivation lies in an attempt to remove the unphysical gain of energy at low jet momentum, obtained by [146, 147] for infinite QGP medium.

Kinematically, the finite size was introduced by constraining the interaction between jet and a medium parton (massless quark, anti-quark or gluon) to occur inside the QGP medium of a finite size L , through step function. Also, produced jet needed to be off-shell, in order to exchange a virtual gluon with medium. Additionally, in [157] there is a smooth interpolation between soft (lower 3D exchanged momentum) to hard (higher 3D exchanged momentum) contributions.

For an infinite medium, they assumed that jet is produced at $t = -\infty$, and thus obtained collisional energy loss per unit length was simply multiplied by the medium thickness L , in order to compare the result with the finite size case.

Regarding the first reason, note that in [158] the finite size effect led to significant decrease of collisional energy loss compared to the infinite medium case. However, in that paper collisional and radiative energy losses were not entirely separated. To this end, in [157] the gluon dispersion relation is consistently applied, and these two energy loss contributions did not overlap nor interfere, although originating from the same 1-HTL diagram (for more details see the next subsection). By using this consistent approach, Djordjevic obtained that introduction of finite size effect barely affects collisional energy loss at all (moreover slightly increases it in finite compared to an infinite case).

Another important aspect of paper [157] reflects in consistently treating lower momentum range, and obtaining positive collisional energy loss in an infinite case at the entire observed momentum range. This corrects the unphysical energy gain at lower momentum region obtained in [146, 147]. The additional reason behind this result lies in smooth transition between soft and hard contributions. More specifically, Djordjevic's result is the general one, that in limiting cases recovers the results obtained in [146, 147]. The advantage of calculations presented in [157] over [146] is the inclusion of hard contribution apart from the soft one and consistent treatment of the integration limits. In comparison to [147], the gain of [157] reflects in smooth compared to abrupt transition from soft to hard limits, and consequently there was no need for introducing the arbitrary intermediate momentum scale, as in [147].

The second step (now in the sphere of radiative energy loss) was made also by Djordjevic and Heinz [194], by calculating heavy quark radiative energy loss in an *infinite* and time-independent QGP medium consisting of dynamical constituents (that is, recoils of the medium constituents are taken into account). For a process embedded in QGP medium consisting of dynamical light quarks and gluons (i.e. massless partons) in thermal equilibrium at temperature T , with zero baryon density number assumed, thermal field theory [187, 195] and Hard-Thermal Loop (HTL) resummed propagators (even for the exchanged gluon, contrary to the static case)

are applied in evaluating diagrams. Standard assumptions of soft-gluon and soft-rescattering were used. The infinite medium implies that the heavy quark, produced at $t = -\infty$, is on-shell, resulting in only central cuts of the appropriate diagrams (see the left panel of Fig. 3.1). In each diagram two HTL gluon propagators are cut, one corresponding to the exchanged virtual gluon of momentum q with a parton in the medium, and the other corresponding to radiated gluon of momentum k . Note that the exchanged gluon momentum is space-like [147, 148, 157] ($q^0 \leq |\vec{\mathbf{q}}|$), while radiated gluon momentum is time-like [187, 188] ($k^0 \geq |\vec{\mathbf{k}}|$).

Thus, they calculated 9 diagrams, each of which was infrared divergent, contrary to the case of static medium, where none of them was divergent. Namely, although the Debye screening restored the infrared convergence of the longitudinal gluon exchange part, the transverse gluon exchange part was the origin of this divergence, due to the absence of magnetic screening mass. However, conveniently but also remarkably, the summation of all diagrams produced an infrared safe result, naturally regulating the divergence, without the necessity of introducing an artificial magnetic mass cut-off.

In order to calculate total energy loss in infinite dynamical medium and to compare the result with the one in infinite static medium, in [194] the following simplification was made: Total energy loss is obtained by multiplying $\frac{dE}{dL}$ by the effective thickness of QGP medium L . The obtained analytical expression to the 1st order in opacity formally resembled very much to the corresponding static infinite case, and simple transcription rule between dynamical and static medium was established:

$$\lambda_{dyn} \rightarrow \lambda_{stat}, \quad v_{eff}^{dyn}(\mu_E, \mathbf{q}) \rightarrow v_{eff}^{stat}(\mu_E, \mathbf{q}), \quad (3.1.1)$$

where λ stands for the effective mean free path, and v_{eff} denotes effective cross section. Note that static radiative energy loss calculated in infinite QGP medium differs from the one obtained in finite size medium (DGLV). However, the numerical comparison of radiative energy loss in dynamical with static infinite medium showed almost two times larger loss in dynamical case. Consequently the recoil of the massless quarks and gluons in the medium was no more to be neglected. It is worth noting, that obtained energy loss increases linearly with the path length through QGP medium, i.e. corresponds to Bethe-Heitler limit. This is nevertheless an expected dependence, as they considered an infinite medium, with (on-shell) jet

produced at remote past, implying short formation time.

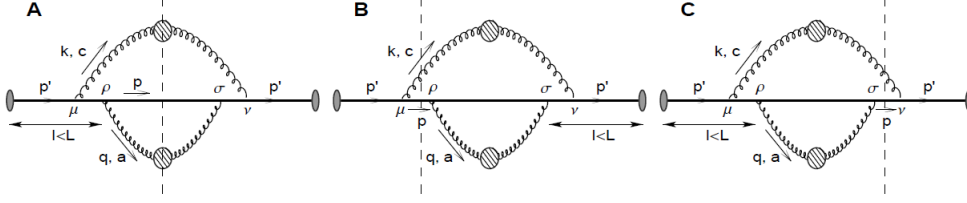


Figure 3.1: Representative 2-HTL Feynman diagram and three on-shell cuts. The left, central and right panels correspond to the central, left and right cut of the same diagram, respectively. In infinite dynamical QGP medium, only left diagram is included, while in finite dynamical medium all tree cuts contribute to the 1^{st} order in opacity quark radiative energy loss. Gray ellipse represents quark-jet source and the large dashed circles ("blob") represent effective HTL gluon propagators (see B appendix from [188]). The radiated gluon is denoted by momentum k and color c , whereas the exchanged gluon is denoted by momentum q and color a . p corresponds to the final quark. Figure adapted from [196].

The next step was including *finite* size medium corrections, which enabled assessment of Landau-Pomeranchuk-Migdal (LPM) effect [160, 197], in radiative energy loss calculation within dynamical QGP medium [196, 198]. The constraint to the finite size is important in order to realistically model the medium, and moreover produce reliable predictions, since QGP created at RHIC and LHC has finite dimensions. The same kinematic approximations were made in calculating 1^{st} order in opacity radiative energy loss of a heavy quark. The finite size effect was implemented through the requirement that the distance between the jet production site and the collisional interaction site has to be smaller than the length of the medium. Also, it was assumed that the heavy quark is produced inside the QGP medium at time $t = 0$.

Furthermore, a finite size medium allows the produced heavy quark to be not only on-shell, but also off-shell (see Fig. 3.1), increasing the number of considered diagrams to 25, by allowing left and/or right cuts of the same 2-HTL Feynman diagrams, where possible, and new ones as well. Off-shellness of the produced jet

and the requirement imposed on the exchanged gluon vertex to be inside the medium are the major differences compared to the infinite dynamical medium case.

Similarly to infinite dynamical medium, also in finite size dynamical medium each diagram has logarithmic divergence in the limit of vanishing exchanged gluon transverse momentum $\mathbf{q} \rightarrow 0$, which again was the consequence of accounting not only longitudinal (which is infrared finite due to Debye screening) but also transverse gluon exchange (which is infrared divergent, due to the absence of magnetic screening). However, the logarithmic divergence is again (surprisingly) naturally regulated after taking into account all relevant diagrams.

By comparing the radiative energy loss in finite size medium for dynamical and static [189] (DGLV) case, the same simple mapping rule (3.1.1) is obtained, which is quite remarkable considering complexity and different form of jet-medium interactions in these calculations. This implies generality of the mapping rule for transition from static to dynamical medium, regardless of its length. Quantitative formulas, and their interpretations in finite medium will be discussed in more details in next section.

Numerically, introduction of parton recoil in medium significantly increased (for 40–70%) radiative energy loss compared to the equally dense static finite QGP. Note that constant energy loss increase of $\approx 20\%$ (regardless of medium T , quark mass, and momentum) comes from shorter effective mean free path [196] $\lambda_{dyn} \approx 0.84\lambda_{stat}$ (which is also the case for infinite medium). Larger portion of increase in radiative energy loss of dynamical compared to static case originate from the effective cross section, and depends on T , quark mass and energy.

Additionally, another important and expected result is that finite size effect in dynamical medium reduces radiative energy loss compared to the an infinite dynamical QGP medium.

Regarding the radiative energy loss dependence on medium thickness (L), note that in finite size dynamical medium this dependence is non-trivial, i.e. neither linear (as in Bethe-Heitler limit) nor quadratic (as in LPM limit), and is also dependent on propagating parton's mass and momentum. However, inclusion of a finite size effect provided a common (framework) platform for addressing two limiting cases: incoherent Gunion-Bertsch [149] (GB) and coherent LPM [160, 197] limits.

The result obtained in *incoherent*, short formation time limit, which corresponds to lower energy heavy quarks, is not the same as Bethe-Heitler limit (infinite dynamical medium case [194]), due to the fact that now off-shell jets are also allowed.

On the other hand, for asymptotically large jet energies (equivalently large formation times), their result recovers LPM *coherent* limit, since dependence of radiative energy loss on L is quadratic. Consequently, for ultra-relativistic jets, inclusion of finite size effects mimics destructive effects of LPM interference in an infinite QGP medium (BDMPS [165, 166]), lowering energy loss compared to the incoherent limit. This could be qualitatively explained by the fact that created medium has finite, potentially smaller thickness compared to jet radiation coherence length ($\sim \tau_f$), which is shown [196] to be the case for light partons or large jet energies. This can also be seen from the formation time in finite dynamical QGP $\tau_f = \frac{2xE}{(\mathbf{k}+\mathbf{q})^2+m_g^2+x^2M^2}$, where E denotes initial jet energy, x the fraction of longitudinal momentum carried away by radiated gluon; \mathbf{k} and \mathbf{q} transverse momentum of radiated and exchanged gluon, respectively, and M is quark mass.

Quantitative assessment on thickness dependence of radiative energy loss [196] confirmed mass hierarchy at low jet-energy: bottom quarks show the weakest departure from the linear Bethe-Heitler pattern, while with decreasing quark mass the LPM effect is more pronounced. However, all quark flavor exhibit quadratic L dependence at very large jet-energies.

It is worth noting that, in finite size dynamical QGP, at asymptotically large jet energies (LPM limit), the approximation of the medium by randomly distributed static scattering centers presents accurate medium description (when scaled by $\frac{\lambda_{dyn}}{\lambda_{stat}}$).

Continuing along these lines (by including dynamical medium, which triggered infrared singularity of each individual diagram), the question of magnetic screening absence emerged and waited for consistent inclusion in radiative energy loss calculus. Note that the HTL pQCD approach requires magnetic mass (μ_M) equal to zero, consistently with the finite temperature field theory at one-loop perturbative level in thermal equilibrium. However, different non-perturbative models [199–203] reported non-zero magnetic screening mass, which, more precisely, is estimated to lie in the region $0.4\mu_E < \mu_M < 0.6\mu_E$. Thus, Djordjevic *et al.* addressed this issue [204],

through the modification of exchanged (and radiated) gluon self-energy. The obtained result has (general) broader range of validity considering any well-defined system of quasi-particles [205] (for details see subsection 5.2).

Namely, radiative energy loss expression can be factorized into: *i*) part representing interaction between the jet and exchanged gluon, referred to as effective cross section ($v(\mathbf{q})$); and *ii*) part corresponding to the interaction between jet and radiated gluon (the remaining part $f(\mathbf{k}, \mathbf{q}, x)$). This factorization cannot be modified by a finite magnetic mass introduction, since it is independent on the particular form of gluon self energy, which on the other hand is only affected by μ_M . Note that $v(\mathbf{q})$ is a function only of the exchanged gluon self-energy, whereas $f(\mathbf{k}, \mathbf{q}, x)$ depends solely on a radiative gluon self-energy. Fortunately, it was shown in [204], that the introduction of finite magnetic mass notably alters only exchanged gluon self-energy, thus the effect of $v(\mathbf{q})$ change needed to be estimated.

The obtained $v(\mathbf{q})$ for a finite magnetic mass has an extra μ_M^2 term in numerator (subtracted from μ_E^2) and in denominator (accompanying single \mathbf{q}^2 and not $(\mathbf{q}^2 + \mu_E^2)$), compared to the zero magnetic mass case.

Numerically, they obtained that finite magnetic mass significantly decreases radiative energy loss (25 – 50%). Unexpectedly, this decrease is mainly a consequence of μ_M^2 from the numerator and not the one in denominator, although the latter could be seen as a cut-off for regulating infrared divergence. Intuitively, this could be understood by the fact that there was no need for introduction of the artificial cut-off, as divergence has already been naturally regulated by taking into account all relevant Feynman diagrams.

And finally, the most up-to-date improvement to the radiative energy loss formula presents introduction of running strong coupling constant [206, 207] (see Eq. (1.1.2)), according to [208]. The off-shellness of the jet ahead of collisional interaction is $Q^2 = ET$ [209], while ahead of gluon radiation is $Q^2 = \frac{\mathbf{k}^2 + M^2 x^2 + m_g^2}{x}$ [198]. Details of implementing running α_s in radiative and collisional energy loss in finite size dynamical QGP medium are outlined in subsection 5.2. It is worth noting that each running coupling is infrared safe, and furthermore of a moderate value, so there was no need to include cut-offs, as was the usual procedure in other approaches.

Finally, we incorporate our up-to-date dynamical energy loss model into numeri-

cal procedure, outlined in the next subsection, which allows generating state-of-the-art suppression predictions.

3.2. Suppression computational formalism

The use of generic pQCD convolution [190, 208] formula in the following form:

$$\frac{E_f d^3\sigma}{dp_f^3} = \frac{E_i d^3\sigma(Q)}{dp_i^3} \otimes P(E_i \rightarrow E_f) \otimes D(Q \rightarrow H_Q) \otimes f(H_Q \rightarrow e, J/\psi), \quad (3.2.1)$$

allows studying each step of particle suppression independently. In the above formula, Q denotes quark (antiquark) or gluon, $\frac{E_f d^3\sigma}{dp_f^3}$ and $\frac{E_i d^3\sigma(Q)}{dp_i^3}$ stands for final and initial particle distributions, respectively. $P(E_i \rightarrow E_f)$ is the energy loss probability, $D(Q \rightarrow H_Q)$ is the fragmentation function (FF) of quark (antiquark) or gluon hadronizing into hadron H_Q , whereas for heavy quarks $f(H_Q \rightarrow e, J/\psi)$ presents decay function of H_Q into single electron or J/ψ .

Thus, we plausibly assume that high p_\perp partons, whose suppression we observe, are produced before QGP is formed (i.e. equilibrated), that is in a QCD vacuum. We also consider that fragmentation and decay steps occur in vacuum. Consequently, the QGP medium affects the propagating particle via medium induced energy loss (the step 2 in Fig. 3.2), which is generally considered to be the crucial ingredient of the suppression computational formalism, and which is the subject of this thesis.

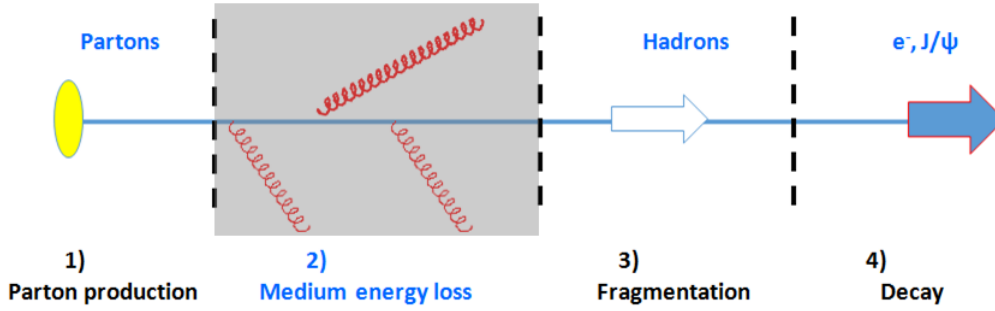


Figure 3.2: Suppression computational scheme. The chronological order of each independent step, separated by vertical dashed lines, in our numerical formalism: high p_{\perp} parton production (yellow ellipse), medium induced energy loss, fragmentation into hadron in vacuum and decay of heavy measons (D , B) into e , J/ψ . Figure adapted from [211].

The chronological order of our computational formalism (see Fig. 3.2), used to obtain the reliable suppression predictions, outlined in more distinct manner and with all effects included reads:

1. Up-to-date initial distribution functions for light and heavy flavors, computed at next to leading order, according to [212].
2. Dynamical energy loss formalism [208], which as mentioned above includes:
 - Radiative energy loss
 - Collisional energy loss
 - Dynamical QGP medium, which considers that the recoil of the medium constituents is taken into account as opposed to static scattering centers
 - Finite size medium, that is, it also takes into account that medium created in ultra-relativistic heavy ion collisions has a realistic finite size
 - Running strong coupling constant [208] introduced in both radiative and collisional energy loss
 - A finite magnetic mass [204] incorporated in the radiative energy loss.

Note that in our numerical formalism, we treat collisional and radiative energy loss separately, which is possible when collisional and radiative processes

are decoupled from each other, which is shown to be the case in HTL approach [213], and in our calculations. Namely, in [213] it was shown that different diagrams (cuts of the same HTL diagram in 0^{th} order) correspond to collisional and radiative contributions (so there is no overlapping and consequently over-counting). More qualitatively, collisional (elastic) processes assume the same number of incoming and outgoing particles, while radiative (inelastic) ones assume an additional gluon among outgoing particles (see Fig. 3.3).

Also there is no interference between the two contributions, since from momentum conservation, it can be inferred that in diagrams corresponding to radiative contributions, condition $|\omega| > |\vec{\mathbf{q}}|$ (quasi-particle state of gluon) has to be fulfilled, while in diagrams corresponding to collisional contributions, the condition $|\omega| \leq |\vec{\mathbf{q}}|$ (virtual gluon) holds (where \mathbf{q} denotes radiated (exchanged) gluon 3D momentum). Thus, these two contributions have zero values in overlapping regions, and therefore avoid the interference.

More precisely, the collisional energy loss is calculated in 0^{th} order, while radiative energy loss is calculated to the 1^{st} order in opacity (although 0^{th} , order goes into FF). The illustration of the difference between collisional and radiative energy losses is displayed in Fig 3.3.

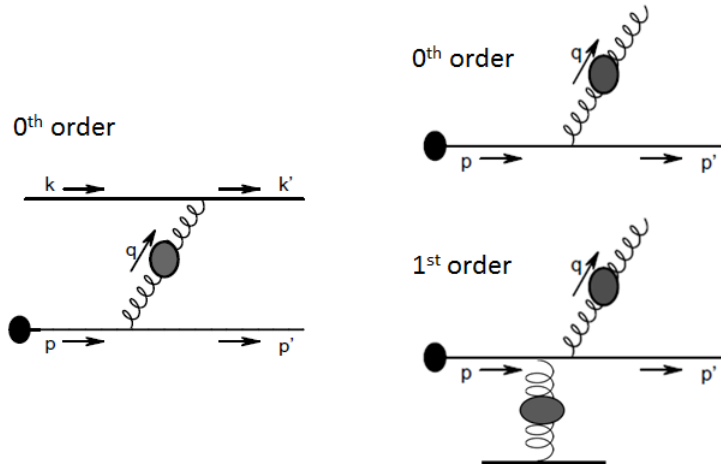


Figure 3.3: Representative diagrams in calculating energy loss in finite size dynamical QGP medium. The left panel corresponds to the collisional process (originating from 1-HTL), while the right panel corresponds to radiative process (upper (lower) originating from 1-HTL (2-HTL) gluon propagator). The black ellipse denotes parton source, the "blob" (gray ellipse) represents the effective HTL gluon propagator for collisional interactions, while denotes the transverse gluon propagator with the effective gluon mass for radiative processes. Figure adapted from [213].

The energy loss probability comprises also the multi-gluon [184] and path-length fluctuations [190]. The multi-gluon fluctuations are introduced under the assumption that the fluctuations of the radiated gluon number are uncorrelated. More specifically, the energy loss probability takes into account that the jet, during its propagation through QGP, can independently radiate number of gluons. Therefore, the spectrum in the 1st order in opacity of the total radiative energy loss fraction ($\epsilon = \sum_i \frac{\omega_i}{E}$, where ω_i and E denotes energy of radiated gluon i and initial jet energy, respectively) is represented via Poisson expansion [184] $P(\epsilon, E) = \sum_{n=0}^{\infty} P_n(\epsilon, E)$, where n counts the number of radiated gluons. Here, $P_0(\epsilon, E) = \exp^{-\langle N_g^{(1)}(E) \rangle} \delta(\epsilon)$, $P_1(\epsilon, E) = \exp^{-\langle N_g^{(1)}(E) \rangle} \frac{dN_g^{(1)}(\epsilon, E)}{d\epsilon}$,

while for $n \geq 2$:

$$\begin{aligned}
P_n(\epsilon, E) &= \frac{1}{n} \int dx_{n-1} \frac{dN_g^{(1)}(x_{n-1}, E)}{dx_{n-1}} P_{n-1}(\epsilon - x_{n-1}, E) \\
&= \frac{e^{-\langle N_g^{(1)}(E) \rangle}}{n!} \int dx_1 \dots dx_{n-1} \frac{dN_g^{(1)}(x_1, E)}{dx_1} \dots \frac{dN_g^{(1)}(x_{n-1}, E)}{dx_{n-1}} \frac{dN_g^{(1)}(\epsilon - x_1 - \dots - x_{n-1})}{d(\epsilon - x_1 - \dots - x_{n-1})},
\end{aligned} \tag{3.2.2}$$

where x_i denote energy fraction of initial jet energy carried away by i^{th} gluon, and where $\langle N_g^{(1)}(E) \rangle = \int d\epsilon \frac{dN_g^{(1)}(\epsilon, E)}{d\epsilon}$ holds. This ensures $\int_0^\infty d\epsilon P(\epsilon, E) = 1$ and $\int d\epsilon P(\epsilon, E) \epsilon = \frac{\Delta E}{E}$.

Regarding the path length fluctuations, note that the single gluon radiation spectrum $\frac{dN_g^{(1)}}{dx}$ (Eq. (5.2.2)) is also a function of L , i.e. of the jet in-medium path length. Instead of assuming the same averaged L for each jet, for more realistic approach, we took into account the fact that jets can be produced anywhere in the nuclei overlapping area, and consequently travel different distances in QGP. Therefore, depending on their production site and motion direction in transverse plane, the jets can lose different amounts of energy. Quantitatively, these features are introduced in our numerical formalism through functional dependence of radiative and collisional energy loss probability distribution on L . The path length probability is calculated according to the procedure described in [100], where one assumes the Glauber [55] model for the collision geometry, with implementation of Woods-Saxon nuclear density profile [214].

Also note that the full fluctuation spectrum in collisional energy loss probability is presented via Gaussian [190, 215], where a mean is determined by the average collisional energy loss $\langle \Delta E_{\text{coll}}(p_\perp, L) \rangle$ (taken from Eq.(14) [157]) and the variance is given by $\sigma^2 = 2T \langle \Delta E_{\text{coll}}(p_\perp, L) \rangle$, where T is the effective temperature of the QGP medium.

3. Up-to-date fragmentation functions, calculated according to [216, 217], and
4. State-of-the-art decay function, taken from [218].

It is very important to emphasize that, contrary to many other suppression formalism, in generating all R_{AA} predictions we use:

- the same numerical procedure
- the same energy loss formalism for both: radiative and collisional parts
- no fitting parameters.

4. EXPERIMENTAL VALIDATION OF DYNAMICAL ENERGY LOSS MODEL AND NUMERICAL PROCEDURE

The main goal of ultra-relativistic heavy-ion collisions at RHIC and LHC is studying the properties of created quark-gluon plasma. As an excellent tool for examination of these properties emerges the comparison of suppression predictions with the corresponding experimental data. Since recently, a wealth of suppression measurements for both light and heavy flavor, for diverse experimental conditions (center of mass energies, different experiments at RHIC and LHC) and centrality regions became available. The accurate predictions require primarily the reliable energy loss calculations, because, as perviously mentioned, the suppression is the consequence of the energy loss of high energy partons while traversing the QGP. Therefore, we applied the state-of-the-art dynamical energy loss formalism [208] (from the previous subsection), together with all aforementioned up-to-date computational formalism ingredients to produce the suppression predictions. This comparison with extensive set of data is also an exceptional test of the formalism, and consequently energy loss model validity. Besides comparing with the available data, our formalism also has predictive power for the upcoming experiments.

4.1. A very good agreement with suppression data

The first test of our understanding of QGP matter properties was done by Djordjevis *et al.* in [208], by generating suppression predictions for comprehensive set of *diverse particles* (from light to heavy flavor observables) in most central 2.76 TeV Pb+Pb collisions at LHC. In particular, they compared predictions, based on dynamical energy loss formalism incorporated in the aforementioned numerical procedure, for momentum dependence of R_{AA} with corresponding data for: charged

(light) hadrons, pions, kaons, D mesons, non-photonic single electrons and non-prompt J/ψ . Namely, the non-prompt J/ψ originates from b -hadron decay, while both D - and B -mesons contribute to non-photonic single electron yield.

They obtained that the suppression predictions for all six observables are in a very good agreement with the experimental data from ALICE [219–222] and CMS [223, 224]. To our knowledge, that presented the first unified suppression predictions for set of probes spanning over huge particle diversity, generated within the same theoretical framework, and the same numerical procedure (i.e. parameter set, without fitting parameters). Consequently, they obtained that the suppression of both *light and heavy flavor particles* at LHC can be reliably described within the dynamical energy loss formalism. However for an unbiased comparison with experimental measurements, different experimental conditions (i.e. RHIC data) should be considered, as well as the non-central collisions.

To address this issue, in [225], we extended the dynamical energy loss formalism towards generating R_{AA} prediction in non-central collisions at the RHIC and the LHC. More specifically, we generated suppression predictions for all (at that time) available centrality ranges, for both LHC and RHIC energies (i.e. 2.76 TeV and 200 GeV, respectively), and for four different probes (both light and heavy flavor): charged hadrons, D mesons, non-prompt J/ψ (at LHC) and neutral pions (at RHIC).

The starting point of an effective temperature T_{eff} for different centralities at LHC, is equal to 304 MeV (as extracted by ALICE [226] for 0–40% centrality $Pb + Pb$ collisions at LHC), while the effective temperature for different centrality ranges is determined from the effective temperature of 221 MeV for 0–20% centrality $Au + Au$ collisions at RHIC (as extracted by PHENIX [133, 134]). For consideration of different centrality collisions, our numerical formalism incorporated the new path-length distributions for each centrality bin starting from [100]. Additionally, new T_{eff} for each centrality region is calculated according to [183, 227] $T^3 \sim \frac{dN_g/dy}{V} \rightarrow T = c(\frac{dN_g/dy}{N_{part}})^{1/3}$, where $\frac{dN_g}{dy}$ presents gluon rapidity density, V ($\sim N_{part}$ assumption) is the volume of created QCD medium and N_{part} is the number of participants in a collision. Moreover, the gluon rapidity density per participants can be inferred from the experimentally measured charged particle multiplicity per participant pair

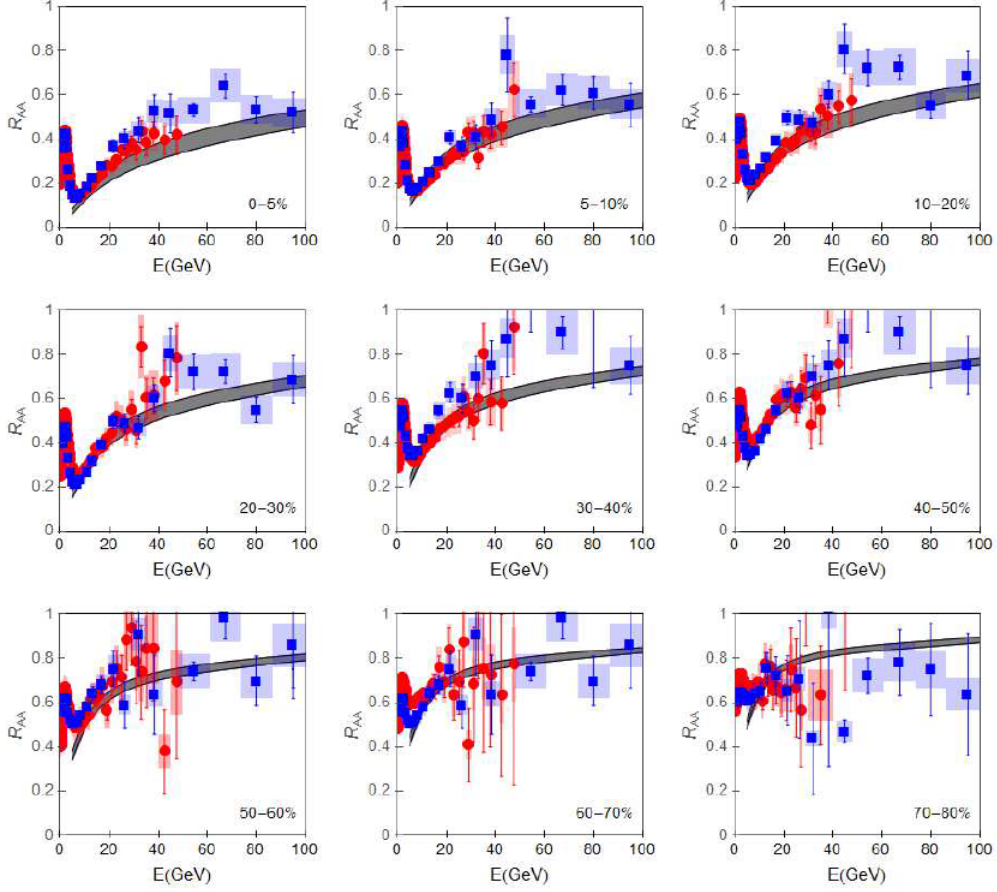


Figure 4.1: Comparison of charged hadron suppression predictions with LHC experimental data at different centralities. The panels show the comparison of charged hadron suppression predictions (gray band) with ALICE [219] (the red circles) and CMS [223] (the blue squares) R_{AA} data in 2.76 TeV $Pb+Pb$ collisions at LHC, for different (fixed) centrality regions, as a function of transverse momentum. The upper (lower) boundary of gray band on each panel corresponds to $\frac{\mu_M}{\mu_E} = 0.6$ ($\frac{\mu_M}{\mu_E} = 0.4$). The centrality ranges, for which the predictions are presented, are indicated in the lower right corner of each panel. Note that, on the third and the fourth panel, the same CMS data for centrality range 10 – 30% are shown; then, on the fifth and the sixth panel, the same CMS data for centrality range 30 – 50% are presented; similarly on the seventh and the eighth panel, the CMS data for centrality range 50 – 70% are shown, while on the ninth panel CMS data for centrality region of 70 – 90% are presented. Figure adapted from [225].

$\frac{dN_{ch}/dy}{N_{part}/2}$ for different centralities at both RHIC [228] and LHC [229], since $\frac{dN_g/dy}{N_{part}} \propto$

$\frac{dN_{ch}/dy}{N_{part}/2}$. The constant c , which characterizes specific colliding energy can be determined from aforementioned ALICE and PHENIX T_{eff} measurements in the central collisions at 2.76 TeV $Pb + Pb$ collisions in LHC and 200 GeV $Au + Au$ collisions in RHIC.

In numerical calculations we used the following standard parameters: effective light quark flavors $n_f = 2.5$ for RHIC and $n_f = 3$ for LHC. The light quark mass is assumed to be dominated by the thermal mass $M = \mu_E/\sqrt{6}$, where temperature dependent Debye mass $\mu_E(T)$ is obtained from [207] (or see Eq. (5.2.8) in the next section), whereas the charm and the bottom masses are, respectively, $M = 1.2$ GeV and $M = 4.75$ GeV. In each figure of this subsection, the gray band corresponds to $0.4\mu_E \leq \mu_M \leq 0.6\mu_E$ [199–203], while the gluon mass is equal to $m_g = \mu_E/\sqrt{2}$ [188]. The values of the remaining ingredients of our suppression computational formalism are specified in the previous section. The suppression is measured either as a function of final transverse momentum (p_\perp) for different fixed centrality bins or as a function of participants number for fixed momentum ranges.

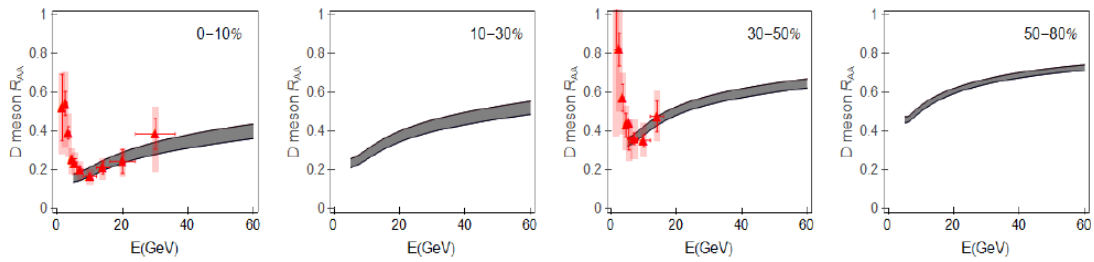


Figure 4.2: Comparison of D meson suppression predictions with LHC experimental data at different centralities, as a function of transverse momentum. The theoretical predictions are presented by gray bands, where upper (lower) boundary of each band corresponds to $\frac{\mu_M}{\mu_E} = 0.6$ ($\frac{\mu_M}{\mu_E} = 0.4$). The centrality regions, for which the predictions are presented, are denoted in the upper right corner of each panel. At that time D meson R_{AA} experimental data for only two centrality bins were available: 0 – 7.5% central 2.76 $Pb + Pb$ collisions at LHC [230] (the red triangles in the left panel), and 30 – 50% ALICE data [231] (the red triangles in the third panel). Figure adapted from [225].

First, we generated suppression predictions, as a function of p_\perp for charged (light)

particles in 2.76 TeV $Pb + Pb$ collisions at LHC, for nine different centrality regions, and compared them with the available ALICE [219] and CMS [223] experimental data in Fig. 4.1. Note that each panel corresponds to different (fixed) centrality bin.

Next, we concentrated on generating R_{AA} vs. p_{\perp} predictions for D mesons (heavy particles) at different centrality bins (also in 2.76 TeV $Pb + Pb$ collisions at LHC), and compared them with, at that time, available ALICE [230, 231] suppression data in Fig. 4.2. Note that R_{AA} predictions for 30 – 50% centrality region were generated before the experimental data, which are now added to figure, became accessible.

From Figs. 4.1 and 4.2 we observe a very good agreement between our predictions and experimentally obtained R_{AA} for both *light* and *heavy flavor* particles in *all available centrality ranges* at the LHC (for $p_{\perp} \gtrsim 10$ GeV).

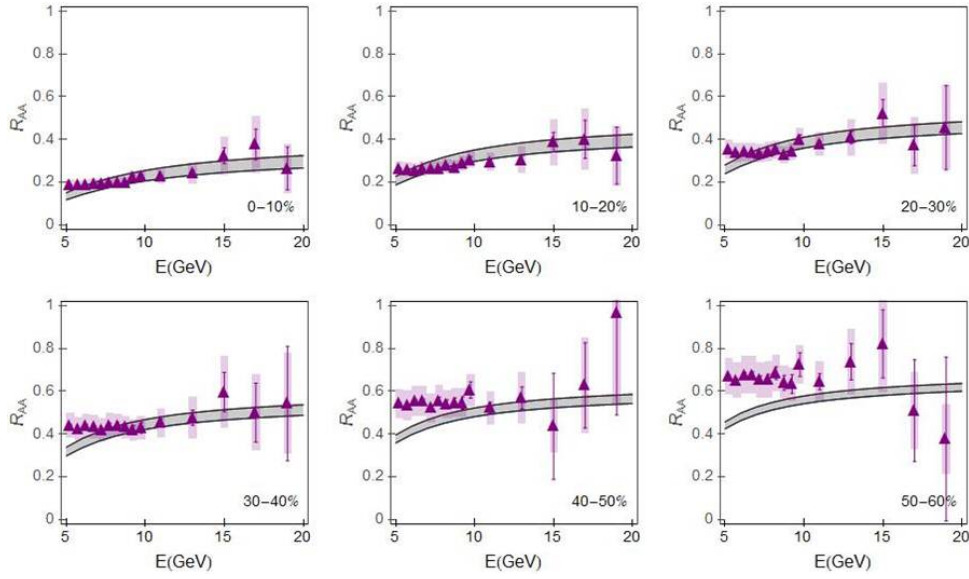


Figure 4.3: Comparison of neutral pion suppression predictions with RHIC experimental data at different centralities. The panels show the comparison of π^0 suppression predictions (gray band) with PHENIX [232] R_{AA} data at 200 GeV $Au + Au$ collisions at RHIC (the purple triangles), for different (fixed) centrality regions, as a function of transverse momentum. The upper (lower) boundary of gray band on each panel corresponds to $\frac{\mu_M}{\mu_E} = 0.6$ ($\frac{\mu_M}{\mu_E} = 0.4$). The centrality bins, for which the predictions and the data are presented, are denoted in the lower right corner of each panel. Figure adapted from [225].

Further, we proceeded with comparing our R_{AA} predictions with RHIC (PHENIX)

data [232] for different centrality bins (Fig. 4.3). To that end, we provided suppression predictions for π^0 as a function of transverse momentum, for six different centrality bins in 200 GeV $Au + Au$ collisions at RHIC. Similarly as for LHC measurements, from Fig. 4.3 we observe a robust agreement between our theoretical predictions and experimental RHIC data for each centrality bin.

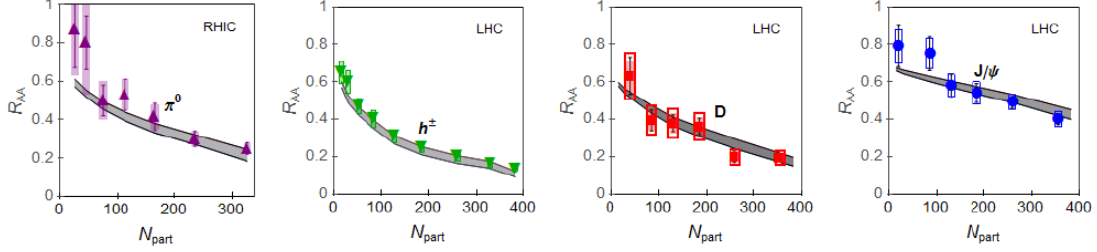


Figure 4.4: Suppression dependence on the number of participants for light and heavy flavor at RHIC and LHC. The first panel compares R_{AA} predictions with PHENIX experimental data [232] for neutral pion in 200 GeV $Au + Au$ collisions at RHIC, where π^0 momentum is larger than 7 GeV. The remaining panels compare R_{AA} predictions with experimental data from 2.76 TeV $Pb + Pb$ collisions at LHC, for: charged hadrons [219], with momentum in 6 – 12 GeV range (the second panel), D mesons [233], with momentum in 8 – 16 GeV range (the third panel) and non-prompt J/ψ [234], with momentum in 6.5 – 30 GeV range (the last panel). Theoretical predictions are presented by gray bands, where upper (lower) boundary of each band corresponds to $\frac{\mu_M}{\mu_E} = 0.6$ ($\frac{\mu_M}{\mu_E} = 0.4$). Figure adapted from [225].

Finally, in Fig. 4.4 instead of fixing the centrality ranges, as done in previous figures of this subsection, we fixed the momentum regions to address how suppression changes as a function of centrality (that is number of participants). To that end, we generated predictions for diverse probes and both RHIC and LHC experiments. In particular, the comparison of our predictions with experimental data is performed for neutral pions at the RHIC and charged hadrons, D mesons and non-prompt J/ψ at the LHC. Again, we obtained a very good agreement of our predictions with the experimental data.

Therefore, we conclude that our theoretical formalism works very well in reproducing R_{AA} data for diverse set of probes (light and heavy flavor) [208, 235], different

collision energies (RHIC and LHC) and all available centrality regions [225].

4.2. The predictions for upcoming measurements

Another convenience of the dynamical energy loss model and our numerical procedure reflects in its reliable predictive power. In that manner, prior to the first suppression measurements at 5.02 TeV $Pb + Pb$ collisions at the LHC, Djordjevic *et al.* provided R_{AA} predictions for heavy flavors ($c, b, D, J/\psi$) [236] in most central collisions. Namely, contrary to (naively) expected significant increase in suppression of 30%, they obtained qualitatively and quantitatively same heavy flavor suppressions at 2.76 TeV and 5.1 TeV. This was explained [236] by cancellation of two opposite effects: *i*) flattening of initial parton distribution at higher collision energy, and *ii*) smaller than expected increase of heavy quark radiative and collisional energy loss (practically only linear dependence on T).

Along these lines, in paper [237] we showed that suppression predictions in central 2.76 TeV and 5.02 TeV $Pb + Pb$ collisions at LHC are practically the same for light probes, i.e. charged hadrons as well (see most up-to-date data, released afterwards, for light and heavy hadrons in subsection 1.5.2, i.e. see Fig. 1.17). Consequently, we argue that predictions for all single particles, regardless of its mass, at 2.76 TeV are also valid for 5.02 TeV beam energies (see Fig. 4.5).

In the same paper [237] we addressed the issue of which particles and at which transverse momentum range are adequate for mass tomography of the QGP. Namely, this issue is of a great importance, since particles with the different masses are expected to interact differently (lose different amounts of energy) in the QGP medium, making the mass tomography an excellent tool for mapping the QGP properties. Also, our predictions point towards the relevant momentum regions and where the future experimental efforts, with regards to this matter, should be concentrated.

To this end, we generated R_{AA} predictions at two p_{\perp} regions: the lower momentum region (i.e. $p_{\perp} \sim 10$ GeV in this context) and high momentum region ($p_{\perp} \sim 100$ GeV), for charged hadrons, D mesons and B meson or non-prompt J/ψ (originating from B meson decay).

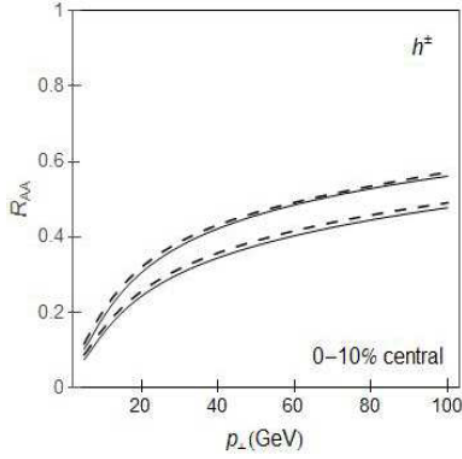


Figure 4.5: Comparison of charged hadron R_{AA} predictions at 2.76 and 5.02 TeV. Suppression predictions for h^\pm , as a function of transverse momentum in 0 – 10% central $Pb + Pb$ collisions at the LHC, are shown as white bands with full (dashed) boundaries for 5.02 TeV (2.76 TeV) center-of-mass energies. The upper (lower) boundary of each band corresponds to $\frac{\mu_M}{\mu_E} = 0.6$ ($\frac{\mu_M}{\mu_E} = 0.4$). Figure adapted from [237].

From Fig. 4.6, we observe that predictions in these two momentum regions displayed different tendencies. While at lower momentum region the mass hierarchy is present, that is J/ψ is notably less suppressed, due to dead cone effect [156], than equally suppressed charged hadrons/ D meson [238]; at high momentum region we predicted almost the same suppressions regardless of the probe’s mass. An intuitive explanation for the latter region would be that particle mass becomes small compared to its momentum, leading to mass irrelevance at high p_\perp region. Note that our predictions at lower p_\perp agree to a great extent with experimental data for both particles, while currently, at higher momentum range only charged hadron data are available (and are in good agreement with our suppression predictions). Therefore, the overlapping light and heavy flavor suppressions at high momentum ranges presented our clear prediction to be experimentally tested in the future.

For the quantitative explanation of the smaller J/ψ suppression at lower p_\perp (left panel of Fig. 4.6) compared to D meson, we individually examined the contribution of initial b and c quark distributions and energy loss to the suppression predictions. From the left panel of Fig. 4.7 we obtained that the contribution from the initial

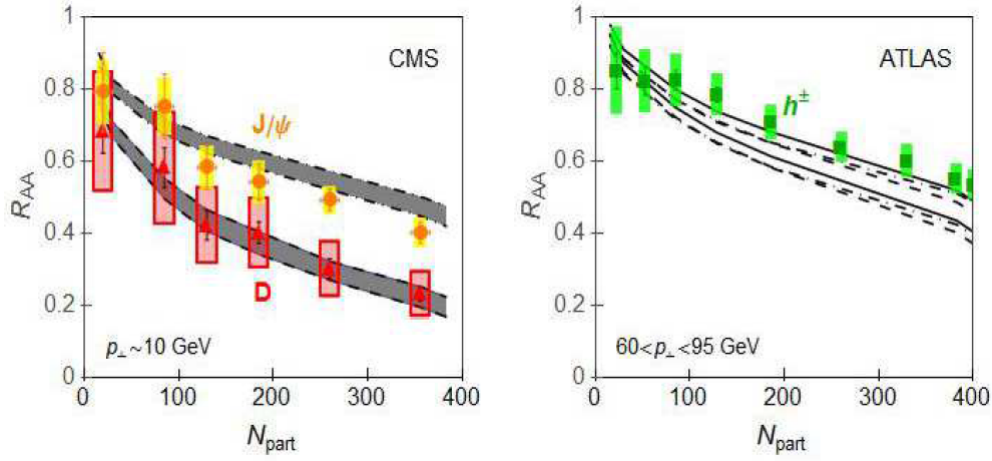


Figure 4.6: R_{AA} as a function of participants number for single particles in $\sqrt{s_{NN}} = 2.76$ TeV $Pb + Pb$ collisions at the LHC. The left panel shows comparison of our suppression predictions and CMS experimental data for D mesons [239] in $8 < p_{\perp} < 16$ GeV region (red triangles) and non-prompt J/ψ [234] in $6.5 < p_{\perp} < 30$ GeV region (orange circles). Gray bands with dashed, and dot-dashed boundaries, correspond to our theoretical predictions for D mesons and non-prompt J/ψ in the appropriate momentum regions, respectively. The right panel compares our R_{AA} predictions for h^{\pm} (white band with full boundaries), D (white band with dashed boundaries) and B meson (white band with dot-dashed boundaries) with ATLAS h^{\pm} data [240] (green squares) in $60 < p_{\perp} < 95$ GeV momentum region. On each panel, the upper (lower) boundary of each band corresponds to $\frac{\mu_M}{\mu_E} = 0.6$ ($\frac{\mu_M}{\mu_E} = 0.4$). Figure adapted from [237].

distributions is small, while the contribution due to the different energy loss is significantly larger. However, note that non-prompt J/ψ suppression is not a clear b suppression probe (there is a notable feed-down from B meson decay), so in order to exclude the decay contribution, we compared D and B meson suppression at lower p_{\perp} region in the middle panel of Fig. 4.7; note that the comparison of the left and the middle panels provides an estimate of decay function effect to the contributions analyzed in the left panel. Thus, the need for new probe: B meson suppression emerged. This led to even further enhancement of the energy loss contribution compared to the initial distribution. Consequently, the strong mass dependence of

R_{AA} (both predicted and observed) at lower momentum range is certainly due to the differences in the energy loss. Therefore, the lower p_{\perp} range is convenient for mass tomography.

Additionally, on the right panel of Fig. 4.7 we showed that there is no momentum region in which initial distribution contributes notably to the suppression difference between different types of particles. Consequently, the examination of different suppression patterns of D and B mesons at lower momentum region allows studying how different types of particles interact with QGP, without inference of production, fragmentation or decay.

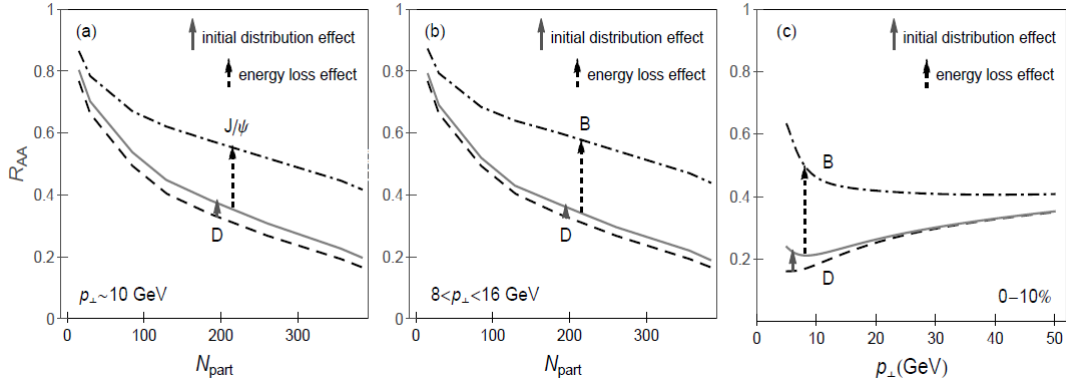


Figure 4.7: Contributions of initial distribution and energy loss to suppression. (a) R_{AA} predictions as a function of N_{part} are compared for D mesons in $8 < p_{\perp} < 16$ GeV region (dashed curve) and non-prompt J/ψ in $6.5 < p_{\perp} < 30$ GeV region (dot-dashed curve). Gray curve shows the analogous non-prompt J/ψ predictions, if the originating bottom quark would have the same energy loss as charm quark in QGP. (b) R_{AA} predictions as a function of N_{part} are compared for D and B mesons in $8 < p_{\perp} < 16$ GeV region. (c) R_{AA} predictions as a function of p_{\perp} are compared for D and B mesons. The full arrow denotes the contribution of the different initial distributions to the difference in the suppression between D meson and non-prompt J/ψ (or B meson), while the dashed arrow indicates the contribution of the different energy losses to the difference between D meson and the non-prompt J/ψ (or B meson) suppression. On each panel the legend is the same as in the first panel. Magnetic to electric mass ratio is set to $\mu_M/\mu_E = 0.4$. Figure adapted from [237].

However, to study the high p_{\perp} range in more detail, we compared R_{AA} predictions

for charged hadrons, D and B mesons at central 5.02 TeV collisions. Note that, since no experimental data existed at the time, this presented pure prediction to be tested in the future.

We obtained that below 50 GeV, B suppression is substantially smaller compared to D mesons and charged hadrons probes (see left panel of Fig. 4.8). However, an additional, non-intuitive feature appeared at $p_{\perp} > 100$ GeV: charged hadrons R_{AA} became notably larger than the one for D and B mesons (that are practically identical). Moreover, we obtained that the difference between light and heavy meson suppression increases with increasing p_{\perp} , leading to more than 10% smaller suppression of charged hadrons compared to heavy mesons for $p_{\perp} > 150$ GeV.

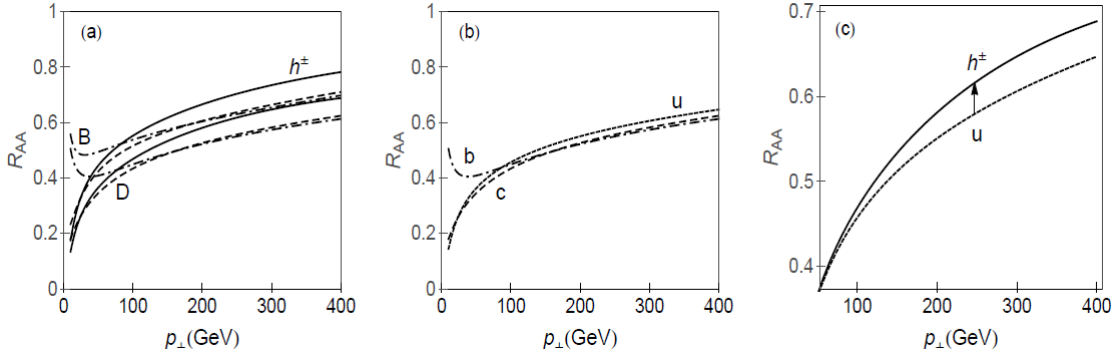


Figure 4.8: Single particles suppression predictions as a function of p_{\perp} in 0 – 10% central 5.02 TeV $Pb + Pb$ collisions at the LHC. (a) R_{AA} predictions for h^{\pm} , D and B meson are presented by white bands with full, dashed and dot-dashed boundaries, respectively. The upper (lower) boundary of each band corresponds to $\mu_M/\mu_E = 0.6$ ($\mu_M/\mu_E = 0.4$). (b) Bare quark R_{AA} predictions for u (dotted curve), c (dashed curve) and b quarks (dot-dashed curve). (c) Comparison of R_{AA} predictions for bare u quark (dotted curve) with h^{\pm} (full curve). In (b) and (c) panels μ_M/μ_E is set to 0.4. Figure adapted from [237].

To that end, we added two additional panels in Fig. 4.8. From the middle panel, where we compared bare u , c , b suppressions, we see that at $p_{\perp} > 100$ GeV, consistently with pQCD, finite mass effects for all types of quarks become negligible, resulting in the same suppressions of both light and heavy flavor partons. We showed that the non-intuitively obtained smaller suppression of charged hadrons compared

to heavy ones had nothing to do with different energy loss (i.e. mass effect, as mass is negligible in this momentum region). Instead we explained (see the right panel of Fig. 4.8) that the FF, which was not compensated by gluon contribution at this high p_{\perp} , was responsible for lowering the suppression of bare u quark.

The one of the main conclusions of paper [237] is that we predict that notable mass tomography effects could be clearly observed below 50 GeV, which is connected with the differences between the bottom, on one side, and the charm/light suppressions, on the other, i.e. energy losses (dead cone effect).

4.3. Conclusions

In this section first we provided comparison of suppression predictions based on our dynamical energy loss formalism with R_{AA} experimental data. The predictions were generated for: *i)* an extensive set of particles - from light to heavy flavor observables, *ii)* different experiments - both RHIC and LHC, and *iii)* all available centrality bins. Note that the predictions were obtained by applying the same theoretical formalism and within the same numerical procedure. Moreover, the same parameter set (corresponding to the standard literature values) was used for generating the predictions for the same experiment. Also, it is worth noting that *no* free parameters (obtained from the best fit) were used when comparing R_{AA} with the experimental data. We obtained robust agreement of our theoretical predictions with all these diverse experimental measurements, for all momentum ranges larger than 10 GeV.

Also, using the same procedure we provided heavy and light flavor suppression predictions prior to 5.02 TeV $Pb + Pb$ measurements at the LHC. Although higher collision energies intuitively imply larger suppression, we anticipated qualitatively and quantitatively the same suppressions for 2.76 and 5.1 TeV collision energies. This unexpected result was explained by coincidental interplay of initial momentum distributions and energy loss, and recently obtained its experimental confirmation.

And finally, we predicted that momentum region below 50 GeV is mostly adequate for mass tomography, directing future experimental efforts on this region, with regard to assessing how different probes interact with QGP, and toward measuring B

meson suppression, as a clear b suppression probe, instead of non-prompt J/ψ . And additionally, our formalism obtained as a prediction abnormal suppression decrease of charged hadron compared to heavier probes (B and D mesons whose suppressions nearly overlap with each other) at $p_{\perp} > 100$ GeV.

The excellent R_{AA} predictions agreement with comprehensive set of data, together with providing accurate predictions for higher collision energies at LHC indicates that our dynamical energy loss model incorporated in previously outlined computational formalism can reliably model hard probe-medium interactions. That is, pQCD is capable of adequately describing the properties of QGP medium created in ultra-relativistic HIC at RHIC and LHC.

5. THE IMPORTANCE OF DIFFERENT ENERGY LOSS EFFECTS IN DYNAMICAL ENERGY LOSS MODEL

In the previous section, we demonstrated that our theoretical predictions of jet suppression, which are based on recently developed dynamical energy loss formalism [208] show a robust agreement with the available suppression data at both colliders, for a diverse set of probes [208, 235] and centrality regions [225]. Additionally, we observed the formalisms predictive power [236, 237].

At this point, it's worth noting (we recall), that the dynamical energy loss model present a sophisticated formalism, which comprises several key ingredients, such as:

1. Radiative energy loss [196, 198]
2. Collisional energy loss [157]
3. QGP medium consisting of dynamical scattering centers
4. QGP medium of a finite size [196, 198]
5. Finite magnetic mass [204]
6. Running coupling [208].

Having all this in mind, a question arises whether such a good agreement of the predictions with the experimental data is a consequence of a single dominant energy

loss effect or is it a result of a cumulative effect of all energy loss ingredients. Therefore, in this section we address the issue of which effect, if not a superposition of several smaller improvements, is responsible for the accurate R_{AA} predictions [159].

5.1. Introduction

This question is moreover important, as various pQCD approaches, such as BDMPS-Z [165–167, 169, 170], ASW [241–243], AMY [172, 174, 175], (GLV) DGLV [181, 183, 189] and HT [244, 245] to the energy loss calculations neglect some (or many) of these effects. In particular, majority of these models consider bremsstrahlung a dominant form of high p_{\perp} parton energy loss [246]. However, there were some models that hinted that collisional energy loss is also important [154, 193], or the complete opposite one, that assume only collisional energy loss [146–148, 153, 155].

It is worth noting that, although accurate energy loss calculation is generally considered to be the crucial ingredient in generating reliable suppression predictions, in our numerical procedure (3.2.1) there are also other important steps, such as: initial parton distribution, fragmentation and decay function. Therefore, in order to isolate energy loss for assessing the importance of different energy loss ingredients in the suppression calculations, it would be convenient to have a probe that is sensitive only to the energy loss, i.e. for which fragmentation and decay functions do not play a role. Luckily, the D meson suppression emerges as a suitable candidate, since the fragmentation functions do not modify bare charm quark suppression, as previously shown in [152, 235, 238]. Additionally, regarding the decay functions, D meson presents genuine charm quark probe, since the feed-down from B meson is subtracted from the experimental data [221].

In order to assess the importance of different energy loss effects, which have been used in our suppression predictions, in this subsection we concentrate on the D meson suppression in central 200 GeV $Au + Au$ collisions at RHIC and 2.76 TeV $Pb + Pb$ collisions at the LHC. Regarding the RHIC, note that suppression measurements only up to 6 GeV are available (this p_{\perp} range is below our model applicability), explaining the omission of our prediction comparison with the data in

the further text. However, high momentum D meson suppression data are available at the LHC, and they serve as a baseline for evaluating the importance of each energy loss effect.

Our analysis is historically driven: we start from the static approximation, which has been the first approach to the energy loss calculations. Then we systematically include different energy loss effects, on-by-one. In particular, we first compare the relative importance of static radiative and collisional contribution to the D meson suppression predictions, to assess the adequacy of the historically widely used static approximation. Next we address the importance of including the dynamical scattering centers, by comparing static with dynamical radiative contributions to R_{AA} . Then we compare radiative and collisional energy loss R_{AA} within the same: dynamical energy loss formalism. Next we examine the significance of constraining the medium to a finite size (LPM effect). Finally, we also investigate the importance of including the finite magnetic mass and the running coupling.

We start our analysis by outlining the analytical differences that each of the energy loss effect brings into fractional energy loss formula. Then we embark on addressing each effect numerically.

5.2. Theoretical framework

In this subsection we first outline details of the up-to-date numerical procedure, that we use, whose main ingredient is the state-of-the-art dynamical energy loss formalism, that gained its validation through comparison with extensive set of experimental data, as previously mentioned. Then we provide a brief overview of how the energy loss expression is modified, as different ingredients are excluded from this formalism. Note that, in the consecutive subsection, we numerically address different energy loss effects in a reverse order: that is we start from the static approximation, and include the effects separately, as such historically-driven approach is previously introduced (see subsection 3.1), and thus easier to follow.

The angular averaged nuclear modification factor R_{AA} will be used for studying the importance of different energy loss effects, since it has traditionally considered to

be a sensitive observable for interaction of high p_{\perp} particles with the QGP medium. The nuclear modification factor [100, 101] reflects how the QGP medium affects the auto-generated jet (or in our case single particle), that propagates through the medium and is given by Eq. (1.4.5).

Since we are interested in assessing the importance of different jet-medium effects, in an orderly fashion, and do not consider the details of the medium evolution in this study, it would be convenient to have an observable, which is insensitive to the specific aspects of the medium evolution. It turns out that angular averaged R_{AA} meets this criteria, as it was previously shown to be sensitive almost entirely to the average properties (temperature) of the evolving medium [102, 103]. Therefore, angular averaged R_{AA} is considered to be practically pure test of the jet-medium interactions, and used throughout this section. On the opposite side of sensitivity scale would be, for instance, elliptic flow v_2 , which is considered highly susceptible to the details of the medium evolution, and therefore inadequate for our study. In this respect, we model the medium by assuming an effective temperature of 304 MeV at the LHC (as extracted by ALICE [226]) and effective temperature of 221 MeV at RHIC (as extracted by PHENIX [126]).

For obtaining the final D meson (charm quark) spectra, upon its passage through QGP medium, as usual, we use generic pQCD formula [190, 208], given by Eq. (3.2.1), but in its reduced form:

$$\frac{E_f d^3\sigma}{dp_f^3} = \frac{E_i d^3\sigma(c)}{dp_i^3} \otimes P(E_i \rightarrow E_f), \quad (5.2.1)$$

where in distinction to Eq. (3.2.1) we omitted fragmentation function of charm quark into D meson ($D(Q \rightarrow H_Q)$), because fragmentation does not modify bare charm quark suppression [235, 238]. Likewise, the decay function ($f(H_Q \rightarrow e)$) is disregarded because D mesons are directly measured in the experiments. In Eq. (5.2.1) $\frac{E_i d^3\sigma(c)}{dp_i^3}$ stands for the initial charm quark spectrum computed at next-to-leading order [212]. Energy loss probability $E_i \rightarrow E_f$, in our most sophisticated dynamical energy loss formalism includes all: radiative and collisional energy losses in a finite size dynamical QGP medium, multi-gluon [184] and path length [190] fluctuations. The path length distributions are extracted from [100]. The implementation of multi-gluon and path-length fluctuations is described in subsection 3.2. Note that, as some effect is excluded the energy loss probability changes accordingly.

The radiative energy loss in a finite size, optically thin, dynamical QGP medium [196, 198], obtained from HTL approximation, at 1st order in opacity [184, 247] is given by the expression:

$$\begin{aligned} \frac{\Delta E_{rad}}{E} &= \frac{C_R \alpha_s L}{\pi \lambda} \int dx \frac{d^2 \mathbf{k}}{\pi} \frac{d^2 \mathbf{q}}{\pi} v(\mathbf{q}) \left(1 - \frac{\sin\left(\frac{(\mathbf{k}+\mathbf{q})^2 + \chi L}{xE^+}\right)}{\frac{(\mathbf{k}+\mathbf{q})^2 + \chi L}{xE^+}} \right) \frac{2(\mathbf{k} + \mathbf{q})}{(\mathbf{k} + \mathbf{q})^2 + \chi} \\ &\times \left(\frac{(\mathbf{k} + \mathbf{q})}{(\mathbf{k} + \mathbf{q})^2 + \chi} - \frac{\mathbf{k}}{\mathbf{k}^2 + \chi} \right), \end{aligned} \quad (5.2.2)$$

where E denotes initial jet energy, L is the dimension of the finite size QGP medium, while \mathbf{k} and \mathbf{q} , typically for this thesis, present transverse momentum of radiated and exchanged gluon, respectively. The color factor for quark-jet is $C_R = 4/3$, $\chi = m_g^2 + M_c^2 x^2$, $m_g = \mu_E/\sqrt{2}$ is the effective (asymptotic) mass for gluon [188] with the hard momenta $k \gtrsim T$, μ_E is Debye (electric) screening mass and $M_c = 1.2$ GeV is the charm quark mass. λ is the mean free path in the QCD medium and in the dynamical case [196] is given by:

$$\frac{1}{\lambda} = 3\alpha_s T. \quad (5.2.3)$$

For an infinite medium case, we use the incoherent limit [198] of Eq. (5.2.2), that is $\frac{\sin\left(\frac{(\mathbf{k}+\mathbf{q})^2 + \chi L}{xE^+}\right)}{\frac{(\mathbf{k}+\mathbf{q})^2 + \chi L}{xE^+}} \rightarrow 0$.

The derivation of collisional energy loss in dynamical QGP medium is provided in paper [157], and in this section for the finite size dynamical QGP medium we use Eq. (14) from that reference (or see Eq. (A.0.6) from Section A). For mimicking an infinite medium, the incoherent limit, i.e. Eq. (16) from [157] is applied (see Eq. (A.0.12) from Section A).

The finite size effect is addressed by assuming dynamical medium and by taking into account both radiative and collisional energy loss contributions, through comparing R_{AA} prediction when both contributions are calculated in finite size medium with the one when both contributions are taken in incoherent limits.

The effective cross section, when the finite magnetic mass is included, according to the paper [204], as qualitatively explained in the previous section, is given by Eq. (5.2.6) below. Here we provide a brief quantitative derivation of this formula. Particularly, by introducing the finite magnetic mass in radiative energy loss, only effective cross section is altered. Although $v(\mathbf{q})$ was previously calculated through

HTL for the self-energy, it is however independent from the particular form of gluon self-energy [205]. Thus, the effective cross section can be written as:

$$v(\mathbf{q}) = v_L(\mathbf{q}) - v_T(\mathbf{q}), \quad (5.2.4)$$

where L and T denote longitudinal and transverse contributions, respectively. The application of sum rules [205] gives:

$$v_{L,T}(\mathbf{q}) = \frac{1}{\mathbf{q}^2 + \text{Re}\Pi_{L,T}(\infty)} - \frac{1}{\mathbf{q}^2 + \text{Re}\Pi_{L,T}(0)}, \quad (5.2.5)$$

where $\Pi_{L,T}(q_0/|\vec{\mathbf{q}}|)$ denotes longitudinal and transverse gluon self-energies. So, the exact expression of gluon propagator is unimportant, but instead only knowledge of gluon self-energies $\Pi_{L,T}(q_0/|\vec{\mathbf{q}}|)$ for $q_0/|\vec{\mathbf{q}}| = \infty$ and $q_0/|\vec{\mathbf{q}}| = 0$ is needed. Note that L and T gluon masses at $|\vec{\mathbf{q}}| = 0$ are equal and called plasmon mass ($\Pi_L(\infty) = \Pi_T(\infty)$, due to inability to distinguish longitudinal and transverse modes for particles at rest), and they cancel each other. In the case of static gluon exchanges ($q_0 = 0$), longitudinal part corresponds to electric (Debye) screening mass $\mu_E^2 = \text{Re}\Pi_L(0)$, while transverse stands for magnetic screening mass squared $\mu_M^2 = \text{Re}\Pi_T(0)$.

Thus, for the effective cross section at finite magnetic mass μ_M the following expression was obtained:

$$v(\mathbf{q}) = \frac{\mu_E^2 - \mu_M^2}{(\mathbf{q}^2 + \mu_M^2)(\mathbf{q}^2 + \mu_E^2)}, \quad (5.2.6)$$

where non-perturbative approaches [199–203] obtained lower and upper limits of magnetic mass: $0.4 < \mu_M/\mu_E < 0.6$.

Note that, in the case when magnetic mass is equal to zero, the above expression reduces to the well-known HTL effective cross section [172, 174, 175, 198] for dynamical medium:

$$v(\mathbf{q}) = \frac{\mu_E^2}{\mathbf{q}^2(\mathbf{q}^2 + \mu_E^2)}. \quad (5.2.7)$$

Thus, the effect of finite magnetic screening mass is assessed by comparing R_{AA} predictions, where the effective cross section that enters radiative energy loss Eq. (5.2.2) is given either by Eq. (5.2.6) or by Eq. (5.2.7).

The running coupling is introduced according to [208] and is defined as in [206], that is, given by Eq. (1.1.2), where $n_f = 2.5$ ($n_f = 3$) for RHIC (LHC) is the number

of the effective light quark flavors. More specifically, in dynamical radiative energy loss, the coupling constant is present in a form $\mu_E^2 \alpha_s^2$ [198], which can be factorized into $\mu_E^2 \alpha_s(Q_v^2) \alpha_s(Q_k^2)$, where $\alpha_s(Q_v^2)$ corresponds to the jet interaction with virtual (exchanged) gluon, while $\alpha_s(Q_k^2)$ originates from jet interaction with radiated gluon. The off-shellness is given by $Q^2 = ET$ [209], and by $Q^2 = \frac{\mathbf{k}^2 + M^2 x^2 + m_q^2}{x}$ [198], as previously mentioned, for the two cases, respectively.

In the case of the running coupling, Debye mass μ_E [207] is obtained by self-consistently solving the equation:

$$\frac{\mu_E^2}{\Lambda_{QCD}^2} \ln \left(\frac{\mu_E^2}{\Lambda_{QCD}^2} \right) = \frac{1 + n_f}{11 - 2/3 n_f} \left(\frac{4\pi T}{\Lambda_{QCD}} \right)^2. \quad (5.2.8)$$

Regarding the collisional energy loss in a finite dynamical QCD medium, the strong coupling enters the expression in the form of α_s^2 [157], which can be factorized as $\alpha_s(\mu_E^2) \alpha_s(Q_v^2)$ [209]. Note that every α_s is given by Eq. (1.1.2).

Otherwise, when the running coupling is not included, fixed values of the strong coupling constant $\alpha_s = 0.3$ for RHIC ($\alpha_s = 0.25$ for LHC) [210] and Debye mass $\mu_E = gT$ are used. In that manner, the effect of running coupling is addressed by comparing suppressions, where the strong coupling that enters both radiative (Eq. (5.2.2)) and collisional (Eq. (14) from [157]) energy losses is given either by constant value or by Eq. (1.1.2), with factorization and appropriate off-shellness incorporated as explained above.

Transition from the dynamical to the static [189] approximation in the case of the radiative energy loss is given by the following two substitutions and according to the paper [196].

1. The mean free path in static and dynamical case is related through:

$$\frac{1}{\lambda_{stat}} = \frac{1}{\lambda_g} + \frac{1}{\lambda_q} = 6 \frac{1.202}{\pi^2} \frac{1 + n_f/4}{1 + n_f/6} 3\alpha_s T = c(n_f) \frac{1}{\lambda_{dyn}}, \quad (5.2.9)$$

where $c(n_f = 2.5) \approx 0.84$ is a slowly increasing function of n_f that varies between $c(0) \approx 0.73$ and $c(1) \approx 1.09$;

2. The effective cross section becomes:

$$v(\mathbf{q})_{stat} = \frac{\mu_E^2}{(\mathbf{q}^2 + \mu_E^2)^2}, \quad (5.2.10)$$

which is already presented in Eq. (2.2.8).

Note that in static medium, the only non-zero contribution to energy loss comes from the radiative part. So the adequacy of static medium approximation is investigated by comparing suppression predictions, when only radiative energy loss is taken into account in energy loss probability, in static and in dynamical medium.

5.3. Numerical results

In this subsection, we concentrate on generating suppression predictions for central 200 GeV $Au + Au$ collisions at RHIC and 2.76 TeV $Pb + Pb$ collisions at the LHC, starting from static QCD medium approximation, and address how the inclusion of different energy loss ingredients affects the D meson R_{AA} predictions. As explained previously, since the high p_{\perp} D meson R_{AA} data were available only at the LHC [221, 233], the comparison with the LHC data is done, in order to obtain qualitative and quantitative estimation of the importance of each individual effect.

Within the static approximation, we use a fixed value of the strong coupling constant $\alpha_s = \frac{g^2}{4\pi} = 0.3$ at RHIC ($\alpha_s = 0.25$ at LHC) and Debye screening mass $\mu_E \approx gT$. Note that these values are used in Figs. 5.1 to 5.5. Also, note that magnetic mass effect is not included ($\mu_M = 0$) in Figs. 5.1 to 5.4 and 5.6, whereas the finite magnetic mass is used in Figs. 5.5 and 5.7. The running coupling is considered in Figs. 5.6 and 5.7. The finite size QCD medium is considered in each figure, whereas Fig. 5.4 addresses the significance of constraining the dimension of created QGP medium.

5.3.1. Adequacy of static approximation

In order to assess the suitability of the static QGP medium approximation, implying that the interaction between jet and medium constituents can be modeled by static Yukawa color screened potential [161, 162], we compare relative importance of static radiative and collisional energy loss contributions to the suppression predictions in a finite size QGP medium. Namely, the static medium approximation implies that collisional energy loss is negligible compared to radiative energy loss, that is collisional energy loss equal to zero is assumed in this approximation.

Nevertheless, the obtained comparable contributions of collisional energy loss - that is even larger at lower p_{\perp} - compared to static radiative energy loss to suppression calculations, as can be observed in Fig. 5.1, pointed to inadequacy of static approximation for D meson R_{AA} predictions.

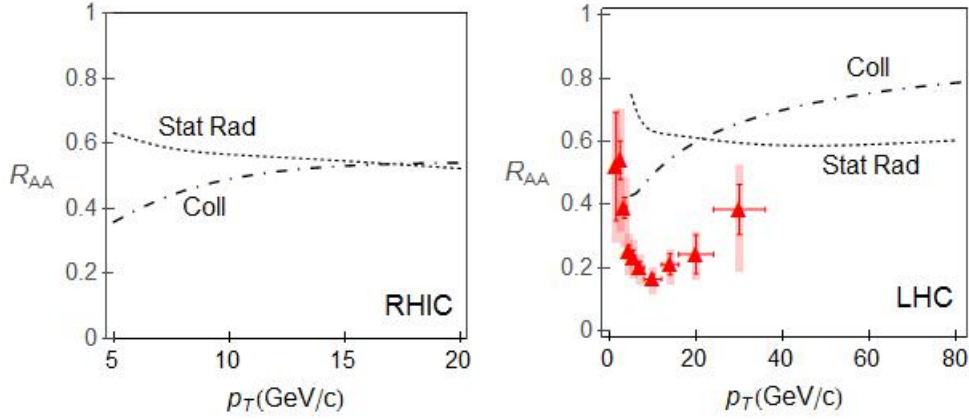


Figure 5.1: Static radiative vs. collisional energy loss R_{AA} . D meson suppression predictions dependence on transverse momentum, is shown assuming only radiative energy loss in static QGP medium (dotted curve), and considering only collisional energy loss in dynamical QGP medium (dot-dashed curve). Left (right) panel corresponds to RHIC (LHC) conditions. Right panel also contains the D meson R_{AA} experimental data for 0–7.5% central 2.76 TeV $Pb+Pb$ collisions at the LHC [221, 233] (red triangles). The standard values for the parameters are assumed: Debye mass $\mu_E = gT$, coupling constant $\alpha_s = 0.3$ ($\alpha_s = 0.25$) for RHIC (LHC). A finite size QGP medium is considered, while the finite magnetic mass effect is not included (i.e. $\mu_M = 0$). Figure adapted from [159].

Additionally, by comparing with a baseline LHC experimental data, from the right panel of Fig. 5.1, we also observe that the static approximation leads to a strong disagreement with the data. Specifically, static radiative energy loss leads to 2–3 times smaller suppression than the one experimentally observed. Consequently, we see that the static approximation is not an adequate one, and also that the collisional energy loss has to be taken into account in the suppression predictions.

Therefore, a number of energy loss models which consider only radiative energy loss (for an overview see e.g. [246]) - and some that consider only collisional energy

loss [146–148, 153, 155] - are clearly not adequate. The next logical step is the inclusion of dynamical QGP medium effect, where, as opposed to static QGP, the recoil of the medium constituents is taken into account. This effect is first assessed on radiative energy loss contribution to R_{AA} .

5.3.2. Radiative energy loss R_{AA} : static vs. dynamical cases

In Fig. 5.2, we compare the D meson suppression predictions obtained only from radiative energy loss in the static, with the one in the dynamical finite size QGP medium. We observe a large discrepancies in the two suppression predictions, with a significant suppression increase in the dynamical case. From the left panel of Fig. 5.2, we see that at the available RHIC jet energies this difference is consistent, implying that there is no momentum range where static approximation would be an adequate. Consequently, the dynamical energy loss effect has to be taken into account at RHIC.

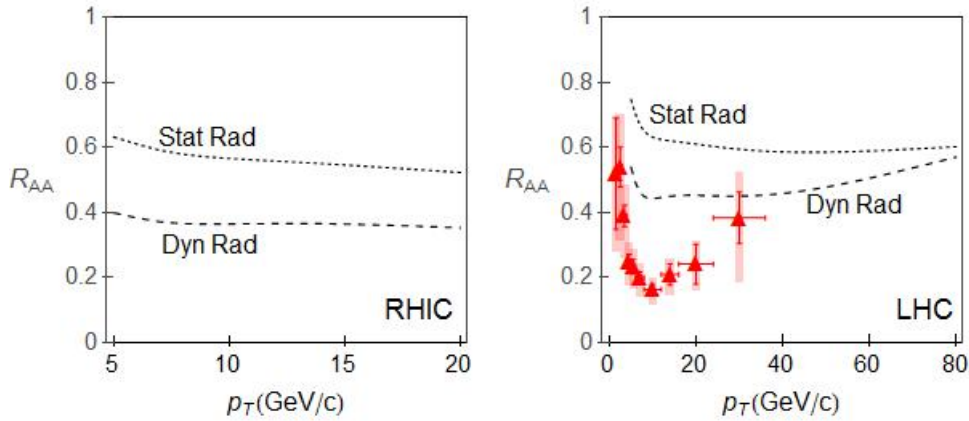


Figure 5.2: Static vs. dynamical radiative energy loss R_{AA} . D meson suppression predictions dependence on transverse momentum is plotted, assuming only radiative energy loss in static (dotted curve) and in dynamical (dashed curve) QGP medium. Left (right) panel corresponds to the RHIC (LHC) conditions. Right panel also shows the D meson R_{AA} experimental data for 0 – 7.5% central 2.76 TeV $Pb + Pb$ collisions at LHC [221, 233] (red triangles). The standard values for the parameters are assumed: Debye mass $\mu_E = gT$, coupling constant $\alpha_s = 0.3$ ($\alpha_s = 0.25$) for RHIC (LHC). A finite size QGP medium is considered, while no finite magnetic mass effect is included (i.e. $\mu_M = 0$). Figure adapted from [159].

From the right panel of Fig. 5.2, we observe that static approximation is not the appropriate one on, at that time available momentum range at the LHC (up to 40 GeV/c), but the results indicate that the static approximation to radiative energy loss may become valid for jet momentum larger than ≈ 100 GeV/c, in general agreement with [165, 196, 198]. However, note that the dynamical effect has to be included even for these higher transverse momenta, since the collisional energy loss (see the right panel of Fig. 5.1) has significant contribution to the jet suppression, which otherwise in the static approximation would be neglected.

Albeit the inclusion of dynamical effect considerably increases the radiative suppression compared to the static approximation, from the right panel of Fig. 5.2 we see that, at least below 40 GeV/c, radiative energy loss alone is not capable of explaining the experimentally obtained D meson R_{AA} neither quantitatively nor qualitatively (see the shape of Dyn Rad R_{AA} curve). Consequently, the model of

jet-medium interactions, which takes into account only the radiative energy loss is inadequate. Therefore, one has to include also the collisional energy loss within the same dynamical formalism, although the increased suppression due to radiative energy loss in dynamical medium compared to static medium (Fig. 5.2) raises the question of the collisional contribution importance, when dynamical medium is considered.

5.3.3. Dynamical formalism: radiative vs. collisional energy loss R_{AA}

To this end, now we concentrate on a finite size dynamical QCD medium and address the relative importance of radiative and collisional energy losses in this medium. In Fig. 5.3 we compare the D meson suppression predictions resulting from: *i*) collisional, *ii*) radiative and *iii*) collisional + radiative (total) energy loss in the dynamical QCD medium. We observe that, even when the dynamical effect is taken into account, again both radiative and collisional contributions are comparable and it is important to include them both in generating suppression predictions, which is in accordance with claims in Refs. [154, 157, 193]. This further underscores the importance of including the collisional energy loss in calculating D meson suppression at both RHIC and the LHC.

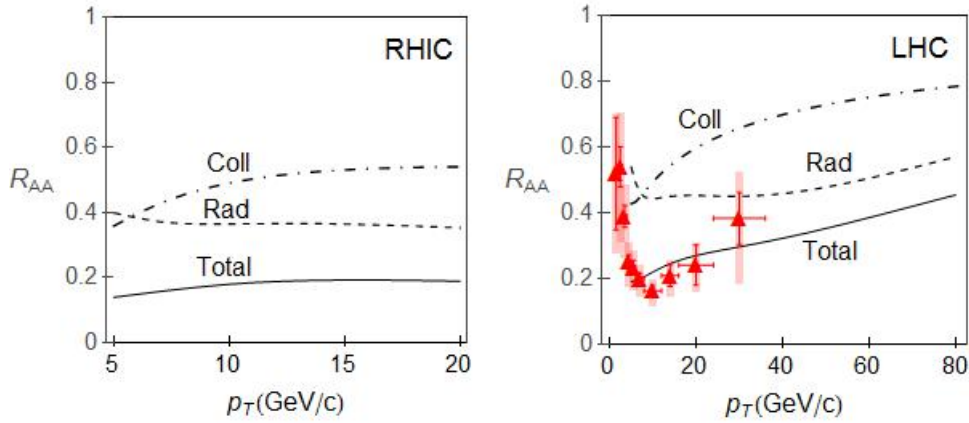


Figure 5.3: Radiative vs. collisional energy loss R_{AA} in dynamical formalism. D meson suppression predictions dependence on transverse momentum is shown for radiative (dashed curve), collisional (dot-dashed curve) and total, i.e. radiative + collisional (solid curve) energy loss. Left (right) panel corresponds to the RHIC (LHC) conditions. Right panel also contains the D meson R_{AA} data for 0 – 7.5% central 2.76 TeV $Pb + Pb$ collisions at LHC [221, 233] (red triangles). Debye mass is $\mu_E = gT$, coupling constant is $\alpha_s = 0.3$ ($\alpha_s = 0.25$) for RHIC (LHC). QGP medium of a finite size is assumed and no finite magnetic mass effect is taken into account (i.e. $\mu_M = 0$). Figure adapted from [159].

Furthermore, we see that taking into account the collisional contribution leads to total D meson suppression prediction, that is: 1) somewhat less than twofold larger than the same resulting only from dynamical radiative energy loss, 2) quantitatively and qualitatively in a rough agreement with the LHC experimental data (see the right panel of Fig. 5.3). Additionally, in accordance with the first perception (1), we observe that the total suppression is significantly larger than either of the two contributions: radiative alone or collisional alone, which leads to the conclusion that they jointly have to be taken into account for the accurate predictions. This finally resolves the issue of the collisional contribution relevance. With regard to 2), we infer that the dynamical effect is the main/necessary ingredient for the correct description of the jet-medium interactions.

Further on, we consider both radiative and collisional energy loss within dynamical QGP medium.

5.3.4. The importance of LPM effect

Upon establishing that both collisional and radiative energy losses are important, we further address how the finite size (LPM) effect influences them, which is initiated by a commonly held belief that for heavy flavor at RHIC this effect is not important. To this end, in Fig. 5.4, we separately investigate the finite size effect on radiative (the left panels), collisional (the central panels) and total, i.e. radiative + collisional (the right panels) energy loss. The first row in Fig. 5.4 presents transverse momentum dependence of R_{AA} at the RHIC, while the second row of Fig. 5.4 corresponds to suppression predictions at the LHC.

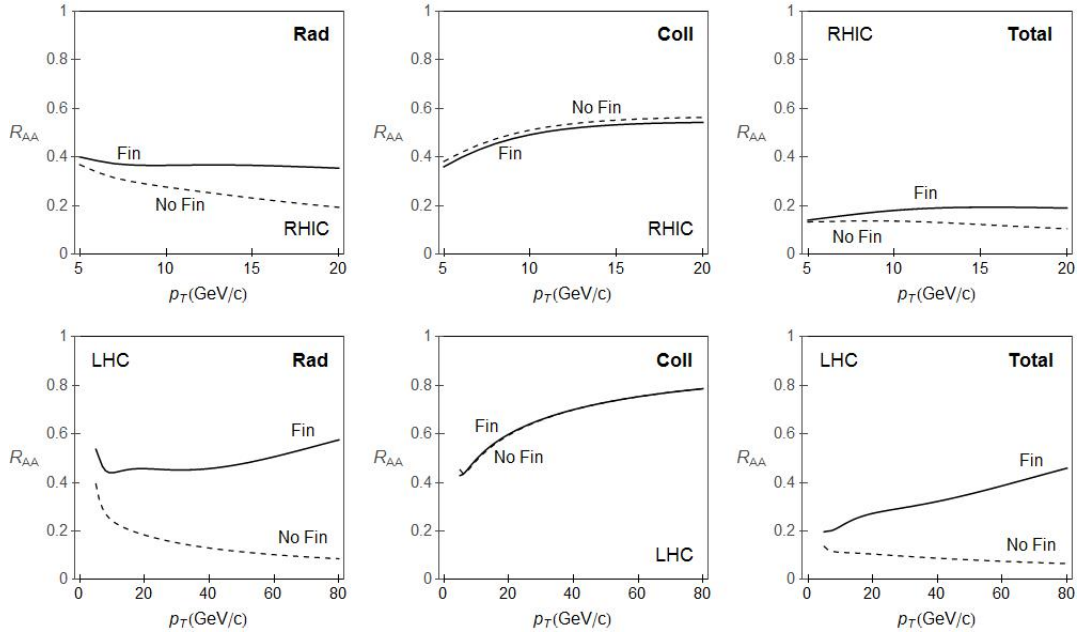


Figure 5.4: Finite size effect on R_{AA} in dynamical formalism. D meson suppression predictions dependence on transverse momentum is plotted with (solid curve) and without (dashed curve) finite size effect included. The first (the second) row corresponds to RHIC (LHC) conditions. Left, central and right column shows, respectively, the finite size effect on radiative, collisional and total (radiative + collisional) energy loss in a dynamical QGP medium. The standard values for the parameters are assumed: Debye mass $\mu_E = gT$, coupling constant $\alpha_s = 0.3$ ($\alpha_s = 0.25$) for RHIC (LHC), whereas no finite magnetic mass effect is included. Figure adapted from [159].

From Fig. 5.4 we observe that for D meson collisional energy loss the finite size effect is indeed negligible at both RHIC and the LHC. However, contrary to the above mentioned expectation, we obtained a substantially different radiative energy loss suppressions with and without finite size effect at both RHIC and LHC, although this difference is larger for LHC conditions. Consequently, the total suppression is significantly altered by abandoning LPM effect, as well. More specifically, we see that neglecting LPM effect can lead to as much as two times larger suppression at RHIC and several times larger suppression at the LHC. Moreover, LPM effect leads not only to quantitatively, but also qualitatively different suppression pattern, since this effect can lead to a decrease - rather than an incorrect increase - of suppression with increasing jet transverse momentum. Taking this into account, we conclude that LPM effect is important ingredient of the energy loss calculations and therefore needs to be included in heavy flavor suppression predictions at both RHIC and the LHC

5.3.5. *The importance of finite magnetic mass and running coupling*

Along the same line of thinking (using the same concept), next we investigate the effects of most recently added: 1) a finite magnetic mass μ_M and 2) running coupling on the suppression predictions, first separately and afterwards jointly. The first step is assessing the significance of including a finite magnetic mass in the radiative energy loss calculations. Namely, consistently with perturbative QCD, all previous energy loss models assumed zero magnetic mass, although the existence of chromo-magnetic, just as chromo-electric, field screening is unambiguous. In favor of this claim, different non-perturbative approaches [199–203] reported a non-zero magnetic mass at RHIC and the LHC. This inevitable indicates that the finite magnetic mass has to be incorporated in the energy loss calculations. Therefore, we consistently included the finite magnetic mass, as determined by lattice QCD [199], in our radiative energy loss calculations through sum-rules [204].

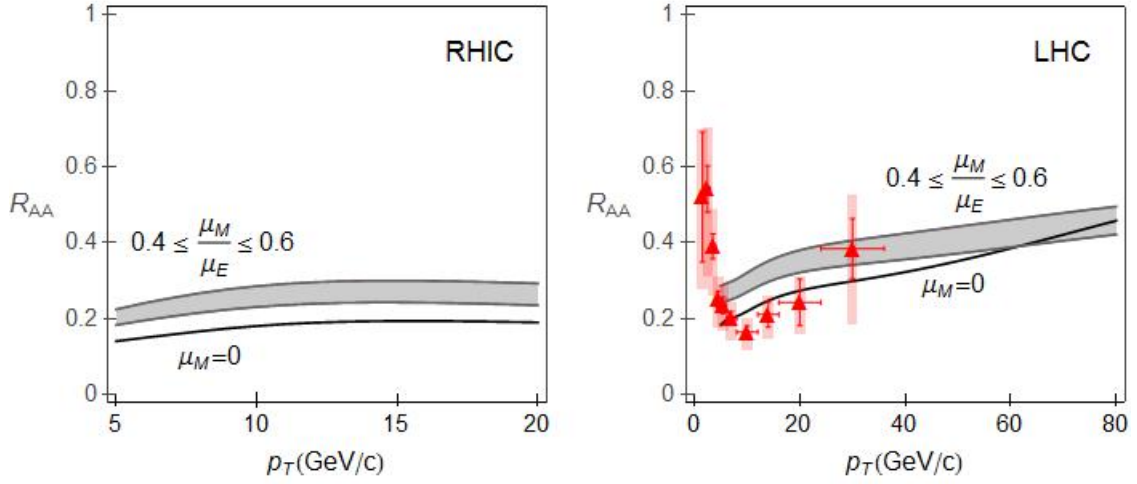


Figure 5.5: Magnetic mass effect on R_{AA} in dynamical formalism. D meson suppression predictions dependence on transverse momentum is shown for (total) radiative + collisional energy loss in dynamical QGP medium of a finite size, with (gray band) and without (solid curve) magnetic mass included. Left (right) panel corresponds to the RHIC (LHC) conditions. Right panel also contains the D meson R_{AA} data for 0 – 7.5% central 2.76 TeV $Pb + Pb$ collisions at LHC [221, 233] (red triangles). Debye mass is $\mu_E = gT$ and coupling constant is $\alpha_s = 0.3$ ($\alpha_s = 0.25$) for RHIC (LHC). Upper (lower) boundary of each band corresponds to $\frac{\mu_M}{\mu_E} = 0.6$ ($\frac{\mu_M}{\mu_E} = 0.4$). Figure adapted from [159].

In order to obtain a quantitative assessment of the importance of a finite magnetic mass introduction, in Fig. 5.5 we compare D meson suppression predictions with and without the finite μ_M . Note that, in this figure we assume a constant strong coupling, and a medium of a finite size. From Fig. 5.5 we infer that the inclusion of the finite magnetic mass *decreases* the suppression by a notable $\sim 30\%$ compared to the case when zero magnetic mass was assumed. Consequently, the finite magnetic mass effect is also important. Additionally, from the comparison of R_{AA} predictions with the available (LHC) experimental data (see the right panel of Fig. 5.5), we observe that the inclusion of magnetic mass leads to somewhat worse agreement with the data, compared to no magnetic mass case.

The second step of the triptych, is investigation of only the running coupling

significance. Therefore, in Fig. 5.6 we compare the D meson suppression predictions obtained by applying the fixed value of strong coupling constant, with the R_{AA} predictions when the running coupling is accounted [208], as a function of the transverse momentum. Note that a finite size medium and zero magnetic mass are assumed.

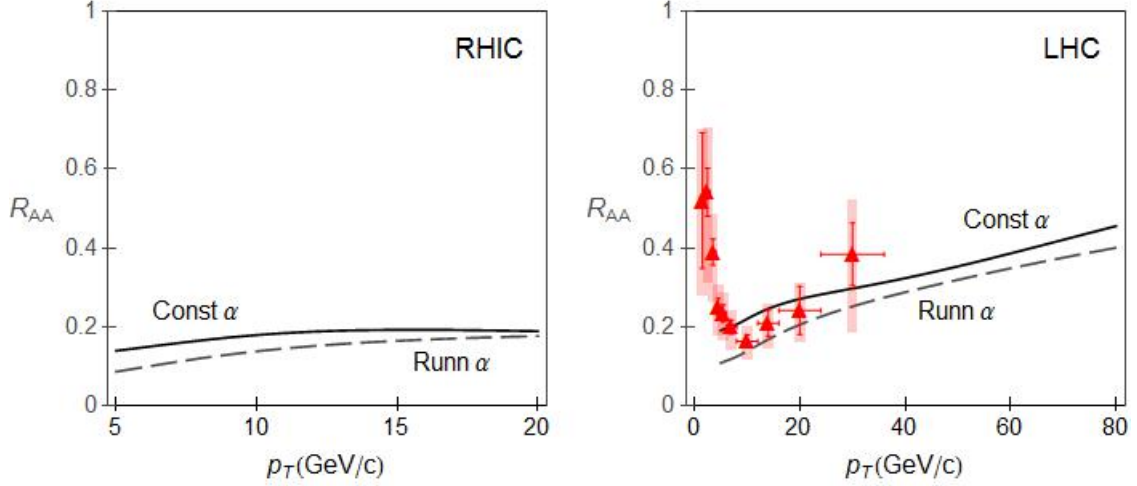


Figure 5.6: Running coupling effect on R_{AA} in dynamical formalism. D meson suppression predictions dependence on transverse momentum is plotted in case of constant coupling $\alpha_s = 0.3$ ($\alpha_s = 0.25$) for RHIC (LHC) (solid curve) and when running coupling (dashed curve) is included. No finite magnetic mass effect is assumed (i.e. $\mu_M = 0$). In both cases radiative + collisional contributions in dynamical QCD medium of a finite size are considered. Left (right) panel corresponds to RHIC (LHC) conditions. Right panel also shows the D meson R_{AA} data for 0 – 7.5% central 2.76 TeV $Pb + Pb$ collisions at LHC [221, 233] (red triangles). Figure adapted from [159].

From Fig. 5.6 we observe that the introduction of the running coupling has an opposite effect on R_{AA} than the effect of the finite magnetic mass, that is, it leads to somewhat less than twofold *increase* in the suppression at lower jet momenta, while it makes no significant difference at higher jet momenta. Notice that such an uneven contribution considerably changes the shape of the curve, which quantifies suppression dependence on transverse momentum. Therefore, the inclusion of the

running coupling for D mesons at both RHIC and the LHC, is also important. Additionally, from comparison of the predictions with the available (LHC) experimental data (see the right panel of Fig. 5.6), we see that the inclusion of running coupling also results in slightly worse agreement with the data (similarly to the inclusion of finite magnetic mass) compared to the predictions with constant strong coupling.

To sum up the findings from Figs. 5.5 and 5.6, the finite magnetic mass and running coupling effects run in the opposite direction, and individually lead to somewhat larger discrepancies between the predictions and experimental data. These two effects present an example, where inclusion of the individual improvements in the energy loss calculations - specifically the magnetic mass alone, or the running coupling alone - does not necessarily lead to the improvement in the reliability of suppression predictions, but would their interplay?

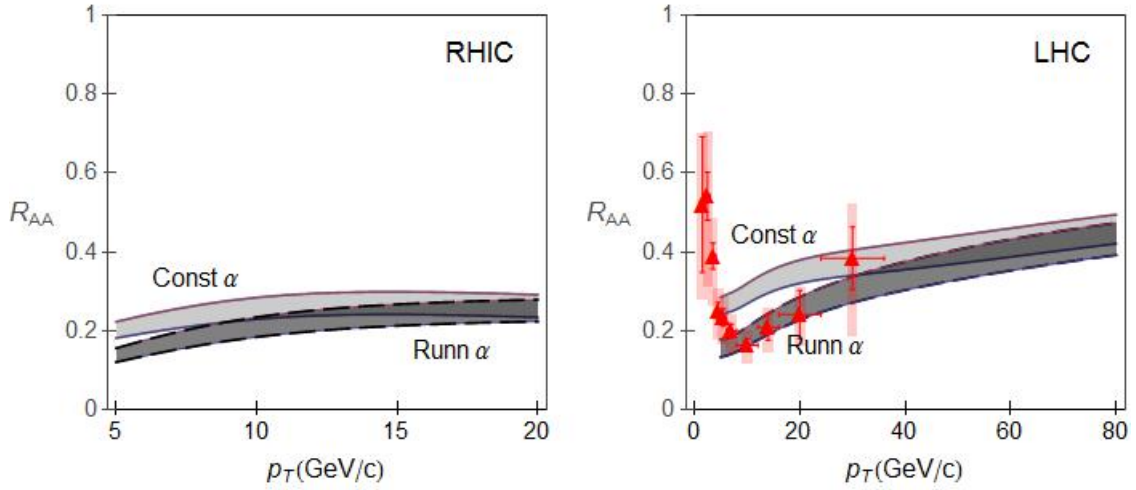


Figure 5.7: Joint effect of magnetic mass and running coupling on R_{AA} . D meson suppression predictions dependence on transverse momentum, with the constant coupling $\alpha_s = 0.3$ ($\alpha_s = 0.25$) for RHIC (LHC) (light gray band) and with the running coupling (dark gray band) accounted. In both cases (total) radiative + collisional contributions in dynamical QGP medium of a finite size are considered. Upper (lower) boundary of each band corresponds to $\frac{\mu_M}{\mu_E} = 0.6$ ($\frac{\mu_M}{\mu_E} = 0.4$). Left (right) panel corresponds to the RHIC (LHC) conditions. Right panel also contains the D meson R_{AA} data for 0–7.5% central 2.76 TeV $Pb+Pb$ collisions at LHC [221, 233] (red triangles). Figure adapted from [159].

This initiates the final figure of this section, where we consider what is the joint effect of including both the running coupling and the magnetic mass on R_{AA} . Therefore, in Fig. 5.7 we assume a finite QGP medium and the finite magnetic mass [204], and compare the D meson suppression predictions considering a fixed value of strong coupling constant, with those when the running coupling is applied, as a function of transverse momentum. Remarkably, from comparison with the available experimental (LHC) data (see the right panel of Fig. 5.7), we observe that these two effects, when taken together, result in a very good agreement with the data. Moreover, the improvement is observed in both quantitative and qualitative domain compared to the case in Fig. 5.3, where both effects are omitted. This illustrates possible synergy in including different energy loss effects: taken individually the finite magnetic mass and the running coupling lead to larger discrepancies between R_{AA} predictions and the experimental data, but taken jointly they notably improve the agreement between suppression predictions and data. Consequently, accounting for all energy losses, relaxing the assumptions in parton energy loss calculations, as well as the inclusion of all important medium effects may be necessary to correctly model the interactions of high p_{\perp} particles with the QGP medium.

5.4. Conclusions

In the previous section we showed that the dynamical energy loss formalism lead to a robust agreement with the experimentally measured nuclear modification factor for different experiments (i.e. collision energies and different colliding systems) [235], probes [208] and experimental conditions (i.e. centrality ranges) [225]. Since our formalism is complex and includes a number of improvements compared to the DGLV formalism, as outlined in subsection 3.1 we wanted to assess how different energy loss effects contribute to such a good agreement. That is, we asked whether there is a single dominant effect, which is responsible for the agreement, or is this agreement a joint effect of several smaller improvements. To answer this question, it would be best to have a probe which is sensitive only to the energy loss, that is, for which the fragmentation and decay functions do not play a role. Therefore, we addressed this issue by using D mesons, whose suppression patterns are not modified

by the fragmentation functions, so that they present a genuine energy loss probe. To that end, we applied a historically driven approach, where we started from the DGLV energy loss model, assuming static QGP medium and which therefore includes only radiative energy loss, and then gradually added different model ingredients on-by-one. The advantage of this approach is that it, apart from assessing the importance of different energy loss effect, also provides a historical perspective on how the energy loss model has been developed.

More specifically, we studied the importance of the transition from the static to the dynamical QGP medium and consequently of including collisional energy loss, the finite size effect, the finite magnetic mass and the running coupling. With the LHC suppression data serving as a baseline, we here showed that, the inclusion of dynamical scattering centers has the largest relative importance in obtaining accurate suppression predictions. Furthermore, we found that all other considered effects are also important and are responsible for the finer agreement with the data. So the good agreement is a result of a superposition of several smaller improvements. Therefore, detailed study of parton's energy loss, as well as the inclusion of all important medium effects is necessary to correctly model the jet-medium interactions.

An interesting side result is that the synergy in including different energy loss effects, in this case a finite magnetic mass and running coupling, may contribute to the better agreement between prediction and data. Namely, taken individually these effects lead to worse agreement with the experimental data, but taken together they notably improve the agreement.

As an outlook, the presented conclusion imply that further improvements of the dynamical energy loss model may contribute to even finer agreement with the data, and also to the accurate predictions outside of the energy ranges and observables (e.g. elliptic flow) that we provided here.

6. RADIATIVE ENERGY LOSS BEYOND SOFT-GLUON APPROXIMATION

The soft-gluon approximation, which assumes that high p_{\perp} parton propagat-

ing through dense QCD matter loses only a small amount of its initial energy via gluon radiation, is a part of many jet-quenching formalisms. Nevertheless, these formalisms predicted a sizable radiative energy loss of high p_{\perp} particles, questioning the approximation reliability and implying necessity of its reconsideration. To address this issue, we relaxed the soft-gluon approximation [248] within (GLV [183]) DGLV [189] formalism to the first order in opacity. We also refer to the extension of this relaxation to the dynamical medium [208], which suggests generality of the conclusions presented here.

6.1. Introduction

One of the most common assumptions in the radiative energy loss calculations of high p_{\perp} parton (in the further text referred to as jet) traversing the QGP medium, is the soft-gluon approximation which assumes that radiated gluon carries away a small fraction of initial jet energy (longitudinal momentum), that is $x = \omega/E \ll 1$, where E denotes the energy of initial jet and ω presents the radiated gluon energy.

Various energy loss models applied this approximation in their calculations, such as: *i*) multiple soft scattering based ASW model [241–243]; *ii*) BDMPS [165, 166] and BDMPS-Z [169, 170]; *iii*) opacity expansion based GLV model [181, 183] and *iv*) multi-gluon evolution based HT approach [244, 245], etc. Since, all these different energy loss models predicted a substantial medium induced radiative energy loss, the legitimacy of the soft-gluon approximation became questionable. In order to address this issue, a finite x (or large x limiting case) was introduced in some of these models [249, 250] or their extensions [251]. Nevertheless, the beyond soft-gluon calculation in these models, did not yield unified conclusion on the importance of relaxing the approximation, but led to different importance estimates, which span from relatively small [251], but noticeable, to moderately large [250].

As mentioned earlier, in the radiative part [196, 198] of our dynamical energy loss formalism [208] the soft-gluon approximation was also employed. In section 4 it was shown that our formalism leads to a robust agreement of angular averaged nuclear modification factor [100, 101] with extensive set of experimental data, in

particular for different beam energies [235, 238], wide diversity of probes (from light to heavy) [208, 235], and all available centrality ranges [225]. Additionally, our formalism was capable of explaining the long-standing heavy-flavor puzzle at both RHIC [235] and LHC [238], and generated credible predictions for future experiments [236, 237]. This might imply the reliability of our energy loss formalism, and consequently the validity of the applied soft-gluon approximation.

Here, it is convenient to recall that our R_{AA} predictions are reliable for p_{\perp} above ≈ 10 GeV. Among the other, the reason for this is that the soft-gluon approximation obviously collapses for intermediate momentum ranges ($5 < p_{\perp} < 10\text{GeV}$), where the experimental data are most abundant and with the smallest error-bars. Furthermore, the approximation is least accurate for gluon radiative energy loss, since due to the color factor of $9/4$ gluons lose significantly more energy compared to quark jets, therefore questioning the adequacy of applying this approximation in such a case. Taken together (and for more precise predictions) these reasons impose necessity of revising the validity of the soft-gluon approximation in dynamical energy loss formalism, by going beyond this approximation.

Along these lines, this section presents our first step toward this goal. Namely, instead of in dynamical medium, we start relaxing the soft-gluon approximation within static QGP medium, i.e. DGLV [189] formalism, which (slightly) reduces the calculation complexity. The revised calculation is done for gluon jets (as they are mostly affected by the approximation) within the pQCD approach for a finite size, optically thin QCD medium, and since being computationally involving it is divided into three stages: *i*) first, the expressions are derived within GLV [183] formalism, i.e. in the simplest case, which assumes massless gluons and medium composed of static scattering centers [161], *ii*) then it is expanded towards the gluons with the effective mass [188], which represents extension of DGLV [189] toward larger energy loss via gluon bremsstrahlung, and *iii*) finally, we discuss generalization of finite x result onto the dynamical medium [208] (i.e. a recoil with the medium constituents is accounted), which is facilitated by the simple mapping rule between static and dynamical medium.

In accordance with [183, 189] the radiative energy loss of gluon jets is calculated to the first order in the number of scattering centers (opacity), where we considered that

the radiation of one gluon is induced by one collisional interaction (i.e. one exchanged gluon) with the medium. Upon assessing the validity of the soft-gluon assumption for gluon jets, the insight will be provided into whether or not radiative energy loss should be generalized onto a finite x for the quark-jets within our formalism as well. In that manner, if the relaxation of the soft-gluon approximation has insignificant effect on gluon-jet radiative energy loss, then one would expect the quark jet to be even less affected, thus making this relaxation in the latter case redundant. Otherwise, if the introduction of a finite x appears to be a significant in gluon-jet case, then the relaxation of the soft-gluon approximation in quark-jet case would also be required, and would represent an important future task.

Another benefit from relaxing the soft-gluon approximation would be broadening the p_{\perp} region of our model [208] applicability, that is its extension towards intermediate momentum region (as stated above).

The sections are organized as follows: In subsection 6.2, we provide the theoretical framework, while subsections starting from 6.3 and ending with 6.5, contain concise description of the computation of gluon-jet radiative energy loss beyond soft-gluon approximation in static QCD medium to: 1) the zeroth order in opacity for both massless and massive gluons; 2) the first order in opacity for massless gluon, and 3) the first order in opacity for gluons with effective mass, as extracted from [188], respectively. As expected, in a limit of very small x , subsections 6.3 to 6.5 recover the corresponding results from [183, 189]. The detailed calculations of the results outlined in these subsections are presented in the Appendices B.4 to B.11.

In subsection 6.6 we compare the numerical estimates based on our beyond soft-gluon calculations for gluon jet with our previous DGLV results [189] (with soft-gluon approximation). More specifically, we assess the effect of finite x on gluon-jet fractional radiative energy loss, mean number of radiated gluons, fractional differential radiative energy loss (intensity spectrum), single gluon radiation spectrum and gluon suppression [90]. Conclusions are presented in subsection 6.7.

6.2. Theoretical framework

As mentioned in subsection 6.1, in this section we concentrate on relaxing soft-gluon approximation in calculating the first order in opacity radiative energy loss of high p_\perp eikonal gluon jets within (GLV) DGLV formalism [183, 189]. That is, we assume that high p_\perp gluon jet is produced inside a "thin" finite QGP medium at some initial point $(t_0, z_0; \mathbf{x}_0)$, that the medium is composed of static scattering centers [161], and that final jet is not significantly deflected from its initial (longitudinal) trajectory. Thus, the jet-static medium interactions are modeled, as in (GLV) DGLV formalism, assuming a static (Debye) colored-screened Yukawa potential [161, 183, 189], given by Eq. (2.2.2), where $T_{a_n}(R)$ now denotes generator in adjoint representation of gluon-jet $SU(N_c = 3)$.

In order to stay consistent with [183, 189], we use the same notation for 4D vectors (e.g. momenta), which is described in more details in Appendix B.1 and proceed throughout using Light-cone coordinates. The same Appendix encloses algebra manipulation and identities for $SU(N_c)$ generators, as well as the Feynman rules, used in the calculations from this section. The approximations that we assume throughout the paper are listed in Appendix B.2.

The small transverse momentum transfer elastic cross section for interaction between gluon jet and target parton according to GW approach [161, 180] is given by Eq. (2.2.4), and now reads:

$$\frac{d\sigma_{el}}{d^2\mathbf{q}_\perp} = \frac{C_2(G)C_2(T)}{d_G} \frac{|v(0, \mathbf{q}_\perp)|^2}{(2\pi)^2}, \quad (6.2.1)$$

where \mathbf{q}_\perp corresponds to transverse momentum of exchanged gluon, C_R is here replaced with $C_2(G)$ Casimir operator in adjoint representation (G) of gluons $SU(N_c = 3)$ with dimension $d_G = 8$, whereas $C_2(T)$ denotes Casimir operator in target (T) representation.

Since (GLV) DGLV formalism assumes optically "thin" plasma, we also expanded our final results in powers of opacity, which may be defined as the mean number of collisions in the medium: $L/\lambda = N\sigma_{el}/A_\perp$ [183], where L is the thickness of the QCD medium, λ is a mean free path, while N denotes the number of scatterers (targets) in transverse area A_\perp . Note that, we restrict our calculations to the first order in opacity, since it was proven [184, 247] to be the dominant term.

To gradually introduce technically demanding beyond soft-gluon calculations, we first concentrate on massless gluons traversing static QCD medium in vacuum

radiation case, then we take into account radiated gluon dispersion relation in QGP medium (i.e. effective gluon mass) and further repeat the procedure when one interaction with the medium constituents is taken into account.

6.3. Zeroth order radiative energy loss

Therefore, we start this subsection with massless gluon case of M_0 Feynman diagram, which corresponds to the source J that produces off-shell gluon with momentum $p + k$, that further, without interactions with QCD medium, radiates on-shell gluon with momentum k and emerges with momentum p (see Fig. 6.1). We will further refer to these two outgoing gluons as the radiated (k) and the final (p) gluon. It is important to notice that, in this and consecutive subsections that involve interactions with one and two scattering centers, we consistently assume that initial jet propagates along the longitudinal z axis. The detailed calculation of M_0 for finite x in massless case is given in Appendix B.4, while all assumptions are stated in Appendix B.2.

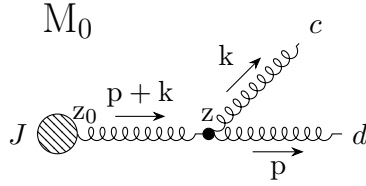


Figure 6.1: Zeroth order diagram that includes no interaction with the QCD medium, and contributes to gluon radiation amplitude to the 1st order in opacity. The dashed circle represents the source J , which at longitudinal coordinate z_0 produces an off-shell gluon jet, propagating along z -axis. z denotes longitudinal coordinate at which the gluon is radiated. k denotes 4-momentum of the radiated gluon carrying the color c , and p denotes 4-momentum of the final gluon jet carrying the color d .

Consistently with DGLV, we also assume that external gluons are transversely polarized particles and although we work in covariant gauge, we can choose any polarization vector for the external on-shell gluons [251, 252], so in accordance with [183, 189, 251, 252] we choose $n^\mu = [0, 2, \mathbf{0}]$ (i.e. $\epsilon(k) \cdot k = 0$, $\epsilon(k) \cdot n = 0$

and $\epsilon(p) \cdot p = 0$, $\epsilon(p) \cdot n = 0$). Likewise, we assume that the off-shell $p + k$ gluon has also the physical polarization as real gluons [251, 252] (i.e. $\epsilon(p + k) \cdot (p + k) = 0$, $\epsilon(p + k) \cdot n = 0$). Thus, the massless gluon momenta acquire the form:

$$p + k = [E^+, E^-, \mathbf{0}], \quad k = [xE^+, \frac{\mathbf{k}^2}{xE^+}, \mathbf{k}], \quad p = [(1-x)E^+, \frac{\mathbf{p}^2}{(1-x)E^+}, \mathbf{p}], \quad (6.3.1)$$

where $E^+ = p^0 + k^0 + p_z + k_z$, $E^- = p^0 + k^0 - p_z - k_z$ and due to 4-momentum conservation:

$$\mathbf{p} + \mathbf{k} = 0. \quad (6.3.2)$$

The polarization vectors are given by:

$$\epsilon_i(k) = [0, \frac{2\epsilon_i \cdot \mathbf{k}}{xE^+}, \epsilon_i], \quad \epsilon_i(p) = [0, \frac{2\epsilon_i \cdot \mathbf{p}}{(1-x)E^+}, \epsilon_i], \quad \epsilon_i(p+k) = [0, 0, \epsilon_i], \quad (6.3.3)$$

where $i = 1, 2$, and we also make use of Eq. (6.3.2). Thus, the amplitude that gluon jet, produced at x_0 inside QCD medium, radiates a gluon of color c without final state interactions reads:

$$M_0 = J_a(p+k) e^{i(p+k)x_0} (-2ig_s)(1-x+x^2) \frac{\epsilon \cdot \mathbf{k}}{\mathbf{k}^2} (T^c)_{da}. \quad (6.3.4)$$

The radiation spectrum is obtained when Eq. (6.3.4) is substituted in:

$$d^3 N_g^{(0)} d^3 N_J \approx \text{Tr} \langle |M_0|^2 \rangle \frac{d^3 \vec{\mathbf{p}}}{(2\pi)^3 2p^0} \frac{d^3 \vec{\mathbf{k}}}{(2\pi)^3 2\omega}, \quad (6.3.5)$$

where $\omega = k_0$, and where $d^3 N_J$ reads:

$$d^3 N_J = d_G |J(p+k)|^2 \frac{d^3 \vec{\mathbf{p}}_J}{(2\pi)^3 2E_J}. \quad (6.3.6)$$

Here $E_J = E = p_0 + k_0$ and $\vec{\mathbf{p}}_J$ denotes energy and 3D momentum of the initial gluon jet, respectively. Note that, E retains the same expression throughout the manuscript (even when interactions with one and two scatterers are accounted).

The jet part can be decoupled by using the equality:

$$\frac{d^3 \vec{\mathbf{p}}}{(2\pi)^3 2p^0} \frac{d^3 \vec{\mathbf{k}}}{(2\pi)^3 2\omega} = \frac{d^3 \vec{\mathbf{p}}_J}{(2\pi)^3 2E_J} \frac{dx d^2 \mathbf{k}}{(2\pi)^3 2x(1-x)}, \quad (6.3.7)$$

which is obtained by substituting $p_z, k_z \rightarrow p_z^J, xE$. Finally, energy spectrum is given by:

$$\frac{xd^3N_g^{(0)}}{dx d\mathbf{k}^2} = \frac{\alpha_s C_2(G)}{\pi \mathbf{k}^2} \frac{(1-x+x^2)^2}{1-x}, \quad (6.3.8)$$

which reproduces the well-known Altarelli-Parisi [68] result.

Next we concentrate on obtaining energy spectrum expression in finite temperature QCD medium. In contrast to the previous case, where gluons are treated as massless particles, note that in finite temperature QGP they obey different dispersion relation and apart from transverse, they also have longitudinal polarization (as previously discussed). In static medium case formally this does not concern exchanged gluon. Luckily, in [188] it was shown that radiated gluons in finite temperature QGP can be approximated as a massive transversely polarized plasmons with mass $m_g = \mu_E/\sqrt{2}$, where μ_E is the Debye mass. In this case, M_0 amplitude becomes:

$$M_0 = J_a(p+k)e^{i(p+k)x_0}(-2ig_s)(1-x+x^2)\frac{\boldsymbol{\epsilon} \cdot \mathbf{k}}{\mathbf{k}^2 + m_g^2(1-x+x^2)}(T^c)_{da}, \quad (6.3.9)$$

leading to:

$$\frac{xd^3N_g^{(0)}}{dx d\mathbf{k}^2} = \frac{\alpha_s}{\pi} \frac{C_2(G) \mathbf{k}^2}{(\mathbf{k}^2 + m_g^2(1-x+x^2))^2} \frac{(1-x+x^2)^2}{1-x}. \quad (6.3.10)$$

6.4. First order radiative energy loss in massless case

Starting point for obtaining the expression for the first order in opacity radiative energy loss of gluon jet for finite x , in accordance with [189], presents:

$$d^3N_g^{(1)}d^3N_J = \left(\frac{1}{d_T} \text{Tr} \langle |M_1|^2 \rangle + \frac{2}{d_T} \text{Re} \text{Tr} \langle M_2 M_0^* \rangle \right) \frac{d^3\vec{\mathbf{p}}}{(2\pi)^3 2p^0} \frac{d^3\vec{\mathbf{k}}}{(2\pi)^3 2\omega}, \quad (6.4.1)$$

where M_0 corresponds to the diagram without final state interactions with QCD medium, introduced in previous subsection, M_1 represents the sum of all diagrams with one scattering center (see the representative in the left panel of Fig. 6.2), M_2 is the sum of all diagrams with two scattering centers (see the representative in the right panel of Fig. 6.2) in the contact-limit case ($z_1 = z_2$), while d_T denotes the

dimension of the target color representation (for pure gluon medium $d_T = 8$). For obtaining differential energy loss expression, we again substitute Eqs. (6.3.6, 6.3.7) in Eq. (6.4.1).

Since we consistently assume that initial jet propagates along z -axis, the momenta acquire the following form in the two cases stated below:

1. One interaction with QGP medium (M_1):

$$p + k - q_1 = [E^+ - q_{1z}, E^- + q_{1z}, \mathbf{0}], \quad (6.4.2)$$

where $p + k - q_1$ corresponds to the initial jet, while k and p retain the same expressions as in Eq. (6.3.1), with the distinction that now $\mathbf{p} \neq -\mathbf{k}$, since due to energy and momentum conservation, the following relation holds:

$$\mathbf{q}_1 = \mathbf{p} + \mathbf{k}; \quad (6.4.3)$$

Exchanged gluon momentum is $q_1 = [[q_{az}, -q_{1z}, \mathbf{q}_1]]$, where $q_1^0 = 0$, due to static potential. The remaining notation is the same as in Eq. (6.3.1).

2. Two interactions with QGP medium (M_2):

$$p + k - q_1 - q_2 = [E^+ - q_{1z} - q_{2z}, E^- + q_{1z} + q_{2z}, \mathbf{0}], \quad (6.4.4)$$

where $p + k - q_1 - q_2$ corresponds to the initial jet and $q_i = [q_{iz}, -q_{iz}, \mathbf{q}_i]$ to exchanged gluons, $i = 1, 2$ with $q_i^0 = 0$, while p, k retain the same expressions as in Eq. (6.3.1). Also, due to 4-momentum conservation, the following relation between gluon transverse momenta holds:

$$\mathbf{p} + \mathbf{k} = \mathbf{q}_1 + \mathbf{q}_2, \quad (6.4.5)$$

which in the contact-limit case (when $\mathbf{q}_1 + \mathbf{q}_2 = 0$) becomes $\mathbf{p} + \mathbf{k} = 0$, as in M_0 case.

Note that Eq. (6.4.3) has to be satisfied for M_1 diagrams in order to claim that initial jet propagates along z -axis, i.e. for M_1 diagrams $\mathbf{p} + \mathbf{k}$ is different from 0. This is an important distinction between the calculations presented here, and the calculations done within SCET formalism (see e.g. [251, 252]), where $\mathbf{p} + \mathbf{k} = 0$ was

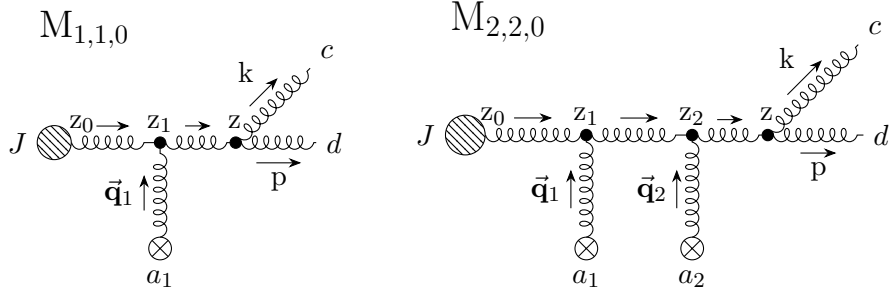


Figure 6.2: Representative diagrams that include interaction with the QCD medium, and potentially contribute to gluon radiation amplitude to the 1^{st} order in opacity. The left panel corresponds to one interaction with QGP medium, while the right panel corresponds to two interactions with the medium, which only in contact-limit ($z_1 = z_2$) case contributes to the 1^{st} order emission spectrum (for more details see Appendices B.6 to B.9). z_i , where $i = 1, (2)$, denotes longitudinal coordinate of the interactions with the consecutive scattering centers. Crossed circles represent scatterers that exchange transverse momentum \vec{q}_i with the jet. Remaining labeling is the same as in Fig. 6.1.

used in calculating *both* M_1 and M_2 diagrams, though the assumption of initial jet propagating along z -axis was used in that study as well.

It is straightforward to show that transverse polarization vectors $\epsilon_i(k)$ and $\epsilon_i(p)$ for both: M_1 and M_2 amplitudes are given by the same expression as in the previous section (but note that in M_1 case: $\mathbf{p} \neq -\mathbf{k}$, as discussed above), while ϵ for initial jets consistently has the same form as in Eq. (6.3.3), that is, for M_1 amplitudes $\epsilon_i(p + k - q_1) = [0, 0, \epsilon_i]$, and for M_2 amplitudes $\epsilon_i(p + k - q_1 - q_2) = [0, 0, \epsilon_i]$.

Here we omitted the expressions for the remaining 10 Feynman diagrams, which contribute to the first order in opacity radiative energy loss. Their numeration as well as their number is explained in Appendix B.3, whereas the thorough calculation of each individual diagram under the same approximations as for M_0 (given in Appendix B.2), is provided in Appendices B.5-B.9. The detailed derivation of the single gluon radiation spectrum beyond soft-gluon approximation in massless case is given in Appendix B.10 and reads:

$$\begin{aligned}
\frac{dN_g^{(1)}}{dx} &= \frac{C_2(G)\alpha_s}{\pi} \frac{L}{\lambda} \frac{(1-x+x^2)^2}{x(1-x)} \int \frac{d^2\mathbf{q}_1}{\pi} \frac{\mu_E^2}{(\mathbf{q}_1^2 + \mu_E^2)^2} \int d\mathbf{k}^2 \\
&\times \left\{ \frac{(\mathbf{k} - \mathbf{q}_1)^2}{\left(\frac{4x(1-x)E}{L}\right)^2 + (\mathbf{k} - \mathbf{q}_1)^4} \left(2 - \frac{\mathbf{k} \cdot (\mathbf{k} - \mathbf{q}_1)}{\mathbf{k}^2} - \frac{(\mathbf{k} - \mathbf{q}_1) \cdot (\mathbf{k} - x\mathbf{q}_1)}{(\mathbf{k} - x\mathbf{q}_1)^2} \right) \right. \\
&\left. + \frac{\mathbf{k}^2}{\left(\frac{4x(1-x)E}{L}\right)^2 + \mathbf{k}^4} \left(1 - \frac{\mathbf{k} \cdot (\mathbf{k} - x\mathbf{q}_1)}{(\mathbf{k} - x\mathbf{q}_1)^2} \right) + \left(\frac{1}{(\mathbf{k} - x\mathbf{q}_1)^2} - \frac{1}{\mathbf{k}^2} \right) \right\}, \quad (6.4.6)
\end{aligned}$$

where we assumed a simple exponential distribution $\frac{2}{L}e^{-\frac{2\Delta z}{L}}$ of longitudinal distance between the gluon-jet production site and target rescattering site, emerging as $\left(\frac{4x(1-x)E}{L}\right)^2$ in the denominators of the integrand. This steep longitudinal distance distribution was chosen, as, among other things, it facilitates the calculations and also mimics rapidly expanding medium. However, the main reason of such a choice was the demand for recovering (GLV) DGLV results for $x \ll 1$, knowing that the predecessors of calculations presented here, i.e. (GLV) DGLV also employed this distribution [181, 182, 184, 189]. To this end, note that, Eq. (6.4.6) reduces to massless case of Eq. (11) from [189] in the soft-gluon limit (i.e. limit of Eq. (2.2.8)), as expected. Note that energy loss expression can be straightforwardly extracted by using this simple relation: $dE^{(1)}/dx \equiv \omega dN_g^{(1)}/dx \approx xEdN_g^{(1)}/dx$.

We also tested the robustness of all results from this manuscript to the longitudinal distance distribution. To this end, we assumed the opposite limit - the uniform distribution (as done in [208]). The obtained same results with the respect to the importance of soft-gluon approximation implied that conclusions presented in this section are robust to the presumed longitudinal distance distribution (see Fig. 6.7).

Additionally, it is straightforward to show that Eq. (6.4.6) is symmetric under the exchange of radiated (k) and final (p) gluon, as expected beyond soft-gluon approximation, and due to inability to distinguish between these two identical gluons.

6.5. Radiative energy loss in finite temperature QGP

Finally, we concentrate on more realistic approach, by acknowledging that medium created in ultra-relativistic HIC has finite temperature T , which modifies the self energies of gluons embedded in such medium, and thus could have

significant impact on gluon's radiative energy loss. Therefore for more accurate calculations beyond soft gluon approximation it became essential to include finite temperature effects. To this end, we recall that in [188], it was shown that gluons with the hard momenta $k \gtrsim T$ can be approximated as massive transverse plasmons with effective mass $m_g = m_\infty = \sqrt{\Pi_T(p_0/|\vec{\mathbf{p}}| = 1)} = \mu_E/\sqrt{2}$ equal to its asymptotic value, which represents non-abelian QCD analogon of Ter-Mikayelian plasmon effect [185, 186] on radiative energy loss in finite temperature QCD medium (within HTL approach [187]), which was already mentioned in subsection 2.2.2. This subsection is dedicated to incorporating finite temperature effects in our calculations.

The assumption of initial jet propagating along z -axis, for massive case, leads to the following form of momenta, in the same three cases considered in the previous subsection:

1. No interaction with QGP medium (M_0):

$$p + k = [E^+, E^-, \mathbf{0}], \quad k = [xE^+, \frac{\mathbf{k}^2 + m_g^2}{xE^+}, \mathbf{k}], \quad p = [(1-x)E^+, \frac{\mathbf{p}^2 + m_g^2}{(1-x)E^+}, \mathbf{p}], \quad (6.5.1)$$

where due to energy and momentum conservation Eq. (6.3.2) holds. Note that throughout this section, the only formal difference in p and k expressions compared to the massless case (see Eq. (6.3.1)) is additional $+m_g^2$ term in numerator of minus Light cone coordinate.

2. One interaction with QGP medium (M_1):

k and p retain the same expressions as in Eq. (6.5.1), with addition that (as in the previous section) Eq. (6.4.3) holds due to conservation of 4-momentum, while initial jet has the momentum of the same form as in Eq. (6.4.2). That is, again $\mathbf{p} \neq -\mathbf{k}$ holds for M_1 diagrams.

3. Two interactions with QGP medium (M_2):

p , k have the same expressions as in Eq. (6.5.1). Also, due to 4-momentum conservation Eq. (6.4.5) holds and in the contact-limit case reduces to $\mathbf{p} + \mathbf{k} = 0$, while initial jet momentum has the same form as in Eq. (6.4.4).

The transverse polarization vectors remain the same as in the massless case.

The calculations are performed under the same approximations, which are legibly outlined in Appendix B.2, as in massless case. We here display only the final result of single gluon radiation spectrum, for which we needed to recalculate the same 11 diagrams from Appendices B.4 to B.9, also beyond soft-gluon approximation. The overview of all intermediate results is contained in Appendix B.11. In that manner obtained $\frac{dN_g^{(1)}}{dx}$ has more involved form than the one in massless case (Eq. (6.4.6)), and reads:

$$\begin{aligned} \frac{dN_g^{(1)}}{dx} = & \frac{C_2(G)\alpha_s L}{\pi \lambda} \frac{(1-x+x^2)^2}{x(1-x)} \int \frac{d^2\mathbf{q}_1}{\pi} \frac{\mu_E^2}{(\mathbf{q}_1^2 + \mu_E^2)^2} \int d\mathbf{k}^2 \\ & \times \left\{ \frac{(\mathbf{k} - \mathbf{q}_1)^2 + \chi}{\left(\frac{4x(1-x)E}{L}\right)^2 + ((\mathbf{k} - \mathbf{q}_1)^2 + \chi)^2} \left(2 \frac{(\mathbf{k} - \mathbf{q}_1)^2}{(\mathbf{k} - \mathbf{q}_1)^2 + \chi} - \frac{\mathbf{k} \cdot (\mathbf{k} - \mathbf{q}_1)}{\mathbf{k}^2 + \chi} \right. \right. \\ & \left. \left. - \frac{(\mathbf{k} - \mathbf{q}_1) \cdot (\mathbf{k} - x\mathbf{q}_1)}{(\mathbf{k} - x\mathbf{q}_1)^2 + \chi} \right) + \frac{\mathbf{k}^2 + \chi}{\left(\frac{4x(1-x)E}{L}\right)^2 + (\mathbf{k}^2 + \chi)^2} \left(\frac{\mathbf{k}^2}{\mathbf{k}^2 + \chi} - \frac{\mathbf{k} \cdot (\mathbf{k} - x\mathbf{q}_1)}{(\mathbf{k} - x\mathbf{q}_1)^2 + \chi} \right) \right. \\ & \left. + \left(\frac{(\mathbf{k} - x\mathbf{q}_1)^2}{((\mathbf{k} - x\mathbf{q}_1)^2 + \chi)^2} - \frac{\mathbf{k}^2}{(\mathbf{k}^2 + \chi)^2} \right) \right\}, \end{aligned} \quad (6.5.2)$$

where $\chi = m_g^2(1-x+x^2)$. In generating the above expression, again we applied the same exponential distribution of longitudinal distance between jet production and interaction with medium constituent sites, as done in the previous subsection. It can easily be verified that, in the soft-gluon limit, we recover Eq. (11) from [189], i.e. Eq. (2.2.8) (note that for gluon jet $M \equiv m_g$, so that the term M^2x^2 from [189] is also negligible), and that in the massless limit Eq. (6.5.2) reduces to our Eq. (6.4.6).

This result, to our knowledge, presents the introduction of effective gluon mass (jet mass) in beyond-soft-gluon-approximation radiative energy loss calculations for the first time. Additionally, we again validated that single gluon radiation spectrum is symmetric to substitution of p and k gluons, as necessary (see the previous section and Appendix B.11). The most striking observation is that the analytical $\frac{dN_g^{(1)}}{dx}$ expressions differ notably in beyond-soft-gluon and soft-gluon cases (compare Eq. (6.5.2) and Eq. (11) from [189]). In the next subsection, we will evaluate the extent of numerical differences that these two different analytical expressions induce.

More precisely, we are mostly interested in how the inclusion of finite x affects gluon fractional radiative energy loss ($\frac{\Delta E^{(1)}}{E}$), mean number of radiated gluons ($N_g^{(1)}$) and the suppression (R_{AA}). We accordingly note that $\frac{dE^{(1)}}{dx} \equiv \omega \frac{dN_g^{(1)}}{dx} \approx xE \frac{dN_g^{(1)}}{dx}$

from which we can further straightforwardly numerically evaluate $\frac{\Delta E^{(1)}}{E}$, as well as the mean number of radiated gluons ($N_g^{(1)}$).

6.6. Numerical results

This subsection contains comparison of numerical predictions based on the calculations presented in this section with the corresponding soft-gluon predictions [189], to assess how the relaxation of soft-gluon approximation modifies gluon-jet energy loss to the 1st order in opacity. The predictions are generated for gluons with effective mass $m_g = \mu_E/\sqrt{2}$, where $\mu_E = \sqrt{4\pi\alpha_s(1 + n_f/6)}T$ is Debye mass, and $n_f = 3$ is the number of the effective light-quark flavors. For all figures, we use the following set of parameters: constant $\alpha_s = \frac{g_s^2}{4\pi} = 0.3$, $L = 5$ fm, $\lambda = 1$ fm and $T = 300$ MeV, to mimic standard LHC conditions. Note that for gluons considered in this section, their energy is approximately equal to their momentum, due to negligible effective gluon mass compared to momentum, and in this sense we use p_\perp throughout this subsection.

First we investigate the effect on the fractional radiative energy loss $\frac{\Delta E^{(1)}}{E}$. To this end, the top left panel of Fig. 6.3 presents comparison of $\frac{\Delta E^{(1)}}{E}$, for calculations beyond the soft-gluon approximation, and with the soft-gluon approximation, as a function of initial jet transverse momentum (p_\perp). In particular, the curve corresponding to beyond soft-gluon approximation (*bsg*) case is obtained from Eq. (6.5.2) multiplied by and integrated over x , while the curve corresponding to soft-gluon approximation (*sg*) case is obtained by numerically integrating Eq. (11) from [189] (Eq. (2.2.8)). These two curves almost overlap, even converge towards one another with increasing p_\perp . Note that, the upper limit of x integration is equal to 1/2 instead of 1, in order to avoid double counting. The upper integration limits for $|\mathbf{k}|$ and $|\mathbf{q}_1|$, determined kinematically, are $2x(1-x)E$ and $\sqrt{4ET}$, respectively [189].

The bottom left panel of Fig. 6.3 shows comparison of the mean number of radiated gluons in *bsg* and *sg* cases. Similarly to the previous variable, these two curves practically overlap as well, with a slight disagreement at higher p_\perp .

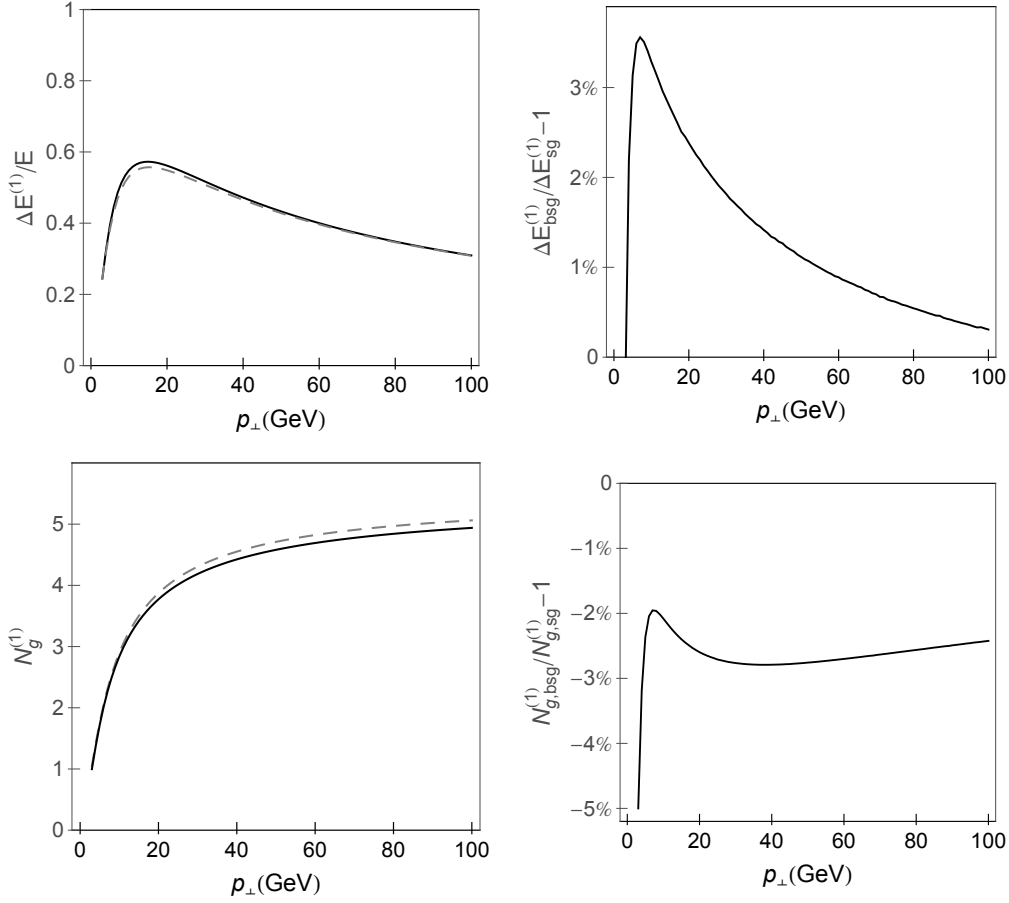


Figure 6.3: Integrated variables: Effect of relaxing soft-gluon approximation to the 1^{st} order in opacity of DGLV formalism, as a function of p_{\perp} . The top left panel compares gluon fractional radiative energy loss without (the solid curve) and with (the dashed curve) the soft-gluon approximation. The top right panel quantifies the effect of relaxing the soft-gluon approximation on $\frac{\Delta E^{(1)}}{E}$ and expresses it in percentage. The bottom left panel compares number of radiated gluons without (the solid curve) and with (the dashed curve) soft-gluon approximation, whereas the bottom right panel shows the relative change in this number with respect to soft-gluon limit. Figure adapted from [248].

Quantitative assessment of relaxing the soft-gluon approximation on these two variables is provided in two right panels of Fig. 6.3. We observe that finite values of x slightly *increase* fractional radiative energy loss by maximum of $\approx 3\%$ up to $p_{\perp} \approx 10$ GeV compared to *sg* case. Thereupon, the difference between *bsg* and *sg* $\frac{\Delta E^{(1)}}{E}$ steeply dies away. On the other hand, finite x *decreases* mean number of

radiated gluons also for a small amount (up to 5%) compared to sg case for very low transverse momenta. Further the relative difference reaches a peak of -2% also at $p_{\perp} \approx 10$ GeV, and for higher transverse momenta remains nearly constant somewhat below -2% . Consequently, the overall conclusion from Fig. 6.3 is that the effect on both variables is small (few percents) and with opposite signs.

Next we assess the finite x effect on two differential variables: the fractional differential radiative energy loss ($\frac{1}{E} \frac{dE^{(1)}}{dx} = x \frac{dN_g^{(1)}}{dx}$) and on single gluon radiation spectrum ($\frac{dN_g^{(1)}}{dx}$) and its relative change. These effects are plotted against x (see Fig. 6.4) for different values of initial jet transverse momentum p_{\perp} . Technical details are as follows: bsg curves for $\frac{1}{E} \frac{dE^{(1)}}{dx}$ are obtained from Eq. (6.5.2) multiplied by x , whereas sg curves correspond to Eq. (11) in [189] (Eq. (2.2.8)). We observe two x regions in Fig. 6.4: the lower region $x \lesssim 0.3$ (that goes roughly up to 0.4) where bsg and sg curves barely differ (for only few percents, max up to 10%), as expected; and the higher region $0.4 < x \leq 0.5$, where the discrepancies between our bsg fractional differential radiative energy loss and previously obtained sg [189] rise to notable values ($\sim 50\%$) and increase with enhancing p_{\perp} . We also recognize $x \approx 0.3$ as a "cross-over" value, below which fractional differential radiative energy loss and single gluon radiation spectrum are somewhat lower in bsg compared to sg case, and above which the opposite is true.

We further address the effect of relaxing the soft-gluon approximation on the single gluon radiation spectrum by adding the third column in Fig. 6.4 (see also Fig. 6.5), showing percentage of $\frac{dN_g^{(1)}}{dx}$ change. In accordance with the above discussion over $\frac{1}{E} \frac{dE^{(1)}}{dx}$, this plot provides quantitative estimation of difference smaller than 10% for $x \lesssim 0.4$. Additionally, at higher x values, there is a notably larger spectra in bsg compared to sg case, and this difference ascends (up to 60% at $p_{\perp} = 50$ GeV) with increasing p_{\perp} .

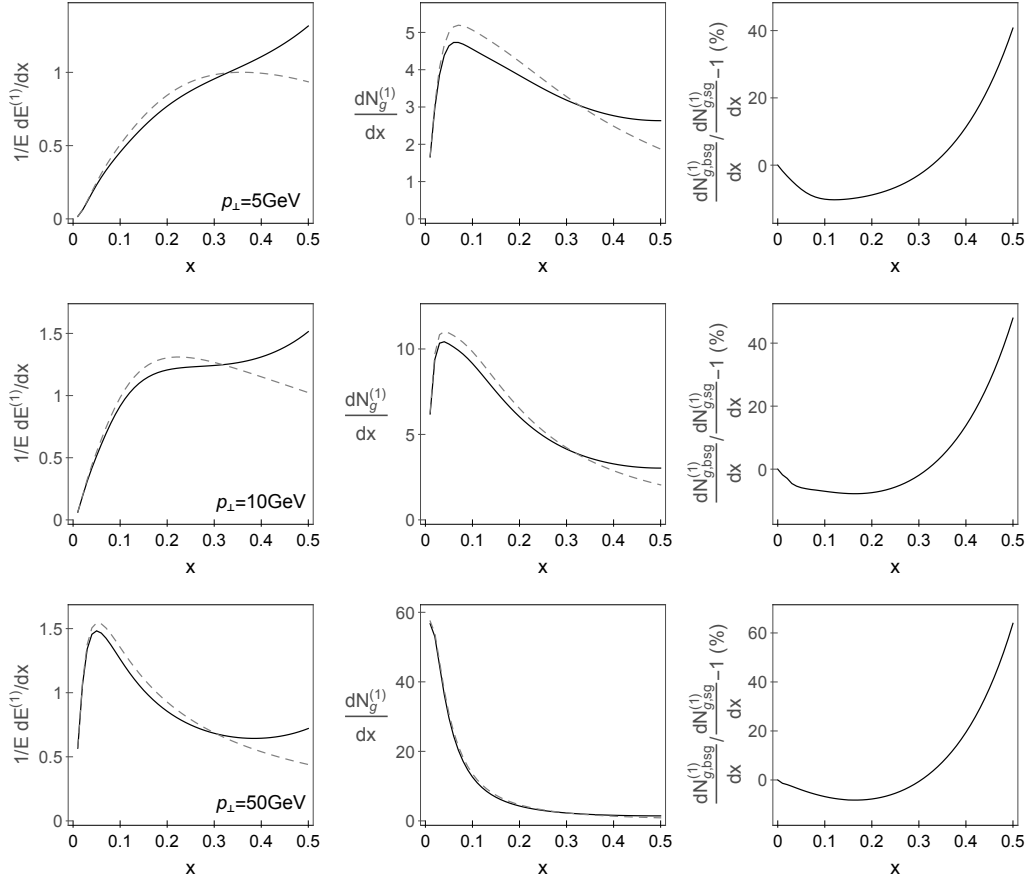


Figure 6.4: Differential variables: Effect of relaxing soft-gluon approximation to the 1^{st} order in opacity of DGLV formalism, as a function of x . The comparison of bsg (the solid curve) and sg (the dashed curve) fractional differential gluon radiative energy loss ($\frac{1}{E} \frac{dE^{(1)}}{dx}$) for different values of initial jet p_{\perp} (5 GeV, 10 GeV, 50 GeV, as indicated in the lower right corner of panels) is presented in the first column. The second column shows comparison of bsg (the solid curve) and sg (the dashed curve) single gluon radiation (spectrum) distribution in momentum fraction ($\frac{dN_g^{(1)}}{dx}$) for the same values of p_{\perp} , as in the first column. The relative change of the single gluon radiation spectrum when the soft-gluon approximation is relaxed with respect to the soft-gluon limit is presented in the third column. Figure adapted from [248].

In order to investigate the effect of finite x on single gluon radiation spectrum for different transverse momentum values of initial gluon jet in more detail, Fig. 6.5 is plotted. We observe that an evident, that is, tenfold increase of p_{\perp} leads to a

modest increase (less than 25%) of $\frac{dN_g^{(1)}}{dx}$ in *bsg* compared to *sg* case. Note that the same conclusion applies for $(\frac{1}{E} \frac{dE_{bsg}^{(1)}}{dx}) / (\frac{1}{E} \frac{dE_{sg}^{(1)}}{dx}) - 1$, since $\frac{1}{E} \frac{dE^{(1)}}{dx} = x \frac{dN_g^{(1)}}{dx}$ so that x cancels when taking the relative ratio. Therefore, we infer that the relaxation of the soft-gluon approximation has nearly the same effect on $\frac{dN_g^{(1)}}{dx}$ and $\frac{1}{E} \frac{dE^{(1)}}{dx}$ across the whole x region independently on p_\perp of the initial jet.

So far, we demonstrated that relaxing the soft-gluon approximation has small numerical effect on: 1) integrated variables, such as $\frac{\Delta E^{(1)}}{E}$, $N_g^{(1)}$, across the whole x region; and 2) differential variables, such as $\frac{1}{E} \frac{dE^{(1)}}{dx}$, $\frac{dN_g^{(1)}}{dx}$, up to $x \approx 0.4$. However, the difference between *bsg* and *sg* cases can run in opposite directions (for $\frac{\Delta E^{(1)}}{E}$, $N_g^{(1)}$), then can ascend to 10% and moreover can be quite large for $x > 0.4$ (e.g. for $\frac{1}{E} \frac{dE^{(1)}}{dx}$, $\frac{dN_g^{(1)}}{dx}$). This, therefore, invokes a question of what is the impact of relaxing the soft-gluon approximation on predictions for measured observables, such as the angular averaged nuclear modification factor R_{AA} [100, 101]. Comparing R_{AA} in *bsg* and *sg* cases provides an insight into how adequate is this approximation in obtaining reliable numerical predictions.

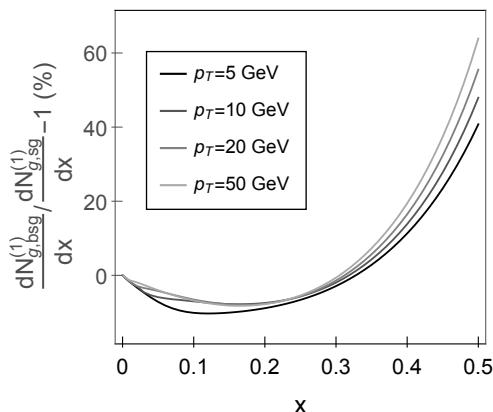


Figure 6.5: Relative change of single gluon radiation distribution in momentum fraction in *bsg* compared to *sg* case for different p_\perp values. The percentage of $\frac{dN_g^{(1)}}{dx}$ change when soft-gluon approximation is relaxed with respect to *sg* case, calculated to the 1st order in opacity of DGLV formalism, for different values of initial transverse momentum (as indicated in the legend) is plotted as a function of x . The curves fade as transverse momentum increases. Figure adapted from [248].

To that end, we next generate the predictions for bare gluon R_{AA} , based only

on radiative energy loss, with and without soft-gluon approximation. The nuclear modification factor is defined as usual by the normalized ratio of the quenched $A+A$ spectrum to the $p+p$ spectrum, and given by Eq. (1.4.5), while in obtaining the gluon quenched spectra the generic pQCD convolution formula is applied (Eq. (3.2.1)) in its reduced form, i.e. Eq. (5.2.1) (see also descriptive Fig. 3.2). Note that we omitted fragmentation and decay functions, as we are considering the parton quenching, because we are primarily interested in how the relaxation of the soft-gluon approximation in energy loss affects R_{AA} . Afterwards, we also assess how the initial gluon distribution affects R_{AA} .

Here the initial gluon spectrum is computed according to [212], while $P(E_i \rightarrow E_f)$ denotes radiative energy loss probability, which includes multi-gluon [184] and path-length [190] fluctuations. The multi-gluon fluctuations are introduced, in accordance with [184], under the assumption that the fluctuations of the gluon number are uncorrelated, and therefore presented via Poisson distribution. Specifically, the energy loss probability takes into account that the jet, during its propagation through QGP, can independently radiate number of gluons (for more details on the implementation procedure, please see ref. [184], as well as section 3.2). The path length distributions are implemented as described in [100]. For more detailed explanation of how the path-length fluctuations are calculated and introduced, see section 3.2.

In the left panel of Fig. 6.6 we compare thus obtained bsg R_{AA} prediction with the one when soft-gluon approximation is accounted, as a function of the final p_{\perp} . The right panel Fig. 6.6 provides the relative change arising from relaxing the approximation. We observe that this relaxation hardly affects R_{AA} , more specifically the relative change is somewhat less than -1% at $p_{\perp} \approx 10$ GeV and further rises to approximately 2% , with increasing p_{\perp} . Thus, we obtained excellent agreement between bsg and sg R_{AA} , which moreover presents an improvement toward matching between two cases compared to previously studied variables. This outstanding agreement initiated questions of:

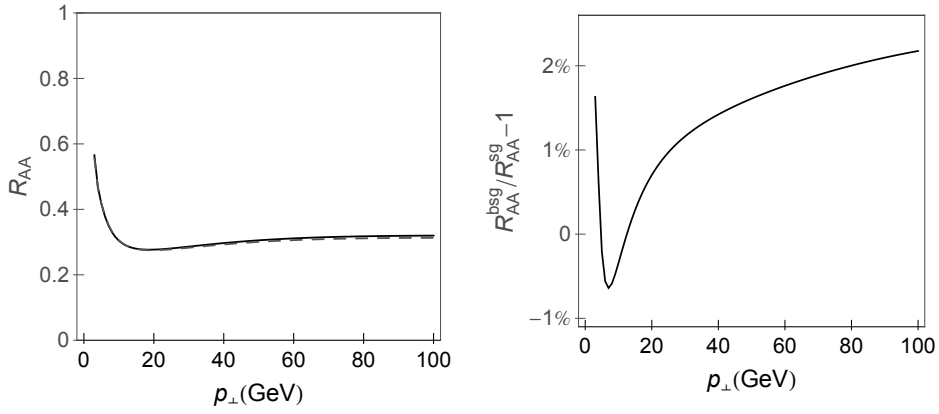


Figure 6.6: The effect of relaxing the soft-gluon approximation on gluon R_{AA} . The comparison of gluon nuclear modification factor R_{AA} between *bsg* (the solid curve) and *sg* (the dashed curve) cases is assessed in the left panel, as a function of the final p_{\perp} . The right panel provides a percentage of gluon suppression change when soft-gluon approximation is relaxed. Figure adapted from [248].

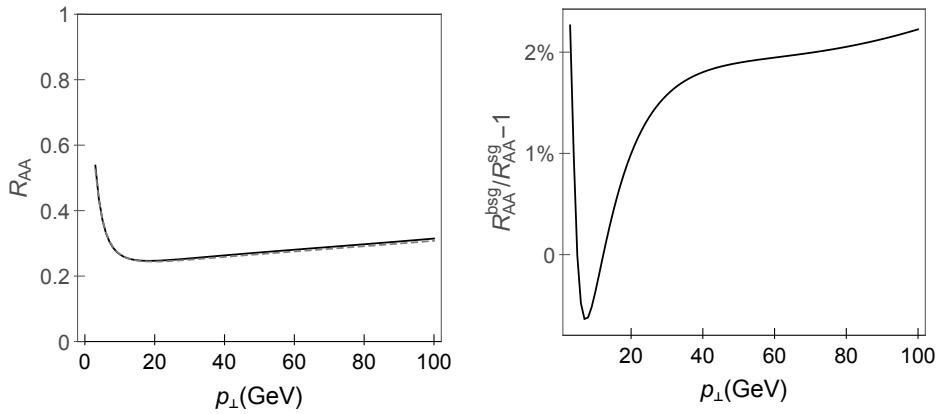


Figure 6.7: The effect of relaxing the soft-gluon approximation on gluon R_{AA} when uniform longitudinal distance distribution is considered. The comparison of gluon nuclear modification factor R_{AA} between *bsg* (the solid curve) and *sg* (the dashed curve) cases is assessed in the left panel, as a function of the final p_{\perp} . The relative change of gluon suppression when soft-gluon approximation is relaxed with respect to *sg* limit is presented in the right panel.

i) why going beyond the soft-gluon approximation has negligible impact on R_{AA}

and *ii*) why the large differences observed in Figs. 6.4 and 6.5 for high x values does not reflect on R_{AA} ?

To answer *i*) above, we claim that this pattern is expected, since it is well-known that in suppression calculations both $\frac{\Delta E^{(1)}}{E}$ and $N_g^{(1)}$ non-trivially enter the R_{AA} . On qualitative level, by comparing the two right panels of Fig. 6.3 with the right panel of Fig. 6.6, we observe that the superposition of the opposite effects of relaxing the soft-gluon approximation on $\frac{\Delta E^{(1)}}{E}$ and $N_g^{(1)}$ results in negligible R_{AA} change. Note that the results are robust to the presumed longitudinal distance distribution, which can be seen from Fig. 6.7, where we assumed the opposite limit - the uniform distribution (as done in [208]).

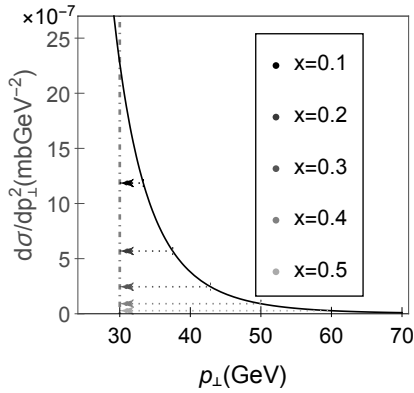


Figure 6.8: Illustrative figure of initial gluon distribution constraining the relevant x region. The initial gluon distribution as a function of p_{\perp} (the solid black curve) at the LHC is extracted from [212]. The final gluon transverse momentum, set at $p_{\perp} = 30$ GeV, is represented by vertical dot-dashed gray boundary. For each x , the dotted arrow links the descendant gluon with its parent gluon (of the corresponding initial transverse momenta), that lost momentum fraction equal to x . The arrows fade as x increases (as indicated in the legend). Figure adapted from [248].

Regarding *ii*) above, it is convenient to recall that suppression of gluon jet (see Eq. (5.2.1)) is not only a function of the energy loss probability, but also of the initial gluon distribution. In order to intuitively understand the role of the initial gluon distribution, we advise a descriptive Fig. 6.8, which depicts its dependence on initial transverse momentum. The idea is the following: Some parent gluon with

unknown initial transverse momentum passes through the QGP, loses its energy via gluon bremsstrahlung, and emerges with final transverse momentum $p_{\perp} = 30$ GeV. This final gluon can originate from the parent gluon with any p_{\perp} higher than its own, but we restrict ourselves to 5 different initial transverse momenta, corresponding to the following fractional momentum loss $x \in \{0.1, 0.2, 0.3, 0.4, 0.5\}$. For instance, $x = 0.5$ corresponds to initial gluon transverse momentum of $30/(1 - 0.5)$ GeV = 60 GeV, i.e. to the parent gluon that lost half of its transverse momentum etc. The question is which of these 5 gluons is the most likely to be the parent one, and how is this probability correlated with x ? The answer is obvious from Fig. 6.8 where, due to the exponentially decreasing initial gluon p_{\perp} distribution, the initial gluon corresponding to $x = 0.1$ is most likely to be the parent one, and as x increases the probability steeply decreases (i.e. for $x \gtrsim 0.4$ it diminishes for 2 orders of magnitude compared to the $x = 0.1$ case).

Therefore, according to the initial distribution, the main contribution to the suppression predictions comes from $x \lesssim 0.4$ region, making this region the most relevant one for differentiating between *bsg* and *sg* R_{AA} . In this region, *bsg* and *sg* $\frac{dN_g^{(1)}}{dx}$ (and equivalently $\frac{1}{E} \frac{dE^{(1)}}{dx}$) curves deflect only slightly from each other (based on Figs. 6.4 and 6.5), which intuitively addresses nearly overlapping R_{AA} in Fig. 6.6. Also, the relevant x region qualitatively resolves the issue of why the large inconsistency between these curves at higher x does not affect R_{AA} .

Along these lines, one could wrongly assume that the $x > 0.4$ region is irrelevant for generating suppression predictions and could be comfortably neglected. Therefore, it is important to make a distinction between terms generally irrelevant and irrelevant (with respect to) for relaxing the soft-gluon approximation. That is, in our suppression calculations we cannot simply reject the $x > 0.4$ region, since non-negligible $\frac{dN_g^{(1)}}{dx}$ contribution to R_{AA} (see the central panel of Fig. 6.4 in both *bsg* and *sg* cases) comes from it. Therefore, for reliable suppression results, one has to take into account the entire x region, while from the above analysis, we argue that only $x \leq 0.4$ region is relevant for studying the importance of relaxing the soft-gluon approximation.

In order to provide more rigorous support to this claim in Fig. 6.9, we compared suppressions obtained from *bsg* expression for the entire $x \leq 0.5$ region, with results

obtained from *bsg* expression for $x \leq 0.4$ combined with *sg* expression for $x > 0.4$. As expected from the above discussion, we obtained that these two approaches lead to almost overlapping suppressions, confirming that the region above $x = 0.4$ is not relevant for the importance of relaxing the soft-gluon approximation. In particular, the obtained difference was less than approximately 3%, and decreased with increasing p_\perp , consistently with the second column in Fig. 6.4, where the area below $\frac{dN_g^{(1)}}{dx}$ curve for $0.4 < x \leq 0.5$ becomes less important compared to the remaining area below the same curve with increasing p_\perp .

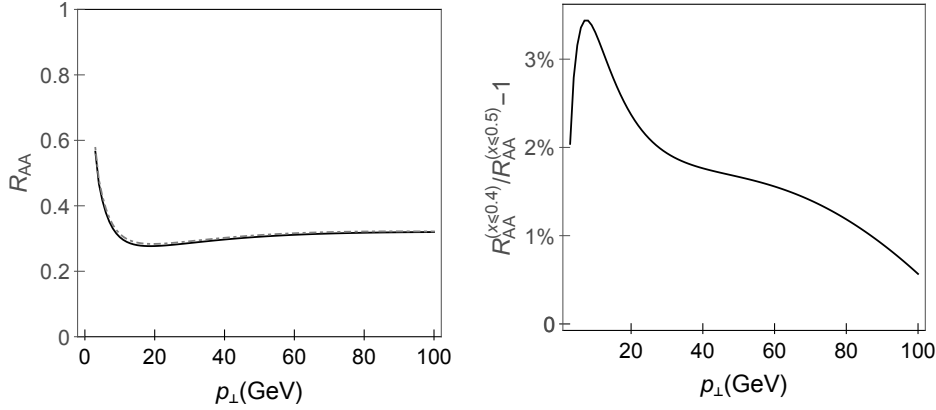


Figure 6.9: The relevant x region for studying importance of relaxing *sg* approximation. The comparison of gluon R_{AA} predictions between *bsg* (the solid curve) and combined: *bsg* for $x \leq 0.4$ + *sg* for $x > 0.4$ (the dashed curve) cases is assessed in the left panel, as a function of the final p_\perp . The right panel provides a percentage of gluon suppression change when soft-gluon-approximation relaxation is omitted at $x > 0.4$.

It is worth noting that the effect of relaxing the soft-gluon approximation on $\frac{dN_g^{(1)}}{dx}$ and $\frac{1}{E} \frac{dE^{(1)}}{dx}$ is practically insensitive to initial transverse momentum (see Fig. 6.5), which is the reason why finite x affects equivalently gluon R_{AA} regardless of its transverse momentum, as observed in Fig. 6.6.

6.7. Conclusions

In our dynamical energy loss model, studied in previous sections, some standard approximations were made in order to facilitate the calculations. The validity of one of the assumptions - the soft-gluon approximation - was rightfully questioned, so the main efforts of the theoretical part of this thesis were directed toward addressing what effect relaxing of the soft-gluon approximation has on radiative energy loss, and consequently on suppression, which depends only on initial distribution and energy loss of high p_{\perp} parton in QGP. To this end, we chose gluon jet, because due to the color factor of $9/4$ compared to the quarks, this assumption has the greatest impact on gluons.

In particular, we analytically calculated 11 Feynman diagrams contributing to the first order in opacity radiative energy loss beyond soft-gluon approximation, first within GLV [183] (massless case), and later within DGLV [189] (massive case) formalism, and generated numerical predictions for: fractional integrated and differential energy loss, mean number of radiated gluons, single gluon radiation spectrum and gluon's suppression. The obtained analytical expressions are notably different from the soft-gluon case, while the numerical effects due to this relaxation are twofold: from *i*) ascending to notable values for single gluon radiation spectrum at $x \gtrsim 0.4$; to *ii*) small changes (within few percents) in fractional radiative energy loss and mean number of radiated gluons, but of opposite signs.

However, we obtained that suppression is not affected by the large discrepancies from *i*), which we explained in terms of the interplay of the initial p_{\perp} distribution and energy loss probability. Namely, due to exponentially decreasing initial gluon distribution, only $x \lesssim 0.4$ region effectively contributes to the differences between *bsg* and *sg* integrated variable predictions. Additionally, the overall effect on suppression is negligible, which can be intuitively understood by the cancellation of the effects on variables mentioned in *ii*).

The obtained nearly indistinguishable suppression patterns in beyond-soft-gluon and soft-gluon cases for gluons in QCD medium composed of static scattering centers, implied that quark radiative energy loss is even less likely to be notably modified, although this still remains to be thoroughly examined.

To our knowledge, this presents the first opportunity to assess the effect of relaxing the soft-gluon approximation on radiative energy loss within DGLV formalism.

Some other radiative energy loss formalisms, which also imply static scatterers, generated their results on a finite x . However, contrary to the conclusions derived for these formalisms (where significant difference in the radiative energy loss was obtained [250–252]) we found that relaxing soft-gluon approximation brings negligible change to the results. Consequently, our results surprisingly indicate that, contrary to the doubts mentioned in subsection 6.1, the soft-gluon approximation remains well-founded within DGLV formalism.

Grounded on the conclusions derived in this section, we believe that the soft-gluon approximation can be reliably applied to the dynamical energy loss formalism, as implicitly suggested by the previous very good agreement [208, 225, 235–238] (see also section 4) of our theoretical predictions with a comprehensive set of experimental data. More specifically, the effective cross section $v(\mathbf{q})$ (which corresponds to interaction between the jet and exchanged gluon) [204] (see also sections 3 and 5) does not depend on x , so introduction of finite x will not affect this term, as anticipated. We also expect that the rest of the energy loss expression (i.e. $f(\mathbf{k}, \mathbf{q}, x)$, which corresponds to interaction between the jet and radiated gluon [204]) will be modified in the similar manner as in the static case, since in the soft-gluon limit, these two expressions coincide. However, relaxing the soft-gluon approximation in dynamical energy loss formalism is out of the scope of this thesis, and this claim still remains to be rigorously tested in the future.

7. CONCLUSIONS AND OUTLOOK

The comparison of angular averaged nuclear modification factor predictions with the wealth of suppression experimental data, currently available, is generally considered to be an excellent tool for mapping the properties of created quark-gluon plasma (sQGP) in ultra-relativistic heavy-ion collisions at the RHIC and the LHC facilities. Among a few steps in suppression calculation, the accurate high p_{\perp} particle energy loss (as the main inducer of jet quenching) calculations are established to be the crucial step. Therefore, in this thesis all our efforts are directed toward: *i)* assessing to what extent our suppression predictions, based on dynamical energy

loss formalism, agree with the measured R_{AA} , which tests our understanding of jet-medium interactions; *ii*) addressing the importance of different dynamical energy loss ingredients in producing reliable suppression predictions; and *iii*) improving the high p_{\perp} particles energy loss calculus, by relaxing one of the long-established approximation in radiative energy loss calculations.

In this final section first we provide a brief summary of all conclusions obtained in this thesis, from both parts: phenomenological and theoretical. Then, we discuss the eventual improvements, that could be introduced in high p_{\perp} particles energy loss calculations, which presents our future course of action. And finally, we provide precise guidelines to experimental researcher on where, based on our suppression predictions, they should concentrate their future efforts.

7.1. Summary of conclusions

First we obtained that our theoretical predictions of high p_{\perp} particles suppression, which are based on recently developed dynamical energy loss formalism, show a robust agreement with various experimental data for $p_{\perp} \gtrsim 10$ GeV, which is, among other, constrained by applying the soft-gluon approximation. This agreement spans across different heavy-ion collision energies (i.e. experiments at both RHIC and LHC), diverse probes (light and heavy one), and experimental conditions (i.e. all available centrality regions). It is worth noting, that in generating the suppression predictions we used: the same numerical procedure, the same energy loss formalism (based on finite temperature QCD calculations) and no fitting parameters in model testing.

Further, under the same computational auspices, we provided heavy and light flavor suppression predictions prior to 5.02 TeV $Pb + Pb$ measurements at the LHC. We surprisingly predicted the same suppression (as well as the pattern) at two LHC energies: $\sqrt{s_{NN}} = 2.76$ TeV and $\sqrt{s_{NN}} = 5.02$, which was explained by cancellation of the opposite impacts of initial momentum distributions and energy loss on suppression predictions. This prediction recently obtained its experimental confirmation. And finally, we predicted that only the momentum region below 50 GeV is the adequate one for mass tomography.

Since our focus is on energy loss (which in dynamical case has several key effects) the above mentioned a very good agreement of our suppression predictions with experimental data, raised a question of what is the individual contribution of each energy loss effect in accurately interpreting the experimental data. To that end, we separately included on-by-one effect, starting from DGLV model, in order of their chronological introduction in model. In particular, we studiously addressed the importance of: inclusion of dynamical scattering centers, collisional energy loss, finite size QCD medium, finite magnetic mass and running coupling, by using the genuine energy loss probe - D meson suppression. This approach allows both investigating the importance of different energy loss effect, and obtaining the historical overview of how the dynamical energy loss model has been improved. We inferred that all ingredients are responsible for the accurate predictions, although the inclusion of the dynamical scattering centers has the largest relative importance, while others contribute to the finer agreement with the data. This implies that further improvements, such as going beyond some approximation in energy loss calculations, could contribute to even greater accuracy of our suppression predictions.

Therefore, our theoretical part of the thesis, addresses the validity of the widely-used soft-gluon approximation, which was also used in dynamical radiative energy loss calculations. The soft-gluon approximation assumes that radiated gluon takes away a small amount of initial jet energy (quantified by $x = \omega/E \ll 1$, where ω, E denote energy of radiated gluon and initial jet, respectively); and breaks down for $5 < p_{\perp} < 10$ GeV, while the gluons are mostly affected by it. Additionally, the well-foundedness of this approximation was generally questioned, as different theoretical approaches reported a notable radiative energy loss of high p_{\perp} particles.

In particular, we relaxed the soft-gluon approximation for 1st order in opacity gluon jet radiative energy loss, within the pQCD approach for a finite size, optically thin QCD medium and since the calculations are technically demanding, they were divided in several steps: *i*) within GLV model, which assumes massless gluons and medium composed of static scatterers *ii*) within DGLV model, which present extension of the previous step toward inclusion of effective gluon mass and *iii*) finally, we discussed the impact of relaxing the approximation in the radiative energy loss, when dynamical medium is considered.

We surprisingly obtained that, although the analytical expressions are substantially different compared to the soft-gluon case, the majority of numerical predictions (apart from differential variables at higher $x \gtrsim 0.4$), i.e. integrated variables such as fractional energy loss, mean number of radiated gluons and suppression, were nearly overlapping with the corresponding soft-gluon predictions. We explained that due to exponentially decreasing initial gluon distribution, only $x \lesssim 0.4$ region effectively contributes to the differentiation between beyond-soft-gluon and soft-gluon cases of integrated variables. Also, we demonstrated that the cancellation of the opposite finite x effects on the fractional energy loss and the mean number of radiated gluons is responsible for negligible suppression change.

To advantage of this theoretical study is that, to our knowledge, this presents the first opportunity to address the importance of the soft-gluon approximation in radiative energy loss of high p_{\perp} particle within DGLV formalism. Some other radiative energy loss models, that also assume medium composed of static scattering centers, generated their results on a finite x , and obtained significant numerical difference compared to the soft-gluon case. Contrary to their conclusions we found that the soft-gluon approximation remains well-founded within DGLV formalism, and that there is no need to go beyond soft-gluon approximation. Finally, we also discussed generalizing this relaxation to the dynamical radiative energy loss, which implies a more general applicability of the conclusions derived in DGLV model.

7.2. Outlook

In this subsection we briefly review some future research directions that could improve our dynamical energy loss model and guide the future experiments, resulting from the study presented in this thesis.

Regarding the collisional energy loss, the introduction of finite magnetic mass lies ahead of us, in order to equalize the amount of improvements incorporated in collisional and radiative contributions to energy loss.

Since we showed that gluon quenching in QCD medium composed of static scattering centers is not altered by the soft-gluon assumption, quark radiative energy loss is even less likely to be notably affected, although this remains to be tested in

the future. Additionally, relaxing the soft-gluon approximation in dynamical energy loss model is out of the scope of this thesis, and this needs to be further rigorously tested.

In our phenomenological part we singled out the importance of directly measuring B mesons instead of non-prompt J/ψ , at relevant momentum region ($p_{\perp} \lesssim 50$ GeV), reducing the uncertainties, and also increasing the number of available measurements for this important mass-tomography probe. Thus, directed where some future experimental efforts should be concentrated.

In addition to the angular average nuclear modification factor predictions, it is also beneficial to extend the set of observables that could be predicted by our formalism, and compare them with the abundance of experimental data. For instance, apart for current calculating suppression for averaged azimuthal angle, our goal is to provide predictions for arbitrary angle (e.g. in-plane, out-of-plane). This, however requires angular dependent nuclear modification factor.

In order to be able to generate predictions for e.g. elliptic flow, for more realistic approach, it is necessary to account for evolving QGP medium, instead using averaged medium properties in modeling the medium. Redeveloping of the complex dynamical energy loss formalism, so that it includes the evolving QGP medium represents a serious undertaking. It requires redoing all calculations, with the distinction that T is no longer a parameter, but changes along the jet propagation path. This significantly complicates the calculations, and also requires hydrodynamical simulations to provide the temperature profiles.

These improvements and recalculations are our immediate future goal, and would further test our formalism, possibly set some restraints and would enable us to accurately explain the data outside the observables that we tested so-far. All this would significantly contribute to better understanding of the jet-medium interactions in QGP, as well as of the nature of quark-gluon plasma and the underlying physics.

-
- [1] S. Glashow, Nucl. Phys. **10**, 107 (1959); A. Salam and J.C. Ward, Nuovo Cimento. **11** (4), 568 (1959); S. Weinberg, Phys. Rev. Lett. **19**, 1264 (1967).
[2] D.J. Gross and F. Wilczek, Phys. Rev. D **8** 3633, (1973); S.R. Coleman and D.J.

- Gross, Phys. Rev. Lett. **31**, 851 (1973).
- [3] H. Kragh, *Quantum generations: A history of physics in the twentieth century*, Princeton, USA: Univ. Pr. 494 (1999).
 - [4] M. Gell-Mann, Phys. Lett. **8**, 214 (1964).
 - [5] G. Zweig, CERN Reports Nos. 8182/TH.401 and 8419/TH.412 (1964).
 - [6] J.J. Thomson, Phil. Mag. **44**, 293 (1897).
 - [7] H. Geiger and E. Marsden, Proc. R. Soc. Lond. A **82**, 495 (1909).
 - [8] E. Rutherford, Phil. Mag. **21**, 669 (1911).
 - [9] J. Chadwick, Nature **129**, 312 (1932).
 - [10] O.W. Greenberg, Phys. Rev. Lett. **13**, 598 (1964).
 - [11] M.Y. Han and Y. Nambu, Phys. Rev. **139**, B1006 (1965).
 - [12] E.D. Bloom *et al.*, Phys. Rev. Lett. **23**, 930 (1969); M. Breidenbach *et al.*, 935 (1969).
 - [13] D. Gross and F. Wilczek, Phys. Rev. Lett. **30**, 1343 (1973); H. D. Politzer, Phys. Rev. Lett. **30**, 1346 (1973).
 - [14] S. Bethke, Prog. Part. Nucl. Phys. **58**, 351 (2007).
 - [15] M. Gazdzicki, M. Gorenstein and P. SeyBoth, Acta Phys. Polon. B **42**, 301 (2011).
 - [16] J. C. Collins and M. J. Perry, Phys. Rev. Lett. **34**, 1353 (1975).
 - [17] N. Cabibbo and G. Parisi, Phys. Lett. B **59**, 67 (1975).
 - [18] L. Susskind, Phys. Rev. D **20**, 2610 (1979).
 - [19] E.V. Shuryak, Phys. Rept. **61**:71 (1980).
 - [20] N. Cabibbo and G. Parisi, Phys. Lett. B **59**, 67 (1975).
 - [21] F. Karsch, E. Laermann and A. Peikert, Phys. Lett. B **478**, 447 (2000).
 - [22] A.M. Polyakov, Phys. Lett. B **72**, 477 (1978).
 - [23] R. Hagedorn, Nuovo Cimento Supplemento, **3**, 147 (1965).
 - [24] M. Gyulassy and L. McLerran, Nucl.Phys. A **750**, 30 (2005).
 - [25] F. Karsch, Nucl. Phys. A **698**, 199 (2002).
 - [26] G. Martinez, arXiv:nucl-ex/1304.1452 (2013).
 - [27] F. Karsch , E. Laermann and A. Peikert, Nucl. Phys. B **605**, 579 (2001).
 - [28] F. Karsch, Lect. Notes Phys. **583**, 209 (2002).
 - [29] M. D’Elia, Talk given at Quark Matter 2018 conference, Venice, Italy (2018).

- [30] P. Petreczky, J. Phys. G **39**, 093002 (2012).
- [31] E. Laermann and O. Philipsen, Ann. Rev. Nucl. Part. Sci. **53**, 163 (2003).
- [32] Z. Fodor and S. D. Katz, JHEP **0404**, 050 (2004).
- [33] Y. Aoki *et al.* Nature **443**, 675 (2006).
- [34] A. Lahiri [for HotQCD collaboration], Talk given at Quark Matter 2018 conference, Venice (2018).
- [35] P. Steinbrecher [for HotQCD collaboration], Talk given at Quark Matter 2018 conference, Venice (2018).
- [36] Z. Fodor, Nucl. Phys. A **715**, 319 (2003);
- [37] K. Splittorff and J.J. M. Verbaarschot, Phys. Rev. Lett. **98**, 031601 (2007).
- [38] G. Baym and S. A. Chin, Phys. Lett. B **62**, 241(1976).
- [39] J. Casalderrey-Solana, H. Liu, D. Mateos, K. Rajagopal, and U. A. Wiedemann, arXiv:1101.0618 (2011).
- [40] S.S. Gubser, Phys. Rev. D **74**, 126005 (2006); Nucl. Phys. A **830**, 657c (2009).
- [41] W. Horowitz, Phys. Rev. D **91**, 085019 (2015).
- [42] J.-P. Blaizot, Acta Phys. Pol. B **4** (2011).
- [43] L.N. Cooper, Phys. Rev. **104**, 1189 (1956).
- [44] M. Alford, A. Schmitt, K. Rajagopal and T. Schäfer, Rev. Mod. Phys. **80**, 1455 (2008).
- [45] J. Bardeen, L.N. Cooper and J.R. Schrieffer Phys. Rev. **106**, 162 (1957).
- [46] A. Turlapov *et al.*, J. Low Temp. Phys. **150**, 567 (2008).
- [47] P. Kovtun, D. T. Son, and A. Starinets, Phys. Rev. Lett. **94**, 111601 (2005).
- [48] C. V. Johnson and P. Steinberg, Phys. Today **63N5**, 29 (2010).
- [49] L. Turko [for the NA61/SHINE collaboration], arxiv:hep-ex/1801.06919 (2018).
- [50] R. Stock, Nature **337**, 319 (1989).
- [51] M.G. Alford, K. Rajagopal and F. Wilczek, Phys. Lett. B **422**, 247 (1998).
- [52] Shusu Shi, *Event anisotropy v_2 at STAR*, PhD Thesis (2010).
- [53] J.D. Bjorken, Phys. Rev. D **27**, 140 (1983).
- [54] R. Pasechnik and M. Šumbera, Universe **3**, no. 1, 7 (2017).
- [55] R.J. Glauber and G. Matthiae, Nucl. Phys. B **21**, 135 (1970).
- [56] M.R. Adams *et al.*, Phys Rev Lett. **68**, 3266 (1992).

- [57] M. Altmann, M. Gluck and E.Reya, Phys. Lett. B **285**, 359 (1992).
- [58] V. Barone and M. Genovese, Phys. Lett. B **412**, 143 (1997).
- [59] D. Kharzeev and E. Levin, Phys. Lett. B **523**, 79 (2001); H.J. Drescher and Y. Nara, Phys. Rev. C **75**, 034905 (2007); C **76**, 041903 (2007).
- [60] B. Schenke, P. Tribedy and R. Venugopalan, Phys. Rev. Lett. **108**, 252301 (2012); Phys. Rev. C **86**, 034908 (2012).
- [61] L.D. McLerran and R. Venugopalan, Phys. Rev. D **49**, 2233 (1994); Phys. Rev. D **49**, 3352 (1994); Phys. Rev. D **50**, 2225 (1994).
- [62] E. Iancu and R. Venugopalan, In *Hwa, R.C. (ed.) *et al.*: Quark gluon plasma* 249-3363 (2003).
- [63] T. Lappi and L. McLerran, Nucl. Phys. A **772**, 200 (2006).
- [64] J. Breitweg *et al.* (ZEUS Collaboration), Eur. Phys. J. C **7**, 609 (1999).
- [65] A.D. Martin, W.J. Stirling, R.S. Thorne and G. Watt, Eur. Phys. J. C **63**, 189 (2009).
- [66] Y.L. Dokshitzer, Sov. Phys. JETP **46**, 641 (1977).
- [67] V.N. Gribov and L.N. Lipatov, Sov. J. Nucl. Phys. **15**, 438 (1972).
- [68] G. Altarelli and G. Parisi, Nucl. Phys. B **126**, 298 (1977).
- [69] P. Romatschke, Eur. Phys. J. C **77**, 21 (2017).
- [70] U. Heinz and R. Snellings, Ann. Rev. Nucl. Part. Sci. **63**, 123 (2013).
- [71] C. Gale, S. Jeon, and B. Schenke, Int. J Mod. Phys. A **28**, 1340011 (2013).
- [72] S. A. Bass *et al.*, Progress in Particle and Nuclear Physics **41**, 255 (1998).
- [73] H. Song, S. A. Bass, and U. Heinz, Phys. Rev. C **83**, 024912 (2011).
- [74] S. Ryu, S. Jeon, C. Gale, B. Schenke, and C. Young, Nucl. Phys. A **904-905**, 389c (2013).
- [75] W. van der Schee, P. Romatschke, and S. Pratt, Phys. Rev. Lett. **111**, 222302 (2013).
- [76] K. Werner, I. Karpenko, T. Pierog, M. Bleicher, and K. Mikhailov, Phys. Rev. C **82**, 044904 (2010).
- [77] C. V. Johnson and P. Steinberg, Physics Today **63**, 29 (2010). PROVERI i dupli
- [78] P. Subrata, Pramana: Journal of Physics, **84**, 717.
- [79] Z. Xu and C. Greiner, Phys. Rev. C **71**, 064901 (2005); Z. Xu, C. Greiner, and H. Stöcker, Phys. Rev. Lett. **101**, 082302 (2008).

- [80] E. Bratkovskaya, W. Cassing, V. Konchakovski, and O. Linnyk, Nucl. Phys. A **856**, 162 (2011).
- [81] Z.W. Lin, L. He, T. Edmonds, F. Liu, D. Molnar, and F. Wang, arXiv:1512.06465 (2015).
- [82] J. Cleymans, EPJ Web Conf. **95**, 03004 (2015).
- [83] F. Bellini [for ALICE collaboration], Talk given at Quark Matter 2018 conference, Venice (2018).
- [84] C.M. Hung and E.V. Shuryak, Phys. Rev. C **57**, 1891 (1998).
- [85] W. Florkowski, Nucl. Phys. A **774**, 179 (2006). Prog. Theor. Phys. Suppl. **187**, 17 (2011).
- [86] E. Iancu, arXiv:hep-ph/1205.0579v1 (2012).
- [87] J.C. Collins, D.E. Soper and G. Sterman, Nucl. Phys. B **261**, 104 (1985).
- [88] M. Mangano, H. Satz and U. Wiedermann, CERN-2004-009; A. Accardi *et al.*, CERN-2004-009-A, arXiv:hep-ph/0308248 (2004); Accardi *et al.*, CERN-2004-009-B, arXiv:hep-ph/0310274 (2004); M. Bedjidian *et al.*, CERN-2004-009-C, arXiv:hep-ph/0311048 (2004).
- [89] P. Jacobs and X.N. Wang, Prog. Part. Nucl. Phys. **54**, 443 (2005).
- [90] J.D. Bjorken, FERMILAB-PUB-82-059-THY, 287 (1982).
- [91] D. d'Enterria, Nucl. Phys. A **827**, 356C (2009).
- [92] D. d'Enterria, J. Phys. G **34**, S53 (2007).
- [93] F. Sikler (for CMS collaboration) J. Phys. G **35**, 104150 (2008).
- [94] H. A. Gustafsson *et al.*, Phys. Rev. Lett. **52**, 1590 (1984).
- [95] K. Adcox *et al.* (PHENIX Collaboration), Nucl. Phys. A **757**, 184 (2005).
- [96] J.Y. Ollitrault, Phys. Rev. D **46**, 229 (1992).
- [97] S. Voloshin and Y. Zhang, Z. Phys. C **70**, 665 (1996).
- [98] B. Guerzoni (for the ALICE collaboration), talk given at IFAE2013, Rome, Italy (2013).
- [99] H. Masui (for the STAR collaboration), talk given at SQM2008, Beijing, China (2008).
- [100] A. Dainese, Eur. Phys. J. C **33**, 495 (2004).
- [101] D. d'Enterria and B. Betz, Lect. Notes Phys. **785**, 285 (2010).

- [102] D. Molnar and D. Sun, Nucl. Phys. A **932**, 140 (2014); Nucl. Phys. A **910-911**, 486 (2013).
- [103] T. Renk, Phys. Rev. C **85**, 044903 (2012).
- [104] M.J. Tannenbaum, J. Phys. Conf. Ser. **589**, 012019 (2015).
- [105] M. Gyulassy and M. Plumer, Nucl. Phys. A 527, 641 (1991).
- [106] X. N. Wang and M. Gyulassy, Phys. Rev. Lett. 68, 1480 (1992)
- [107] M. Gyulassy, M. Plumer, M. Thoma and X.N. Wang, Nucl. Phys. A **538**, 37C (1992).
- [108] M.H. Thoma and M. Gyulassy, Nucl. Phys. A **544**, 573C (1992).
- [109] *New State of Matter created at CERN*, CERN press release, February 10th 2000.
- [110] J.W. Cronin *et al.*, Phys. Rev. D **11**,3105 (1975).
- [111] J.W. Cronin, H.J. Frisch, M.J. Shochet, J.P. Boymond, R. Mermod, P.A. Piroue and R.L. Sumner, Phys. Rev. D **11**, 3105 (1975).
- [112] A. Krzywicki, J. Engels, B. Petersson, and U. Sukhatme, Phys. Lett. B **85**, 407 (1979).
- [113] M. Lev and B. Petersson, Z. Phys. C **21**, 155 (1983).
- [114] A. Accardi, arXiv:hep-ph/0212148 (2002).
- [115] D. d'Enterria, Phys. Lett. B **596**, 32 (2004).
- [116] S.S. Adler *et al.*, (PHENIX Collaboration), Phys. Rev. Lett. **91**, 072303 (2003).
- [117] J. Adams *et al.* (STAR Collaboration), Phys. Rev. Lett. **92**, 052302 (2004).
- [118] S.S. Adler *et al.* (PHENIX Collaboration), Phys. Rev. Lett. **91**, 182301 (2003).
- [119] P.F. Kolb, P. Huovinen, U.W. Heinz and H. Heiselberg, Phys. Lett. B **500**, 232 (2001).
- [120] J. Adams *et al.* (STAR Collaboration), Phys. Rev. Lett. **91**, 072304 (2003); C. Adler *et al.* (STAR Collaboration), Phys. Rev. Lett. **90**, 082302 (2003).
- [121] I. Arsene *et al.*, Nucl. Phys. A 757, 1 (2005); B. B. Back *et al.* (PHOBOS Collaboration), *ibid.* 757, 28 (2005); J. Adams *et al.* (STAR Collaboration), 757, 102 (2005); K. Adcox *et al.* (PHENIX Collaboration), 757, 184 (2005);[<http://www.bnl.gov/rhic/newPhysics.asp>]
- [122] *'Perfect' Liquid Hot Enough to be Quark Soup (Protons, neutrons melt to produce 'quark-gluon plasma' at RHIC)*, RHIC press release, February 15th 2010.
- [123] V. Khachatryan *et al.* (CMS collaboration), JHEP **1704**, 039 (2017).

- [124] J. Adam *et al.* (the ALICE collaboration), JHEP **1603**, 081 (2016). Rev. Phys. **1**, 172 (2016).
- [125] A. M. Sirunyan *et al.* (CMS Collaboration), Phys. Lett. B **782**, 474 (2018).
- [126] A. Adare *et al.* (PHENIX Collaboration), Phys. Rev. Lett. **104**, 252301 (2010).
- [127] M.M. Aggarwal *et al.* (STAR Collaboration), Phys. Rev. C **82**, 024912 (2010).
- [128] K. Aamodt *et al.* (ALICE Collaboration), arXiv:nucl-ex/110.0121v3 (2017).
- [129] D. d’Enterria, PoS QNP **2012**, 018 (2012).
- [130] B.B. Abelev *et al.*, Eur. Phys. J. C **74**, (9) 3054 (2014).
- [131] D.G. d’Enterria and D. Peressounko, Eur. Phys. J. C **46**, 451–464 (2006).
- [132] J. Adam (ALICE collaboration), Phys. Lett. B **754**, 235 (2016); R. Haake [for the ALICE collaboration], Talk given at Moriond QCD 2017, La Thuile, Italy (2017).
- [133] M. Csanad, Gribov-80 Memorial Volume, 319 (2011).
- [134] A. Adare *et al.*, Phys. Rev. Lett. **104** 132301 (2010).
- [135] T. Matsui and H. Satz., Phys. Lett. B **178**, 416 (1986).
- [136] H. Stocker, F. Jundt and G. Guillaume, Toute la physique, DUNOD (1999).
- [137] S. Datta, F. Karsch, P. Petreczky and I. Wetzorke, Phys. Rev. D **69**, 094507 (2004); S. Digal, P. Petreczky and H. Satz, hep-ph/0110406.
- [138] R. J. Fries, B. Muller, C. Nonaka and S. A. Bass, Phys. Rev. Lett. **90**, 202303 (2003).
- [139] B.B. Abelev *et al.* (ALICE Collaboration), Phys. Lett. B **734**, 314 (2014).
- [140] D. Weise [for ALICE collaboration], Talk given at SQM2017, Utrecht, Netherlands (2017).
- [141] A.M. Sirunyan *et al.* (CMS Collaboration), arXiv:hep-ex/1805.09215 (2018).
- [142] X. Du, R. Rapp and M. He, Phys. Rev. C **96**, no. 5, 054901 (2017); B. Krouppa and M. Strickland, Universe 2 (2016) 16.
- [143] V. Pacik (for the ALICE collaboration), Talk given at Quark Matter 2018, Venice, Italy (2018); K. Gajdosova (for the ALICE collaboration), talk given at Quark Matter 2018, Venice, Italy (2018);
- [144] Y. Zhou (for the ALICE collaboration), J. Phys.: Conf. Ser. **779**, 012055 (2017).
- [145] V. Pacik [for the ALICE collaboration], Talk given at Quark Matter 2018, Venice, Italy (2018)

- [146] M.H. Thoma and M. Gyulassy, Nucl. Phys. B **351**, 491 (1991).
- [147] E. Braaten and M.H. Thoma, Phys. Rev. D **44**, 1298 (1991).
- [148] E. Braaten and M.H. Thoma, Phys. Rev. D **44**, 2625 (1991).
- [149] J.F. Gunion and G. Bertsch, Phys. Rev. D **25**, 746 (1982).
- [150] A. Adare et al. [PHENIX collaboration], Phys. Rev. Lett. **98**, 172301 (2007).
- [151] J. Bielcik [STAR Collaboration], Nucl. Phys. A **774**, 697 (2006).
- [152] M. Djordjevic, M. Gyulassy, R. Vogt and S. Wicks, Phys. Lett. B **632**, 81 (2006).
- [153] M.H. Thoma, Phys. Lett. B **273**, 128 (1991).
- [154] M.G. Mustafa, Phys. Rev. C **72**, 014905 (2005).
- [155] M.G. Mustafa and M.H. Thoma, Acta Phys. Hung. A **22**, 93 (2005).
- [156] Y.L. Dokshitzer and D.E. Kharzeev, Phys. Lett. B **519**, 199 (2001).
- [157] M. Djordjevic, Phys. Rev. C **74**, 064907 (2006).
- [158] S. Peigne, P.B. Gossiaux and T. Gousset, JHEP **0604**, 011 (2006).
- [159] B. Blagojevic and M. Djordjevic, J. Phys. G **42**, 075105 (2015).
- [160] L.D. Landau and I.Y. Pomeranchuk, Dokl. Akad. Nauk. SSSR **92**, 535, 735 (1953);
A.B. Migdal, Phys. Rev. **103**, 1811 (1956).
- [161] M. Gyulassy and X.N. Wang, Nucl. Phys. B **420**, 583 (1994).
- [162] X.N. Wang, M. Gyulassy and M. Plumer, Phys. Rev. D **51**, 3436 (1995). JHEP
0604, 011 (2006).
- [163] R. Baier, Y.L. Dokshitzer, S. Peigne and D. Schiff, Phys. Lett. B **345**, 277 (1995).
- [164] R. Baier, Y.L. Dokshitzer, A.H. Mueller, S. Peigne and D. Schiff, Nucl. Phys. B **478**,
577 (1996).
- [165] R. Baier, Y.L. Dokshitzer, A.H. Mueller, S. Peigne and D. Schiff, Nucl. Phys. B **483**,
291 (1997).
- [166] R. Baier, Y.L. Dokshitzer, A.H. Mueller, S. Peigne and D. Schiff, Nucl. Phys. B **484**,
265 (1997).
- [167] R. Baier, Y.L. Dokshitzer, A.H. Mueller and D. Schiff, Phys. Rev. C **58**, 1706 (1998).
- [168] J.D. Bjorken, Phys. Rev. D **27**, 140 (1983).
- [169] B.G. Zakharov, JETP Lett. **63**, 952 (1996).
- [170] B.G. Zakharov, JETP Lett. **65**, 615 (1997).
- [171] B.G. Zakharov, Phys. Atom. Nucl. **61**, 838 (1998).

- [172] P.B. Arnold, G.D. Moore and L.G. Yaffe, JHEP **0111**, 057 (2001).
- [173] P.B. Arnold, G.D. Moore and L.G. Yaffe, JHEP **0112**, 009 (2001).
- [174] P.B. Arnold, G.D. Moore and L.G. Yaffe, JHEP **0206**, 030 (2002).
- [175] P.B. Arnold, G.D. Moore and L.G. Yaffe, JHEP **0301**, 030 (2003).
- [176] G.Y. Qin, J. Ruppert, C. Gale, S. Jeon, G.D. Moore and M.G. Mustafa, Phys. Rev. Lett. **100**, 072301 (2008).
- [177] B. Schenke, C. Gale and G.Y. Qin, Phys. Rev. C **79**, 054908 (2009).
- [178] S. Jeon and G.D. Moore, Phys. Rev. C **71**, 034901 (2005).
- [179] S. Caron-Hout and C. Gale, Phys. Rev. C **82**, 064902 (2010).
- [180] M. Gyulassy, P. Levai and I. Vitev, Nucl. Phys. A **661**, 637 (1999).
- [181] M. Gyulassy, P. Levai and I. Vitev, Nucl. Phys. B **571**, 197 (2000).
- [182] M. Gyulassy, P. Levai and I. Vitev, Phys. Rev. Lett. **85**, 5535 (2000).
- [183] M. Gyulassy, P. Levai and I. Vitev, Nucl. Phys. B **594**, 371 (2001).
- [184] M. Gyulassy, P. Levai and I. Vitev, Phys. Lett. B **538**, 282 (2002).
- [185] M.L. Ter-Mikayelian, Dokl. Akad. Nauk SSSR **94**, 1033 (1954).
- [186] M.L. Ter-Mikayelian, High-Energy Electromagnetic Processes in Condensed Media, John Wiley and sons, New York (1972).
- [187] M. Le Bellac, *Thermal Field Theory*, Cambridge Monographs on Mathematical Physics (2000).
- [188] M. Djordjevic and M. Gyulassy, Phys. Rev. C **68**, 034914 (2003).
- [189] M. Djordjevic and M. Gyulassy, Nucl. Phys. A **733**, 265 (2004).
- [190] S. Wicks, W. Horowitz, M. Djordjevic and M. Gyulassy, Nucl. Phys. A **784**, 426 (2007).
- [191] S. Wicks, W. Horowitz, M. Djordjevic and M. Gyulassy, Nucl. Phys. A **783**, 493 (2007).
- [192] S.S. Adler *et al.* (PHENIX Collaboration), Phys. Rev. Lett. **96**, 032301 (2006); Y. Akiba *et al.* (PHENIX Collaboration), Nucl. Phys. A **774**, 403 (2006).
- [193] A.K. Dutt-Mazumder, J. Alam, P. Roy and B. Sinha, Phys. Rev. D **71** 094016 (2005).
- [194] M. Djordjevic and U. Heinz, Phys. Rev. C **77**, 024905 (2008).
- [195] J.I. Kapusta, *Finite-Temperature Field Theory*, Cambridge University Press (1989).

- [196] M. Djordjevic and U. Heinz, Phys. Rev. Lett. **101**, 022302 (2008).
- [197] L.D. Landau and I. Pomeranchuk, Dokl. Akad. Nauk Ser. Fiz. **92**, 535 and 735 (1953).
- [198] M. Djordjevic, Phys. Rev. C **80**, 064909 (2009).
- [199] Yu. Maezawa *et al.* (WHOT-QCD Collaboration), Phys. Rev. D **81**, 091501 (2010).
- [200] Yu. Maezawa *et al.* (WHOT-QCD Collaboration), PoS Lattice, 194 (2008).
- [201] A. Nakamura, T. Saito and S. Sakai, Phys. Rev. D **69**, 014506 (2004).
- [202] A. Hart, M. Laine and O. Philipsen, Nucl. Phys. B **586**, 443 (2000).
- [203] D. Bak, A. Karch and L.G. Yaffe, JHEP **0708**, 049 (2007).
- [204] M. Djordjevic and M. Djordjevic, Phys. Lett. B **709**, 229 (2012).
- [205] P. Aurenche, F. Gelis and H. Zaraket, JHEP **0205**, 043 (2002).
- [206] R. Field, Applications of Perturbative QCD, Perseus Books, Cambridge, Massachusetts (1995).
- [207] A. Peshier, arXiv:hep-ph/0601119 (2006).
- [208] M. Djordjevic and M. Djordjevic, Phys. Lett. B **734**, 286 (2014).
- [209] S. Peigne, A. Peshier, Phys. Rev. D **77**, 114017 (2008).
- [210] B. Betz and M. Gyulassy, Phys. Rev. C **86**, 024903 (2012).
- [211] M. Djordjevic, J. Phys. G **32**, S333 (2006).
- [212] Z.B. Kang, I. Vitev and H. Xing, Phys. Lett. B **718**, 482 (2012); R. Sharma, I. Vitev and B.W. Zhang, Phys. Rev. C **80**, 054902 (2009).
- [213] M. Djordjevic, Nucl. Phys. A **783**, 197 (2007).
- [214] B. Hahn, D.G. Ravenhall and R. Hoftstadter, Phys. Repts. **101**, 1131 (1956).
- [215] G.D. Moore, D. Teaney, Phys. Rev. C **71**, 064904 (2005).
- [216] D. de Florian, R. Sassot and M. Stratmann, Phys. Rev. D **75**, 114010 (2007).
- [217] M. Cacciari and P. Nason, JHEP **0309**, 006 (2003).
- [218] M. Cacciari *et al.*, JHEP **1210**, 137 (2012).
- [219] B. Abelev *et al.* (ALICE Collaboration), Phys. Lett. B **720**, 52 (2013).
- [220] A. O. Velasquez (for the ALICE collaboration), Nucl. Phys. A **904-905**, 763c (2013).
- [221] A. Grelli (for the ALICE collaboration), Nucl. Phys. A **904-905**, 635c (2013).
- [222] S. Sakai (for the ALICE collaboration), Nucl. Phys. A **904-905**, 661c (2013).
- [223] S. Chatrchyan *et al.* (CMS Collaboration), Eur. Phys. J. C **72**, 1945 (2012).

- [224] J. Mihee (for the CMS collaboration) Nucl. Phys. A **904-905**, 657c (2013).
- [225] M.D. Djordjevic, M. Djordjevic and B. Blagojevic, Phys. Lett. B **737**, 298 (2014).
- [226] M. Wilde (for the ALICE Collaboration) Nucl. Phys. A **904-905**, 573c (2013).
- [227] M. Djordjevic, M. Gyulassy and S. Wicks, Phys. Rev. Lett. **94**, 112301 (2005).
- [228] S.S. Adler *et al.* (PHENIX Collaboration), Phys. Rev. C **71**, 034908 (2005).
- [229] K. Aamodt *et al.* (ALICE Collaboration), Phys. Rev. Lett. **106**, 032301 (2011).
- [230] J. Otwinowski [ALICE Collaboration], PoS ConfinementX **170** (2012).
- [231] A. Festanti [for the ALICE Collaboration], Talk given at Quark Matter 2014, Darmstadt, Germany.
- [232] A. Adare *et al.* (PHENIX Collaboration), Phys. Rev. C **87**, 034911 (2013).
- [233] B. Abelev *et al.*, JHEP **1209**, 112 (2012).
- [234] S. Chatrchyan *et al.* (CMS Collaboration), JHEP **5** 063 (2012).
- [235] M. Djordjevic and M. Djordjevic, Phys. Rev. C **90**, 034910 (2014).
- [236] M. Djordjevic and M. Djordjevic, Phys. Rev. C **92**, 024918 (2015).
- [237] M. Djordjevic, B. Blagojevic and L. Zivkovic, Phys. Rev. C **94**, 044908 (2016).
- [238] M. Djordjevic, Phys. Rev. Lett. **112**, 042302 (2014).
- [239] B. Hong, (CMS Collaboration) Talk given at Quark Matter 2015, Kobe, Japan.
- [240] G. Aad *et al.* (ATLAS Collaboration), JHEP **1509**, 050 (2015).
- [241] U.A. Wiedemann, Nucl. Phys. B **588**, 303 (2000).
- [242] C.A. Salgado and U.A. Wiedemann, Phys. Rev. D **68**, 014008 (2003).
- [243] N. Armesto, C.A. Salgado and U.A. Wiedemann, Phys. Rev. D **69**, 114003 (2004).
- [244] X.N. Wang and X.F. Guo, Nucl. Phys. A **696**, 788 (2001).
- [245] A. Majumder and M. Van Leeuwen, Prog. Part. Nucl. Phys. A **66**, 41 (2011).
- [246] N. Armesto *et al.*, Phys. Rev. C **86**, 064904 (2012).
- [247] S. Wicks, arXiv:0804.4704 (2008).
- [248] B. Blagojevic, M. Djordjevic and M. Djordjevic, arXiv:nucl-th/1804.07593 (2018).
- [249] L. Apolinario, N. Armesto and C.A. Salgado, Phys. Lett. B **718**, 160 (2012).
- [250] B.W. Zhang and X.N. Wang, Nucl. Phys. A **720**, 429 (2003).
- [251] G. Ovanessian and I. Vitev, Phys. Lett. B **706**, 371 (2012).
- [252] G. Ovanessian and I. Vitev, JHEP **1106**, 080 (2011).
- [253] O.K. Kalashnikov and V.V. Klimov, Sov. J. Nucl. Phys. **31**, 69 (1980).

- [254] V.V. Klimov, Sov. Phys. JETP **55**, 199 (1982).
 [255] R.D. Pisarski, Physica A **158**, 146 (1989).
 [256] A.V. Selikhov, M. Gyulassy, Phys. Lett. B **316**, 373 (1993); Phys. Rev. C **49**, 1726 (1994).
 [257] J. Ellis, TikZ-Feynman: Feynman diagrams with TikZ, arXiv:hep-ph/1601.05437 (2016).

Appendix A: Expressions for collisional energy loss

The expressions outlined in this appendix are adapted from [157]. The effective gluon propagator for gluon embedded in a finite temperature QGP medium has both transverse and longitudinal contributions [253–256], and in Coulomb gauge (for simplicity chosen, although final results are gauge invariant) reads:

$$D^{\mu\nu}(\omega, \vec{\mathbf{q}}) = -P^{\mu\nu} \Delta_T(\omega, \vec{\mathbf{q}}) - Q^{\mu\nu} \Delta_L(\omega, \vec{\mathbf{q}}), \quad (\text{A.0.1})$$

where $q = (\omega, \vec{\mathbf{q}})$ denotes (exchanged between high p_\perp quark and medium partons) gluon 4-momentum, while Δ_T and Δ_L , respectively, are effective transverse and longitudinal gluon propagators, given by [256]:

$$\Delta_T^{-1} = \omega^2 - \vec{\mathbf{q}}^2 - \frac{\mu_E^2}{2} - \frac{(\omega^2 - \vec{\mathbf{q}}^2)\mu_E^2}{2\vec{\mathbf{q}}^2} \left(1 + \frac{\omega}{2|\vec{\mathbf{q}}|} \ln \left| \frac{\omega - |\vec{\mathbf{q}}|}{\omega + |\vec{\mathbf{q}}|} \right| \right), \quad (\text{A.0.2})$$

$$\Delta_L^{-1} = \vec{\mathbf{q}}^2 + \mu_E^2 \left(1 + \frac{\omega}{2|\vec{\mathbf{q}}|} \ln \left| \frac{\omega - |\vec{\mathbf{q}}|}{\omega + |\vec{\mathbf{q}}|} \right| \right), \quad (\text{A.0.3})$$

where Debye mass is given by $\mu_E = g_s T \sqrt{1 + n_f/6}$. In transverse ($P^{\mu\nu}$) and longitudinal ($Q^{\mu\nu}$) projectors the only surviving terms are:

$$P^{ij} = \delta^{ij} - \frac{q^i q^j}{|\vec{\mathbf{q}}|}, \quad (\text{A.0.4})$$

$$Q^{00} = 1. \quad (\text{A.0.5})$$

The contribution for collisional (elastic) energy loss (up to the 0^{th} order in opacity) comes from 1-HTL gluon propagator, and for jet produced in a finite size (L) QGP

medium expression for heavy quark collisional energy loss acquires the following form [157]:

$$\begin{aligned} \Delta E_{coll} &= \frac{C_R g_s^4}{2\pi^4} \int_0^\infty n_{eq}(|\vec{\mathbf{k}}|) d|\vec{\mathbf{k}}| \left(\int_0^{|\vec{\mathbf{k}}|} |\vec{\mathbf{q}}| d|\vec{\mathbf{q}}| \int_{-|\vec{\mathbf{q}}|}^{|\vec{\mathbf{q}}|} \omega d\omega + \int_{|\vec{\mathbf{k}}|}^{|\vec{\mathbf{q}}|_{max}} |\vec{\mathbf{q}}| d|\vec{\mathbf{q}}| \int_{|\vec{\mathbf{q}}|-2|\vec{\mathbf{k}}|}^{|\vec{\mathbf{q}}|} \omega d\omega \right) \\ &\times \left(|\Delta_L(q)|^2 \frac{(2|\vec{\mathbf{k}}| + \omega)^2 - |\vec{\mathbf{q}}|^2}{2} J_1 + |\Delta_T(q)|^2 \frac{(|\vec{\mathbf{q}}|^2 - \omega^2)((2|\vec{\mathbf{k}}| + \omega)^2 + |\vec{\mathbf{q}}|^2)}{4|\vec{\mathbf{q}}|^4} \right) \\ &\times [(v^2|\vec{\mathbf{q}}|^2 - \omega^2)J_1 + 2\omega J_2 - J_3], \end{aligned} \quad (\text{A.0.6})$$

where $n_{eq}(|\vec{\mathbf{k}}|)$ is equilibrium momentum distribution [147] at temperature T taking into account quarks (Fermi-Dirac statistics) and gluons (Bose-Einstein statistics), and reads:

$$n_{eq}(|\vec{\mathbf{k}}|) = \frac{n}{e^{|\vec{\mathbf{k}}|/T} - 1} + \frac{n_f}{e^{|\vec{\mathbf{k}}|/T} + 1}. \quad (\text{A.0.7})$$

Here n and n_f stand for number of colors and number of light-quark flavors, respectively, whereas medium partons (k) are considered to be massless $k = (|\vec{\mathbf{k}}|, \vec{\mathbf{k}})$. The upper limit of $|\vec{\mathbf{q}}|$ integration [146] is:

$$|\vec{\mathbf{q}}|_{max} = \text{Min} \left[E, \frac{2|\vec{\mathbf{k}}|(1 - |\vec{\mathbf{k}}|/E)}{1 - v + 2|\vec{\mathbf{k}}|/E} \right], \quad (\text{A.0.8})$$

where E and v represent energy and velocity magnitude of initial quark jet, respectively. The integrals J_i from Eq. (A.0.6) are given by [157]:

$$\begin{aligned} J_1 &= \int \frac{d\Omega}{4\pi} \frac{\sin[(\omega - \vec{\mathbf{v}} \cdot \vec{\mathbf{q}}) \frac{L}{2v}]^2}{(\omega - \vec{\mathbf{v}} \cdot \vec{\mathbf{q}})^2} \\ &= \frac{L}{4|\vec{\mathbf{q}}|v^2} \left[Si((v|\vec{\mathbf{q}}| + \omega) \frac{L}{v}) + Si((v|\vec{\mathbf{q}}| - \omega) \frac{L}{v}) \right] \\ &- \frac{1}{4v|\vec{\mathbf{q}}|} \left[\frac{1 - \cos((v|\vec{\mathbf{q}}| - \omega) \frac{L}{v})}{v|\vec{\mathbf{q}}| - \omega} + \frac{1 - \cos((v|\vec{\mathbf{q}}| + \omega) \frac{L}{v})}{v|\vec{\mathbf{q}}| + \omega} \right], \end{aligned} \quad (\text{A.0.9})$$

$$\begin{aligned} J_2 &= \int \frac{d\Omega}{4\pi} \frac{\sin[(\omega - \vec{\mathbf{v}} \cdot \vec{\mathbf{q}}) \frac{L}{2v}]^2}{(\omega - \vec{\mathbf{v}} \cdot \vec{\mathbf{q}})^2} (\omega - \vec{\mathbf{v}} \cdot \vec{\mathbf{q}}) \\ &= \frac{1}{4v|\vec{\mathbf{q}}|} \left[Ci((v|\vec{\mathbf{q}}| - \omega) \frac{L}{v}) - Ci((v|\vec{\mathbf{q}}| + \omega) \frac{L}{v}) + \ln\left(\frac{v|\vec{\mathbf{q}}| + \omega}{v|\vec{\mathbf{q}}| - \omega}\right) \right], \end{aligned} \quad (\text{A.0.10})$$

$$J_3 = \int \frac{d\Omega}{4\pi} \frac{\sin[(\omega - \vec{\mathbf{v}} \cdot \vec{\mathbf{q}}) \frac{L}{2v}]^2}{(\omega - \vec{\mathbf{v}} \cdot \vec{\mathbf{q}})^2} (\omega - \vec{\mathbf{v}} \cdot \vec{\mathbf{q}})^2 = \frac{1}{2} \left(1 - \frac{\cos(\frac{L\omega}{v}) \sin(L|\vec{\mathbf{q}}|)}{L|\vec{\mathbf{q}}|} \right), \quad (\text{A.0.11})$$

which corresponds to integrand averaging over the direction of $\vec{\mathbf{v}}$.

The expression for the heavy quark collisional energy loss per unit length in an infinite QGP medium reads [157]:

$$\begin{aligned} \frac{dE_{coll}}{dL} &= \frac{g_s^4}{6v^2\pi^3} \int_0^\infty n_{eq}(|\vec{\mathbf{k}}|) d|\vec{\mathbf{k}}| \left(\int_0^{|\vec{\mathbf{k}}|/(1+v)} d|\vec{\mathbf{q}}| \int_{-v|\vec{\mathbf{q}}|}^{v|\vec{\mathbf{q}}|} \omega d\omega + \int_{|\vec{\mathbf{k}}|/(1+v)}^{|\vec{\mathbf{q}}|_{max}} d|\vec{\mathbf{q}}| \int_{|\vec{\mathbf{q}}|-2|\vec{\mathbf{k}}|}^{v|\vec{\mathbf{q}}|} \omega d\omega \right) \\ &\times \left(|\Delta_L(q)|^2 \frac{(2|\vec{\mathbf{k}}| + \omega)^2 - |\vec{\mathbf{q}}|^2}{2} + |\Delta_T(q)|^2 \frac{(|\vec{\mathbf{q}}|^2 - \omega^2)((2|\vec{\mathbf{k}}| + \omega)^2 + |\vec{\mathbf{q}}|^2)}{4|\vec{\mathbf{q}}|^4} \right) \\ &\times (v^2|\vec{\mathbf{q}}|^2 - \omega^2). \end{aligned} \quad (\text{A.0.12})$$

Appendix B: Beyond soft-gluon approximation calculus

Note that all diagrams from this appendix are obtained by using [257].

B.1. Notations and useful formulas

In this paper we used the following notation for vectors, in consistency with both [183, 189]:

- $\vec{\mathbf{p}}$ denotes momentum 3D vector
- \mathbf{p} denotes transverse momentum 2D vector
- p_z denotes component of momentum vector along the initial jet
- $p = (p^0, p_z, \mathbf{p}) = [p^+, p^-, \mathbf{p}]$ denotes momentum 4D vector in Minkowski and Light Cone coordinates, respectively, where $p^+ = p^0 + p_z$ and $p^- = p^0 - p_z$.

For simplicity, we here consider QCD medium consisting of static partons and model the interactions of the gluon jet with the medium via static color-screened Yukawa potential, whose Fourier and color structure acquires the following form ([161, 183]):

$$V_n = V(q_n) e^{iq_n x_n} = 2\pi \delta(q_n^0) v(\vec{\mathbf{q}}_n) e^{-i\vec{\mathbf{q}}_n \vec{x}_n} T_{a_n}(R) \otimes T_{a_n}(n), \quad (\text{B.1.1})$$

$$v(\vec{\mathbf{q}}_n) = \frac{4\pi\alpha_s}{\vec{\mathbf{q}}_n^2 + \mu_E^2}, \quad (\text{B.1.2})$$

where x_n denotes space-time coordinate of the n^{th} scatterer (target), $T_{a_n}(R)$ and $T_{a_n}(n)$ denote generators in $SU(N_c = 3)$ color representation of jet and target,

respectively, while μ_E is Debye screening mass and $\alpha_s = g_s^2/4\pi$ is strong coupling constant. In the following lines we will briefly display the identities and algebra that $SU(N_c = 3)$ generators meet:

$$\text{Tr}(T^a(n)) = 0 \tag{B.1.3}$$

$$\text{Tr}(T^a(i)T^b(j)) = \delta_{ij}\delta^{ab}\frac{C_2(i)d_i}{d_G}, \tag{B.1.4}$$

where $d_G = 8$ is the dimension of the adjoint representation (G). We assume that all target partons are in the same d_T dimensional representation (T) with Casimir operator $C_2(T)$, while the gluon jet is in the adjoint representation (G), with Casimir operator $C_2(G)$.

In $SU(N_c = 3)$ color algebra, the following identities hold as well:

$$[T^a, T^b] = if^{abc}T^c, \tag{B.1.5}$$

while in the adjoint representation we have:

$$(T^b)_{ab} = if^{abc}, \tag{B.1.6}$$

$$T^a(G)T^a(G) = C_2(G)I, \tag{B.1.7}$$

where I denotes identity matrix of dimension d_G and the $SU(N_c = 3)$ structure constants f^{abc} are completely antisymmetric to indices permutations, which we frequently apply. In the adjoint representation the following equalities also stand:

$$C(G) = C_2(G) = N_c = 3, \tag{B.1.8}$$

$$\text{Tr}(T^a(G)T^a(G)) = d_G C_2(G). \tag{B.1.9}$$

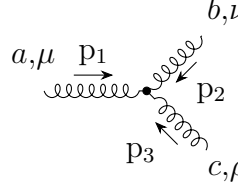
And finally, in our computations we frequently make use of the fact that trace is invariant under cyclic permutations and that generators are Hermitian matrices.

Since our extensive calculations are done in pQCD at finite temperature and include only gluon interactions, below we list the necessary Feynman rules in covariant gauge that we employ:

- massless gluon propagator in Feynman gauge:

$$a, \mu \xrightarrow{P} b, \nu = \frac{-i \delta_{ab} g_{\mu\nu}}{p^2 + i\epsilon}, \quad (\text{B.1.10})$$

- 3-gluon vertex:



$$= g_s f^{abc} \left(g^{\mu\rho} (p_1 - p_3)^\nu + g^{\mu\nu} (p_2 - p_1)^\rho + g^{\nu\rho} (p_3 - p_2)^\mu \right). \quad (\text{B.1.11})$$

Since only physical transverse gluon states must be accounted, summing over final and averaging over initial helicity states is done according to Eq. (57) from [68]:

$$\sum_{\lambda} \epsilon^i(k, \lambda) \epsilon^j(k, \lambda) = \delta^{ij} - \frac{k^i k^j}{\vec{k}^2} \quad (\text{B.1.12})$$

where $i, j = 1, 2, 3$.

B.2. Assumptions

Throughout the paper we assume that initial gluon jet propagates along the z -axis, i.e. has transverse momentum equal to zero, while radiated gluon carries away a finite rate x of initial gluon longitudinal momentum and energy, and final gluon emerges with momentum p . Therefore, instead of assuming soft-gluon approximation ($x \ll 1$), as it was done in [183, 189], we allow x to acquire finite non-zero values, thus relaxing the soft-gluon approximation.

Since we are calculating radiative energy loss within the (GLV) DGLV formalism apart from abandoning the soft-gluon approximation, the following assumptions remain:

- *The soft-rescattering approximation.* Consistently with [183, 189] we assume that partons energies and longitudinal momenta are high compare to their transverse momenta, which disables the radiated and the final gluon to digress much from the initial longitudinal direction (the eikonal approximation).

$$E^+ \sim (1 - x)E^+ \sim xE^+ \gg |\mathbf{p}|, |\mathbf{k}|, |\mathbf{q}_i|, \quad (\text{B.2.1})$$

- *The first order approximation.* The gluon-jet radiative energy loss is calculated up to the first order in opacity expansion, as argued in [183, 184, 247].
- *Scattering centers distribution and ensemble average.* We consider that all scattering centers x_i are distributed with the same transversely homogeneous density:

$$\rho(\vec{\mathbf{x}}) = \frac{N}{A_{\perp}} \bar{\rho}(z), \quad (\text{B.2.2})$$

where $\int dz \bar{\rho}(z) = 1$ and also that impact parameter (i.e. relative transverse coordinate) $\mathbf{b} = \mathbf{x}_i - \mathbf{x}_0$ alters within a large transverse area A_{\perp} compared to the interaction area $\frac{1}{\mu_E^2}$. Therefore, the ensemble average over the scattering center locations reduces to an impact parameter average:

$$\langle \dots \rangle = \int \frac{d^2 \mathbf{b}}{A_{\perp}} \dots, \quad (\text{B.2.3})$$

which in our case is mainly used in the following form:

$$\langle e^{-i(\mathbf{q}_i + \mathbf{q}_j) \mathbf{b}} \rangle = \frac{(2\pi)^2}{A_{\perp}} \delta^2(\mathbf{q}_i + \mathbf{q}_j). \quad (\text{B.2.4})$$

We also assume that the energy of initial hard probe is large compared to the potential screening scale:

$$E^+, (1-x)E^+, xE^+ \gg \mu_E, \mu_{i\perp}, \quad (\text{B.2.5})$$

where $i, j = 1, 2$ count for the scattering centers.

Next, we assume that the distance between the source J and the scattering centers is large relative to the interaction length:

$$z_i - z_0 \gg \frac{1}{\mu_E}, \quad (\text{B.2.6})$$

then, that source current varies slowly with momentum:

$$J(p+k-q) \approx J(p+k), \quad (\text{B.2.7})$$

and that the source current can be written explicitly in terms of polarization vectors:

$$\begin{aligned} J_a^{\mu}(p+k-q) &\equiv J_a(p+k-q) \epsilon^{\mu}(p+k-q) \\ &\approx J_a(p+k) \epsilon^{\mu}(p+k-q). \end{aligned} \quad (\text{B.2.8})$$

In the following sections first we assume that gluons are massless (GLV) in order to make the comprehensive derivations more straightforward and easier to follow, but later we recalculate all the results with gluon mass [188] included (DGLV) (Appendix Section B.11).

B.3. Amplitude numeration

As a digression, in this subsection we briefly outline the general rule for numerating the amplitudes to radiate a gluon including final state interactions with n_s static scattering centers. Note however that, we restrict our calculations to $n_s \leq 2$. As pointed out in [181], each diagram is unambiguously characterized by a label $M_{n_s, m, l}$, where m ($0 \leq m \leq n_s$) denotes at which time interval, between two consecutive scatterings $t_m < t < t_{m+1}$, the gluon has been radiated, while t_0 marks the jet creation moment (source). l carries the information, whether or not the gluon radiated at the mentioned moment t interacts with any of the succeeding scattering centers sited at: $m + 1, m + 2, \dots, n_s$.

Therefore, for a given n_s and m the number of different diagrams is $2^{n_s - m}$ (since either jet or radiated gluon can interact with each $m + 1, m + 2, \dots, n_s$ scatterer), which gives the overall number of diagrams for known number of scattering centers: $\sum_{m=0}^{n_s} 2^{n_s - m} = 2^{n_s + 1} - 1$. Thus, the number of diagrams containing interaction with: *i*) only one scatterer is equal to 3; *ii*) two scatterers equals 7. Also, for a given n_s and m , l is associated with an $n_s - m$ binary array, in the following manner:

$$\vec{\sigma} = (\sigma_{m+1}, \sigma_{m+2}, \dots, \sigma_{n_s}) \iff l = \frac{\sum_{j=m+1}^{n_s} \sigma_j 2^j}{2^{m+1}}, \quad (\text{B.3.1})$$

where each σ_j can be either 1 or 0, depending on whether or not the radiated gluon interacts with j scattering center. Thus, we obtain the upper limit: $l \leq 2^{n_s - m} - 1$, so, for instance, for fixed m , $l = 0$ corresponds to no final state radiated gluon rescattering, while $l = 2^{n_s - m} - 1$ corresponds to the radiated gluon rescattering with all $n_s - m$ remaining scattering centers after t_m .

B.4. Gluon jet M_0

First we calculate gluon-jet radiation amplitude to emit a gluon, carrying a finite fraction x of initial jet energy, with momentum, polarization and color (k, ϵ, c) and without interactions with the medium M_0 .

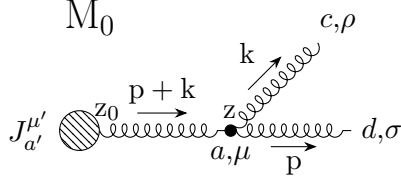


Figure B.1: Zeroth order diagram that includes no interaction with the QCD medium, and contributes to gluon radiation amplitude to the first order in opacity L/λ . The dashed circle represents the source J , which at longitudinal coordinate z_0 produces an off-shell gluon jet, propagating along z -axis. z denotes longitudinal coordinate at which the gluon is radiated. Latin indices denote color charges, while Greek indices denote components of 4-vectors. k denotes 4-momentum of the radiated gluon carrying the color c , and p denotes 4-momentum of the final gluon jet carrying the color d .

We assume that initial gluon $(p+k)$ propagates along z -axis. By using M_0 amplitude as an example, we will implement the aforementioned assumptions in order to acquire momentum and polarization expressions. Thus, the initial gluon 4-momentum reads:

$$\begin{aligned} p+k &= (p^0+k^0, p_z+k_z, \mathbf{0}), \\ p+k &= [E^+, E^-, \mathbf{0}], \end{aligned} \quad (\text{B.4.1})$$

where $E^+ = p^0+k^0+p_z+k_z$ and $E^- = p^0+k^0-p_z-k_z$. Assuming massless (real) gluons for simplicity, the momentum vectors of the radiated (k) and the final (p) gluons acquire the following form:

$$k^2 = 0 \Rightarrow k = [xE^+, \frac{\mathbf{k}^2}{xE^+}, \mathbf{k}], \quad (\text{B.4.2})$$

$$p^2 = 0 \Rightarrow p = [(1-x)E^+, \frac{\mathbf{p}^2}{(1-x)E^+}, \mathbf{p}]. \quad (\text{B.4.3})$$

We also assume that gluons are transversely polarized particles. Although we work in covariant gauge, we can choose any polarization vector for the external on-shell

gluons, so in accordance with [183, 189, 252] we choose $n^\mu = [0, 2, \mathbf{0}]$, as stated above:

$$\begin{aligned}\epsilon(k) \cdot k &= 0, & \epsilon(k) \cdot n &= 0, & \epsilon(k)^2 &= -1, \\ \epsilon(p) \cdot p &= 0, & \epsilon(p) \cdot n &= 0, & \epsilon(p)^2 &= -1,\end{aligned}\tag{B.4.4}$$

while we assume that the source, even though a virtual (off-shell) particle, has also the same polarization as real gluons [252]:

$$\epsilon(p+k) \cdot (p+k) = 0, \quad \epsilon(p+k) \cdot n = 0, \quad \epsilon(p+k)^2 = -1.\tag{B.4.5}$$

Using Eqs.(B.4.2- B.4.5) we can now obtain the following expressions for the gluon polarizations:

$$\epsilon_i(k) = [0, \frac{2\epsilon_i \cdot \mathbf{k}}{xE^+}, \epsilon_i], \quad \epsilon_i(p) = [0, \frac{2\epsilon_i \cdot \mathbf{p}}{(1-x)E^+}, \epsilon_i], \quad \epsilon_i(p+k) = [0, 0, \epsilon_i].\tag{B.4.6}$$

where $i = 1, 2$ counts for polarization vectors. Note that the 4-momentum is conserved, which leads to the relation:

$$\mathbf{p} + \mathbf{k} = 0,\tag{B.4.7}$$

that we implement in Eqs.(B.4.3, B.4.6) in order to ensure that everything is expressed in terms of \mathbf{k} . Also, $E^+ \approx 2E$, $E^- = \frac{\mathbf{k}^2}{x(1-x)E^+}$, where $E = p^0 + k^0$ is the energy of initial jet.

Using the notation from Fig. B.1 we may write:

$$\begin{aligned}M_0 &= \epsilon_\sigma^*(p, \lambda_1) \epsilon_\rho^*(k, \lambda_2) g_s f^{acd} \left(g^{\mu\sigma} (2p+k)^\rho + g^{\mu\rho} (-p-2k)^\sigma + g^{\rho\sigma} (-p+k)^\mu \right) \frac{-i\delta_{aa'} g_{\mu\mu'}}{(p+k)^2 + i\epsilon} \\ &\quad \times iJ_{a'}(p+k) e^{i(p+k)x_0} \epsilon^{\mu'}(p+k, \lambda_3) \approx J_a(p+k) e^{i(p+k)x_0} (-2g_s)(1-x+x^2) \frac{\epsilon \cdot \mathbf{k}}{\mathbf{k}^2} f^{acd} \\ &= J_a(p+k) e^{i(p+k)x_0} (-2ig_s)(1-x+x^2) \frac{\epsilon \cdot \mathbf{k}}{\mathbf{k}^2} (T^c)_{da},\end{aligned}\tag{B.4.8}$$

where λ_i , $i = 1, 2, 3$ denotes helicity of corresponding gluons. Eq. (B.4.8) after summation over helicities of final and radiated gluon, and averaging over helicity of initial gluon by using Eq. (B.1.12) gives:

$$\langle |M_0|^2 \rangle = |J(p+k)|^2 (4g_s^2) \frac{C_2(G)d_G}{\mathbf{k}^2} (1-x+x^2)^2.\tag{B.4.9}$$

Next we substitute the Eq. (B.4.9) in:

$$d^3 N_g^{(0)} d^3 N_J \approx \text{Tr} \langle |M_0|^2 \rangle \frac{d^3 \vec{\mathbf{p}}}{(2\pi)^3 2p^0} \frac{d^3 \vec{\mathbf{k}}}{(2\pi)^3 2\omega}, \quad (\text{B.4.10})$$

Note that, contrary to soft-gluon approximation [189], where:

$$d^3 N_J \approx d_G |J(p+k)|^2 \frac{d^3 \vec{\mathbf{p}}}{(2\pi)^3 2p^0}, \quad (\text{B.4.11})$$

now p , denoting the momentum of the final gluon jet, is not approximately equal to the momentum of initial gluon jet (i.e. the radiated gluon can carry away a substantial amount of the initial jet energy and longitudinal momentum). Thus instead of Eq. (B.4.11) throughout this paper we use the general one:

$$d^3 N_J = d_G |J(p+k)|^2 \frac{d^3 \vec{\mathbf{p}}_J}{(2\pi)^3 2E_J}, \quad (\text{B.4.12})$$

where $E_J = E$ and $\vec{\mathbf{p}}_J$ denotes energy and momentum of the initial gluon jet.

Knowing that the substitution of variables ($p_z, k_z \rightarrow p_z^J, xE$) gives:

$$\frac{d^3 \vec{\mathbf{p}}}{(2\pi)^3 2p^0} \frac{d^3 \vec{\mathbf{k}}}{(2\pi)^3 2\omega} = \frac{d^3 \vec{\mathbf{p}}_J}{(2\pi)^3 2E_J} \frac{dx d^2 \mathbf{k}}{(2\pi)^3 2x(1-x)}, \quad (\text{B.4.13})$$

and by substituting Eqs.(B.4.9, B.4.12, B.4.13) in Eq. (B.4.10), for radiation spectrum we now obtain:

$$\frac{x d^3 N_g^{(0)}}{dx d\mathbf{k}^2} = \frac{\alpha_s C_2(G)}{\pi} \frac{(1-x+x^2)^2}{\mathbf{k}^2 (1-x)}, \quad (\text{B.4.14})$$

which recovers well-known Altarelli-Parisi result [68] and for $x \ll 1$ reduces to the massless soft-gluon limit of Eq.(9) from [189]. The same result can be obtained by directly implementing polarization vectors (Eq. (B.4.6)) in Eq. (B.4.8), instead of using Eq.(B.1.12) when averaging.

B.5. Diagrams $M_{1,1,0}$, $M_{1,0,0}$, $M_{1,0,1}$

In this section we provide a detailed calculations of Feynman amplitudes, corresponding to gluon-jet interaction with one scattering center, which are depicted in Fig. B.2. Again for consistency, we assume that initial jet ($p+k-q$) propagates along z-axis. Throughout this section, momentum and polarization vector for initial gluon read:

$$p+k-q_1 = [E^+ - q_{1z}, E^- + q_{1z}, \mathbf{0}], \quad (\text{B.5.1})$$

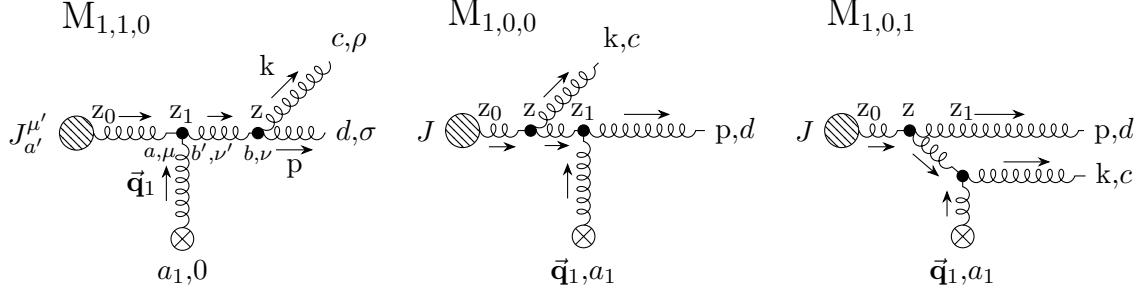


Figure B.2: Three diagrams, corresponding to interaction with one static scattering center, that contribute to gluon-jet radiation amplitude to the first order in opacity L/λ . z_1 denotes longitudinal coordinate of the interactions with one scattering center. Crossed circle represents scatterer that exchange transverse momentum \vec{q}_1 with the jet. Note that, all three diagrams assume equivalently ordered Latin and Greek indices as indicated by the first diagram. Remaining labeling is the same as in Fig. B.1.

$$\epsilon_i(p + k - q_1) = [0, 0, \epsilon_i], \quad (\text{B.5.2})$$

where $q_1 = [q_{1z}, -q_{1z}, \mathbf{q}_1]$, with $q_1^0 = 0$, while p , k and corresponding polarization vectors retain the same expression as in Eqs.(B.4.2, B.4.3, B.4.6), with the distinction that the following relation between gluon transverse momenta, due to 4-momentum conservation, holds:

$$\mathbf{q}_1 = \mathbf{p} + \mathbf{k}. \quad (\text{B.5.3})$$

B.5.1. Computation of $M_{1,1,0}$ diagram

We chose to start with thorough derivation of the expression for $M_{1,1,0}$ amplitude, simply because it has no counterpart regarding the symmetry under $(p \leftrightarrow k, x \leftrightarrow (1-x), c \leftrightarrow d)$ substitutions, and it provides all necessary steps for calculating the remaining two amplitudes from this chapter, apart from having one less singularity compared to the amplitudes $M_{1,0,0}$ and $M_{1,0,1}$. Thus, using the notation from the

left diagram of Fig. B.2, we write:

$$\begin{aligned}
M_{1,1,0} &= \int \frac{d^4 q_1}{(2\pi)^4} \epsilon_\sigma^*(p) \epsilon_\rho^*(k) g_s f^{bcd} \left(g^{\nu\sigma} (2p+k)^\rho + g^{\nu\rho} (-p-2k)^\sigma + g^{\rho\sigma} (-p+k)^\nu \right) \\
&\times \frac{(-i) \delta_{bb'} g_{\nu\nu'}}{(p+k)^2 + i\epsilon} f^{ab'a_1} \left(g^{\mu 0} (p+k-2q_1)^{\nu'} + g^{\mu\nu'} (-2p-2k+q_1)^0 + g^{\nu'0} (p+k+q_1)^\mu \right) \\
&\times T_{a_1} V(q_1) e^{iq_1 x_1} \frac{(-i) \delta_{aa'} g_{\mu\mu'}}{(p+k-q_1)^2 + i\epsilon} i J_{a'}(p+k-q_1) \epsilon^{\mu'} (p+k-q_1) e^{i(p+k-q_1)x_0} \\
&\approx J_a(p+k) e^{i(p+k)x_0} f^{bcd} f^{a_1 ab} T_{a_1} (-i) (1-x+x^2) \int \frac{d^2 \mathbf{q}_1}{(2\pi)^2} e^{-i\mathbf{q}_1 \cdot (\mathbf{x}_1 - \mathbf{x}_0)} 2g_s \\
&\times \frac{(1-x)\boldsymbol{\epsilon} \cdot \mathbf{k} - x\boldsymbol{\epsilon} \cdot \mathbf{p}}{x(1-x)} E^+ \int \frac{dq_{1z}}{2\pi} \frac{v(q_{1z}, \mathbf{q}_1) e^{-iq_{1z}(z_1-z_0)}}{((p+k-q_1)^2 + i\epsilon)((p+k)^2 + i\epsilon)}, \tag{B.5.4}
\end{aligned}$$

where we used the equation:

$$(p+k)^2 = \frac{((1-x)\mathbf{k} - x\mathbf{p})^2}{x(1-x)}, \tag{B.5.5}$$

and assumed that J varies slowly with momentum q_1 , i.e. $J(p+k-q_1) \approx J(p+k)$. The longitudinal momentum transfer integral:

$$I_1(p, k, \mathbf{q}_1, z_1 - z_0) \equiv \int \frac{dq_{1z}}{2\pi} \frac{1}{(p+k-q_1)^2 + i\epsilon} v(q_{1z}, \mathbf{q}_1) e^{-iq_{1z}(z_1-z_0)} \tag{B.5.6}$$

has to be performed in the lower half-plane of the complex plain, since $z_1 > z_0$. In order to determine the pole arising from potential, we rewrite Eq. (B.1.2) in a more appropriate form:

$$v(\vec{\mathbf{q}}_n) = \frac{4\pi\alpha_s}{(q_{nz} + i\mu_{n\perp})(q_{nz} - i\mu_{n\perp})}, \tag{B.5.7}$$

where $\mu_{n\perp}^2 = \mu_E^2 + \mathbf{q}_n^2$. Aside from the pole originating from the potential ($q_{1z} = -i\mu_{1\perp}$ from Eq. (B.5.7)), there is also a singularity emerging from the gluon propagator:

$$\bar{q}_1 = -\frac{\mathbf{k}^2}{xE^+} - \frac{\mathbf{p}^2}{(1-x)E^+} - i\epsilon = -\frac{\mathbf{k}^2}{2\omega} - \frac{x}{1-x} \frac{(\mathbf{k} - \mathbf{q}_1)^2}{2\omega} - i\epsilon \tag{B.5.8}$$

The residue around the pole at \bar{q}_1 is computed as (the negative sign is due to the clock-wise orientation of the closed contour in the complex plain):

$$\begin{aligned}
Res(\bar{q}_1) &\approx -v\left(-\frac{\mathbf{k}^2}{xE^+} - \frac{\mathbf{p}^2}{(1-x)E^+}, \mathbf{q}_1\right) \frac{i}{E^+} e^{i\left(\frac{\mathbf{k}^2}{xE^+} + \frac{\mathbf{p}^2}{(1-x)E^+}\right)(z_1-z_0)} \\
&= -v\left(-\frac{\mathbf{k}^2}{2\omega} - \frac{x}{1-x} \frac{(\mathbf{k} - \mathbf{q}_1)^2}{2\omega}, \mathbf{q}_1\right) \frac{i}{E^+} e^{\frac{i}{2\omega} (\mathbf{k}^2 + \frac{x}{1-x} (\mathbf{k} - \mathbf{q}_1)^2)(z_1-z_0)}, \tag{B.5.9}
\end{aligned}$$

while the second pole ($q_{1z} = -i\mu_{1\perp}$) does not contribute to the longitudinal integral, since residue around that pole is exponentially suppressed in the well-separated case $\mu_E(z_1 - z_0) = \mu_E\lambda \gg 1$ (and $\mu_E \sim \mu_{1\perp}$):

$$\text{Res}(-i\mu_{1\perp}) \approx -i \frac{4\pi\alpha_s}{(-2i\mu_{1\perp})E^+(-i\mu_{1\perp})} e^{-\mu_{1\perp}(z_1-z_0)} \longrightarrow 0, \quad (\text{B.5.10})$$

where we assumed that $E^+ \gg \mu_E$ and soft rescattering approximation.

This makes only \bar{q}_1 singularity relevant for calculating longitudinal integral. Therefore I_1 coincides with (B.5.9), i.e.:

$$\begin{aligned} I_1(p, k, \mathbf{q}_1, z_1 - z_0) &\approx -v\left(-\frac{\mathbf{k}^2}{xE^+} - \frac{\mathbf{p}^2}{(1-x)E^+}, \mathbf{q}_1\right) \frac{i}{E^+} e^{i\left(\frac{\mathbf{k}^2}{xE^+} + \frac{\mathbf{p}^2}{(1-x)E^+}\right)(z_1-z_0)} \\ &\approx -v(0, \mathbf{q}_1) \frac{i}{E^+} e^{i\left(\frac{\mathbf{k}^2}{xE^+} + \frac{\mathbf{p}^2}{(1-x)E^+}\right)(z_1-z_0)} \\ &= -v(0, \mathbf{q}_1) \frac{i}{E^+} e^{\frac{i}{2\omega}(\mathbf{k}^2 + \frac{x}{1-x}(\mathbf{k}-\mathbf{q}_1)^2)(z_1-z_0)}, \end{aligned} \quad (\text{B.5.11})$$

where we used eikonal approximation (i.e. for a finite x : $\frac{\mathbf{k}^2}{(xE^+)^2} \ll 1$ and $\frac{\mathbf{p}^2}{((1-x)E^+)^2} \ll 1$). Finally, $M_{1,1,0}$ amplitude reads:

$$\begin{aligned} M_{1,1,0} &= J_a(p+k) e^{i(p+k)x_0} (-i)(1-x+x^2) f^{bcd} f^{a_1ab} T_{a_1} \int \frac{d^2\mathbf{q}_1}{(2\pi)^2} v(0, \mathbf{q}_1) e^{-i\mathbf{q}_1 \cdot \mathbf{b}_1} \\ &\quad \times (-2ig_s) \frac{\boldsymbol{\epsilon} \cdot ((1-x)\mathbf{k} - x\mathbf{p})}{((1-x)\mathbf{k} - x\mathbf{p})^2} e^{i\left(\frac{\mathbf{k}^2}{xE^+} + \frac{\mathbf{p}^2}{(1-x)E^+}\right)(z_1-z_0)} \\ &= J_a(p+k) e^{i(p+k)x_0} (-i)(1-x+x^2) (T^c T^{a_1})_{da} T_{a_1} \int \frac{d^2\mathbf{q}_1}{(2\pi)^2} v(0, \mathbf{q}_1) e^{-i\mathbf{q}_1 \cdot \mathbf{b}_1} \\ &\quad \times (-2ig_s) \frac{\boldsymbol{\epsilon} \cdot (\mathbf{k} - x\mathbf{q}_1)}{(\mathbf{k} - x\mathbf{q}_1)^2} e^{\frac{i}{2\omega}(\mathbf{k}^2 + \frac{x}{1-x}(\mathbf{k}-\mathbf{q}_1)^2)(z_1-z_0)}, \end{aligned} \quad (\text{B.5.12})$$

where we denoted $\mathbf{b}_1 \equiv \mathbf{x}_1 - \mathbf{x}_0$. In this subsection, we constantly make use of the following relation between gluon transverse momenta, that holds for all three diagrams corresponding to the interaction with one scattering center:

$$\mathbf{q}_1 = \mathbf{p} + \mathbf{k} \Rightarrow \mathbf{p}^2 = (\mathbf{k} - \mathbf{q}_1)^2, \quad (\text{B.5.13})$$

and also manipulate with $\text{SU}(N_c = 3)$ structure constants by using (B.1.5, B.1.6). Eq. (B.5.12) in soft-gluon approximation (i.e. for $x \ll 1$) leads to Eq.(A8) from [183] and also to the massless limit of Eq.(51) from [189]. Note also from Fig. B.2 that, as expected, $M_{1,1,0}$ is symmetric under the substitutions: ($p \leftrightarrow k, x \leftrightarrow (1-x), c \leftrightarrow d$), where the symmetry can be straightforwardly verified by implementing these substitutions in the first two lines of (B.5.12).

B.5.2. Computation of $M_{1,0,0}$ diagram

Applying the same procedure as in the previous subsection, we proceed with calculating $M_{1,0,0}$. Note that the order of the color and Dirac indices denoting vertices is the same for all three diagrams in Fig. B.2, and are therefore omitted in the last two diagrams.

$$\begin{aligned}
M_{1,0,0} &= \int \frac{d^4 q_1}{(2\pi)^4} \epsilon_\sigma^*(p) f^{bda_1} \left(g^{\nu 0} (p - 2q_1)^\sigma + g^{\nu\sigma} (-2p + q_1)^0 + g^{\sigma 0} (p + q_1)^\nu \right) T_{a_1} V(q_1) e^{iq_1 x_1} \\
&\times \frac{(-i) \delta_{bb'} g_{\nu\nu'}}{(p - q_1)^2 + i\epsilon} g_s f^{acb'} \left(g^{\mu\nu'} (2p + k - 2q_1)^\rho + g^{\mu\rho} (-p - 2k + q_1)^{\nu'} + g^{\rho\nu'} (-p + k + q_1)^\mu \right) \\
&\times \epsilon_\rho^*(k) \frac{(-i) \delta_{aa'} g_{\mu\mu'}}{(p + k - q_1)^2 + i\epsilon} i J_{a'} (p + k - q_1) \epsilon^{\mu'} (p + k - q_1) e^{i(p+k-q_1)x_0} \\
&\approx J_a(p+k) e^{i(p+k)x_0} f^{bda_1} f^{acb} T_{a_1} (-i) (1-x+x^2) E^+ \int \frac{d^2 \mathbf{q}_1}{(2\pi)^2} e^{-i\mathbf{q}_1 \cdot \mathbf{b}_1} 2g_s \frac{\boldsymbol{\epsilon} \cdot \mathbf{k}}{x} I_2,
\end{aligned} \tag{B.5.14}$$

where:

$$I_2(p, k, \mathbf{q}_1, z_1 - z_0) \equiv \int \frac{dq_{1z}}{2\pi} \frac{v(q_{1z}, \mathbf{q}_1) e^{-iq_{1z}(z_1 - z_0)}}{((p+k-q_1)^2 + i\epsilon)((p-q_1)^2 + i\epsilon)}. \tag{B.5.15}$$

In order to calculate the previous integral, due to $z_1 > z_0$ we again have to close the contour below the real axis. Similarly as in $M_{1,1,0}$ amplitude, again only the poles originating from the propagators contribute to the integral: $(-\frac{\mathbf{k}^2}{xE^+} - \frac{\mathbf{p}^2}{(1-x)E^+} - i\epsilon)$ and $(\frac{\mathbf{k}^2 - \mathbf{p}^2}{(1-x)E^+} - i\epsilon)$, while $(-i\mu_{1\perp})$ is exponentially suppressed (due to $\mu_E(z_1 - z_0) \gg 1$). Therefore we obtain:

$$\begin{aligned}
I_2(p, k, \mathbf{q}_1, z_1 - z_0) &\approx \frac{ix}{E+\mathbf{k}^2} v(0, \mathbf{q}_1) \left(e^{i(\frac{\mathbf{k}^2}{xE^+} + \frac{\mathbf{p}^2}{(1-x)E^+})(z_1 - z_0)} - e^{i(\frac{\mathbf{p}^2 - \mathbf{k}^2}{(1-x)E^+})(z_1 - z_0)} \right) \\
&\approx \frac{ix}{E+\mathbf{k}^2} v(0, \mathbf{q}_1) \left(e^{\frac{i}{2\omega}(\mathbf{k}^2 + \frac{x}{1-x}(\mathbf{k} - \mathbf{q}_1)^2)(z_1 - z_0)} - e^{\frac{i}{2\omega} \frac{x}{1-x}((\mathbf{k} - \mathbf{q}_1)^2 - \mathbf{k}^2)(z_1 - z_0)} \right),
\end{aligned} \tag{B.5.16}$$

leading to:

$$\begin{aligned}
M_{1,0,0} &= J_a(p+k) e^{i(p+k)x_0} (-i) (1-x+x^2) f^{bda_1} f^{acb} T_{a_1} \int \frac{d^2 \mathbf{q}_1}{(2\pi)^2} v(0, \mathbf{q}_1) e^{-i\mathbf{q}_1 \cdot \mathbf{b}_1} \\
&\times (2ig_s) \frac{\boldsymbol{\epsilon} \cdot \mathbf{k}}{\mathbf{k}^2} \left(e^{i(\frac{\mathbf{k}^2}{xE^+} + \frac{\mathbf{p}^2}{(1-x)E^+})(z_1 - z_0)} - e^{i(\frac{\mathbf{p}^2 - \mathbf{k}^2}{(1-x)E^+})(z_1 - z_0)} \right) \\
&= J_a(p+k) e^{i(p+k)x_0} (-i) (1-x+x^2) (T^{a_1} T^c)_{da} T_{a_1} \int \frac{d^2 \mathbf{q}_1}{(2\pi)^2} v(0, \mathbf{q}_1) e^{-i\mathbf{q}_1 \cdot \mathbf{b}_1} \\
&\times (2ig_s) \frac{\boldsymbol{\epsilon} \cdot \mathbf{k}}{\mathbf{k}^2} \left(e^{\frac{i}{2\omega}(\mathbf{k}^2 + \frac{x}{1-x}(\mathbf{k} - \mathbf{q}_1)^2)(z_1 - z_0)} - e^{-\frac{i}{2\omega} \frac{x}{1-x}(\mathbf{k}^2 - (\mathbf{k} - \mathbf{q}_1)^2)(z_1 - z_0)} \right).
\end{aligned} \tag{B.5.17}$$

Also (B.5.17) in soft-gluon approximation (i.e. for $x \ll 1$) leads to the massless limit of Eq.(45) from [189].

B.5.3. Computation of $M_{1,0,1}$ diagram

Finally, we calculate $M_{1,0,1}$ amplitude:

$$\begin{aligned}
M_{1,0,1} &= \int \frac{d^4 q_1}{(2\pi)^4} \epsilon_\rho^*(k) f^{bca_1} \left(g^{\nu 0} (k - 2q_1)^\rho + g^{\nu\rho} (-2k + q_1)^0 + g^{\rho 0} (k + q_1)^\nu \right) T_{a_1} V(q_1) e^{iq_1 x_1} \\
&\times \frac{(-i) \delta_{bb'} g_{\nu\nu'}}{(k - q_1)^2 + i\epsilon} g_s f^{adb'} \left(g^{\mu\nu'} (p + 2k - 2q_1)^\sigma + g^{\mu\sigma} (-2p - k + q_1)^{\nu'} + g^{\sigma\nu'} (p - k + q_1)^\mu \right) \\
&\times \epsilon_\sigma^*(p) \frac{(-i) \delta_{aa'} g_{\mu\mu'}}{(p + k - q_1)^2 + i\epsilon} i J_{a'} (p + k - q_1) \epsilon^{\mu'} (p + k - q_1) e^{i(p+k-q_1)x_0} \\
&\approx J_a (p + k) e^{i(p+k)x_0} f^{bca_1} f^{adb} T_{a_1} (-i) (1 - x + x^2) \int \frac{d^2 \mathbf{q}_1}{(2\pi)^2} e^{-i\mathbf{q}_1 \cdot \mathbf{b}_1} 2g_s \frac{\boldsymbol{\epsilon} \cdot \mathbf{P}}{(1-x)E^+} E^+ I_3
\end{aligned} \tag{B.5.18}$$

where the longitudinal momentum transfer integral:

$$I_3(p, k, \mathbf{q}_1, z_1 - z_0) \equiv \int \frac{dq_{1z}}{2\pi} \frac{v(q_{1z}, \mathbf{q}_1) e^{-iq_{1z}(z_1 - z_0)}}{((p + k - q_1)^2 + i\epsilon)((k - q_1)^2 + i\epsilon)} \tag{B.5.19}$$

again has to be performed in the lower half-plane of the complex plain, since $z_1 > z_0$. Aside from the pole originating from the potential ($q_{1z} = -i\mu_{1\perp}$), which is again exponentially suppressed, there are also singularities emerging from the gluon propagators ($-\frac{\mathbf{k}^2}{xE^+} - \frac{\mathbf{p}^2}{(1-x)E^+} - i\epsilon$) and ($\frac{\mathbf{p}^2 - \mathbf{k}^2}{xE^+} - i\epsilon$), which are the only two poles contributing to the longitudinal integral:

$$\begin{aligned}
I_3(p, k, \mathbf{q}_1, z_1 - z_0) &\approx \frac{i(1-x)}{E^+ \mathbf{p}^2} v(0, \mathbf{q}_1) \left(e^{i\left(\frac{\mathbf{k}^2}{xE^+} + \frac{\mathbf{p}^2}{(1-x)E^+}\right)(z_1 - z_0)} - e^{i\frac{\mathbf{k}^2 - \mathbf{p}^2}{xE^+}(z_1 - z_0)} \right) \\
&\approx \frac{i(1-x)}{E^+ (\mathbf{k} - \mathbf{q}_1)^2} v(0, \mathbf{q}_1) \left(e^{\frac{i}{2\omega} (\mathbf{k}^2 + \frac{x}{1-x} (\mathbf{k} - \mathbf{q}_1)^2)(z_1 - z_0)} - e^{\frac{i}{2\omega} (\mathbf{k}^2 - (\mathbf{k} - \mathbf{q}_1)^2)(z_1 - z_0)} \right).
\end{aligned} \tag{B.5.20}$$

Finally, by substituting (B.5.20) in (B.5.18), for $M_{1,0,1}$ amplitude we obtain:

$$\begin{aligned}
M_{1,0,1} &= J_a(p+k)e^{i(p+k)x_0}(-i)(1-x+x^2)f^{bca_1}f^{adb}T_{a_1}\int\frac{d^2\mathbf{q}_1}{(2\pi)^2}v(0,\mathbf{q}_1)e^{-i\mathbf{q}_1\cdot\mathbf{b}_1} \\
&\quad\times(2ig_s)\frac{\boldsymbol{\epsilon}\cdot\mathbf{p}}{\mathbf{p}^2}\left(e^{i(\frac{\mathbf{k}^2}{xE^+}+\frac{\mathbf{p}^2}{(1-x)E^+})(z_1-z_0)}-e^{i\frac{(\mathbf{k}^2-\mathbf{p}^2)}{xE^+}(z_1-z_0)}\right) \\
&= J_a(p+k)e^{i(p+k)x_0}(-i)(1-x+x^2)[T^c,T^{a_1}]_{da}T_{a_1}\int\frac{d^2\mathbf{q}_1}{(2\pi)^2}v(0,\mathbf{q}_1)e^{-i\mathbf{q}_1\cdot\mathbf{b}_1} \\
&\quad\times(2ig_s)\frac{\boldsymbol{\epsilon}\cdot(\mathbf{k}-\mathbf{q}_1)}{(\mathbf{k}-\mathbf{q}_1)^2}\left(e^{\frac{i}{2\omega}(\mathbf{k}^2+\frac{x}{1-x}(\mathbf{k}-\mathbf{q}_1)^2)(z_1-z_0)}-e^{\frac{i}{2\omega}(\mathbf{k}^2-(\mathbf{k}-\mathbf{q}_1)^2)(z_1-z_0)}\right).
\end{aligned}
\tag{B.5.21}$$

Eq. (B.5.21) in soft gluon approximation (i.e. for $x \ll 1$) leads to Eq.(A7) from [183] and also to the massless limit of Eq.(41) from [189].

Notice from Fig. B.2 that $M_{1,0,1}$ and $M_{1,0,0}$ are symmetric under the following substitutions: ($p \leftrightarrow k, x \leftrightarrow (1-x), c \leftrightarrow d$); it can be straightforwardly verified that Eqs.(B.5.17, B.5.21) are symmetric under these substitutions.

B.6. Diagram M_{220}

Next we concentrate on the diagrams containing two interactions with the static scattering centers, since they also contribute to the gluon radiative energy loss to the first order in opacity, when multiplied by M_0^* . There are seven such diagrams, that we gather into four groups, each of which contains two (or one) diagrams symmetric under ($p \leftrightarrow k, x \leftrightarrow (1-x), c \leftrightarrow d$) substitutions.

For consistency the initial g-jet (with momentum $p+k-q_1-q_2$) propagates along z-axis, i.e.:

$$p+k-q_1-q_2=[E^+-q_{1z}-q_{2z},E^-+q_{1z}+q_{2z},\mathbf{0}],\tag{B.6.1}$$

$$\epsilon_i(p+k-q_1-q_2)=[0,0,\epsilon_i],\tag{B.6.2}$$

where $q_i=[q_{iz},-q_{iz},\mathbf{q}_i]$, $i=1,2$ with $q_i^0=0$, while p, k and corresponding polarizations retain the same expressions as in Eqs.(B.4.2, B.4.3, B.4.6), with distinction that, due to 4-momentum conservation, the following relation between gluon transverse momenta holds:

$$\mathbf{p}+\mathbf{k}=\mathbf{q}_1+\mathbf{q}_2.\tag{B.6.3}$$

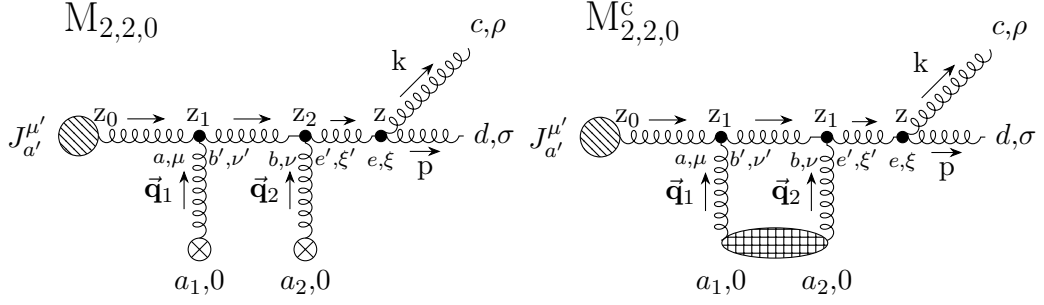


Figure B.3: Feynman diagram $M_{2,2,0}$ and its contribution to the first order in opacity gluon-jet radiative energy loss: contact-limit $M_{2,2,0}^c$. z_i , where $i = 1, 2$, denotes longitudinal coordinate of the interactions with the consecutive scattering centers (or in the contact limit $z_1 = z_2$). Crossed circles represent scatterers that exchange transverse momentum \vec{q}_i with the jet, which in contact-limit case merge into one gridded ellipse. Note that, all the following figures assume equivalently ordered Latin and Greek indices as in this figure. Remaining labeling is the same as in Figs.(B.1, B.2).

Again, from seven diagrams we chose one model diagram $M_{2,2,0}$, based on the same reason as in section D, for thorough derivation of the final amplitude expression. From Fig. B.3, where gluon-jet after two consecutive interactions with scattering centers radiates a gluon with momentum k , we observe that there are two limiting cases that we consider.

Using the notation from Fig. B.3 we write:

$$\begin{aligned}
M_{2,2,0} &= \int \frac{d^4 q_1}{(2\pi)^4} \frac{d^4 q_2}{(2\pi)^4} \epsilon_\sigma^*(p) \epsilon_\rho^*(k) g_s f^{ecd} \left(g^{\xi\sigma} (2p+k)^\rho + g^{\xi\rho} (-p-2k)^\sigma + g^{\rho\sigma} (-p+k)^\xi \right) \\
&\times \frac{-i\delta_{ee'} g_{\xi\xi'}}{(p+k)^2 + i\epsilon} f^{be'a_2} \left(g^{\nu 0} (p+k-2q_2)^{\xi'} + g^{\nu\xi'} (-2p-2k+q_2)^0 \right) \\
&+ g^{\xi'0} (p+k+q_2)^\nu T_{a_2} V(q_2) e^{iq_2 x_2} \frac{-i\delta_{bb'} g_{\nu\nu'}}{(p+k-q_2)^2 + i\epsilon} T_{a_1} V(q_1) e^{iq_1 x_1} f^{ab'a_1} \\
&\times \left(g^{\mu 0} (p+k-2q_1-q_2)^{\nu'} + g^{\mu\nu'} (-2p-2k+q_1+2q_2)^0 + g^{\nu'0} (p+k+q_1-q_2)^\mu \right) \\
&\times \frac{-i\delta_{aa'} g_{\mu\mu'}}{(p+k-q_1-q_2)^2 + i\epsilon} iJ_{a'}(p+k-q_1-q_2)\epsilon^{\mu'}(p+k-q_1-q_2) e^{i(p+k-q_1-q_2)x_0} \\
&\approx iJ_a(p+k) e^{i(p+k)x_0} f^{ecd} f^{bea_2} f^{aba_1} T_{a_2} T_{a_1} (1-x+x^2) (-i) \int \frac{d^2 \mathbf{q}_1}{(2\pi)^2} \\
&\times (-i) \int \frac{d^2 \mathbf{q}_2}{(2\pi)^2} 2ig_s \frac{\boldsymbol{\epsilon} \cdot ((1-x)\mathbf{k} - x\mathbf{p})}{((1-x)\mathbf{k} - x\mathbf{p})^2} e^{-i\mathbf{q}_1 \cdot \mathbf{b}_1} e^{-i\mathbf{q}_2 \cdot \mathbf{b}_2} (E^+)^2 \\
&\times \int \frac{dq_{1z}}{2\pi} \frac{dq_{2z}}{2\pi} \frac{v(q_{1z}, \mathbf{q}_1) v(q_{2z}, \mathbf{q}_2) e^{-iq_{1z}(z_1-z_0)} e^{-iq_{2z}(z_2-z_0)}}{((p+k-q_1-q_2)^2 + i\epsilon)((p+k-q_2)^2 + i\epsilon)}, \tag{B.6.4}
\end{aligned}$$

where $\mathbf{b}_i \equiv \mathbf{x}_i - \mathbf{x}_0$, $i = 1, 2$ denote transverse impact parameters. We used Eq. (B.5.5) and assumed that J varies slowly with momentum q_i , i.e. $J(p+k-q_1-q_2) \approx J(p+k)$.

Regarding the longitudinal q_{1z} integral, we introduce a new variable: $q_z = q_{1z} + q_{2z}$ throughout this, and the following sections involving Feynman amplitudes which include interactions with two scattering centers. Therefore, we rewrite the exponent in the following manner: $e^{-iq_{1z}(z_1-z_0)}e^{-iq_{2z}(z_2-z_0)} = e^{-iq_z(z_1-z_0)}e^{-iq_{2z}(z_2-z_1)}$. Rewriting q_{1z} longitudinal integral in terms of q_z , i.e. changing the variables, we obtain:

$$I_2(p, k, \mathbf{q}_1, \vec{\mathbf{q}}_2, z_1 - z_0) = \int \frac{dq_z}{2\pi} \frac{v(q_z - q_{2z}, \mathbf{q}_1) e^{-iq_z(z_1-z_0)}}{(p+k-q_1-q_2)^2 + i\epsilon} \quad (\text{B.6.5})$$

Again, due to $z_1 > z_0$, the contour must be closed in the lower half-plane of complex q_z plain, so additional minus sign arises from the negative orientation of the contour and also we neglect the pole at $q_z = -i\mu_{1\perp} + q_{2z}$, since it is exponentially suppressed in the well-separated case $\mu_E(z_1 - z_0) = \mu_E \lambda \gg 1$. Thus, only one pole, originating from the gluon propagator, contributes to the first longitudinal integral:

$$\bar{q} = -\frac{\mathbf{k}^2}{xE^+} - \frac{\mathbf{p}^2}{(1-x)E^+} - i\epsilon = -\frac{\mathbf{k}^2}{2\omega} - \frac{x}{1-x} \frac{(\mathbf{k} - \mathbf{q}_1 - \mathbf{q}_2)^2}{2\omega} - i\epsilon, \quad (\text{B.6.6})$$

where we used, as well as throughout Appendix Sections B.7 to B.9, the relation between transverse momenta given by Eq. (B.6.3). The residue at (B.6.6) then gives:

$$I_2(p, k, \mathbf{q}_1, \vec{\mathbf{q}}_2, z_1 - z_0) \approx -v\left(-q_{2z} - \frac{\mathbf{k}^2}{2\omega} - \frac{x}{1-x} \frac{(\mathbf{k} - \mathbf{q}_1 - \mathbf{q}_2)^2}{2\omega}, \mathbf{q}_1\right) \frac{i}{E^+} \\ \times e^{\frac{i}{2\omega}(\mathbf{k}^2 + \frac{x}{1-x}(\mathbf{k} - \mathbf{q}_1 - \mathbf{q}_2)^2)(z_1 - z_0)} \quad (\text{B.6.7})$$

Next we need to solve the remaining q_{2z} longitudinal momentum transfer integral:

$$I_3(p, k, \mathbf{q}_1, \mathbf{q}_2, z_2 - z_1) = \int \frac{dq_{2z}}{2\pi} \frac{v\left(-q_{2z} - \frac{\mathbf{k}^2}{2\omega} - \frac{x}{1-x} \frac{(\mathbf{k} - \mathbf{q}_1 - \mathbf{q}_2)^2}{2\omega}, \mathbf{q}_1\right) v(q_{2z}, \mathbf{q}_2) e^{-iq_{2z}(z_2-z_1)}}{(p+k-q_2)^2 + i\epsilon} \quad (\text{B.6.8})$$

Luckily, we are interested only in two limiting cases:

- The limit of well separated scattering centers $z_2 - z_1 \gg 1/\mu_E$, where poles originating from Yukawa potentials are exponentially suppressed;
- The contact limit $z_1 = z_2$, where these poles contribute to the final results.

In the case of two distinct scatterers ($z_1 \neq z_2$) and in the limit of well-separated scattering centers there is only one pole that contributes to the residue (the singularities originating from Yukawa potential once again are exponential suppressed):

$$\bar{q} = -\frac{\mathbf{k}^2}{xE^+} - \frac{\mathbf{p}^2}{(1-x)E^+} + \frac{\mathbf{q}_1^2}{E^+} - i\epsilon = -\frac{\mathbf{k}^2}{2\omega} - \frac{x}{1-x} \frac{(\mathbf{k} - \mathbf{q}_1 - \mathbf{q}_2)^2}{2\omega} + \frac{\mathbf{q}_1^2}{E^+} - i\epsilon, \quad (\text{B.6.9})$$

Since $z_2 > z_1$ again we close the contour below the real q_{2z} axis and thus obtain:

$$I_3(p, k, \mathbf{q}_1, \mathbf{q}_2, z_2 - z_1) \approx -v(0, \mathbf{q}_1)v(0, \mathbf{q}_2) \frac{i}{E^+} e^{\frac{i}{2\omega}(\mathbf{k}^2 + \frac{x}{1-x}(\mathbf{k} - \mathbf{q}_1 - \mathbf{q}_2)^2 - x\mathbf{q}_1^2)(z_2 - z_1)} \quad (\text{B.6.10})$$

In the special case of contact limit, i.e. when $z_1 = z_2$, instead of (B.6.8) we need to calculate the following q_{2z} integral:

$$I_3^c(p, k, \mathbf{q}_1, \mathbf{q}_2, 0) = \int \frac{dq_{2z}}{2\pi} \frac{v(-q_{2z} - \frac{\mathbf{k}^2}{2\omega} - \frac{x}{1-x} \frac{(\mathbf{k} - \mathbf{q}_1 - \mathbf{q}_2)^2}{2\omega}, \mathbf{q}_1)v(q_{2z}, \mathbf{q}_2)}{(p + k - q_2)^2 + i\epsilon} \quad (\text{B.6.11})$$

Now, the contributions from Yukawa singularities ($q_{2z} = -i\mu_{1\perp}$, $q_{2z} = -i\mu_{2\perp}$) are not negligible and need to be included together with (B.6.6). By choosing the same integration contour we obtain:

$$\begin{aligned} I_3^c(p, k, \mathbf{q}_1, \mathbf{q}_2, 0) &\approx \frac{-i}{E^+} \left(v(0, \mathbf{q}_1)v(0, \mathbf{q}_2) - \frac{(4\pi\alpha_s)^2}{2} \frac{1}{\mu_{2\perp}^2 - \mu_{1\perp}^2} \left(\frac{1}{\mu_{1\perp}^2} - \frac{1}{\mu_{2\perp}^2} \right) \right) \\ &= -v(0, \mathbf{q}_1)v(0, \mathbf{q}_2) \frac{i}{2E^+}, \end{aligned} \quad (\text{B.6.12})$$

which is exactly $\frac{1}{2}$ of the strength of Eq. (B.6.10). Note that, in previous calculations we applied soft rescattering approximation and also assumed $E^+ \gg \mu_{i\perp}$, $i = 1, 2$.

Finally, contact limit of this amplitude reads:

$$\begin{aligned} M_{2,2,0}^c &= -iJ_a(p+k)e^{i(p+k)x_0} f^{ecd} f^{bea_2} f^{aba_1} T_{a_2} T_{a_1} (1-x+x^2) \\ &\quad \times (-i) \int \frac{d^2\mathbf{q}_1}{(2\pi)^2} (-i) \int \frac{d^2\mathbf{q}_2}{(2\pi)^2} v(0, \mathbf{q}_1)v(0, \mathbf{q}_2) e^{-i(\mathbf{q}_1 + \mathbf{q}_2) \cdot \mathbf{b}_1} \\ &\quad \times \frac{1}{2} 2ig_s \frac{\boldsymbol{\epsilon} \cdot ((1-x)\mathbf{k} - x\mathbf{p})}{((1-x)\mathbf{k} - x\mathbf{p})^2} e^{i(\frac{\mathbf{k}^2}{xE^+} + \frac{\mathbf{p}^2}{(1-x)E^+})(z_1 - z_0)} \\ &= -J_a(p+k)e^{i(p+k)x_0} (T^c T^{a_2} T^{a_1})_{da} T_{a_2} T_{a_1} (1-x+x^2) \\ &\quad \times (-i) \int \frac{d^2\mathbf{q}_1}{(2\pi)^2} (-i) \int \frac{d^2\mathbf{q}_2}{(2\pi)^2} v(0, \mathbf{q}_1)v(0, \mathbf{q}_2) e^{-i(\mathbf{q}_1 + \mathbf{q}_2) \cdot \mathbf{b}_1} \\ &\quad \times \frac{1}{2} 2ig_s \frac{\boldsymbol{\epsilon} \cdot (\mathbf{k} - x(\mathbf{q}_1 + \mathbf{q}_2))}{(\mathbf{k} - x(\mathbf{q}_1 + \mathbf{q}_2))^2} e^{\frac{i}{2\omega}(\mathbf{k}^2 + \frac{x}{1-x}(\mathbf{k} - \mathbf{q}_1 - \mathbf{q}_2)^2)(z_1 - z_0)}, \end{aligned} \quad (\text{B.6.13})$$

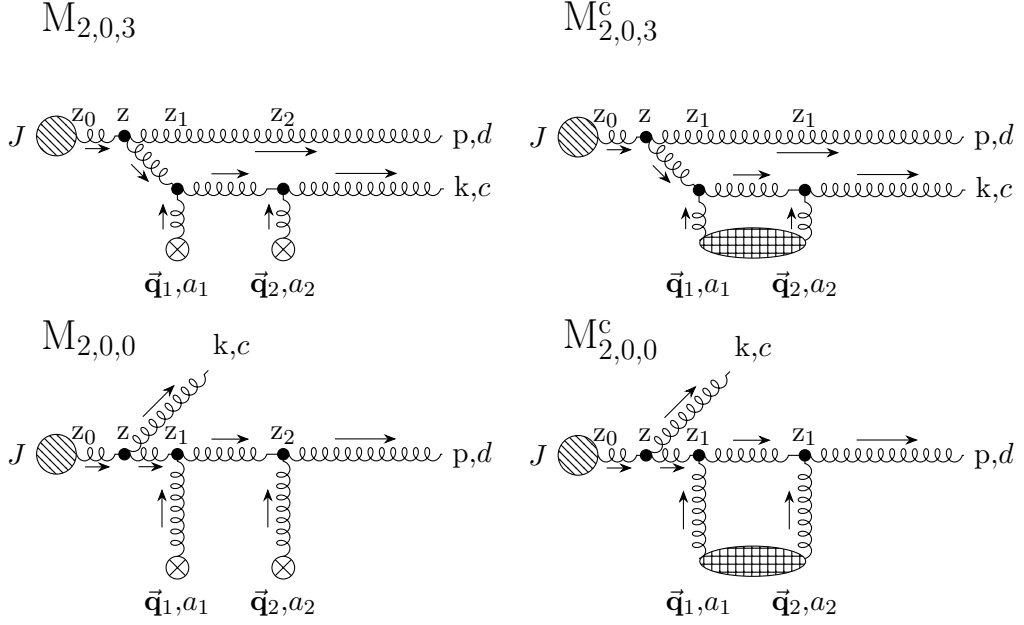


Figure B.4: Feynman diagrams $M_{2,0,3}$ and $M_{2,0,0}$ in well separated (left column) and in contact-limit case ($z_1 = z_2$), which contributes to the first order in opacity of gluon-jet radiative energy loss: $M_{2,0,3}^c$ and $M_{2,0,0}^c$ (right column). Remaining labeling is the same as in Fig. B.3.

where we applied (B.6.3) and manipulated with $SU(N_c = 3)$ structure constants by using (B.1.5, B.1.6). Also we assumed that $\mathbf{x}_1 = \mathbf{x}_2$, since we are interested in ensemble averaged values.

Note also that, we would naturally come to "contact-limit" case and the aforementioned assumption in our calculations of radiative energy loss, since according to Eq.(B.1.4) the trace would demand the equalities $z_1 = z_2$ and $\mathbf{b}_1 = \mathbf{b}_2$. Eq. (B.6.13) in soft gluon approximation (i.e. for $x \ll 1$) leads to the massless limit of Eq.(67) from [189]. Note also from Fig. B.3 that $M_{2,2,0}$ is symmetric under the substitutions: ($p \leftrightarrow k, x \leftrightarrow (1 - x), c \leftrightarrow d$), which can be straightforwardly verified by implementing these substitutions in the first three lines of (B.6.13).

B.7. Diagrams $M_{2,0,3}$ and $M_{2,0,0}$

Next we consider $M_{2,0,3}$ diagram, where the radiated gluon suffers two consecutive interactions with the QCD medium (the first row of Fig. B.4). Note that the order

of the color and Dirac indices denoting vertices is the same for all the remaining diagrams containing two interactions with the scatterers as in Fig. B.3, and therefore omitted onward.

$$\begin{aligned}
M_{2,0,3} &= \int \frac{d^4 q_1}{(2\pi)^4} \frac{d^4 q_2}{(2\pi)^4} \epsilon_\rho^*(k) f^{eca_2} \left(g^{\xi 0} (k - 2q_2)^\rho + g^{\xi \rho} (-2k + q_2)^0 + g^{\rho 0} (k + q_2)^\xi \right) T_{a_2} V(q_2) e^{iq_2 x_2} \\
&\times \frac{-i\delta_{ee'} g_\xi \xi'}{(k - q_2)^2 + i\epsilon} f^{be'a_1} \left(g^{\nu 0} (k - 2q_1 - q_2)^{\xi'} + g^{\nu \xi'} (-2k + q_1 + 2q_2)^0 + g^{\xi' 0} (k + q_1 - q_2)^\nu \right) \\
&\times T_{a_1} V(q_1) e^{iq_1 x_1} \frac{-i\delta_{bb'} g_{\nu\nu'}}{(k - q_1 - q_2)^2 + i\epsilon} \epsilon_\sigma^*(p) g_s f^{adb'} \left(g^{\mu\nu'} (p + 2k - 2q_1 - 2q_2)^\sigma \right. \\
&\left. + g^{\mu\sigma} (-2p - k + q_1 + q_2)^{\nu'} + g^{\sigma\nu'} (p - k + q_1 + q_2)^\mu \right) \frac{-i\delta_{aa'} g_{\mu\mu'}}{(p + k - q_1 - q_2)^2 + i\epsilon} \\
&\times iJ_{a'}(p + k - q_1 - q_2) \epsilon^{\mu'}(p + k - q_1 - q_2) e^{i(p+k-q_1-q_2)x_0} \\
&\approx iJ_a(p + k) e^{i(p+k)x_0} f^{eca_2} f^{bea_1} f^{adb} T_{a_2} T_{a_1} \frac{(1 - x + x^2)}{1 - x} \\
&\times (-i) \int \frac{d^2 \mathbf{q}_1}{(2\pi)^2} (-i) \int \frac{d^2 \mathbf{q}_2}{(2\pi)^2} (2ig_s) \boldsymbol{\epsilon} \cdot \mathbf{p} e^{-i\mathbf{q}_1 \cdot \mathbf{b}_1} e^{-i\mathbf{q}_2 \cdot \mathbf{b}_2} \\
&\times \int \frac{dq_{1z}}{2\pi} \frac{dq_{2z}}{2\pi} \frac{E^+ k^+ v(q_{1z}, \mathbf{q}_1) v(q_{2z}, \mathbf{q}_2) e^{-iq_{1z}(z_1 - z_0)} e^{-iq_{2z}(z_2 - z_0)}}{((p + k - q_1 - q_2)^2 + i\epsilon)((k - q_1 - q_2)^2 + i\epsilon)((k - q_2)^2 + i\epsilon)}.
\end{aligned} \tag{B.7.1}$$

Next, again by changing the variables $q_{1z} \rightarrow q_z = q_{1z} + q_{2z}$, we define the following integral:

$$I_2(p, k, \mathbf{q}_1, \vec{\mathbf{q}}_2, z_1 - z_0) = \int \frac{dq_z}{2\pi} \frac{v(q_z - q_{2z}, \mathbf{q}_1) e^{-iq_z(z_1 - z_0)}}{((p + k - q_1 - q_2)^2 + i\epsilon)((k - q_1 - q_2)^2 + i\epsilon)}. \tag{B.7.2}$$

Again, as explained in the previous section, we close the contour in lower half-plane, and since $\mu_E(z_1 - z_0) \gg 1$ the pole at $q_z = -i\mu_{1\perp} + q_{2z}$ is again exponentially suppressed. Therefore the remaining q_z singularities originating from gluon propagators are:

$$\begin{aligned}
\bar{q}_1 &= -\frac{\mathbf{k}^2}{xE^+} - \frac{\mathbf{p}^2}{(1-x)E^+} - i\epsilon = -\frac{\mathbf{k}^2}{2\omega} - \frac{x}{1-x} \frac{(\mathbf{k} - \mathbf{q}_1 - \mathbf{q}_2)^2}{2\omega} - i\epsilon, \\
\bar{q}_2 &= -\frac{\mathbf{k}^2}{xE^+} + \frac{\mathbf{p}^2}{xE^+} - i\epsilon = -\frac{\mathbf{k}^2}{2\omega} + \frac{(\mathbf{k} - \mathbf{q}_1 - \mathbf{q}_2)^2}{2\omega} - i\epsilon.
\end{aligned} \tag{B.7.3}$$

After performing the integration, i.e. summing the residues at these two poles, I_2 now reads:

$$I_2(p, k, \mathbf{q}_1, \vec{\mathbf{q}}_2, z_1 - z_0) \approx v(-q_{2z}, \mathbf{q}_1) \frac{i(1-x)}{E^+(\mathbf{k} - \mathbf{q}_1 - \mathbf{q}_2)^2} \left(e^{\frac{i}{2\omega}(\mathbf{k}^2 + \frac{x}{1-x}(\mathbf{k} - \mathbf{q}_1 - \mathbf{q}_2)^2)(z_1 - z_0)} - e^{\frac{i}{2\omega}(\mathbf{k}^2 - (\mathbf{k} - \mathbf{q}_1 - \mathbf{q}_2)^2)(z_1 - z_0)} \right). \quad (\text{B.7.4})$$

The remaining integral over q_{2z} is:

$$I_3(p, k, \mathbf{q}_1, \mathbf{q}_2, z_2 - z_1) = \int \frac{dq_{2z}}{2\pi} \frac{v(-q_{2z}, \mathbf{q}_1)v(q_{2z}, \mathbf{q}_2)e^{-iq_{2z}(z_2 - z_1)}}{(k - q_2)^2 + i\epsilon}, \quad (\text{B.7.5})$$

and since we are interested only in the contact-limit case (i.e. $z_1 = z_2$), we need to calculate:

$$I_3^c(p, k, \mathbf{q}_1, \mathbf{q}_2, 0) = \int \frac{dq_{2z}}{2\pi} \frac{v(-q_{2z}, \mathbf{q}_1)v(q_{2z}, \mathbf{q}_2)}{(k - q_2)^2 + i\epsilon}, \quad (\text{B.7.6})$$

which gives:

$$I_3^c(p, k, \mathbf{q}_1, \mathbf{q}_2, 0) \approx -v(0, \mathbf{q}_1)v(0, \mathbf{q}_2) \frac{i}{2xE^+}, \quad (\text{B.7.7})$$

which can readily be shown to represent exactly $\frac{1}{2}$ of the strength of the well-separated limit Eq. (B.7.5), as for $M_{2,2,0}$ amplitude. The contact limit of this amplitude reduces to:

$$\begin{aligned} M_{2,0,3}^c &= iJ_a(p+k)e^{i(p+k)x_0} f^{eca_2} f^{bea_1} f^{adb} T_{a_2} T_{a_1} (1-x+x^2) \\ &\times (-i) \int \frac{d^2\mathbf{q}_1}{(2\pi)^2} (-i) \int \frac{d^2\mathbf{q}_2}{(2\pi)^2} v(0, \mathbf{q}_1)v(0, \mathbf{q}_2) e^{-i(\mathbf{q}_1 + \mathbf{q}_2) \cdot \mathbf{b}_1} \\ &\times \frac{1}{2}(2ig_s) \frac{\boldsymbol{\epsilon} \cdot \mathbf{p}}{\mathbf{p}^2} \left(e^{i(\frac{\mathbf{k}^2}{xE^+} + \frac{\mathbf{p}^2}{(1-x)E^+})(z_1 - z_0)} - e^{i(\frac{\mathbf{k}^2 - \mathbf{p}^2}{xE^+})(z_1 - z_0)} \right) \\ &= J_a(p+k)e^{i(p+k)x_0} [[T^c, T^{a_2}], T^{a_1}]_{da} T_{a_2} T_{a_1} (1-x+x^2) \\ &\times (-i) \int \frac{d^2\mathbf{q}_1}{(2\pi)^2} (-i) \int \frac{d^2\mathbf{q}_2}{(2\pi)^2} v(0, \mathbf{q}_1)v(0, \mathbf{q}_2) e^{-i(\mathbf{q}_1 + \mathbf{q}_2) \cdot \mathbf{b}_1} \\ &\times \frac{1}{2}(2ig_s) \frac{\boldsymbol{\epsilon} \cdot (\mathbf{k} - \mathbf{q}_1 - \mathbf{q}_2)}{(\mathbf{k} - \mathbf{q}_1 - \mathbf{q}_2)^2} \left(e^{\frac{i}{2\omega}(\mathbf{k}^2 + \frac{x}{1-x}(\mathbf{k} - \mathbf{q}_1 - \mathbf{q}_2)^2)(z_1 - z_0)} - e^{\frac{i}{2\omega}(\mathbf{k}^2 - (\mathbf{k} - \mathbf{q}_1 - \mathbf{q}_2)^2)(z_1 - z_0)} \right). \end{aligned} \quad (\text{B.7.8})$$

In the soft-gluon approximation (i.e. for $x \ll 1$) Eq. (B.7.8) leads to Eq.(B10) from [183] and also to the massless limit of Eq.(60) from [189].

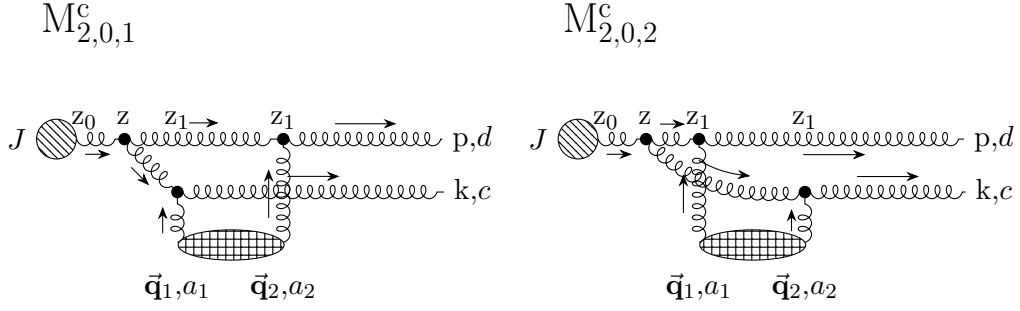


Figure B.5: Topologically indistinct Feynman diagrams $M_{2,0,1}^c$ and $M_{2,0,2}^c$ in contact limit ($z_1 = z_2$), which contribute to the first order in opacity of gluon-jet radiative energy loss. Remaining labeling is the same as in Fig. B.3.

Proceeding in the same manner, for $M_{2,0,0}^c$ amplitude we obtain:

$$\begin{aligned}
M_{2,0,0}^c &= iJ_a(p+k)e^{i(p+k)x_0}f^{eda_2}f^{bea_1}f^{acb}T_{a_2}T_{a_1}(1-x+x^2) \\
&\quad \times (-i)\int\frac{d^2\mathbf{q}_1}{(2\pi)^2}(-i)\int\frac{d^2\mathbf{q}_2}{(2\pi)^2}v(0,\mathbf{q}_1)v(0,\mathbf{q}_2)e^{-i(\mathbf{q}_1+\mathbf{q}_2)\cdot\mathbf{b}_1} \\
&\quad \times \frac{1}{2}(2ig_s)\frac{\boldsymbol{\epsilon}\cdot\mathbf{k}}{\mathbf{k}^2}\left(e^{i\left(\frac{\mathbf{k}^2}{xE^+}+\frac{\mathbf{p}^2}{(1-x)E^+}\right)(z_1-z_0)}-e^{i\frac{(\mathbf{p}^2-\mathbf{k}^2)}{(1-x)E^+}(z_1-z_0)}\right) \\
&= J_a(p+k)e^{i(p+k)x_0}(T^{a_2}T^{a_1}T^c)_{da}T_{a_2}T_{a_1}(1-x+x^2) \\
&\quad \times (-i)\int\frac{d^2\mathbf{q}_1}{(2\pi)^2}(-i)\int\frac{d^2\mathbf{q}_2}{(2\pi)^2}v(0,\mathbf{q}_1)v(0,\mathbf{q}_2)e^{-i(\mathbf{q}_1+\mathbf{q}_2)\cdot\mathbf{b}_1} \\
&\quad \times \frac{1}{2}(2ig_s)\frac{\boldsymbol{\epsilon}\cdot\mathbf{k}}{\mathbf{k}^2}\left(e^{\frac{i}{2\omega}(\mathbf{k}^2+\frac{x}{1-x}(\mathbf{k}-\mathbf{q}_1-\mathbf{q}_2)^2)(z_1-z_0)}-e^{\frac{i}{2\omega}\frac{x}{1-x}((\mathbf{k}-\mathbf{q}_1-\mathbf{q}_2)^2-\mathbf{k}^2)(z_1-z_0)}\right),
\end{aligned} \tag{B.7.9}$$

which in soft-gluon approximation (i.e. for $x \ll 1$) reduces to contact-limit analogon of Eq.(C6) from [183] and also to the massless limit of Eq.(66) from [189]. From Fig. B.4 we infer that $M_{2,0,3}$ and $M_{2,0,0}$ are symmetric under the following substitutions: ($p \leftrightarrow k, x \leftrightarrow (1-x), c \leftrightarrow d$), which can be straightforwardly verified by implementing these substitutions in Eqs.(B.7.8, B.7.9).

B.8. Diagrams $M_{2,0,1}$ and $M_{2,0,2}$

Here we consider the case when both initial gluon jet and radiated gluon interact with one scattering center. We provide only the contact-limit case diagrams $M_{2,0,1}^c$ and $M_{2,0,2}^c$ (Fig. B.5), since, in the end, only they are used in calculating radiative

energy loss to the first order in opacity.

$$\begin{aligned}
M_{2,0,1} &= \int \frac{d^4 q_1}{(2\pi)^4} \frac{d^4 q_2}{(2\pi)^4} \epsilon_\sigma^*(p) f^{eda_2} \left(g^{\xi 0} (p - 2q_2)^\sigma + g^{\xi\sigma} (-2p + q_2)^0 + g^{\sigma 0} (p + q_2)^\xi \right) T_{a_2} V(q_2) e^{iq_2 x_2} \\
&\times \frac{-i\delta_{ee'} g_{\xi\xi'}}{(p - q_2)^2 + i\epsilon} g_s f^{ae'b'} \left(g^{\mu\nu'} (p + 2k - 2q_1 - q_2)^{\xi'} + g^{\mu\xi'} (-2p - k + q_1 + 2q_2)^{\nu'} \right. \\
&+ \left. g^{\xi'\nu'} (p - k + q_1 - q_2)^\mu \right) \epsilon_\rho^*(k) f^{bca_1} \left(g^{\nu 0} (k - 2q_1)^\rho + g^{\nu\rho} (-2k + q_1)^0 + g^{\rho 0} (k + q_1)^\nu \right) \\
&\times T_{a_1} V(q_1) e^{iq_1 x_1} \frac{-i\delta_{bb'} g_{\nu\nu'}}{(k - q_1)^2 + i\epsilon} \times \frac{-i\delta_{aa'} g_{\mu\mu'}}{(p + k - q_1 - q_2)^2 + i\epsilon} \\
&\times iJ_{a'}(p + k - q_1 - q_2) \epsilon^{\mu'}(p + k - q_1 - q_2) e^{i(p+k-q_1-q_2)x_0} \\
&\approx -iJ_a(p + k) e^{i(p+k)x_0} f^{eda_2} f^{aeb} f^{bca_1} T_{a_2} T_{a_1} (1 - x + x^2) \\
&\times (-i) \int \frac{d^2 \mathbf{q}_1}{(2\pi)^2} (-i) \int \frac{d^2 \mathbf{q}_2}{(2\pi)^2} (2ig_s) \boldsymbol{\epsilon} \cdot (\mathbf{k} - \mathbf{q}_1) e^{-i\mathbf{q}_1 \cdot \mathbf{b}_1} e^{-i\mathbf{q}_2 \cdot \mathbf{b}_2} (E^+)^2 \\
&\times \int \frac{dq_{1z}}{2\pi} \frac{dq_{2z}}{2\pi} \frac{v(q_{1z}, \mathbf{q}_1) v(q_{2z}, \mathbf{q}_2) e^{-iq_{1z}(z_1 - z_0)} e^{-iq_{2z}(z_2 - z_0)}}{((p + k - q_1 - q_2)^2 + i\epsilon)((k - q_1)^2 + i\epsilon)((p - q_2)^2 + i\epsilon)}. \tag{B.8.1}
\end{aligned}$$

Again, by changing the variables $q_{1z} \rightarrow q_z = q_{1z} + q_{2z}$, we define the following integral:

$$I_2(p, k, \mathbf{q}_1, \bar{\mathbf{q}}_2, z_1 - z_0) = \int \frac{dq_z}{2\pi} \frac{v(q_z - q_{2z}, \mathbf{q}_1) e^{-iq_z(z_1 - z_0)}}{((p + k - q_1 - q_2)^2 + i\epsilon)((k - q_1)^2 + i\epsilon)}. \tag{B.8.2}$$

Since $z_1 > z_0$, we must close the contour in lower half-plane, and since $\mu_E(z_1 - z_0) \gg 1$ again we neglect the pole at $q_z = -i\mu_{1\perp} + q_{2z}$. Therefore the remaining q_z singularities originating from gluon propagators are:

$$\begin{aligned}
\bar{q}_1 &= -\frac{\mathbf{k}^2}{2\omega} - \frac{x}{1-x} \frac{(\mathbf{k} - \mathbf{q}_1 - \mathbf{q}_2)^2}{2\omega} - i\epsilon, \\
\bar{q}_2 &= -\frac{\mathbf{k}^2}{2\omega} + \frac{(\mathbf{k} - \mathbf{q}_1)^2}{2\omega} + q_{2z} - i\epsilon.
\end{aligned} \tag{B.8.3}$$

Summing the residues gives:

$$\begin{aligned}
I_2(p, k, \mathbf{q}_1, \bar{\mathbf{q}}_2, z_1 - z_0) &\approx \frac{ie^{i\frac{\mathbf{k}^2}{2\omega}(z_1 - z_0)}}{E^+ k^+ (q_{2z} + \frac{(\mathbf{k} - \mathbf{q}_1)^2}{2\omega} + \frac{x}{1-x} \frac{(\mathbf{k} - \mathbf{q}_1 - \mathbf{q}_2)^2}{2\omega})} \\
&\times \left(v(-q_{2z} - \frac{\mathbf{k}^2}{2\omega} - \frac{x}{1-x} \frac{(\mathbf{k} - \mathbf{q}_1 - \mathbf{q}_2)^2}{2\omega}, \mathbf{q}_1) e^{i\frac{x}{1-x} \frac{(\mathbf{k} - \mathbf{q}_1 - \mathbf{q}_2)^2}{2\omega} (z_1 - z_0)} \right. \\
&\left. - v\left(\frac{(\mathbf{k} - \mathbf{q}_1)^2}{2\omega} - \frac{\mathbf{k}^2}{2\omega}, \mathbf{q}_1\right) e^{-i(q_{2z} + \frac{(\mathbf{k} - \mathbf{q}_1)^2}{2\omega})(z_1 - z_0)} \right). \tag{B.8.4}
\end{aligned}$$

The remaining q_{2z} integral is:

$$\begin{aligned}
I_3(p, k, \mathbf{q}_1, \mathbf{q}_2, z_1 - z_0, z_2 - z_1) &= \int \frac{dq_{2z}}{2\pi} \frac{1}{q_{2z} + \frac{(\mathbf{k}-\mathbf{q}_1)^2}{2\omega} + \frac{x}{1-x} \frac{(\mathbf{k}-\mathbf{q}_1-\mathbf{q}_2)^2}{2\omega}} v(q_{2z}, \mathbf{q}_2) \\
&\times \left(\frac{e^{-iq_{2z}(z_2-z_1)} e^{\frac{i}{2\omega}(\mathbf{k}^2 + \frac{x}{1-x}(\mathbf{k}-\mathbf{q}_1-\mathbf{q}_2)^2)(z_1-z_0)}}{(p-q_2)^2 + i\epsilon} v\left(-q_{2z} - \frac{\mathbf{k}^2}{2\omega} - \frac{x}{1-x} \frac{(\mathbf{k}-\mathbf{q}_1-\mathbf{q}_2)^2}{2\omega}, \mathbf{q}_1\right) \right. \\
&\quad \left. - \frac{e^{-iq_{2z}(z_2-z_0)} e^{-\frac{i}{2\omega}((\mathbf{k}-\mathbf{q}_1)^2 - \mathbf{k}^2)(z_1-z_0)}}{(p-q_2)^2 + i\epsilon} v\left(\frac{(\mathbf{k}-\mathbf{q}_1)^2}{2\omega} - \frac{\mathbf{k}^2}{2\omega}, \mathbf{q}_1\right) \right), \tag{B.8.5}
\end{aligned}$$

where the singularity on q_{2z} real axis: $q_{2z} = -\frac{(\mathbf{k}-\mathbf{q}_1)^2}{2\omega} - \frac{x}{1-x} \frac{(\mathbf{k}-\mathbf{q}_1-\mathbf{q}_2)^2}{2\omega} \equiv -a$, ($a > 0$) has to be avoided by taking Cauchy Principal Value of I_3 according to the Fig. B.6, i.e.:

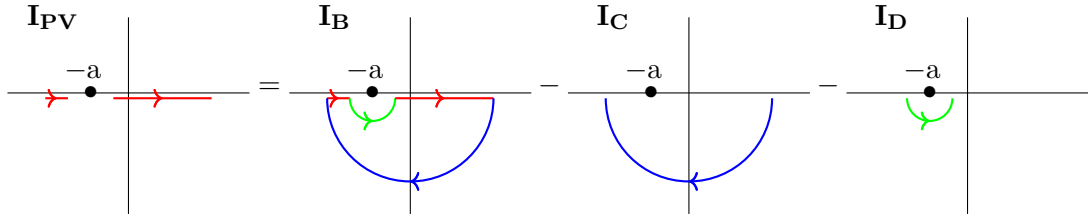


Figure B.6: Illustration of calculating Cauchy principal value (I_{PV}) in the case when singularity on the real axis arises.

$$I_3 \equiv I_{PV} = I_B - I_C - I_D, \tag{B.8.6}$$

where $I_B = -2\pi i \sum_i \text{Res}(I_3(\bar{q}_i))$, with i counting the poles in the lower-half plane. Additionally $I_C = 0$, and it's straightforward to show, that after the following substitution $q_{2z} = -a + re^{i\varphi}$, where $r \rightarrow 0$, also $I_D = 0$. Therefore, principal value of I_3 reduces to I_B , i.e. $-2\pi i \sum_i \text{Res}(I_3(\bar{q}_i))$.

In the well separated case (B.8.5) poles originating from Yukawa potentials ($q_{2z} = -\frac{\mathbf{k}^2}{2\omega} - \frac{x}{1-x} \frac{(\mathbf{k}-\mathbf{q}_1-\mathbf{q}_2)^2}{2\omega} - i\mu_{1\perp}$ and $q_{2z} = -i\mu_{2\perp}$) are again exponentially suppressed ($e^{-\mu_{i\perp}(z_2-z_{0,1})} \rightarrow 0$, $i = 1, 2$) and therefore can be neglected, so only the pole from the propagator survives $q_{2z} = \frac{x}{1-x} \left(\frac{(\mathbf{k}-\mathbf{q}_1)^2}{2\omega} - \frac{(\mathbf{k}-\mathbf{q}_1-\mathbf{q}_2)^2}{2\omega} \right) - i\epsilon$. However, since we are interested only in the contact-limit case (i.e. $z_1 = z_2$), instead of (B.8.5) we need to

calculate the principal value of the following integral:

$$\begin{aligned}
I_3^c(p, k, \mathbf{q}_1, \mathbf{q}_2, z_1 - z_0) &= \int \frac{dq_{2z}}{2\pi} \frac{1}{q_{2z} + \frac{(\mathbf{k}-\mathbf{q}_1)^2}{2\omega} + \frac{x}{1-x} \frac{(\mathbf{k}-\mathbf{q}_1-\mathbf{q}_2)^2}{2\omega}} v(q_{2z}, \mathbf{q}_2) \\
&\times \left(\frac{e^{\frac{i}{2\omega}(\mathbf{k}^2 + \frac{x}{1-x}(\mathbf{k}-\mathbf{q}_1-\mathbf{q}_2)^2)(z_1-z_0)}}{(p-q_2)^2 + i\epsilon} v\left(-q_{2z} - \frac{\mathbf{k}^2}{2\omega} - \frac{x}{1-x} \frac{(\mathbf{k}-\mathbf{q}_1-\mathbf{q}_2)^2}{2\omega}, \mathbf{q}_1\right) \right. \\
&\left. - \frac{e^{-iq_{2z}(z_1-z_0)} e^{-\frac{i}{2\omega}((\mathbf{k}-\mathbf{q}_1)^2 - \mathbf{k}^2)(z_1-z_0)}}{(p-q_2)^2 + i\epsilon} v\left(\frac{(\mathbf{k}-\mathbf{q}_1)^2}{2\omega} - \frac{\mathbf{k}^2}{2\omega}, \mathbf{q}_1\right) \right), \quad (\text{B.8.7})
\end{aligned}$$

which again reduces to the sum of residua, with $-a$ effectively not being a pole (Fig. B.6). Particularly, for the second term in the bracket of Eq. (B.8.7), only the propagator pole survives, while for the first term in the bracket all three poles have to be accounted, although residues at poles from potentials sum to the order of $\mathcal{O}\left(\frac{(\mathbf{k}-\mathbf{q}_1)^2}{x(1-x)E^+(\mu_{1\perp}+\mu_{2\perp})}\right)$, and thus can be neglected compared to the remaining residue.

Finally, in the contact-limit case we obtain:

$$\begin{aligned}
M_{2,0,1}^c &\approx -iJ_a(p+k)e^{i(p+k)x_0} f^{eda_2} f^{aeb} f^{bca_1} T_{a_2} T_{a_1} (1-x+x^2) \\
&\times (-i) \int \frac{d^2\mathbf{q}_1}{(2\pi)^2} (-i) \int \frac{d^2\mathbf{q}_2}{(2\pi)^2} v(0, \mathbf{q}_1) v(0, \mathbf{q}_2) e^{-i(\mathbf{q}_1+\mathbf{q}_2)\cdot\mathbf{b}_1} (2ig_s) \\
&\times \frac{\boldsymbol{\epsilon} \cdot (\mathbf{k} - \mathbf{q}_1)}{(\mathbf{k} - \mathbf{q}_1)^2} \left(e^{i(\frac{\mathbf{k}^2}{xE^+} + \frac{\mathbf{p}^2}{(1-x)E^+})(z_1-z_0)} - e^{i(\frac{\mathbf{k}^2}{xE^+} + \frac{\mathbf{p}^2}{(1-x)E^+} - \frac{(\mathbf{k}-\mathbf{q}_1)^2}{x(1-x)E^+})(z_1-z_0)} \right) \\
&= J_a(p+k)e^{i(p+k)x_0} (T^{a_2}[T^c, T^{a_1}])_{da} T_{a_2} T_{a_1} (1-x+x^2) \\
&\times (-i) \int \frac{d^2\mathbf{q}_1}{(2\pi)^2} (-i) \int \frac{d^2\mathbf{q}_2}{(2\pi)^2} v(0, \mathbf{q}_1) v(0, \mathbf{q}_2) e^{-i(\mathbf{q}_1+\mathbf{q}_2)\cdot\mathbf{b}_1} (2ig_s) \frac{\boldsymbol{\epsilon} \cdot (\mathbf{k} - \mathbf{q}_1)}{(\mathbf{k} - \mathbf{q}_1)^2} \\
&\times \left(e^{\frac{i}{2\omega}(\mathbf{k}^2 + \frac{x}{1-x}(\mathbf{k}-\mathbf{q}_1-\mathbf{q}_2)^2)(z_1-z_0)} - e^{\frac{i}{2\omega}(\mathbf{k}^2 - \frac{(\mathbf{k}-\mathbf{q}_1)^2}{1-x} + \frac{x}{1-x}(\mathbf{k}-\mathbf{q}_1-\mathbf{q}_2)^2)(z_1-z_0)} \right). \quad (\text{B.8.8})
\end{aligned}$$

Notice that, contrary to the previous three amplitudes that also included two scattering centers, in Eq. (B.8.8) no factor $\frac{1}{2}$ when comparing to well-separated limit appears. In soft-gluon limit approximation Eq. (B.8.8) reduces to Eq.(D6) from [183] and also to the massless limit of Eq.(72) from [189].

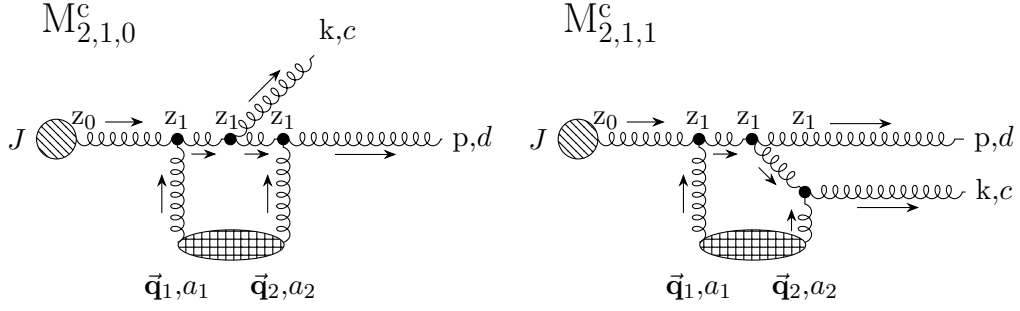


Figure B.7: Feynman diagrams $M_{2,1,0}^c$ and $M_{2,1,1}^c$ in contact limit ($z_1 = z_2$), which have negligible contribution to the first order in opacity gluon-jet radiative energy loss. Remaining labeling is the same as in Fig. B.3.

Proceeding in the same manner, for $M_{2,0,2}^c$ we obtain:

$$\begin{aligned}
M_{2,0,2}^c &\approx iJ_a(p+k)e^{i(p+k)x_0} f^{eca_2} f^{abe} f^{bda_1} T_{a_2} T_{a_1} (1-x+x^2) \\
&\times (-i) \int \frac{d^2\mathbf{q}_1}{(2\pi)^2} (-i) \int \frac{d^2\mathbf{q}_2}{(2\pi)^2} v(0, \mathbf{q}_1) v(0, \mathbf{q}_2) e^{-i(\mathbf{q}_1+\mathbf{q}_2)\cdot\mathbf{b}_1} \\
&\times (2ig_s) \frac{\boldsymbol{\epsilon}\cdot(\mathbf{p}-\mathbf{q}_1)}{(\mathbf{p}-\mathbf{q}_1)^2} \left(e^{i(\frac{\mathbf{k}^2}{xE^+} + \frac{\mathbf{p}^2}{(1-x)E^+})(z_1-z_0)} - e^{i(\frac{\mathbf{k}^2}{xE^+} + \frac{\mathbf{p}^2}{(1-x)E^+} - \frac{(\mathbf{p}-\mathbf{q}_1)^2}{x(1-x)E^+})(z_1-z_0)} \right) \\
&= J_a(p+k)e^{i(p+k)x_0} (T^{a_1}[T^c, T^{a_2}])_{da} T_{a_2} T_{a_1} (1-x+x^2) \\
&\times (-i) \int \frac{d^2\mathbf{q}_1}{(2\pi)^2} (-i) \int \frac{d^2\mathbf{q}_2}{(2\pi)^2} v(0, \mathbf{q}_1) v(0, \mathbf{q}_2) e^{-i(\mathbf{q}_1+\mathbf{q}_2)\cdot\mathbf{b}_1} (2ig_s) \frac{\boldsymbol{\epsilon}\cdot(\mathbf{k}-\mathbf{q}_2)}{(\mathbf{k}-\mathbf{q}_2)^2} \\
&\times \left(e^{\frac{i}{2\omega}(\mathbf{k}^2 + \frac{x}{1-x}(\mathbf{k}-\mathbf{q}_1-\mathbf{q}_2)^2)(z_1-z_0)} - e^{\frac{i}{2\omega}(\mathbf{k}^2 - \frac{(\mathbf{k}-\mathbf{q}_2)^2}{1-x} + \frac{x}{1-x}(\mathbf{k}-\mathbf{q}_1-\mathbf{q}_2)^2)(z_1-z_0)} \right).
\end{aligned} \tag{B.8.9}$$

As for $M_{2,0,1}^c$ amplitude, no factor of $\frac{1}{2}$ appears. From well-separated analogon of Fig. B.5 we could infer that $M_{2,0,1}$ and $M_{2,0,2}$ are symmetric under the following substitutions: ($p \leftrightarrow k, x \leftrightarrow (1-x), c \leftrightarrow d$), which can readily be verified by implementing these substitutions in the first three lines of either of the two Eqs.(B.8.8, B.8.9) and by using structure constant asymmetry as well as (B.6.3). Also, since in contact-limit case these two diagrams are topologically indistinct, we need to either omit one of them in order to avoid over counting, or to include both, but multiply each by a factor $\frac{1}{2}$ (we will do the latter).

B.9. Diagrams $M_{2,1,0}$ and $M_{2,1,1}$

The contact-limit case of the remaining two diagrams is presented in Fig. B.7. These diagrams correspond to the case when one interaction with the scattering center located at $\vec{\mathbf{x}}_1$ occurs before and the other interaction at the same place occurs after the gluon has been radiated.

In order to avoid redundant derivations (i.e. repetition of the above calculations) we briefly outline our derivation of Feynman amplitudes for only contact-limit case.

In the light of time-ordered perturbation theory from [180, 181] these two diagrams are identically equal to zero, since $\int_{t_1}^{t_1} dt \dots = 0$, but for the consistency we will provide a brief verification of this argument.

$$\begin{aligned}
M_{2,1,0} &= \int \frac{d^4 q_1}{(2\pi)^4} \frac{d^4 q_2}{(2\pi)^4} \epsilon_\sigma^*(p) f^{eda_2} \left(g^{\xi 0} (p - 2q_2)^\sigma + g^{\xi\sigma} (-2p + q_2)^0 + g^{\sigma 0} (p + q_2)^\xi \right) \\
&\times T_{a_2} V(q_2) e^{iq_2 x_2} \frac{-i\delta_{ee'} g_{\xi\xi'}}{(p - q_2)^2 + i\epsilon} \epsilon_\rho^*(k) g_s f^{bce'} \left(g^{\nu\xi'} (2p + k - 2q_2)^\rho + g^{\nu\rho} (-p - 2k + q_2)^{\xi'} \right. \\
&+ \left. g^{\rho\xi'} (-p + k + q_2)^\nu \right) \frac{-i\delta_{bb'} g_{\nu\nu'}}{(p + k - q_2)^2 + i\epsilon} f^{ab'a_1} \left(g^{\mu 0} (p + k - 2q_1 - q_2)^\nu \right. \\
&+ \left. g^{\mu\nu'} (-2p - 2k + q_1 + 2q_2)^0 + g^{\nu'0} (p + k + q_1 - q_2)^\mu \right) T_{a_1} V(q_1) e^{iq_1 x_1} \\
&\times \frac{-i\delta_{aa'} g_{\mu\mu'}}{(p + k - q_1 - q_2)^2 + i\epsilon} iJ_{a'}(p + k - q_1 - q_2) \epsilon^{\mu'} (p + k - q_1 - q_2) e^{i(p+k-q_1-q_2)x_0} \\
&\approx iJ_a(p + k) e^{i(p+k)x_0} f^{eda_2} f^{bce} f^{aba_1} T_{a_2} T_{a_1} \frac{(1 - x + x^2)}{x} \\
&\times (-i) \int \frac{d^2 \mathbf{q}_1}{(2\pi)^2} (-i) \int \frac{d^2 \mathbf{q}_2}{(2\pi)^2} (2ig_s) \boldsymbol{\epsilon} \cdot (\mathbf{k} - x\mathbf{q}_1) e^{-i\mathbf{q}_1 \cdot \mathbf{b}_1} e^{-i\mathbf{q}_2 \cdot \mathbf{b}_2} (E^+)^2 \\
&\times \int \frac{dq_{2z}}{2\pi} \frac{v(q_{2z}, \mathbf{q}_2) e^{-iq_{2z}(z_2 - z_1)}}{((p + k - q_2)^2 + i\epsilon)((p - q_2)^2 + i\epsilon)} \int \frac{dq_z}{2\pi} \frac{v(q_z - q_{2z}, \mathbf{q}_1) e^{-iq_z(z_1 - z_0)}}{(p + k - q_1 - q_2)^2 + i\epsilon} \\
&\approx J_a(p + k) e^{i(p+k)x_0} f^{eda_2} f^{bce} f^{aba_1} T_{a_2} T_{a_1} (1 - x + x^2) \\
&\times (-i) \int \frac{d^2 \mathbf{q}_1}{(2\pi)^2} (-i) \int \frac{d^2 \mathbf{q}_2}{(2\pi)^2} (2ig_s) \boldsymbol{\epsilon} \cdot (\mathbf{k} - x\mathbf{q}_1) e^{-i\mathbf{q}_1 \cdot \mathbf{b}_1} e^{-i\mathbf{q}_2 \cdot \mathbf{b}_2} (E^+)^2 \\
&\times \int \frac{dq_{2z}}{2\pi} \frac{v(q_{2z}, \mathbf{q}_2) e^{-iq_{2z}(z_2 - z_1)}}{((p + k - q_2)^2 + i\epsilon)((p - q_2)^2 + i\epsilon)} \frac{1}{k^+} \\
&\times v \left(-\frac{\mathbf{k}^2}{2\omega} - \frac{x}{1-x} \frac{(\mathbf{k} - \mathbf{q}_1 - \mathbf{q}_2)^2}{2\omega} + \frac{\mathbf{q}_1^2}{E^+} - i\epsilon, \frac{x}{1-x} \left(\frac{(\mathbf{k} - \mathbf{q}_1)^2}{2\omega} - \frac{(\mathbf{k} - \mathbf{q}_1 - \mathbf{q}_2)^2}{2\omega} \right) - i\epsilon, -i\mu_{1\perp} \right) e^{\frac{i}{2\omega} (\mathbf{k}^2 + \frac{x}{1-x} (\mathbf{k} - \mathbf{q}_1 - \mathbf{q}_2)^2) (z_1 - z_0)}.
\end{aligned} \tag{B.9.1}$$

In the contact-limit case there are four q_{2z} poles of the above integral in the lower half-plane: $-\frac{\mathbf{k}^2}{2\omega} - \frac{x}{1-x} \frac{(\mathbf{k} - \mathbf{q}_1 - \mathbf{q}_2)^2}{2\omega} + \frac{\mathbf{q}_1^2}{E^+} - i\epsilon$, $\frac{x}{1-x} \left(\frac{(\mathbf{k} - \mathbf{q}_1)^2}{2\omega} - \frac{(\mathbf{k} - \mathbf{q}_1 - \mathbf{q}_2)^2}{2\omega} \right) - i\epsilon$, $-i\mu_{1\perp}$ and

$-i\mu_{2\perp}$, which give:

$$\begin{aligned}
M_{2,1,0}^c &\approx -J_a(p+k)e^{i(p+k)x_0} f^{eda_2} f^{bce} f^{aba_1} T_{a_2} T_{a_1} (1-x+x^2) \\
&\times (-i) \int \frac{d^2\mathbf{q}_1}{(2\pi)^2} (-i) \int \frac{d^2\mathbf{q}_2}{(2\pi)^2} v(0, \mathbf{q}_1) v(0, \mathbf{q}_2) e^{-i(\mathbf{q}_1+\mathbf{q}_2)\cdot\mathbf{b}_1} \\
&\times (ig_s) \frac{\boldsymbol{\epsilon}\cdot(\mathbf{k}-x\mathbf{q}_1)}{(\mathbf{k}-x\mathbf{q}_1)^2} e^{i(\frac{\mathbf{k}^2}{xE^+} + \frac{\mathbf{p}^2}{(1-x)E^+})(z_1-z_0)} \frac{\mu_{1\perp}^2 + \mu_{1\perp}\mu_{2\perp} + \mu_{2\perp}^2}{\mu_{1\perp}\mu_{2\perp}} \frac{(\mathbf{k}-x\mathbf{q}_1)^2}{x(1-x)E^+(\mu_{1\perp} + \mu_{2\perp})} \\
&= iJ_a(p+k)e^{i(p+k)x_0} (T^{a_2} T^c T^{a_1})_{da} T_{a_2} T_{a_1} (1-x+x^2) \\
&\times (-i) \int \frac{d^2\mathbf{q}_1}{(2\pi)^2} (-i) \int \frac{d^2\mathbf{q}_2}{(2\pi)^2} v(0, \mathbf{q}_1) v(0, \mathbf{q}_2) e^{-i(\mathbf{q}_1+\mathbf{q}_2)\cdot\mathbf{b}_1} \\
&\times (ig_s) \frac{\boldsymbol{\epsilon}\cdot(\mathbf{k}-x\mathbf{q}_1)}{(\mathbf{k}-x\mathbf{q}_1)^2} e^{\frac{i}{2\omega}(\mathbf{k}^2 + \frac{x}{1-x}(\mathbf{k}-\mathbf{q}_1-\mathbf{q}_2)^2)(z_1-z_0)} \frac{\mu_{1\perp}^2 + \mu_{1\perp}\mu_{2\perp} + \mu_{2\perp}^2}{\mu_{1\perp}\mu_{2\perp}} \\
&\times \frac{(\mathbf{k}-x\mathbf{q}_1)^2}{x(1-x)E^+(\mu_{1\perp} + \mu_{2\perp})}, \tag{B.9.2}
\end{aligned}$$

where the residues at first two poles (i.e. originating from the gluon propagators) cancel each other exactly, leading to the result (B.9.2) that is suppressed by a factor of $\mathcal{O}(\frac{(\mathbf{k}-x\mathbf{q}_1)^2}{x(1-x)E^+(\mu_{1\perp} + \mu_{2\perp})})$ compared to the all previous amplitudes (note that x is finite), as in the case of soft gluon approximation [183, 189]. In soft gluon approximation Eq. (B.9.2) reduces to the massless limit of Eq.(74) from [189].

The same conclusion applies to $M_{2,1,1}^c$ amplitude, as one can see in the following

lines:

$$\begin{aligned}
M_{2,1,1} &= \int \frac{d^4 q_1}{(2\pi)^4} \frac{d^4 q_2}{(2\pi)^4} \epsilon_\rho^*(k) f^{eca_2} \left(g^{\xi 0} (k - 2q_2)^\rho + g^{\xi \rho} (-2k + q_2)^0 + g^{\rho 0} (k + q_2)^\xi \right) \\
&\quad \times T_{a_2} V(q_2) e^{iq_2 x_2} \frac{-i\delta_{ee'} g_{\xi\xi'}}{(k - q_2)^2 + i\epsilon} \epsilon_\sigma^*(p) g_s f^{bde'} \left(g^{\nu\xi'} (p + 2k - 2q_2)^\sigma + g^{\nu\sigma} (-2p - k + q_2)^\xi \right) \\
&\quad + g^{\sigma\xi'} (p - k + q_2)^\nu \frac{-i\delta_{bb'} g_{\nu\nu'}}{(p + k - q_2)^2 + i\epsilon} f^{ab'a_1} \left(g^{\mu 0} (p + k - 2q_1 - q_2)^\nu \right) \\
&\quad + g^{\mu\nu'} (-2p - 2k + q_1 + 2q_2)^0 + g^{\nu'0} (p + k + q_1 - q_2)^\mu \Big) T_{a_1} V(q_1) e^{iq_1 x_1} \\
&\quad \times \frac{-i\delta_{aa'} g_{\mu\mu'}}{(p + k - q_1 - q_2)^2 + i\epsilon} iJ_{a'} (p + k - q_1 - q_2) \epsilon^{\mu'} (p + k - q_1 - q_2) e^{i(p+k-q_1-q_2)x_0} \\
&\approx iJ_a (p + k) e^{i(p+k)x_0} f^{eca_2} f^{bde} f^{aba_1} T_{a_2} T_{a_1} \frac{(1 - x + x^2)}{(1 - x)} \\
&\quad \times (-i) \int \frac{d^2 \mathbf{q}_1}{(2\pi)^2} (-i) \int \frac{d^2 \mathbf{q}_2}{(2\pi)^2} (2ig_s) \boldsymbol{\epsilon} \cdot (\mathbf{p} - (1 - x)\mathbf{q}_1) e^{-i\mathbf{q}_1 \cdot \mathbf{b}_1} e^{-i\mathbf{q}_2 \cdot \mathbf{b}_2} (E^+)^2 \\
&\quad \times \int \frac{dq_{2z}}{2\pi} \frac{v(q_{2z}, \mathbf{q}_2) e^{-iq_{2z}(z_2 - z_1)}}{((p + k - q_2)^2 + i\epsilon)((k - q_2)^2 + i\epsilon)} \int \frac{dq_z}{2\pi} \frac{v(q_z - q_{2z}, \mathbf{q}_1) e^{-iq_z(z_1 - z_0)}}{(p + k - q_1 - q_2)^2 + i\epsilon} \\
&\approx -J_a (p + k) e^{i(p+k)x_0} f^{eca_2} f^{bde} f^{aba_1} T_{a_2} T_{a_1} (1 - x + x^2) \\
&\quad \times (-i) \int \frac{d^2 \mathbf{q}_1}{(2\pi)^2} (-i) \int \frac{d^2 \mathbf{q}_2}{(2\pi)^2} (2ig_s) \boldsymbol{\epsilon} \cdot (\mathbf{k} - x\mathbf{q}_1 - \mathbf{q}_2) e^{-i\mathbf{q}_1 \cdot \mathbf{b}_1} e^{-i\mathbf{q}_2 \cdot \mathbf{b}_2} (E^+)^2 \\
&\quad \times \int \frac{dq_{2z}}{2\pi} \frac{v(q_{2z}, \mathbf{q}_2) e^{-iq_{2z}(z_2 - z_1)}}{((p + k - q_2)^2 + i\epsilon)((k - q_2)^2 + i\epsilon)} \frac{1}{(1 - x)E^+} \\
&\quad \times v\left(-\frac{\mathbf{k}^2}{2\omega} - \frac{x}{1 - x} \frac{(\mathbf{k} - \mathbf{q}_1 - \mathbf{q}_2)^2}{2\omega} - q_{2z}, \mathbf{q}_1\right) e^{\frac{i}{2\omega} (\mathbf{k}^2 + \frac{x}{1-x} (\mathbf{k} - \mathbf{q}_1 - \mathbf{q}_2)^2)(z_1 - z_0)}
\end{aligned} \tag{B.9.3}$$

Similar to the previous amplitude, again there are four q_{2z} poles in the lower half-plane for the contact-limit case : $-\frac{\mathbf{k}^2}{2\omega} - \frac{x}{1-x} \frac{(\mathbf{k} - \mathbf{q}_1 - \mathbf{q}_2)^2}{2\omega} + \frac{\mathbf{q}_1^2}{E^+} - i\epsilon, \frac{(\mathbf{k} - \mathbf{q}_2)^2}{2\omega} - \frac{\mathbf{k}^2}{2\omega} - i\epsilon,$

$-i\mu_{1\perp}$ and $-i\mu_{2\perp}$, which give:

$$\begin{aligned}
M_{2,1,1}^c &\approx -J_a(p+k)e^{i(p+k)x_0} f^{eca_2} f^{bde} f^{aba_1} T_{a_2} T_{a_1} (1-x+x^2) \\
&\times (-i) \int \frac{d^2\mathbf{q}_1}{(2\pi)^2} (-i) \int \frac{d^2\mathbf{q}_2}{(2\pi)^2} v(0, \mathbf{q}_1) v(0, \mathbf{q}_2) e^{-i(\mathbf{q}_1+\mathbf{q}_2)\cdot\mathbf{b}_1} \\
&\times (ig_s) \frac{\boldsymbol{\epsilon}\cdot(\mathbf{p}-(1-x)\mathbf{q}_1)}{(\mathbf{p}-(1-x)\mathbf{q}_1)^2} e^{i(\frac{\mathbf{k}^2}{xE^+} + \frac{\mathbf{p}^2}{(1-x)E^+})(z_1-z_0)} \frac{\mu_{1\perp}^2 + \mu_{1\perp}\mu_{2\perp} + \mu_{2\perp}^2}{\mu_{1\perp}\mu_{2\perp}} \\
&\times \frac{(\mathbf{p}-(1-x)\mathbf{q}_1)^2}{x(1-x)E^+(\mu_{1\perp} + \mu_{2\perp})} \\
&= iJ_a(p+k)e^{i(p+k)x_0} ([T^c, T^{a_2}]T^{a_1})_{da} T_{a_2} T_{a_1} (1-x+x^2) \\
&\times (-i) \int \frac{d^2\mathbf{q}_1}{(2\pi)^2} (-i) \int \frac{d^2\mathbf{q}_2}{(2\pi)^2} v(0, \mathbf{q}_1) v(0, \mathbf{q}_2) e^{-i(\mathbf{q}_1+\mathbf{q}_2)\cdot\mathbf{b}_1} \\
&\times (ig_s) \frac{\boldsymbol{\epsilon}\cdot(\mathbf{k}-x\mathbf{q}_1-\mathbf{q}_2)}{(\mathbf{k}-x\mathbf{q}_1-\mathbf{q}_2)^2} e^{\frac{i}{2\omega}(\mathbf{k}^2 + \frac{x}{1-x}(\mathbf{k}-\mathbf{q}_1-\mathbf{q}_2)^2)(z_1-z_0)} \frac{\mu_{1\perp}^2 + \mu_{1\perp}\mu_{2\perp} + \mu_{2\perp}^2}{\mu_{1\perp}\mu_{2\perp}} \\
&\times \frac{(\mathbf{k}-x\mathbf{q}_1-\mathbf{q}_2)^2}{x(1-x)E^+(\mu_{1\perp} + \mu_{2\perp})}, \tag{B.9.4}
\end{aligned}$$

where again, the residues at first two poles (i.e. originating from the gluon propagators) cancel each other exactly, leading to the result (B.9.4) that is, similarly to $M_{2,1,0}^c$, suppressed by a factor of $\mathcal{O}(\frac{(\mathbf{k}-x\mathbf{q}_1-\mathbf{q}_2)^2}{x(1-x)E^+(\mu_{1\perp} + \mu_{2\perp})})$ compared to the amplitudes from the previous sections, as in the case of soft gluon approximation [183, 189]. Therefore, we will neglect the contributions from $M_{2,1,0}^c$ and $M_{2,1,1}^c$ when calculating energy loss.

Also, from Fig. B.7 we infer that $M_{2,1,0}$ and $M_{2,1,1}$ are symmetric to the exchange ($p \leftrightarrow k$, $x \leftrightarrow 1-x$ and $c \leftrightarrow d$), which can easily be verified by comparing the first three lines of Eqs.(B.9.2, B.9.4).

B.10. Calculation of radiative energy loss

In this section we provide concise outline of calculating the first order in opacity radiative energy loss. We start with the equation:

$$d^3N_g^{(1)}d^3N_J = \left(\frac{1}{d_T} \text{Tr} \langle |M_1|^2 \rangle + \frac{2}{d_T} \text{Re} \text{Tr} \langle M_2 M_0^* \rangle \right) \frac{d^3\vec{\mathbf{p}}}{(2\pi)^3 2p^0} \frac{d^3\vec{\mathbf{k}}}{(2\pi)^3 2\omega}, \tag{B.10.1}$$

where M_1 is sum of all diagrams with one scattering center and M_2 is sum of all diagrams with two scattering centers in the contact limit.

The final results from Appendix Section B.5 yield:

$$\begin{aligned}
M_1 &= M_{1,1,0} + M_{1,0,0} + M_{1,0,1} = J_a(p+k)e^{i(p+k)x_0}(1-x+x^2)T_{a_1}(-i) \int \frac{d^2\mathbf{q}_1}{(2\pi)^2} \\
&\times v(0, \mathbf{q}_1)e^{-i\mathbf{q}_1 \cdot \mathbf{b}_1}(2ig_s) \left\{ \left(\frac{\boldsymbol{\epsilon} \cdot (\mathbf{k} - \mathbf{q}_1)}{(\mathbf{k} - \mathbf{q}_1)^2} [T^c, T^{a_1}]_{da} - \frac{\boldsymbol{\epsilon} \cdot (\mathbf{k} - x\mathbf{q}_1)}{(\mathbf{k} - x\mathbf{q}_1)^2} (T^c T^{a_1})_{da} \right. \right. \\
&+ \left. \frac{\boldsymbol{\epsilon} \cdot \mathbf{k}}{\mathbf{k}^2} (T^{a_1} T^c)_{da} \right) e^{\frac{i}{2\omega}(\mathbf{k}^2 + \frac{x}{1-x}(\mathbf{k}-\mathbf{q}_1)^2)(z_1-z_0)} - \frac{\boldsymbol{\epsilon} \cdot (\mathbf{k} - \mathbf{q}_1)}{(\mathbf{k} - \mathbf{q}_1)^2} [T^c, T^{a_1}]_{da} \\
&\times \left. e^{\frac{i}{2\omega}(\mathbf{k}^2 - (\mathbf{k}-\mathbf{q}_1)^2)(z_1-z_0)} - \frac{\boldsymbol{\epsilon} \cdot \mathbf{k}}{\mathbf{k}^2} (T^{a_1} T^c)_{da} e^{\frac{i}{2\omega} \frac{x}{1-x}((\mathbf{k}-\mathbf{q}_1)^2 - \mathbf{k}^2)(z_1-z_0)} \right\}, \quad (\text{B.10.2})
\end{aligned}$$

leading to:

$$\begin{aligned}
\frac{1}{d_T} \text{Tr} \langle |M_1|^2 \rangle &= N |J(p+k)|^2 (4g_s^2) \frac{1}{A_\perp} (1-x+x^2)^2 \int \frac{d^2\mathbf{q}_1}{(2\pi)^2} |v(0, \mathbf{q}_1)|^2 \frac{C_2(T)}{d_G} \\
&\left\{ 2\alpha \left(2 \frac{\boldsymbol{\epsilon} \cdot (\mathbf{k} - \mathbf{q}_1)}{(\mathbf{k} - \mathbf{q}_1)^2} - \frac{\boldsymbol{\epsilon} \cdot \mathbf{k}}{\mathbf{k}^2} - \frac{\boldsymbol{\epsilon} \cdot (\mathbf{k} - x\mathbf{q}_1)}{(\mathbf{k} - x\mathbf{q}_1)^2} \right) \frac{\boldsymbol{\epsilon} \cdot (\mathbf{k} - \mathbf{q}_1)}{(\mathbf{k} - \mathbf{q}_1)^2} + \left(\frac{\boldsymbol{\epsilon} \cdot (\mathbf{k} - x\mathbf{q}_1)}{(\mathbf{k} - x\mathbf{q}_1)^2} \right)^2 \text{Tr}((T^c)^2 (T^{a_1})^2) \right. \\
&+ 2 \left(\frac{\boldsymbol{\epsilon} \cdot \mathbf{k}}{\mathbf{k}^2} \text{Tr}((T^c)^2 (T^{a_1})^2) - \frac{\boldsymbol{\epsilon} \cdot (\mathbf{k} - x\mathbf{q}_1)}{(\mathbf{k} - x\mathbf{q}_1)^2} \text{Tr}(T^c T^{a_1} T^c T^{a_1}) \right) \frac{\boldsymbol{\epsilon} \cdot \mathbf{k}}{\mathbf{k}^2} \\
&- 2\alpha \left(\frac{\boldsymbol{\epsilon} \cdot (\mathbf{k} - \mathbf{q}_1)}{(\mathbf{k} - \mathbf{q}_1)^2} - \frac{1}{2} \frac{\boldsymbol{\epsilon} \cdot \mathbf{k}}{\mathbf{k}^2} - \frac{1}{2} \frac{\boldsymbol{\epsilon} \cdot (\mathbf{k} - x\mathbf{q}_1)}{(\mathbf{k} - x\mathbf{q}_1)^2} \right) \frac{\boldsymbol{\epsilon} \cdot (\mathbf{k} - \mathbf{q}_1)}{(\mathbf{k} - \mathbf{q}_1)^2} 2 \cos \left(\frac{(\mathbf{k} - \mathbf{q}_1)^2}{x(1-x)E^+} (z_1 - z_0) \right) \\
&+ \left(\alpha \frac{\boldsymbol{\epsilon} \cdot (\mathbf{k} - \mathbf{q}_1)}{(\mathbf{k} - \mathbf{q}_1)^2} - \frac{\boldsymbol{\epsilon} \cdot \mathbf{k}}{\mathbf{k}^2} \text{Tr}((T^c)^2 (T^{a_1})^2) + \frac{\boldsymbol{\epsilon} \cdot (\mathbf{k} - x\mathbf{q}_1)}{(\mathbf{k} - x\mathbf{q}_1)^2} \text{Tr}(T^c T^{a_1} T^c T^{a_1}) \right) \frac{\boldsymbol{\epsilon} \cdot \mathbf{k}}{\mathbf{k}^2} \\
&\times \left. 2 \cos \left(\frac{\mathbf{k}^2}{x(1-x)E^+} (z_1 - z_0) \right) - \alpha \frac{\boldsymbol{\epsilon} \cdot \mathbf{k}}{\mathbf{k}^2} \frac{\boldsymbol{\epsilon} \cdot (\mathbf{k} - \mathbf{q}_1)}{(\mathbf{k} - \mathbf{q}_1)^2} 2 \cos \left(\frac{\mathbf{k}^2 - (\mathbf{k} - \mathbf{q}_1)^2}{x(1-x)E^+} (z_1 - z_0) \right) \right\}, \quad (\text{B.10.3})
\end{aligned}$$

where the number of scattering centers N comes from summation over scattering centers (B.2.2, B.2.3), then $\alpha \equiv \text{Tr}((T^c)^2 (T^{a_1})^2 - T^c T^{a_1} T^c T^{a_1})$, and we also used the definition of commutator, the fact that trace is invariant under the cyclic permutations, Eq. (B.1.4) (with $i = j$ and $d_i = d_T$) and the relation $E^+ \approx 2E$. We verified that this result is also symmetric under the substitutions: ($p \leftrightarrow k, x \leftrightarrow (1-x), c \leftrightarrow d$) when written in terms of structure constants.

Next, we summarize contact limits of all diagrams that contain two scattering centers from Appendix Sections B.6 to B.8 and then take their ensemble average

according to Eqs.(B.2.2, B.2.3, B.2.4) in order to obtain M_2 :

$$\begin{aligned}
M_2 &= M_{2,2,0}^c + M_{2,0,3}^c + M_{2,0,0}^c + \frac{1}{2}(M_{2,0,1}^c + M_{2,0,2}^c) = \frac{1}{2}N J_a(p+k) e^{i(p+k)x_0} (-2ig_s) \frac{1}{A_\perp} \\
&\times (1-x+x^2) T_{a_2} T_{a_1} \int \frac{d^2\mathbf{q}_1}{(2\pi)^2} |v(0, \mathbf{q}_1)|^2 \left\{ \frac{\boldsymbol{\epsilon} \cdot \mathbf{k}}{\mathbf{k}^2} \left(e^{\frac{i}{2\omega} \frac{\mathbf{k}^2}{1-x} (z_1-z_0)} \left([[T^c, T^{a_2}], T^{a_1}]_{da} \right. \right. \right. \\
&+ [T^{a_2} T^{a_1}, T^c]_{da} \left. \left. \left. \right) - [[T^c, T^{a_2}], T^{a_1}]_{da} - (T^{a_2} T^{a_1} T^c)_{da} \right) \right. \\
&\left. + \frac{\boldsymbol{\epsilon} \cdot (\mathbf{k} - \mathbf{q}_1)}{(\mathbf{k} - \mathbf{q}_1)^2} \left(e^{\frac{i}{2\omega} \frac{\mathbf{k}^2}{1-x} (z_1-z_0)} - e^{\frac{i}{2\omega} \frac{\mathbf{k}^2 - (\mathbf{k} - \mathbf{q}_1)^2}{1-x} (z_1-z_0)} \right) \left((T^{a_2} [T^c, T^{a_1}])_{da} + (T^{a_1} [T^c, T^{a_2}])_{da} \right) \right\}.
\end{aligned} \tag{B.10.4}$$

Then, by multiplying the previous expression by M_0^* , we obtain:

$$\begin{aligned}
\frac{2}{d_T} Re \text{Tr} \langle M_2 M_0^* \rangle &= N |J(p+k)|^2 (4g_s^2) \frac{1}{A_\perp} (1-x+x^2)^2 \int \frac{d^2\mathbf{q}_1}{(2\pi)^2} |v(0, \mathbf{q}_1)|^2 \frac{C_2(T)}{d_G} \\
&\times \left\{ \left(\frac{\boldsymbol{\epsilon} \cdot \mathbf{k}}{\mathbf{k}^2} \right)^2 \left(2\alpha \cos \left(\frac{\mathbf{k}^2}{x(1-x)E^+} (z_1-z_0) \right) - 2\alpha - \text{Tr}((T^c)^2 (T^{a_1})^2) \right) \right. \\
&\left. - 2\alpha \frac{\boldsymbol{\epsilon} \cdot \mathbf{k}}{\mathbf{k}^2} \frac{\boldsymbol{\epsilon} \cdot (\mathbf{k} - \mathbf{q}_1)}{(\mathbf{k} - \mathbf{q}_1)^2} \left(\cos \left(\frac{\mathbf{k}^2}{x(1-x)E^+} (z_1-z_0) \right) - \cos \left(\frac{\mathbf{k}^2 - (\mathbf{k} - \mathbf{q}_1)^2}{x(1-x)E^+} (z_1-z_0) \right) \right) \right\},
\end{aligned} \tag{B.10.5}$$

which can easily be verified to be symmetric to the exchange ($p \leftrightarrow k$, $x \leftrightarrow (1-x)$, $c \leftrightarrow d$), when written in terms of structure constants. By summing the expressions (B.10.3, B.10.5) we obtain:

$$\begin{aligned}
\frac{1}{d_T} \text{Tr} \langle |M_1|^2 \rangle + \frac{2}{d_T} Re \text{Tr} \langle M_2 M_0^* \rangle &= N d_G |J(p+k)|^2 (4g_s^2) \frac{C_2(T)}{d_G} C_2^2(G) \frac{1}{A_\perp} (1-x+x^2)^2 \\
&\times \int \frac{d^2\mathbf{q}_1}{(2\pi)^2} |v(0, \mathbf{q}_1)|^2 \left\{ \left(1 - \cos \left(\frac{\mathbf{k}^2}{x(1-x)E^+} (z_1-z_0) \right) \right) \left(\frac{\boldsymbol{\epsilon} \cdot \mathbf{k}}{\mathbf{k}^2} - \frac{\boldsymbol{\epsilon} \cdot (\mathbf{k} - x\mathbf{q}_1)}{(\mathbf{k} - x\mathbf{q}_1)^2} \right) \frac{\boldsymbol{\epsilon} \cdot \mathbf{k}}{\mathbf{k}^2} \right. \\
&+ \left(1 - \cos \left(\frac{(\mathbf{k} - \mathbf{q}_1)^2}{x(1-x)E^+} (z_1-z_0) \right) \right) \left(2 \frac{\boldsymbol{\epsilon} \cdot (\mathbf{k} - \mathbf{q}_1)}{(\mathbf{k} - \mathbf{q}_1)^2} - \frac{\boldsymbol{\epsilon} \cdot \mathbf{k}}{\mathbf{k}^2} - \frac{\boldsymbol{\epsilon} \cdot (\mathbf{k} - x\mathbf{q}_1)}{(\mathbf{k} - x\mathbf{q}_1)^2} \right) \frac{\boldsymbol{\epsilon} \cdot (\mathbf{k} - \mathbf{q}_1)}{(\mathbf{k} - \mathbf{q}_1)^2} \\
&\left. + \left(\left(\frac{\boldsymbol{\epsilon} \cdot (\mathbf{k} - x\mathbf{q}_1)}{(\mathbf{k} - x\mathbf{q}_1)^2} \right)^2 - \left(\frac{\boldsymbol{\epsilon} \cdot \mathbf{k}}{\mathbf{k}^2} \right)^2 \right) \right\},
\end{aligned} \tag{B.10.6}$$

which in soft-gluon approximation coincides with massless limit of Eq.(82) from [189].

In obtaining the Eq. (B.10.6) we used the following equalities that are valid in adjoint representation: $\text{Tr}(T^c T^{a_1} T^c T^{a_1}) = \frac{1}{2} C_2^2(G) d_G = \alpha = \frac{1}{2} \text{Tr}((T^{a_1})^2 (T^c)^2)$, which follow from Eqs.(B.1.4-B.1.9) and the commutator definition.

Since we are considering optically "thin" QCD plasma, it would be convenient to expand energy loss in powers of opacity, which is defined by the mean number of collisions in QCD medium [183]:

$$\bar{n} = \frac{L}{\lambda} = \frac{N \sigma_{el}}{A_\perp}, \tag{B.10.7}$$

where the small transverse momentum transfer elastic cross section between the jet and the target partons is taken from GW model (Eq.(6) from [183]), which in our case reads:

$$\frac{d\sigma_{el}}{d^2\mathbf{q}_1} = \frac{C_2(G)C_2(T)}{d_G} \frac{|v(0, \mathbf{q}_1)|^2}{(2\pi)^2}. \quad (\text{B.10.8})$$

Combining the Eqs.(B.10.7, B.10.8) we obtain:

$$\frac{L}{\lambda} = \frac{N}{A_\perp} \frac{C_2(G)C_2(T)}{4\pi d_G} \frac{(4\pi\alpha_s)^2}{\mu_E^2}. \quad (\text{B.10.9})$$

Next we incorporate Eq. (B.10.9) in Eq. (B.10.6), substitute obtained expression in Eq. (B.10.1), keeping in mind that p is 3D momentum of a final jet, and that we need to apply (B.4.12, B.4.13). The single gluon radiation spectrum in the first order in opacity then becomes:

$$\begin{aligned} \frac{dN_g^{(1)}}{dx} &= \frac{C_2(G)\alpha_s}{\pi} \frac{L}{\lambda} \frac{(1-x+x^2)^2}{x(1-x)} \int \frac{d^2\mathbf{q}_1}{\pi} \frac{\mu_E^2}{(\mathbf{q}_1^2 + \mu_E^2)^2} \int \frac{d^2\mathbf{k}}{\pi} \\ &\times \left\{ -\frac{\boldsymbol{\epsilon} \cdot (\mathbf{k} - \mathbf{q}_1)}{(\mathbf{k} - \mathbf{q}_1)^2} \left(\frac{\boldsymbol{\epsilon} \cdot \mathbf{k}}{\mathbf{k}^2} + \frac{\boldsymbol{\epsilon} \cdot (\mathbf{k} - x\mathbf{q}_1)}{(\mathbf{k} - x\mathbf{q}_1)^2} - 2\frac{\boldsymbol{\epsilon} \cdot (\mathbf{k} - \mathbf{q}_1)}{(\mathbf{k} - \mathbf{q}_1)^2} \right) \right. \\ &\times \int dz_1 (1 - \cos(\frac{(\mathbf{k} - \mathbf{q}_1)^2}{x(1-x)E^+}(z_1 - z_0))) \frac{2}{L} e^{-\frac{2(z_1 - z_0)}{L}} + \frac{\boldsymbol{\epsilon} \cdot \mathbf{k}}{\mathbf{k}^2} \\ &\times \left(\frac{\boldsymbol{\epsilon} \cdot \mathbf{k}}{\mathbf{k}^2} - \frac{\boldsymbol{\epsilon} \cdot (\mathbf{k} - x\mathbf{q}_1)}{(\mathbf{k} - x\mathbf{q}_1)^2} \right) \int dz_1 (1 - \cos(\frac{\mathbf{k}^2}{x(1-x)E^+}(z_1 - z_0))) \frac{2}{L} e^{-\frac{2(z_1 - z_0)}{L}} \\ &\left. + \left(\left(\frac{\boldsymbol{\epsilon} \cdot (\mathbf{k} - x\mathbf{q}_1)}{(\mathbf{k} - x\mathbf{q}_1)^2} \right)^2 - \left(\frac{\boldsymbol{\epsilon} \cdot \mathbf{k}}{\mathbf{k}^2} \right)^2 \right) \int dz_1 \frac{2}{L} e^{-\frac{2(z_1 - z_0)}{L}} \right\}, \quad (\text{B.10.10}) \end{aligned}$$

and the differential radiative energy loss $\frac{dE^{(1)}}{dx} \equiv \omega \frac{dN_g^{(1)}}{dx} \approx xE \frac{dN_g^{(1)}}{dx}$ acquires the form:

$$\begin{aligned} \frac{dE^{(1)}}{dx} &= \frac{C_2(G)\alpha_s}{\pi} \frac{L}{\lambda} E \frac{(1-x+x^2)^2}{1-x} \int \frac{d^2\mathbf{q}_1}{\pi} \frac{\mu_E^2}{(\mathbf{q}_1^2 + \mu_E^2)^2} \int \frac{d^2\mathbf{k}}{\pi} \\ &\times \left\{ -\frac{\boldsymbol{\epsilon} \cdot (\mathbf{k} - \mathbf{q}_1)}{(\mathbf{k} - \mathbf{q}_1)^2} \left(\frac{\boldsymbol{\epsilon} \cdot \mathbf{k}}{\mathbf{k}^2} + \frac{\boldsymbol{\epsilon} \cdot (\mathbf{k} - x\mathbf{q}_1)}{(\mathbf{k} - x\mathbf{q}_1)^2} - 2\frac{\boldsymbol{\epsilon} \cdot (\mathbf{k} - \mathbf{q}_1)}{(\mathbf{k} - \mathbf{q}_1)^2} \right) \right. \\ &\times \int dz_1 (1 - \cos(\frac{(\mathbf{k} - \mathbf{q}_1)^2}{x(1-x)E^+}(z_1 - z_0))) \frac{2}{L} e^{-\frac{2(z_1 - z_0)}{L}} + \frac{\boldsymbol{\epsilon} \cdot \mathbf{k}}{\mathbf{k}^2} \\ &\times \left(\frac{\boldsymbol{\epsilon} \cdot \mathbf{k}}{\mathbf{k}^2} - \frac{\boldsymbol{\epsilon} \cdot (\mathbf{k} - x\mathbf{q}_1)}{(\mathbf{k} - x\mathbf{q}_1)^2} \right) \int dz_1 (1 - \cos(\frac{\mathbf{k}^2}{x(1-x)E^+}(z_1 - z_0))) \frac{2}{L} e^{-\frac{2(z_1 - z_0)}{L}} \\ &\left. + \left(\left(\frac{\boldsymbol{\epsilon} \cdot (\mathbf{k} - x\mathbf{q}_1)}{(\mathbf{k} - x\mathbf{q}_1)^2} \right)^2 - \left(\frac{\boldsymbol{\epsilon} \cdot \mathbf{k}}{\mathbf{k}^2} \right)^2 \right) \int dz_1 \frac{2}{L} e^{-\frac{2(z_1 - z_0)}{L}} \right\}, \quad (\text{B.10.11}) \end{aligned}$$

where we assumed a simple exponential distribution $e^{-2\frac{z_1 - z_0}{L}}$ between the scattering

centers (as in [189]). So we finally obtain:

$$\begin{aligned} \frac{dN_g^{(1)}}{dx} &= \frac{C_2(G)\alpha_s L}{\pi \lambda} \frac{(1-x+x^2)^2}{x(1-x)} \int \frac{d^2\mathbf{q}_1}{\pi} \frac{\mu_E^2}{(\mathbf{q}_1^2 + \mu_E^2)^2} \int d\mathbf{k}^2 \\ &\times \left\{ \frac{(\mathbf{k} - \mathbf{q}_1)^2}{\left(\frac{4x(1-x)E}{L}\right)^2 + (\mathbf{k} - \mathbf{q}_1)^4} \left(2 - \frac{\mathbf{k} \cdot (\mathbf{k} - \mathbf{q}_1)}{\mathbf{k}^2} - \frac{(\mathbf{k} - \mathbf{q}_1) \cdot (\mathbf{k} - x\mathbf{q}_1)}{(\mathbf{k} - x\mathbf{q}_1)^2} \right) \right. \\ &\left. + \frac{\mathbf{k}^2}{\left(\frac{4x(1-x)E}{L}\right)^2 + \mathbf{k}^4} \left(1 - \frac{\mathbf{k} \cdot (\mathbf{k} - x\mathbf{q}_1)}{(\mathbf{k} - x\mathbf{q}_1)^2} \right) + \left(\frac{1}{(\mathbf{k} - x\mathbf{q}_1)^2} - \frac{1}{\mathbf{k}^2} \right) \right\}, \end{aligned} \quad (\text{B.10.12})$$

which is symmetric to the exchange of p and k gluons, and:

$$\begin{aligned} \frac{dE^{(1)}}{dx} &= \frac{C_2(G)\alpha_s L}{\pi \lambda} E \frac{(1-x+x^2)^2}{1-x} \int \frac{d^2\mathbf{q}_1}{\pi} \frac{\mu_E^2}{(\mathbf{q}_1^2 + \mu_E^2)^2} \int d\mathbf{k}^2 \\ &\times \left\{ \frac{(\mathbf{k} - \mathbf{q}_1)^2}{\left(\frac{4x(1-x)E}{L}\right)^2 + (\mathbf{k} - \mathbf{q}_1)^4} \left(2 - \frac{\mathbf{k} \cdot (\mathbf{k} - \mathbf{q}_1)}{\mathbf{k}^2} - \frac{(\mathbf{k} - \mathbf{q}_1) \cdot (\mathbf{k} - x\mathbf{q}_1)}{(\mathbf{k} - x\mathbf{q}_1)^2} \right) \right. \\ &\left. + \frac{\mathbf{k}^2}{\left(\frac{4x(1-x)E}{L}\right)^2 + \mathbf{k}^4} \left(1 - \frac{\mathbf{k} \cdot (\mathbf{k} - x\mathbf{q}_1)}{(\mathbf{k} - x\mathbf{q}_1)^2} \right) + \left(\frac{1}{(\mathbf{k} - x\mathbf{q}_1)^2} - \frac{1}{\mathbf{k}^2} \right) \right\}, \end{aligned} \quad (\text{B.10.13})$$

which in soft-gluon approximation reduces to massless limit of Eq.(84) from [189].

B.11. Diagrams and radiative energy loss with gluon mass included

Finally, we recalculate the results from Appendices Sections B.4 to B.9 when the gluon mass $m_g = \frac{\mu_E}{\sqrt{2}}$ is included, i.e. gluon propagator has the following form [188]:

- gluon propagator with mass m_g in Feynman gauge:

$$a, \mu \quad \begin{array}{c} \text{P} \\ \longrightarrow \\ \text{~~~~~} \end{array} \quad b, \nu \quad = \quad \frac{-i\delta_{ab}P_{\mu\nu}}{p^2 - m_g^2 + i\epsilon}, \quad (\text{B.11.1})$$

where $P_{\mu\nu}$, given by Eq.(12) from [188] (specifically $P_{\mu\nu} = g_{\mu\nu} - \frac{p_\mu p_\nu n^2 + n_\mu n_\nu p^2 - n_\mu p_\nu (np) - n_\nu p_\mu (np)}{n^2 p^2 - (np)^2}$), represents the transverse projector. Note that, since the transverse projectors act directly or indirectly on transverse polarization vectors one may immediately replace $P_{\mu\nu}$ with $g_{\mu\nu}$ in gluon propagators, in order to facilitate the calculations. This observation is obvious for off-shell gluon propagator, whereas the derivation for the remaining internal gluon lines is straightforward.

Consistently throughout this section, initial jet propagates long z-axis, 4-momentum is conserved and minus Light cone coordinate of all momenta acquire an additional

term $+m_g^2$ in the numerator compared to massless case (Appendices B.4-B.9), due to relations $k^2 = p^2 = m_g^2$, while the polarizations remain the same.

For the sake of simplicity, in this section we outline only the final expressions for all 11 Feynman diagrams beyond soft-gluon approximation, when the gluon mass is included, since its derivation is similar to the case of massless gluons (Appendix Section B.4-Section B.9) and in order to avoid redundant derivations.

Thus, for M_0 we obtain:

$$M_0 = J_a(p+k)e^{i(p+k)x_0}(-2ig_s)(1-x+x^2)\frac{\boldsymbol{\epsilon} \cdot \mathbf{k}}{\mathbf{k}^2 + m_g^2(1-x+x^2)}(T^c)_{da}. \quad (\text{B.11.2})$$

The expression for $M_{1,1,0}$ now reads:

$$\begin{aligned} M_{1,1,0} = & J_a(p+k)e^{i(p+k)x_0}(-i)(1-x+x^2)(T^c T^{a_1})_{da} T_{a_1} \int \frac{d^2 \mathbf{q}_1}{(2\pi)^2} v(0, \mathbf{q}_1) e^{-i\mathbf{q}_1 \cdot \mathbf{b}_1} \\ & \times (-2ig_s) \frac{\boldsymbol{\epsilon} \cdot (\mathbf{k} - x\mathbf{q}_1)}{(\mathbf{k} - x\mathbf{q}_1)^2 + m_g^2(1-x+x^2)} e^{\frac{i}{2\omega}(\mathbf{k}^2 + \frac{x}{1-x}(\mathbf{k}-\mathbf{q}_1)^2 + \frac{m_g^2(1-x+x^2)}{1-x})(z_1-z_0)}, \end{aligned} \quad (\text{B.11.3})$$

which differs from Eq. (B.5.12) in the term $m_g^2(1-x+x^2)$, which now appears in the denominator and in exponent, accompanying the squared transverse momentum.

Similarly, for $M_{1,0,0}$ and $M_{1,0,1}$ we obtain, respectively:

$$\begin{aligned} M_{1,0,0} = & J_a(p+k)e^{i(p+k)x_0}(-i)(1-x+x^2)(T^{a_1} T^c)_{da} T_{a_1} \int \frac{d^2 \mathbf{q}_1}{(2\pi)^2} v(0, \mathbf{q}_1) e^{-i\mathbf{q}_1 \cdot \mathbf{b}_1} \\ & \times (2ig_s) \frac{\boldsymbol{\epsilon} \cdot \mathbf{k}}{\mathbf{k}^2 + m_g^2(1-x+x^2)} \left(e^{\frac{i}{2\omega}(\mathbf{k}^2 + \frac{x}{1-x}(\mathbf{k}-\mathbf{q}_1)^2 + \frac{m_g^2(1-x+x^2)}{1-x})(z_1-z_0)} \right. \\ & \left. - e^{-\frac{i}{2\omega} \frac{x}{1-x}(\mathbf{k}^2 - (\mathbf{k}-\mathbf{q}_1)^2)(z_1-z_0)} \right), \end{aligned} \quad (\text{B.11.4})$$

$$\begin{aligned} M_{1,0,1} = & J_a(p+k)e^{i(p+k)x_0}(-i)(1-x+x^2)[T^c, T^{a_1}]_{da} T_{a_1} \int \frac{d^2 \mathbf{q}_1}{(2\pi)^2} v(0, \mathbf{q}_1) e^{-i\mathbf{q}_1 \cdot \mathbf{b}_1} \\ & \times (2ig_s) \frac{\boldsymbol{\epsilon} \cdot (\mathbf{k} - \mathbf{q}_1)}{(\mathbf{k} - \mathbf{q}_1)^2 + m_g^2(1-x+x^2)} \left(e^{\frac{i}{2\omega}(\mathbf{k}^2 + \frac{x}{1-x}(\mathbf{k}-\mathbf{q}_1)^2 + \frac{m_g^2(1-x+x^2)}{1-x})(z_1-z_0)} \right. \\ & \left. - e^{\frac{i}{2\omega}(\mathbf{k}^2 - (\mathbf{k}-\mathbf{q}_1)^2)(z_1-z_0)} \right). \end{aligned} \quad (\text{B.11.5})$$

Proceeding in the similar manner, we obtain the following expressions for contact

limit diagrams which include interactions with two scattering centers:

$$\begin{aligned}
M_{2,2,0}^c &= -J_a(p+k)e^{i(p+k)x_0}(T^c T^{a_2} T^{a_1})_{da} T_{a_2} T_{a_1} (1-x+x^2) \\
&\times (-i) \int \frac{d^2 \mathbf{q}_1}{(2\pi)^2} (-i) \int \frac{d^2 \mathbf{q}_2}{(2\pi)^2} v(0, \mathbf{q}_1) v(0, \mathbf{q}_2) e^{-i(\mathbf{q}_1 + \mathbf{q}_2) \cdot \mathbf{b}_1} \frac{1}{2} (2ig_s) \\
&\times \frac{\boldsymbol{\epsilon} \cdot (\mathbf{k} - x(\mathbf{q}_1 + \mathbf{q}_2))}{(\mathbf{k} - x(\mathbf{q}_1 + \mathbf{q}_2))^2 + m_g^2(1-x+x^2)} e^{\frac{i}{2\omega}(\mathbf{k}^2 + \frac{x}{1-x}(\mathbf{k} - \mathbf{q}_1 - \mathbf{q}_2)^2 + \frac{m_g^2(1-x+x^2)}{1-x})(z_1 - z_0)},
\end{aligned} \tag{B.11.6}$$

$$\begin{aligned}
M_{2,0,3}^c &= J_a(p+k)e^{i(p+k)x_0} [[T^c, T^{a_2}], T^{a_1}]_{da} T_{a_2} T_{a_1} (1-x+x^2) (-i) \int \frac{d^2 \mathbf{q}_1}{(2\pi)^2} \\
&\times (-i) \int \frac{d^2 \mathbf{q}_2}{(2\pi)^2} v(0, \mathbf{q}_1) v(0, \mathbf{q}_2) e^{-i(\mathbf{q}_1 + \mathbf{q}_2) \cdot \mathbf{b}_1} \frac{1}{2} (2ig_s) \frac{\boldsymbol{\epsilon} \cdot (\mathbf{k} - \mathbf{q}_1 - \mathbf{q}_2)}{(\mathbf{k} - \mathbf{q}_1 - \mathbf{q}_2)^2 + m_g^2(1-x+x^2)} \\
&\times \left(e^{\frac{i}{2\omega}(\mathbf{k}^2 + \frac{x}{1-x}(\mathbf{k} - \mathbf{q}_1 - \mathbf{q}_2)^2 + \frac{m_g^2(1-x+x^2)}{1-x})(z_1 - z_0)} - e^{\frac{i}{2\omega}(\mathbf{k}^2 - (\mathbf{k} - \mathbf{q}_1 - \mathbf{q}_2)^2)(z_1 - z_0)} \right),
\end{aligned} \tag{B.11.7}$$

$$\begin{aligned}
M_{2,0,0}^c &= J_a(p+k)e^{i(p+k)x_0} (T^{a_2} T^{a_1} T^c)_{da} T_{a_2} T_{a_1} (1-x+x^2) (-i) \int \frac{d^2 \mathbf{q}_1}{(2\pi)^2} \\
&\times (-i) \int \frac{d^2 \mathbf{q}_2}{(2\pi)^2} v(0, \mathbf{q}_1) v(0, \mathbf{q}_2) e^{-i(\mathbf{q}_1 + \mathbf{q}_2) \cdot \mathbf{b}_1} \frac{1}{2} (2ig_s) \frac{\boldsymbol{\epsilon} \cdot \mathbf{k}}{\mathbf{k}^2 + m_g^2(1-x+x^2)} \\
&\times \left(e^{\frac{i}{2\omega}(\mathbf{k}^2 + \frac{x}{1-x}(\mathbf{k} - \mathbf{q}_1 - \mathbf{q}_2)^2 + \frac{m_g^2(1-x+x^2)}{1-x})(z_1 - z_0)} - e^{\frac{i}{2\omega} \frac{x}{1-x} ((\mathbf{k} - \mathbf{q}_1 - \mathbf{q}_2)^2 - \mathbf{k}^2)(z_1 - z_0)} \right),
\end{aligned} \tag{B.11.8}$$

$$\begin{aligned}
M_{2,0,1}^c &= J_a(p+k)e^{i(p+k)x_0} (T^{a_2} [T^c, T^{a_1}])_{da} T_{a_2} T_{a_1} (1-x+x^2) (-i) \int \frac{d^2 \mathbf{q}_1}{(2\pi)^2} \\
&\times (-i) \int \frac{d^2 \mathbf{q}_2}{(2\pi)^2} v(0, \mathbf{q}_1) v(0, \mathbf{q}_2) e^{-i(\mathbf{q}_1 + \mathbf{q}_2) \cdot \mathbf{b}_1} (2ig_s) \frac{\boldsymbol{\epsilon} \cdot (\mathbf{k} - \mathbf{q}_1)}{(\mathbf{k} - \mathbf{q}_1)^2 + m_g^2(1-x+x^2)} \\
&\times \left(e^{\frac{i}{2\omega}(\mathbf{k}^2 + \frac{x}{1-x}(\mathbf{k} - \mathbf{q}_1 - \mathbf{q}_2)^2 + \frac{m_g^2(1-x+x^2)}{1-x})(z_1 - z_0)} - e^{\frac{i}{2\omega}(\mathbf{k}^2 - \frac{(\mathbf{k} - \mathbf{q}_1)^2}{1-x} + \frac{x}{1-x}(\mathbf{k} - \mathbf{q}_1 - \mathbf{q}_2)^2)(z_1 - z_0)} \right),
\end{aligned} \tag{B.11.9}$$

$$\begin{aligned}
M_{2,0,2}^c &= J_a(p+k)e^{i(p+k)x_0} (T^{a_1} [T^c, T^{a_2}])_{da} T_{a_2} T_{a_1} (1-x+x^2) (-i) \int \frac{d^2 \mathbf{q}_1}{(2\pi)^2} \\
&\times (-i) \int \frac{d^2 \mathbf{q}_2}{(2\pi)^2} v(0, \mathbf{q}_1) v(0, \mathbf{q}_2) e^{-i(\mathbf{q}_1 + \mathbf{q}_2) \cdot \mathbf{b}_1} (2ig_s) \frac{\boldsymbol{\epsilon} \cdot (\mathbf{k} - \mathbf{q}_2)}{(\mathbf{k} - \mathbf{q}_2)^2 + m_g^2(1-x+x^2)} \\
&\times \left(e^{\frac{i}{2\omega}(\mathbf{k}^2 + \frac{x}{1-x}(\mathbf{k} - \mathbf{q}_1 - \mathbf{q}_2)^2 + \frac{m_g^2(1-x+x^2)}{1-x})(z_1 - z_0)} - e^{\frac{i}{2\omega}(\mathbf{k}^2 - \frac{(\mathbf{k} - \mathbf{q}_2)^2}{1-x} + \frac{x}{1-x}(\mathbf{k} - \mathbf{q}_1 - \mathbf{q}_2)^2)(z_1 - z_0)} \right).
\end{aligned} \tag{B.11.10}$$

$$\begin{aligned}
M_{2,1,0}^c &= iJ_a(p+k)e^{i(p+k)x_0}(T^{a_2}T^cT^{a_1})_{da}T_{a_2}T_{a_1}(1-x+x^2)(-i)\int\frac{d^2\mathbf{q}_1}{(2\pi)^2} \\
&\times(-i)\int\frac{d^2\mathbf{q}_2}{(2\pi)^2}v(0,\mathbf{q}_1)v(0,\mathbf{q}_2)e^{-i(\mathbf{q}_1+\mathbf{q}_2)\cdot\mathbf{b}_1}(ig_s)\frac{\boldsymbol{\epsilon}\cdot(\mathbf{k}-x\mathbf{q}_1)}{(\mathbf{k}-x\mathbf{q}_1)^2+m_g^2(1-x+x^2)} \\
&\times e^{\frac{i}{2\omega}(\mathbf{k}^2+\frac{x}{1-x}(\mathbf{k}-\mathbf{q}_1-\mathbf{q}_2)^2+\frac{m_g^2(1-x+x^2)}{1-x})(z_1-z_0)}\frac{\mu_{1\perp}^2+\mu_{1\perp}\mu_{2\perp}+\mu_{2\perp}^2}{\mu_{1\perp}\mu_{2\perp}} \\
&\times\frac{(\mathbf{k}-x\mathbf{q}_1)^2+m_g^2(1-x+x^2)}{x(1-x)E^+(\mu_{1\perp}+\mu_{2\perp})}, \tag{B.11.11}
\end{aligned}$$

and:

$$\begin{aligned}
M_{2,1,1}^c &= iJ_a(p+k)e^{i(p+k)x_0}([T^c,T^{a_2}]T^{a_1})_{da}T_{a_2}T_{a_1}(1-x+x^2)(-i)\int\frac{d^2\mathbf{q}_1}{(2\pi)^2} \\
&\times(-i)\int\frac{d^2\mathbf{q}_2}{(2\pi)^2}v(0,\mathbf{q}_1)v(0,\mathbf{q}_2)e^{-i(\mathbf{q}_1+\mathbf{q}_2)\cdot\mathbf{b}_1}(ig_s)\frac{\boldsymbol{\epsilon}\cdot(\mathbf{k}-x\mathbf{q}_1-\mathbf{q}_2)}{(\mathbf{k}-x\mathbf{q}_1-\mathbf{q}_2)^2+m_g^2(1-x+x^2)} \\
&\times e^{\frac{i}{2\omega}(\mathbf{k}^2+\frac{x}{1-x}(\mathbf{k}-\mathbf{q}_1-\mathbf{q}_2)^2+\frac{m_g^2(1-x+x^2)}{1-x})(z_1-z_0)}\frac{\mu_{1\perp}^2+\mu_{1\perp}\mu_{2\perp}+\mu_{2\perp}^2}{\mu_{1\perp}\mu_{2\perp}} \\
&\times\frac{(\mathbf{k}-x\mathbf{q}_1-\mathbf{q}_2)^2+m_g^2(1-x+x^2)}{x(1-x)E^+(\mu_{1\perp}+\mu_{2\perp})}. \tag{B.11.12}
\end{aligned}$$

Again we notice that amplitudes $M_{2,1,0}^c$ and $M_{2,1,1}^c$ are suppressed, respectively, by factors of $\mathcal{O}(\frac{(\mathbf{k}-x\mathbf{q}_1)^2+m_g^2(1-x+x^2)}{x(1-x)E^+(\mu_{1\perp}+\mu_{2\perp})})$ and $\mathcal{O}(\frac{(\mathbf{k}-x\mathbf{q}_1-\mathbf{q}_2)^2+m_g^2(1-x+x^2)}{x(1-x)E^+(\mu_{1\perp}+\mu_{2\perp})})$ compared to the remaining amplitudes, and therefore will be omitted in further calculations.

After adding Eqs.(B.11.3, B.11.4, B.11.5), we obtain:

$$\begin{aligned}
\frac{1}{d_T}\text{Tr}\langle|M_1|^2\rangle &= N|J(p+k)|^2(4g_s^2)\frac{1}{A_\perp}(1-x+x^2)^2\int\frac{d^2\mathbf{q}_1}{(2\pi)^2}|v(0,\mathbf{q}_1)|^2\frac{C_2(T)}{d_G} \\
&\left\{2\alpha\left(2\frac{\boldsymbol{\epsilon}\cdot(\mathbf{k}-\mathbf{q}_1)}{(\mathbf{k}-\mathbf{q}_1)^2+\chi}-\frac{\boldsymbol{\epsilon}\cdot\mathbf{k}}{\mathbf{k}^2+\chi}-\frac{\boldsymbol{\epsilon}\cdot(\mathbf{k}-x\mathbf{q}_1)}{(\mathbf{k}-x\mathbf{q}_1)^2+\chi}\right)\frac{\boldsymbol{\epsilon}\cdot(\mathbf{k}-\mathbf{q}_1)}{(\mathbf{k}-\mathbf{q}_1)^2+\chi}\right. \\
&+2\left(\frac{\boldsymbol{\epsilon}\cdot\mathbf{k}}{\mathbf{k}^2+\chi}\text{Tr}((T^c)^2(T^{a_1})^2)-\frac{\boldsymbol{\epsilon}\cdot(\mathbf{k}-x\mathbf{q}_1)}{(\mathbf{k}-x\mathbf{q}_1)^2+\chi}\text{Tr}(T^cT^{a_1}T^cT^{a_1})\right)\frac{\boldsymbol{\epsilon}\cdot\mathbf{k}}{\mathbf{k}^2+\chi} \\
&-2\alpha\left(\frac{\boldsymbol{\epsilon}\cdot(\mathbf{k}-\mathbf{q}_1)}{(\mathbf{k}-\mathbf{q}_1)^2+\chi}-\frac{1}{2}\frac{\boldsymbol{\epsilon}\cdot\mathbf{k}}{\mathbf{k}^2+\chi}-\frac{1}{2}\frac{\boldsymbol{\epsilon}\cdot(\mathbf{k}-x\mathbf{q}_1)}{(\mathbf{k}-x\mathbf{q}_1)^2+\chi}\right)\frac{\boldsymbol{\epsilon}\cdot(\mathbf{k}-\mathbf{q}_1)}{(\mathbf{k}-\mathbf{q}_1)^2+\chi} \\
&\times 2\cos\left(\frac{(\mathbf{k}-\mathbf{q}_1)^2+\chi}{x(1-x)E^+}(z_1-z_0)\right)+\left(\frac{\boldsymbol{\epsilon}\cdot(\mathbf{k}-x\mathbf{q}_1)}{(\mathbf{k}-x\mathbf{q}_1)^2+\chi}\right)^2\text{Tr}((T^c)^2(T^{a_1})^2) \\
&+ \left(\alpha\frac{\boldsymbol{\epsilon}\cdot(\mathbf{k}-\mathbf{q}_1)}{(\mathbf{k}-\mathbf{q}_1)^2+\chi}-\frac{\boldsymbol{\epsilon}\cdot\mathbf{k}}{\mathbf{k}^2+\chi}\text{Tr}((T^c)^2(T^{a_1})^2)+\frac{\boldsymbol{\epsilon}\cdot(\mathbf{k}-x\mathbf{q}_1)}{(\mathbf{k}-x\mathbf{q}_1)^2+\chi}\text{Tr}(T^cT^{a_1}T^cT^{a_1})\right) \\
&\times\frac{\boldsymbol{\epsilon}\cdot\mathbf{k}}{\mathbf{k}^2+\chi}2\cos\left(\frac{\mathbf{k}^2+\chi}{x(1-x)E^+}(z_1-z_0)\right)-\alpha\frac{\boldsymbol{\epsilon}\cdot\mathbf{k}}{\mathbf{k}^2+\chi}\frac{\boldsymbol{\epsilon}\cdot(\mathbf{k}-\mathbf{q}_1)}{(\mathbf{k}-\mathbf{q}_1)^2+\chi} \\
&\times 2\cos\left(\frac{\mathbf{k}^2-(\mathbf{k}-\mathbf{q}_1)^2}{x(1-x)E^+}(z_1-z_0)\right)\left.\right\}, \tag{B.11.13}
\end{aligned}$$

where we introduced a shorthand notation $\chi = m_g^2(1-x+x^2)$ in order to obtain more concise expressions, and which we will use further in this section.

Likewise, after adding Eqs.(B.11.6)-(B.11.10), we obtain:

$$\begin{aligned}
\frac{2}{d_T} Re \text{Tr} \langle M_2 M_0^* \rangle &= N |J(p+k)|^2 (4g_s^2) \frac{1}{A_\perp} (1-x+x^2)^2 \int \frac{d^2 \mathbf{q}_1}{(2\pi)^2} |v(0, \mathbf{q}_1)|^2 \frac{C_2(T)}{d_G} \\
&\times \left\{ \left(\frac{\boldsymbol{\epsilon} \cdot \mathbf{k}}{\mathbf{k}^2 + \chi} \right)^2 \left(2\alpha \cos \left(\frac{\mathbf{k}^2 + \chi}{x(1-x)E^+} (z_1 - z_0) \right) - 2\alpha - \text{Tr}((T^c)^2 (T^{a_1})^2) \right) \right. \\
&- 2\alpha \frac{\boldsymbol{\epsilon} \cdot \mathbf{k}}{\mathbf{k}^2 + \chi} \frac{\boldsymbol{\epsilon} \cdot (\mathbf{k} - \mathbf{q}_1)}{(\mathbf{k} - \mathbf{q}_1)^2 + \chi} \left(\cos \left(\frac{\mathbf{k}^2 + \chi}{x(1-x)E^+} (z_1 - z_0) \right) \right. \\
&\left. \left. - \cos \left(\frac{\mathbf{k}^2 - (\mathbf{k} - \mathbf{q}_1)^2}{x(1-x)E^+} (z_1 - z_0) \right) \right) \right\}, \tag{B.11.14}
\end{aligned}$$

leading to:

$$\begin{aligned}
\frac{1}{d_T} \text{Tr} \langle |M_1|^2 \rangle + \frac{2}{d_T} Re \text{Tr} \langle M_2 M_0^* \rangle &= N d_G |J(p+k)|^2 (4g_s^2) \frac{C_2(T)}{d_G} C_2^2(G) \frac{1}{A_\perp} (1-x+x^2)^2 \\
&\times \int \frac{d^2 \mathbf{q}_1}{(2\pi)^2} |v(0, \mathbf{q}_1)|^2 \left\{ \left(1 - \cos \left(\frac{\mathbf{k}^2 + \chi}{x(1-x)E^+} (z_1 - z_0) \right) \right) \left(\frac{\boldsymbol{\epsilon} \cdot \mathbf{k}}{\mathbf{k}^2 + \chi} - \frac{\boldsymbol{\epsilon} \cdot (\mathbf{k} - x\mathbf{q}_1)}{(\mathbf{k} - x\mathbf{q}_1)^2 + \chi} \right) \frac{\boldsymbol{\epsilon} \cdot \mathbf{k}}{\mathbf{k}^2 + \chi} \right. \\
&+ \left(1 - \cos \left(\frac{(\mathbf{k} - \mathbf{q}_1)^2 + \chi}{x(1-x)E^+} (z_1 - z_0) \right) \right) \left(2 \frac{\boldsymbol{\epsilon} \cdot (\mathbf{k} - \mathbf{q}_1)}{(\mathbf{k} - \mathbf{q}_1)^2 + \chi} - \frac{\boldsymbol{\epsilon} \cdot \mathbf{k}}{\mathbf{k}^2 + \chi} - \frac{\boldsymbol{\epsilon} \cdot (\mathbf{k} - x\mathbf{q}_1)}{(\mathbf{k} - x\mathbf{q}_1)^2 + \chi} \right) \\
&\left. \times \frac{\boldsymbol{\epsilon} \cdot (\mathbf{k} - \mathbf{q}_1)}{(\mathbf{k} - \mathbf{q}_1)^2 + \chi} + \left(\left(\frac{\boldsymbol{\epsilon} \cdot (\mathbf{k} - x\mathbf{q}_1)}{(\mathbf{k} - x\mathbf{q}_1)^2 + \chi} \right)^2 - \left(\frac{\boldsymbol{\epsilon} \cdot \mathbf{k}}{\mathbf{k}^2 + \chi} \right)^2 \right) \right\}. \tag{B.11.15}
\end{aligned}$$

In the soft-gluon approximation the previous expression coincides with Eq.(82) from [189] (note that contrary to the cited paper, we here consider gluon jet, so that M no longer denotes heavy quark mass, but instead $M \equiv m_g$ and therefore the term $M^2 x^2$ is also negligible).

If we further apply the same procedure as in Appendix Section B.10, and again assume the simple exponential distribution $e^{-2\frac{z_1-z_0}{L}}$ between the scattering centers, we obtain:

$$\begin{aligned}
\frac{dN_g^{(1)}}{dx} &= \frac{C_2(G)\alpha_s}{\pi} \frac{L}{\lambda} \frac{(1-x+x^2)^2}{x(1-x)} \int \frac{d^2 \mathbf{q}_1}{\pi} \frac{\mu_E^2}{(\mathbf{q}_1^2 + \mu_E^2)^2} \int d\mathbf{k}^2 \\
&\times \left\{ \frac{(\mathbf{k} - \mathbf{q}_1)^2 + \chi}{\left(\frac{4x(1-x)E}{L} \right)^2 + ((\mathbf{k} - \mathbf{q}_1)^2 + \chi)^2} \left(2 \frac{(\mathbf{k} - \mathbf{q}_1)^2}{(\mathbf{k} - \mathbf{q}_1)^2 + \chi} - \frac{\mathbf{k} \cdot (\mathbf{k} - \mathbf{q}_1)}{\mathbf{k}^2 + \chi} \right) \right. \\
&- \frac{(\mathbf{k} - \mathbf{q}_1) \cdot (\mathbf{k} - x\mathbf{q}_1)}{(\mathbf{k} - x\mathbf{q}_1)^2 + \chi} \left. + \frac{\mathbf{k}^2 + \chi}{\left(\frac{4x(1-x)E}{L} \right)^2 + (\mathbf{k}^2 + \chi)^2} \left(\frac{\mathbf{k}^2}{\mathbf{k}^2 + \chi} - \frac{\mathbf{k} \cdot (\mathbf{k} - x\mathbf{q}_1)}{(\mathbf{k} - x\mathbf{q}_1)^2 + \chi} \right) \right. \\
&\left. + \left(\frac{(\mathbf{k} - x\mathbf{q}_1)^2}{((\mathbf{k} - x\mathbf{q}_1)^2 + \chi)^2} - \frac{\mathbf{k}^2}{(\mathbf{k}^2 + \chi)^2} \right) \right\}, \tag{B.11.16}
\end{aligned}$$

which is symmetric to the exchange of p and k gluons, as expected, and also:

$$\begin{aligned}
\frac{dE^{(1)}}{dx} &= \frac{C_2(G)\alpha_s L}{\pi \lambda} E \frac{(1-x+x^2)^2}{1-x} \int \frac{d^2\mathbf{q}_1}{\pi} \frac{\mu_E^2}{(\mathbf{q}_1^2 + \mu_E^2)^2} \int d\mathbf{k}^2 \\
&\times \left\{ \frac{(\mathbf{k} - \mathbf{q}_1)^2 + \chi}{\left(\frac{4x(1-x)E}{L}\right)^2 + ((\mathbf{k} - \mathbf{q}_1)^2 + \chi)^2} \left(2 \frac{(\mathbf{k} - \mathbf{q}_1)^2}{(\mathbf{k} - \mathbf{q}_1)^2 + \chi} - \frac{\mathbf{k} \cdot (\mathbf{k} - \mathbf{q}_1)}{\mathbf{k}^2 + \chi} \right. \right. \\
&- \left. \frac{(\mathbf{k} - \mathbf{q}_1) \cdot (\mathbf{k} - x\mathbf{q}_1)}{(\mathbf{k} - x\mathbf{q}_1)^2 + \chi} \right) + \frac{\mathbf{k}^2 + \chi}{\left(\frac{4x(1-x)E}{L}\right)^2 + (\mathbf{k}^2 + \chi)^2} \left(\frac{\mathbf{k}^2}{\mathbf{k}^2 + \chi} - \frac{\mathbf{k} \cdot (\mathbf{k} - x\mathbf{q}_1)}{(\mathbf{k} - x\mathbf{q}_1)^2 + \chi} \right) \\
&+ \left. \left(\frac{(\mathbf{k} - x\mathbf{q}_1)^2}{((\mathbf{k} - x\mathbf{q}_1)^2 + \chi)^2} - \frac{\mathbf{k}^2}{(\mathbf{k}^2 + \chi)^2} \right) \right\}, \tag{B.11.17}
\end{aligned}$$

which, in the soft-gluon approximation, reduces to Eq.(84) from [189], and which for $m_g \rightarrow 0$ coincides with our massless beyond soft-gluon approximation expression (B.10.13).

Further, we display the beyond soft-gluon approximation expressions needed for numerical evaluation of the corresponding variables. So the number of radiated gluons to the first order in opacity for gluons with effective mass m_g and for a finite x reads:

$$\begin{aligned}
N_g^{(1)} &= \frac{C_2(G)\alpha_s L}{\pi \lambda} \int_0^{\frac{1}{2}} dx \frac{(1-x+x^2)^2}{x(1-x)} \int \frac{d^2\mathbf{q}_1}{\pi} \frac{\mu_E^2}{(\mathbf{q}_1^2 + \mu_E^2)^2} \int d\mathbf{k}^2 \\
&\times \left\{ \frac{(\mathbf{k} - \mathbf{q}_1)^2 + \chi}{\left(\frac{4x(1-x)E}{L}\right)^2 + ((\mathbf{k} - \mathbf{q}_1)^2 + \chi)^2} \left(2 \frac{(\mathbf{k} - \mathbf{q}_1)^2}{(\mathbf{k} - \mathbf{q}_1)^2 + \chi} - \frac{\mathbf{k} \cdot (\mathbf{k} - \mathbf{q}_1)}{\mathbf{k}^2 + \chi} \right. \right. \\
&- \left. \frac{(\mathbf{k} - \mathbf{q}_1) \cdot (\mathbf{k} - x\mathbf{q}_1)}{(\mathbf{k} - x\mathbf{q}_1)^2 + \chi} \right) + \frac{\mathbf{k}^2 + \chi}{\left(\frac{4x(1-x)E}{L}\right)^2 + (\mathbf{k}^2 + \chi)^2} \left(\frac{\mathbf{k}^2}{\mathbf{k}^2 + \chi} - \frac{\mathbf{k} \cdot (\mathbf{k} - x\mathbf{q}_1)}{(\mathbf{k} - x\mathbf{q}_1)^2 + \chi} \right) \\
&+ \left. \left(\frac{(\mathbf{k} - x\mathbf{q}_1)^2}{((\mathbf{k} - x\mathbf{q}_1)^2 + \chi)^2} - \frac{\mathbf{k}^2}{(\mathbf{k}^2 + \chi)^2} \right) \right\}. \tag{B.11.18}
\end{aligned}$$

Similarly, the fractional energy loss is obtained after numerically integrating the following expression:

$$\begin{aligned}
\frac{\Delta E^{(1)}}{E} &= \frac{C_2(G)\alpha_s L}{\pi \lambda} \int_0^{\frac{1}{2}} dx \frac{(1-x+x^2)^2}{1-x} \int \frac{d^2\mathbf{q}_1}{\pi} \frac{\mu_E^2}{(\mathbf{q}_1^2 + \mu_E^2)^2} \int d\mathbf{k}^2 \\
&\times \left\{ \frac{(\mathbf{k} - \mathbf{q}_1)^2 + \chi}{\left(\frac{4x(1-x)E}{L}\right)^2 + ((\mathbf{k} - \mathbf{q}_1)^2 + \chi)^2} \left(2 \frac{(\mathbf{k} - \mathbf{q}_1)^2}{(\mathbf{k} - \mathbf{q}_1)^2 + \chi} - \frac{\mathbf{k} \cdot (\mathbf{k} - \mathbf{q}_1)}{\mathbf{k}^2 + \chi} \right. \right. \\
&- \left. \frac{(\mathbf{k} - \mathbf{q}_1) \cdot (\mathbf{k} - x\mathbf{q}_1)}{(\mathbf{k} - x\mathbf{q}_1)^2 + \chi} \right) + \frac{\mathbf{k}^2 + \chi}{\left(\frac{4x(1-x)E}{L}\right)^2 + (\mathbf{k}^2 + \chi)^2} \left(\frac{\mathbf{k}^2}{\mathbf{k}^2 + \chi} - \frac{\mathbf{k} \cdot (\mathbf{k} - x\mathbf{q}_1)}{(\mathbf{k} - x\mathbf{q}_1)^2 + \chi} \right) \\
&+ \left. \left(\frac{(\mathbf{k} - x\mathbf{q}_1)^2}{((\mathbf{k} - x\mathbf{q}_1)^2 + \chi)^2} - \frac{\mathbf{k}^2}{(\mathbf{k}^2 + \chi)^2} \right) \right\}. \tag{B.11.19}
\end{aligned}$$

Биографија

Бојана Благојевић је рођена у Приједору, Босна и Херцеговина, 24. VIII 1984. године. У Добоју је завршила основну школу и гимназију Јован Дучић, као ђак генерације. Јуна 2003. године била је победник Физичке олимпијаде Босне и Херцеговине, а августа 2003. учествовала је на 34. Међународној физичкој олимпијади у Тајпеху, Тајван.

Основне академске студије на Физичком факултету Универзитета у Београду, смер Теоријска и експериментална физика, започиње 2003. године и завршава их 2013. године са просечном оценом 10,00, одбранивши дипломски рад на тему Продукција, масе и распада суперсиметричних честица у оквиру m_{SSM} модела на LHC-у. Дипломски рад је израђен у Лабораторији за физику високих енергија Института за физику у Београду, а израдом рада руководила је др Марија Враћеш Милосављевић, са Института за физику. Академске 2013/2014. године уписује докторске академске студије на Физичком факултету Универзитета у Београду, ужа научна област Физика честица и поља.

Бојана Благојевић је започела свој истраживачки рад у Лабораторији за физику високих енергија Института за физику у Београду, у новембру 2012. године, а запослена је од 30. VI 2013. године. Ангажована је на пројекту основних истраживања ОН171004 (ATLAS експеримент и физика честица на LHC енергијама) Министарства просвете, науке и технолошког развоја Републике Србије, где се бави теоријском физиком кварк-глуонске плазме (QGP) под менторством др Магдалене Ђорђевић, научног саветника Института за физику. QGP је ново стање материје у којем су кваркови и глуони асимптотски слободни, и које је креирано у ултра-релативистичким сударима тешких јона у RHIC (Relativistic Heavy Ion Collider, Brookhaven National Laboratory) и LHC (Large Hadron Collider, CERN) експериментима. Конкретно, кандидаткиња ради на теоријским предвиђањима супресије (промене дистрибуција енергије) цетова, на поређењу добијених предвиђања са експерименталним резултатима и теоријским прорачунима. Од јуна 2014. године ангажована је и на пројекту SNSF SCOPES IZ73Z0-152297, под менторством др Марка Ђорђевића (ванредног професора на Биолошком факултету Универзитета у Београду) и др Магдалене Ђорђевић, где се бави теоријским проучавањем имуног система бактерија и

регулације експресије гена.

Током основних академских студија Бојана Благојевић је награђена Eurobank EFG школариницом, која се додељује најбољим студентима завршне године државних факултета за остварене изванредне резултате током студија. Током академске 2006/2007. године била је стипендиста фонда Проф. др Ђорђе Живановић као један од најбољих студената III године физике на Физичком факултету.

Током септембра 2014. године Бојана Благојевић је била учесник конференције Hot Quarks 2014, Workshop for young scientists on the physics of ultrarelativistic nucleus-nucleus collisions у Лас Неграсу, Андалузија, Шпанија, где је одржала предавање под називом Energy loss in jet suppression - what effects matter?. Током јуна и јула 2015. године била је полазник летње школе Helmholtz International Summer School, Dubna International Advanced School of Theoretical Physics, Dense Matter 2015 која је одржана у Дубни, Русија. Такође у Дубни је, током јула 2015. учествовала на конференцији Strangeness in Quark Matter, где је одржала предавање под називом Importance of different energy loss effects in jet suppression at RHIC and LHC.

Током јуна 2016. године била је учесник конференције Belgrade BioInformatics Conference 2016, у Београду, Србија, где је одржала предавање под називом Explaining regulatory features of bacterial R-M systems through theoretical modeling. Током августа 2016. године кандидаткиња је била полазник школе Young Scientists School, Systems Biology and Bioinformatics 2016 у Новосибирску, Русија, где је одржала предавање под називом The role of different regulatory features in achieving safe and efficient R-M system establishment. Такође у Новосибирску је, током августа и септембра 2016. године, учествовала на конференцији The 10th International Multiconference Bioinformatics of Genome Regulation and Structure/Systems Biology 2016 (BGRS/SB 2016), где је презентovala постер под називом Design of bacterial restriction-modification systems: relating the system architecture with its dynamical response. Крајем децембра 2016. године, заједно са Анђелом Родић, одржала је предавање на Биоинформатичком семинару Математичког факултета Универзитета у Београду под називом: CRISPR/Cas and restriction-modification systems: modeling dynamics of bacterial immune system

expression.

У мају 2018. године учествовала је на конференцији The 27th International Conference on Ultrarelativistic Nucleus-Nucleus Collisions, Quark Matter 2018, у Венецији, Италија, где је презентovala постер под називом Soft-gluon approximation in calculating radiative energy loss of high p_{\perp} particles - is it well-founded?. Током јуна исте године била је учесник конференције Belgrade BioInformatics Conference 2018, у Београду, Србија, где је презентovala е-постер под називом Defining dynamical property observables which ensure efficient restriction-modification systems establishment in bacterial host. Од 8. до 13. септембра 2018. године суделује на конференцији Hot Quarks 2018, 8th Workshop for young scientists on the physics of ultrarelativistic nucleus-nucleus collisions у Текселу, Холандија, где је одржала предавање под називом Testing reliability of the soft-gluon approximation in calculating radiative energy loss of high p_{\perp} particles. Крајем септембра и почетком октобра 2018. године учествовала је на конференцији Hard Probes 2018: International Conference on Hard and Electromagnetic Probes of High-Energy Nuclear Collisions, у Савоју, Француска, где је одржала предавање под називом Hard probe radiative energy loss beyond soft-gluon approximation.

Објављени радови у водећим међународним научним часописима М21:

1. Magdalena Djordjevic, Marko Djordjevic and Bojana Blagojevic, RHIC and LHC jet suppression in non-central collisions, Phys. Lett. B 737, 298-302 (2014).
2. Bojana Blagojevic and Magdalena Djordjevic, Importance of different energy loss effects in jet suppression at RHIC and LHC, J. Phys. G 42, 075105 (2015); такође истакнут и у LabTalk-у.
3. Magdalena Djordjevic, Bojana Blagojevic and Lidija Zivkovic, Mass tomography at different momentum ranges in quark-gluon plasma, Phys. Rev. C 94, 044908 (2016).
4. B. Blagojevic, M. Djordjevic and M. Djordjevic, Calculating hard probe radiative energy loss beyond soft-gluon approximation: Examining the approximation validity, arXiv:nucl-th/1804.07593, Phys. Rev. C (in Press) (2018).

5. Andjela Rodic, Bojana Blagojevic, Evgeny Zdobnov, Magdalena Djordjevic and Marko Djordjevic, Understanding key features of bacterial restriction-modification systems through quantitative modeling , BMC Systems Biology, 11:377, (2017).
6. Andjela Rodic, Bojana Blagojevic, Magdalena Djordjevic, Konstantin Severinov and Marko Djordjevic, Features of CRISPR-Cas Regulation Key to Highly Efficient and Temporally-Specific crRNA Production, Front. Microbiol., 03 November 2017. doi.org/10.3389/fmicb.2017.02139.

Предавање по позиву са скупа националног значаја штампано у целини М61:

1. Jelena Guzina, Andjela Rodic, Bojana Blagojevic and Marko Djordjevic, Modeling and bioinformatics of bacterial immune systems: understanding regulation of CRISPR/Cas and restriction-modification systems, Biologia Serbica: 39 pp. 112-122 (2017).

Објављена саопштења са међународних скупова штампана у целини М33:

1. Bojana Blagojevic and Magdalena Djordjevic, Energy loss in jet suppression - what effects matter?, J. Phys. Conf. Ser. 612, 012006 (2015).
2. Bojana Blagojevic and Magdalena Djordjevic, Modeling jet-medium interactions at RHIC and LHC - which energy loss effect is crucial?, J. Phys. Conf. Ser. 668, 012044 (2016).

Поглавље у Истакнутој монографији међународног значаја М11:

1. Rodic A., Blagojevic B., Djordjevic M. (2018) Systems Biology of Bacterial Immune Systems: Regulation of Restriction-Modification and CRISPR-Cas Systems. In: Rajewsky N., Jurga S., Barciszewski J. (eds) Systems Biology. RNA Technologies. Springer, Cham

Говори два страна језика, енглески (ниво С2 према Заједничком европском оквиру за језике) и немачки (ниво В2 према Заједничком европском оквиру за језике).